The clustering and evolution of optically selected quasi-stellar objects

Boyle, Brian John

THE CLUSTERING AND EVOLUTION OF OPTICALLY SELECTED QUASI-STELLAR OBJECTS

by

Brian John Boyle

January 1986

An account of work done at the Department of Physics and submitted to the University of Durham in accordance with the regulations for admission to the degree of Doctor of Philosophy.

In memoriam

John Bryce Boyle

1915-1967

Preface

The work presented in this thesis was carried out between 1982 and 1985 while the author was a research student under the supervision of Dr. R. Fong, in the Physics department at the University of Durham.

Some of the research was carried out in collaboration with Dr. T. Shanks and Dr. Fong but the majority is the author's own work. This work has not been submitted for any degree, diploma or other qualification at any other university.

Certain results have appeared in the following papers:

Boyle,B.J. 1984, Observatory, **104**, 216.

Boyle,B.J.,Fong,R. and Shanks,T. 1983, in *Quasars and Gravitational Lenses*, 24th Liege Astrophysical Symposium, p348.

Boyle,B.J.,Fong,R. and Shanks,T. 1984, in *Astronomy with Schmidt-Type Telescopes*, ed. M. Capaccioli, (D. Reidel), p467.

Boyle,B.J.,Fong,R.,Shanks,T. and Clowes,R.G. 1985, MNRAS, **216**, 623.

Boyle,B.J.,Fong,R.,Shanks,T. and Peterson,B.A. 1986, in *The Structure and Evolution of Active Galactic Nuclei*, ed. F. Mardirossian, (D. Reidel), in the press.

Shanks,T.,Fong,R. and Boyle,B.J. 1983, Nature, **303**, 156

Contents

ABSTRACT

We investigate methods of selecting complete, redshift limited samples of QSOs, based on broadband search techniques applied to COSMOS machine measurements of UK Schmidt photographic plates. In particular we discuss the ultra-violet excess (UVX) technique, employed to compile unbiased samples of low redshift ($z<2.2$) QSO candidates. Using both conventional and multi-object spectroscopy, we have obtained slit spectra for 450 faint ($17.5<B<20.9$) UVX stellar images, of which 200 are QSOs. The resulting QSO catalogue is therefore amongst the largest and faintest of its kind yet produced. From the QSOs observed in the survey, we confirm that the number magnitude relation, n(B), for low redshift ($z<2.2$) QSOs exhibits a steep power law slope ($d\log n/dB=0.86$) at bright magnitudes ($17.5<B<19.5$), with a sharp turnover to a much flatter slope ($d\log n/dB=0.35$) at fainter magnitudes ($19.5<B<20.9$). Such behaviour in the n(B) relation thus precludes a pure density evolution model from being an adequate representation for the evolution of the QSO luminosity function (LF). On explicit calculation of the QSO LF in discrete redshift intervals, we find that this evolution can, most simply, be parameterised by a pure luminosity evolution model in which the luminosities of QSOs increase as a power law with look-back time. The form of the QSO LF itself is best represented by a 2 power law function which, at $z=0$, is similar in shape and number to the Seyfert galaxy LF. QSOs observed in the spectroscopic survey are also used to provide estimates for $\xi(r)$, the 2-point correlation function, employed to investigate the spatial clustering of QSOs. We find that, at small comoving separations ($r<10h^{-1}$ Mpc), QSOs exhibit strong clustering. The amplitude of this clustering appears to be stronger than that observed for galaxies but not as strong as that observed for Abell clusters. At large scales ($r>50h^{-1}$ Mpc) the lack of clustering evident in the QSO correlation function places strong constraints on the homogeneity of the universe. From a study of the clustering properties of the UVX sample as a whole we find that, on the plane of the sky, UVX stellar objects are significantly anti-correlated with respect to galaxies in clusters. This observation is explained by postulating that dust, lying in foreground clusters of galaxies obscures the QSOs situated behind these clusters at distances implied by a cosmological interpretation of the QSO redshift. Only $A_B=0.2$ mag. of dust absorption is required to produce the observed anti-correlation. Broadband colour techniques have also been extended to search for QSOs at high ($z>2.2$) redshifts. From the surface densities of QSOs found in these searches, we tentatively conclude that, if significant absorption by dust at high redshifts can be ruled out, the rate of luminosity evolution observed for UVX ($z<2.2$) QSOs is slowing down at $z \simeq 2.5$. A physical model in which QSOs are long lived, gradually dimming in luminosity from their epoch of formation at $z>2.2$, to become Seyfert galaxies at the present day, is shown to be compatible with the above observations.

Acknowledgements

I would first like to thank my supervisor, Dr. Richard Fong, for the many useful discussions throughout my postgraduate degree from which I have benefited greatly. I am also indebted to Dr. Tom Shanks whose help and guidance provided much of the inspiration for the work contained within this thesis.

I would also like to thank the following members of staff and postgraduate students (many of whom kindly made data available to me prior to publication) at the Physics department for their valued comments and suggestions: Professor Richard Ellis, Drs Warrick Couch, John Lucey, Nigel Metcalfe, Ray Sharples, Fred Stevenson and fellow students Iain MacLabhrainn and Bahram Mobasher. My thanks also go to Alan Lotts and Dick Myers whose expertise on the SERC STARLINK VAX at the University of Durham was greatly appreciated.

Much of the work contained within this thesis would not have been possible without the combined resources of the COSMOS measuring machine and UK Schmidt Telescope Unit at the Royal Observatory, Edinburgh. I would therefore like to extend my thanks to those responsible for their continued smooth running, in particular Dr Harvey MacGillivray and Eve Thompson at COSMOS and Andy Good, David Morgan and Sue Tritton at UKSTU for putting up with my 'impossible' requests over the last three years.

I am also grateful to the SERC and the University of Durham for providing me with the funds to travel to the Anglo-Australian Telescope and to various conferences both in the U.K. and Europe. I have benefited a great deal from these trips and would like to take this opportunity to thank all those astronomers with whom I have had particularly valuable discussions during the course of my travels: Drs Russell Cannon, Roger Clowes, Peter Gray, Dave Koo, Hermann Marshall, Lance Millar, John Peacock, Bruce Peterson, Steve Phillipps, and Ann Savage.

Finally I would like to thank my family and friends, especially my mother and Shona, without whose continued love, support and encouragement this thesis would never have been completed.

CHAPTER ONE

INTRODUCTION

1.1 General

In the twenty years since the identification of the first quasi-stellar object (QSO) by Maarten Schmidt (1963), a great deal of study has been devoted to understanding the nature of these most extraordinary objects. Much of the motivation for such study rests on a cosmological interpretation of their high redshifts, making them the most luminous and distant objects in the universe. As such, analysis of their clustering and evolution makes it possible to investigate the nature of the universe at early epochs and affords an opportunity to understand the physical processes which are responsible for the spectacular properties that QSOs exhibit.

As QSOs exhibit a wide range in their observed properties, a statistical approach will be followed in this thesis to establish the clustering and evolutionary properties of the QSO population as a whole, rather than as individual (and perhaps unrepresentative) objects. The purpose of this introduction will be to present the motivation for the work contained within this thesis by summarising briefly previous results obtained from the statistical analyses of QSO catalogues, highlighting those areas where this thesis may contribute further to our understanding of the QSO phenomenon.

1.2 Selection Techniques

Because QSOs form such a small fraction of the stellar images at high Galactic latitudes, typically less than 1% at B = 16 mag., with this proportion only rising to 5% at B = 20 mag. (Woltjer and Setti 1982), the success of any statistical analysis of the optically selected QSO population is wholly dependent on the technique used to identify the QSOs from amongst the plethora of ordinary Galactic stars. Therefore, the slow progress that has typified statistical studies of these QSOs is perhaps best understood with reference to the manner in which successive selection techniques have come into and gone out of favour and the limitations imposed by such techniques.

Even prior to the identification of the star-like radio source 3C273 as the first QSO (Schmidt 1963), it had been noted that, besides their unusual radio properties, these 'radio-stars' exhibited much bluer colours ($U-B < -0.4$) than ordinary Galactic stars (Matthews and Sandage 1963). As a consequence, ultra-violet excess (UVX) soon became an additional criterion for isolating QSO candidates originally selected from radio source catalogues (Ryle and Sandage 1964). In the course of these searches UVX 'stars' were identified which had no radio emission (Sandage and Veron 1965). Many of these 'radio-quiet' objects were subsequently found to have the same highly redshifted broad emission line spectra as their 'radio-loud' counterparts. Indeed Sandage (1965) went on to demonstrate that the 'radio-quiet' QSOs formed a large fraction of all faint ($B < 19.0$ mag.), UVX stellar images at high Galactic latitudes and, as a result, greatly

outnumbered (by at least 10:1) the QSOs with radio emission.

Although the UVX technique subsequently proved a popular method of selecting candidate QSOs (see eg Braccesi *et al.* 1970), it suffered from two drawbacks. Firstly, large amounts of telescope time were required to obtain redshifts for the QSOs and to reject the not inconsiderable number of Galactic stars. Secondly it soon became clear that the UVX technique was systematically biased against finding high redshift ($z > 2.2$) QSOs (Sandage 1972).

At about this time the first objective prism plates were being successfully used in detecting QSOs from their broad emission lines (Hoag and Schroeder 1970). As redshifts were readily obtainable from the photographic plates and there was no systematic bias against non-UVX objects, the focus of attention changed from UVX to slitless spectroscopy as the favoured QSO technique. For the next few years this technique flourished, producing many QSO catalogues (Hoag and Smith 1977, MacAlpine *et al.* 1977). However, it also became clear that the objective prism technique was subject to numerous, complicated selection effects which could be invoked (Clowes 1981) to account for puzzling differences in the QSO surface density found between different catalogues selected using this technique. In particular slitless spectroscopy is critically dependent on seeing (Sramek and Weedman 1978) and biased towards selecting QSOs in particular redshift ranges where the observed wavelengths of broad emission lines make them easily visible on the photographic emulsion used (Clowes and Savage 1983). These

selection effects thus rendered such QSO catalogues unsuitable for statistically based studies into the clustering and evolution of QSOs (Smith 1981), although they still provide one of the most efficient ways of searching for unusual QSOs, such as broad absorption line QSOs (Hazard *et al.* 1984) and gravitational lenses (Chen 1984). More recently the advance in machine measurement of objective prism plates has led to automated search procedures for QSOs being adopted (see e.g. Clowes *et al.* 1984), but their success in yielding catalogues with well defined selection criteria has yet to be firmly established.

In recent years, therefore, attention has switched back to the UVX technique, with Veron (1983) convincingly demonstrating that the vast majority (>95%) of all low redshift QSOs ($z < 2.2$) can be selected with an appropriate choice of UVX criterion (see figure 1.1). Many new catalogues of UVX objects have therefore been compiled (Formiggini *et al.* 1980, Usher 1981), although the prohibitive amounts of telescope time required to obtain spectra for large numbers of faint objects have led to few having complete spectroscopic coverage. The notable exceptions are the surveys of Schmidt and Green (1983), Marshall and his collaborators (1983b,1984) and Mitchell *et al.* (1984). Even so, these catalogues only contain information for $\simeq$ 200 relatively bright ($B < 19.8$ mag) QSOs in total.

However, with the advent of multi-object spectroscopy, spectra can now be obtained for large numbers of faint objects quickly and efficiently. The compilation of a large, faint QSO catalogue in this manner forms the basis for much of the work

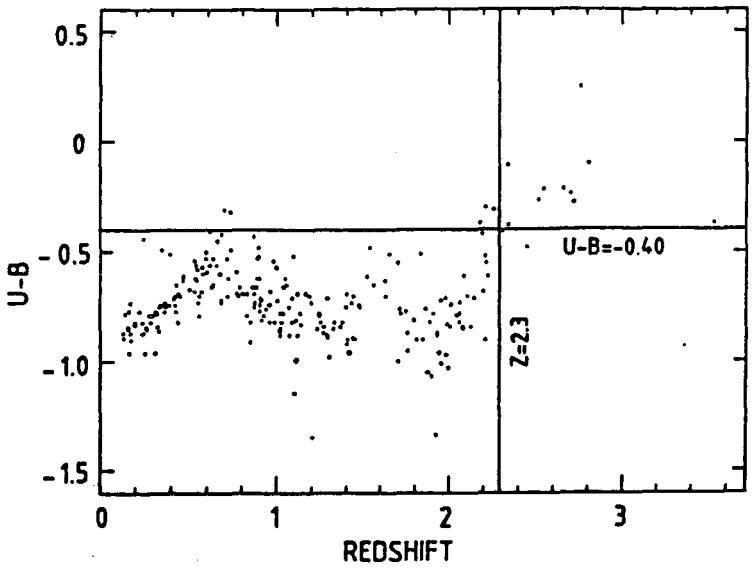

Figure 1.1 U-B v redshift plot for all radio and radioquiet QSOs which have accurate photoelectric photometry. Reproduced from Veron (1983).

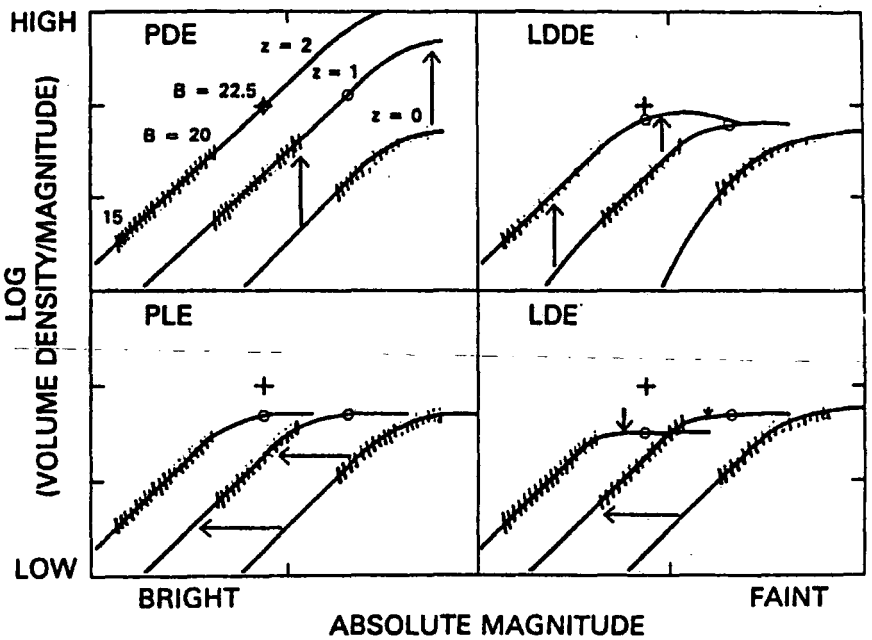

Figure 1.2 Schematic representation of the QSO luminosity function for different evolutionary models. The cross is used as a fiducial mark and circles represent predictions for B = 22.5 mag QSOs. Shaded regions denote previously available observational data on spectroscopically confirmed UVX QSOs. Reproduced from Koo (1986).

presented in this thesis. For the reasons discussed above we choose to select our QSO candidates using the UVX technique. The application of this technique to COSMOS machine measurements of UK Schmidt photographic plates is described in chapter 2. Subsequent spectroscopic observations, carried out using the multi-object facility presently available at the Anglo-Australian Telescope (AAT) are detailed in chapter 3. The resulting QSO catalogue, containing $\simeq$ 200 QSOs to a limiting magnitude of B $\simeq$ 21.0 mag., is amongst the largest and faintest of its kind yet produced. The following sections will demonstrate the role of such a survey in the context of the evolutionary and clustering studies of QSOs.

1.3 QSO Evolution

As with most other classes of astronomical object, the evolutionary time-scale for QSOs is so long that we can not hope to observe individual QSOs evolving directly. We must therefore derive constraints on the form of the evolution through statistical analysis of large QSO catalogues.

The fact that QSOs evolve within a framework of a Friedmann universe has long been established. Number counts, N(<B), for optical QSOs were shown early on to exhibit much steeper slopes (e.g. dlogN/dB = 0.75 from Sandage and Luyten 1969) than those predicted for a non-evolving population (dlogN/dB $\simeq$ 0.35, Schmidt 1978). Such results have been criticised on the basis that the sample size used to derive the evolution was small (Setti and Woltjer 1973) and/or subject to subtle selection effects (Hawkins

and Stewart 1981). However, larger samples (see e.g. Schmidt and Green 1983) and due consideration of the selection effects (Wills 1983), confirm that strong evolution does occur in the QSO population. The nature of this evolution is, however, far less well known and is one of the fundamental goals in the statistical analyses of QSO catalogues.

The form of this evolution is essentially determined by establishing the shape of the QSO luminosity function (i.e. the space density of QSOs as a function of magnitude) and obtaining a parametric representation for its change in shape or position with redshift. This is, however, no mere exercise in statistics as this evolution can provide fundamental insight into the physical mechanisms that are responsible for the QSO phenomemon (Cavaliere *et al.* 1985) as well as establishing the evolutionary link between QSOs and other active galactic nuclei (see e.g. Weedman 1986)

Various models for QSO evolution are illustrated in figure 1.2 (taken from Koo 1986). Pure density evolution (PDE), first proposed to explain the evolution seen in the radio QSO population (Schmidt 1968) and later adopted for optically selected QSOs (Schmidt 1970), involves a uniform shift in the luminosity function (independent of magnitude) towards higher densities at higher redshifts. Such an evolution can, therefore, be strictly described in terms of there being more QSOs in the past, with their numbers typically increasing with redshift as a power law $(1+z)^{6}$ or as an exponential in look back time τ, $\exp(5\tau)$, see Schmidt (1972).

Mathez (1976), however, showed that pure luminosity evolution (PLE) provided an equally good fit to the data for optical QSOs, and this form of evolution has recently come much into favour (Marshall *et al.* 1984). In this model, the luminosity function again preserves its shape but shifts towards brighter magnitudes in the past. As such this parameterisation could represent the gradual dimming of long lived QSOs (Marshall 1985) or the statistical properties of an ensemble of short lived QSOs (Koo 1986).

Recently, more complex evolutionary forms have been proposed. Following models for radio source evolution (Peacock and Gull 1981), Schmidt and Green (1983) proposed luminosity dependent density evolution (LDDE). In this case the amount of density evolution is dependent on the luminosity of the QSO with the brightest QSOs evolving the fastest. Koo (1986) has also provided another variant, namely luminosity and density evolution (LDE). Here the luminosity function preserves its shape but moves both in luminosity and density space.

From figure 1.2 it can easily be seen that all these different forms of evolution appear very nearly identical if the constructed luminosity function is close to a power law. Indeed Longair and Scheuer (1970) have demonstrated that PDE and PLE are entirely equivalent for a pure power law luminosity function.

Unfortunately, the data previously available for optically selected QSOs revealed just such a power law (Marshall 1985) and consequently discrimination between the various evolutionary

models was impossible using solely QSO catalogues limited at bright (B < 20) magnitudes (Marshall *et al.* 1984). However, the turn-over in the number magnitude counts for QSOs, indicated by the low surface densities found by Koo and Kron (1982) at faint magnitudes (see figure 1.3), argues strongly for a feature in the luminosity function (Marshall *et al.* 1983b) and that the evolution can not be modelled by PDE (Cavaliere *et al.* 1983). It is indeed unfortunate that this break should manifest itself at magnitudes where there has been such a scarcity of data - prior to this thesis, there were, in total, less than 40 spectroscopically confirmed QSOs with B > 19.8 mag. As such any feature in the luminosity function could not be determined explicitly, and any preferred evolutionary form could only be derived using an ad hoc representation of the luminosity function at low luminosities (Marshall *et al.* 1983b).

It is clear, therefore, that the large, faint (B < 21.0 mag) UVX QSO survey presented in this thesis provides a unique opportunity to calculate directly the QSO LF at these low luminosities and thus help to discriminate between the evolutionary models proposed. The results of such an analysis are presented in chapter 4.

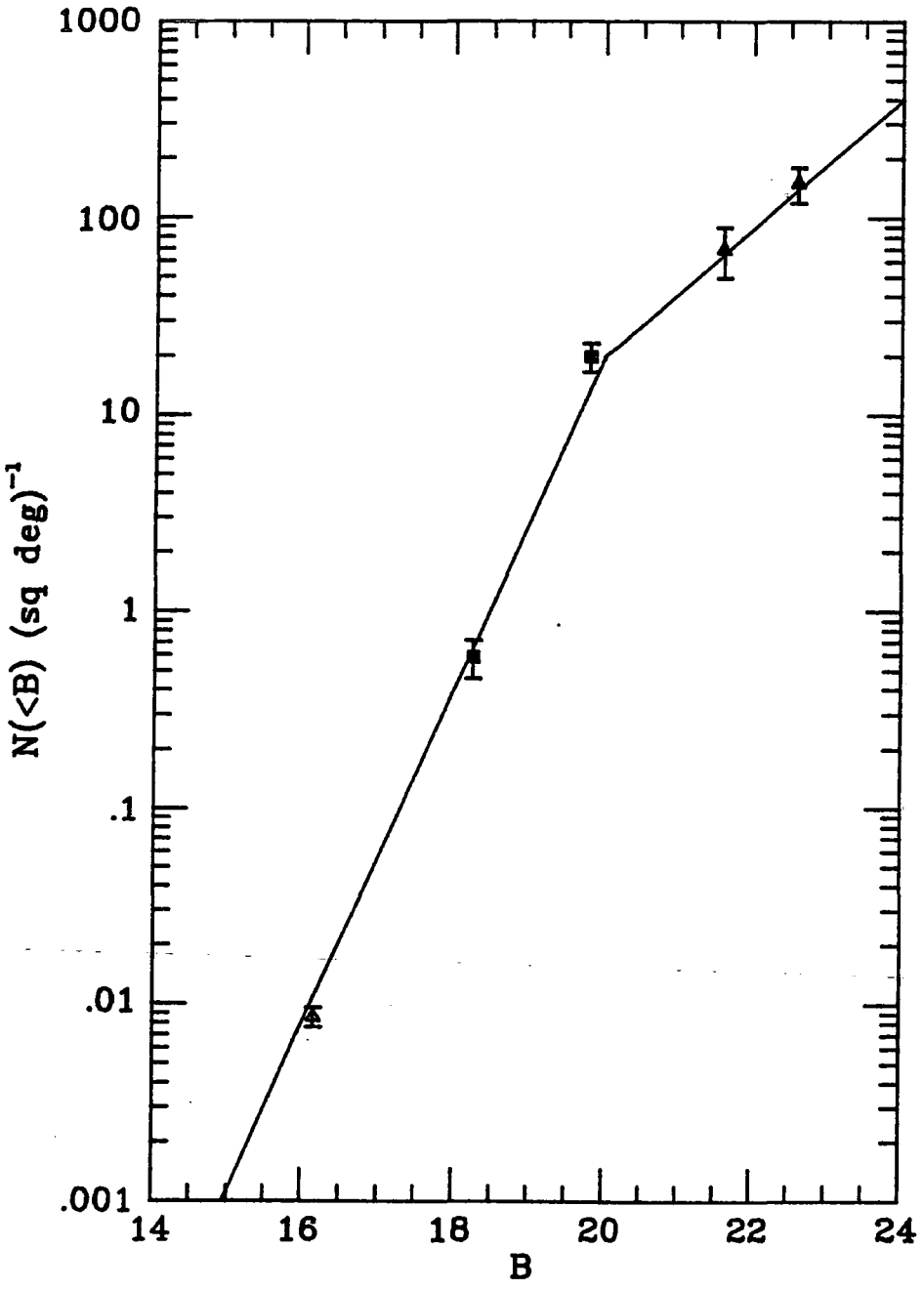

Figure 1.3 Integral N(<B) counts for spectroscopically confirmed QSOs. ▲ denote surface densities obtained from the survey of Schmidt and Green (1983), ■ Marshall *et al.* (1984) and ▲ Koo and Kron (1982).

1.4 QSO Clustering

a) 3D Clustering

The study of the clustering of QSOs affords not only the opportunity to investigate the nature and environment of QSOs themselves but also the possibility of using QSOs as probes to test the structure of the universe at epochs unobservable with galaxies (e.g. Oort *et al.* 1981).

Such studies are, however, critically hampered by the lack of redshift information for QSOs. As a result of the extremely low surface density of QSOs at bright magnitudes, meaningful results on the clustering of QSOs at cosmologically interesting scales (i.e. $< 100h^{-1}$ Mpc [1], the scales at which we observe galaxies and clusters of galaxies to be strongly clustered at the present day, Peebles 1980, Bachall and Soniera 1983) can only be obtained from surveys limited at faint ($B < 20.5$) magnitudes. Until this thesis no UVX selected QSO catalogue contained spectroscopic information to this depth (see e.g. Marshall 1985) and thus most of the work on QSO clustering had centred on catalogues produced from objective prism surveys (Osmer 1981, Chu and Zhu 1983). Although this has revealed some interesting groupings of QSOs (Webster 1982a), the inaccuracy of the redshifts obtainable from prism spectra effectively invalidates the results of any clustering studies at scales less than $50h^{-1}$ Mpc (Savage *et al.* 1985). Moreover, careful account has

[1] Throughout this thesis, h will be used to denote Hubble's constant H_0 in units of 100 km s^{-1} Mpc^{-1}

also to be taken of the complicated redshift dependent selection effects inherent in slitless techniques, before reliable information can be extracted from clustering of prism selected QSOs at the largest scales.

Indeed, knowledge of the 3D clustering of QSOs is so poor that Webster (1982a) found it 'hard to overstate' the case for a large, complete and unbiased QSO sample with which to tackle this problem. As such, the large QSO catalogue presented here is ideally suited to this task. In chapter 5 we therefore report on a 3D correlation analysis of this catalogue, providing the first detailed results on the clustering of QSOs at scales less than $50h^{-1}$ Mpc In addition, such an analysis will provide an accurate indication of the structure of the universe at large scales ($>$ $100h^{-1}$ Mpc) from the form of the QSO correlation function at these separations.

b) 2D Clustering

In the absence of reliable redshift information, much attention has been focussed on the 2D clustering of QSOs on the sky. In particular, this has provoked much speculation about the cosmological interpretation of the QSO redshift (see Field, Arp and Bachall 1973 for a lively discussion!). Scepticism has been fuelled by observations that

a. High redshift QSOs are found preferentially close to low redshift galaxies (Arp 1970, Arp 1981).

b. QSOs with discordant redshifts appear to be clustered on the sky, often in striking collinear associations (Arp and Hazard 1980).

The significance of these groupings is, however, difficult to assess. Some claims for a high statistical significance (Arp 1981) have been criticised for their *a posteriori* reasoning and inconsistent statistical arguments (Webster 1982b).

However, a more rigorous application of statistical techniques has also yielded apparent support for QSO/galaxy associations (Seldner and Peebles 1979), although subtle biases in the catalogues used may account for their result (Nieto and Seldner 1982).

In contrast, strong evidence for QSOs being situated at the distances implied by a cosmological interpretation for their redshifts has come from Stockton (1978) and Yee and Green (1984). Both find faint galaxies preferentially associated with low redshift QSOs.

In chapter 6 we therefore re-test for discordant redshift associations using similar techniques to those employed by Seldner and Peebles (1979) but with the unbiased UVX and galaxy catalogues produced from machine measurement of photographic plates. Moreover, with the results of the spectroscopic survey performed on a sub-sample of the UVX catalogue, we will be able to define precisely the contamination by Galactic stars of such catalogues and thus quantify any effects seen.

1.5 QSOs at High Redshift

Until now we have centred our discussion on the clustering and evolution of low redshift QSOs, primarily because we have been concerned with the implications of the large UVX QSO catalogue compiled in this thesis. However, study of low redshift QSOs has an important part to play when we consider the evolution of high redshift QSOs.

Obtaining the correct form for the evolution of QSOs at low redshift forms an integral step in addressing the study of the QSO 'cut-off' i.e. determining the redshift at which this evolution slows down, stops or reverses sign. The problem of the QSO 'cut-off' is probably one of the most important in cosmology, pointing, as it does, to to an epoch of formation for QSOs and possibly galaxies themselves (Sandage 1972). Establishing the existence of this 'cut-off' is, however, critically dependent on on the selection effects present in searches used to find high redshift QSOs.

In the early 1970s the scarcity of QSOs with redshifts greater than 2.5 prompted many authors (see e.g. Sandage 1972) to consider the possibility of a redshift cut-off in the distribution of QSOs beyond z=2.5. The discovery within a few months of each other, of two radio QSOs 3 at redshifts of 3.40 (Carswell and Strittmatter 1973) and 3.53 (Wampler *et al.* 1973) largely put paid to such speculations and highlighted the shortcomings of the UVX technique then in use for QSO detection. Subsequent work involving extensive searches of objective prism

plates revealed many further QSOs with $3.0 < z < 3.3$ (Osmer and Smith 1977). These QSOs were found in sufficient numbers to prompt Osmer (1980) into claiming that the density of QSOs between $1.9 < z < 3.2$ was consistent with an extrapolation of Schmidt's (1970) pure density evolution law derived at low redshifts.

Although 0Q172 (Wampler *et al.* 1973) remained the highest redshift QSO for ten years, during this period there was some reluctance to accept that a QSO cut-off had been found. This was because many of the searches for high redshift QSOs had been conducted using IIIaJ (blue sensitive) photographic emulsion, whose use was known to be biased against detecting high redshift QSOs (Smith 1978). Osmer (1982) concluded, however, that this cut-off was likely to be real when he discovered no higher redshift QSOs on searches of objective prism plates taken on red sensitive IIIaF emulsion. Futhermore he postulated that, for bright QSOs, the form of the cut-off was indeed dramatic, occurring within the narrow redshift range $3.2 < z < 3.5$. However the recent increase in the number of different methods used in the search for high redshift QSOs (e.g broadband colours, Koo and Kron 1982, proper motion studies, Kron and Chiu 1981) have produced results which challenge the abrupt nature of this 'cut-off', pointing instead to a more gradual fall-off in the numbers of QSOs beyond a redshift as low as 2.5 (see e.g. Koo 1986). Such conclusions are corroborated by the results of recent, conventional prism surveys for high redshift QSOs (Hazard and McMahon 1984). In addition, the recent discoveries of

several QSOs with z > 3.5 (PKS2000-330 z = 3.78 Peterson *et al.* 1982, DHM0054-284 z = 3.61 Shanks *et al.* 1983b, Q0055-2659 z = 3.67 Hazard and McMahon 1984) indicate that the 'cut-off' can not occur as rapidly beyond z = 3.5 as was first thought.

It is the nature of this 'cut-off' that is central to the problem of the QSO formation epoch. Consequently the task of finding yet higher redshift QSOs is secondary to that of determining at which redshift the evolution of QSOs begins to show significant deviation from that observed at low redshift. It is this course that will be followed in chapter 7, when we will compare the surface densities of high redshift QSOs, detected using new broadband techniques, with those predicted from extrapolations of the evolution determined in chapter 4 for the UVX (z < 2.2) QSOs.

Throughout the previous sections we have emphasised the statistical nature of the analysis which will be undertaken in the following chapters. However, as stressed at the beginning of this chapter, one of the fundamental goals in QSO research is to obtain a better physical understanding of the processes that govern the QSO phenomenon. In chapter 8 we therefore conclude this thesis by considering the results presented in the previous chapters in terms of a coherent physical model for QSOs. In doing so we will attempt to reconcile our results with predictions from theoretical studies. Future observations and possible developments in QSO research are also discussed.

CHAPTER TWO

MEASUREMENT OF PHOTOGRAPHIC PLATES

2.1 Introduction

Despite its nonlinearity and low quantum efficiency when compared to modern 2D electronic detectors, the photographic plate is still unrivalled in its panoramic capabilities. Indeed the image content of photographic plates is so high that the objectivity and speed with which they can be measured using modern machines are essential for exploiting their potential to the full. As we will see in this chapter, machine measurement does, however, introduce many problems of its own. These have to be recognised and carefully accounted for before reliable inferences can be drawn from the data produced by such measurement.

In this chapter we will describe the reduction techniques associated with the COSMOS machine measurements of UK Schmidt photographic plates. The star and galaxy catalogues thus produced will form the basis of the work in the following chapters.

2.2 Photographic Material

All the photographic plates used in this work were taken with the 1.2m UK Schmidt Telescope (UKST) at Siding Spring. Table 2.1 contains a complete listing of the plates which are generally of good quality (evidenced by the A and B grades given

Plate	Field Name	RA(1950)	Dec	Date Taken	Emulsion	Filter	Exp. Time (minutes)	Grade
J3721	SGP	00h 53m	-28° 03'	4/11/77	IIIaJ	GG395	80	A
J1921	SGP	00 54	-28 03	25/11/75	IIIaJ	GG395	60	B
B3499	SGP	00 53	-28 03	15/08/77	IIaO	GG385	60	A
U2639	SGP	00 53	-28 03	28/09/76	IIaO	UG1	180	A
U6380	SGP	00 53	-28 03	25/09/80	IIIaJ	UG1	180	A
V3475	SGP	00 53	-28 03	9/08/77	IIaD	GG495	60	A
R2775	SGP	00 53	-28 03	29/09/80	127-04	RG630	90	A
I6427	SGP	00 53	-28 03	29/09/80	IV-N	RG715	90	A
J6124	QSN	01 12	-35 00	12/07/80	IIIaJ	GG395	65	A
J1862	QSC	01 39	-55 00	26/10/75	IIIaJ	GG395	56	B
J1891	QSD	02 00	-50 00	07/11/75	IIIaJ	GG395	65	A
U3487	QSD	02 00	-50 00	13/08/77	IIaO	UG1	90	A
J2672	QSF	03 44	-45 00	28/10/76	IIIaJ	GG395	70	A
U8226	QSF	03 44	-45 00	12/11/82	IIIaJ	UG1	130	A
J7674	QNB	10 40	00 00	17/04/82	IIIaJ	GG395	55	B
J9133S	QNB	10 40	00 00	27/03/84	IIIaJ	GG395	60	A
U7714	QNB	10 40	00 00	26/04/82	IIIaJ	UG1	120	B
V7769	QNB	10 40	00 00	20/05/82	IIaD	GG495	60	B
J5701	QNY	12 30	00 23	21/02/80	IIIaJ	GG395	65	A
U5707	QNY	12 30	00 23	25/02/80	IIIaJ	UG1	180	B
U9216	QNY	12 40	00 00	24/04/84	IIIaJ	UG1	180	A
J9108	QNA	13 40	00 00	7/03/84	IIIaJ	GG395	60	A
U7715	QNA	13 40	00 00	26/04/82	IIIaJ	UG1	120	A
J3390	QSM	22 03	-20 00	17/07/77	IIIaJ	GG395	70	A
U1736	QSM	22 03	-18 55	5/08/75	103aO	UG1	90	A
J3585	QSI	22 32	-40 00	16/09/77	IIIaJ	GG395	75	A
U7120	QSI	22 32	-40 00	7/08/81	IIIaJ	UG1	120	B

Table 2.1 UKST Photographic Plates

to them by the UKST unit). The optical configuration (spherical mirror and corrector) of the UKST allows plates to be taken with a large unvignetted field of view ($5^{\circ} \times 5^{\circ}$). The plates taken represent a number of high Galactic latitude ($b^{II} > 45^{\circ}$) fields spread widely over the sky, affording not only the opportunity to makes tests on the large scale isotropy of the Universe, but also, from a purely practical point of view, allowing follow up spectroscopy to be obtained for at least one of the fields at any time of the year on the Anglo-Australian Telescope (AAT).

Since many fields either fall on non-standard (i.e. non sky-survey) centres or the plates taken in different passbands for the 'same' field do not share exactly the same centre, the fields are assigned the names listed in the second column of table 2.1. These names will be used throughout the thesis, although, apart from the SGP (i.e. South Galactic Pole) field, the names are of historic importance only.

The emulsion-filter combinations used to obtain the U,J,V,R and I plates produce different passbands to those normally encountered in the standard Johnson (1963) UBVRI system (see figure 2.1). As a result we may expect the calibrated magnitudes for both stars and galaxies obtained here to show significant discrepancies from those quoted in the Johnson system. To avoid confusion later, we set out here the definitions of the magnitude systems to be used in this thesis, which will differ for stars and galaxies.

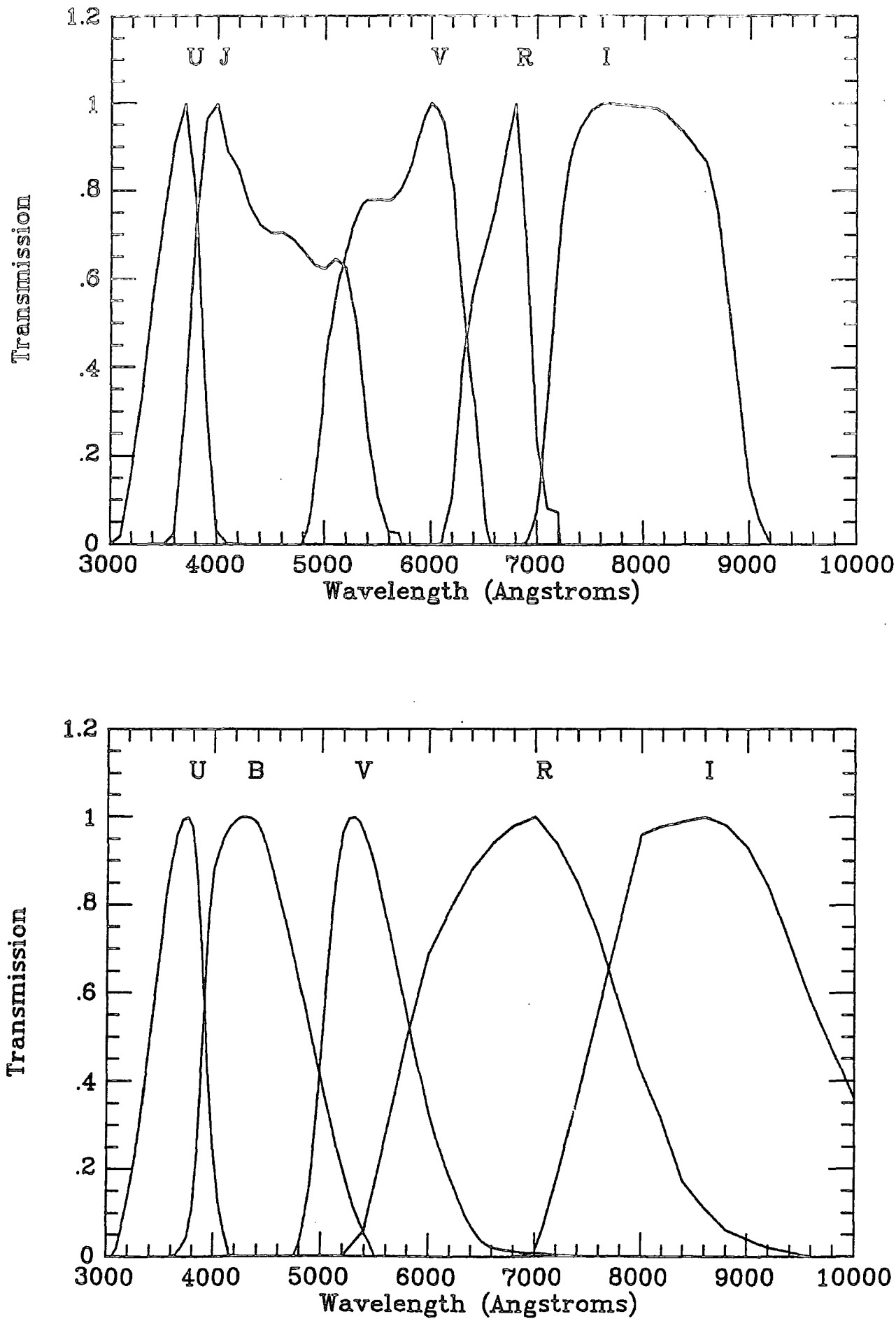

Figure 2.1 a) Bandpasses corresponding to standard emulsion filter combinations of the UK Schmidt telescope. U: IIIaJ/UG1, J: IIIaJ/GG395, V:IIaD/GG495, R:127-04/RG630, I: IV-N/RG715
b) Bandpasses corresponding to the standard Johnson (1963) system.

The magnitudes for stellar images on the JVRI plates have been calibrated using standard photoelectric, electronographic or CCD star sequences quoted in the Johnson BVR and Kron-Cousins I systems with no prior correction for the passband used. Similarly, no passband correction has been applied to the variety of U magnitude systems (i.e. Johnson, photographic and CCD) in which the calibration standards for the U plates were measured. The resulting calibrated stellar magnitudes will therefore be referred to in lower case e.g. ubvri, to illustrate clearly their non-standard nature. However, transformation between b and Johnson B magnitudes (using measurements of the IIaO B plate on the SGP) will be considered in chapter 2.5 as will the relative calibration of the different u magnitudes obtained.

Galaxy magnitudes (only calibrated on J plates) were zero-pointed using photoelectric and CCD measurements which, in contrast to the procedure followed for the stellar calibration, had previously been converted to the Schmidt J passband. Calibrated galaxy magnitudes will therefore be given the designation b_J, to differentiate them clearly from the stellar b magnitude system.

Most fields are covered by at least one pair of U and J plates, enabling the construction of UVX catalogues on these fields. In addition to U and J plates, the SGP field is also covered by V, R and I plates, allowing the compilation of catalogues based on other broadband colour combinations. On the SGP it is also possible to check the accuracy of the photometry using the 2 U and 2 J plates taken on this field. The B plate on

the SGP, B3499, will also be of use when, as indicated above, we come to consider the transformation from the b magnitude system used here to the more standard photoelectric B band (see chapter 2.5). Two fields (QSC and QSN) only have a J plate available. These fields are still useful for providing the galaxy catalogues used in the cross-correlation analysis of chapter 6.

2.3 The COSMOS Machine

The COSMOS measuring machine is basically a computer controlled, high speed microdensitometer. Full details of its operation are given in MacGillivray and Stobie (1985) and only a brief discussion of its relevant features will be entered into here.

Like all microdensitometers, COSMOS measures a photographic plate by recording the amount of light transmitted through the emulsion from a focussed microspot. COSMOS then digitises this information into one of 256 transmission (T) levels. This transmission value is subsequently converted into relative intensity (I) using the log T v log I 'characteristic curve' derived for the plate from measurements of the step wedge provided on each UKST photographic plate. Unlike most other microdensitometers, however, COSMOS uses a flying spot in a raster scan, the consequent gain in speed allowing the unvignetted area ($\simeq$ 25 deg^2) of a UKST plate to be measured in 3.5 hours with a pixel size of 16μm. Unfortunately, the flying spot has a large halo associated with it. This considerably reduces the dynamic range of the COSMOS machine, the implications

of which will become apparent when we come to discuss the calibration of the stellar magnitudes in chapter 2.4.4.

At present COSMOS operates in two modes. Mapping mode (MM) records the transmission value for every pixel on the measured area and is used primarily where complex image processing is needed (e.g objective prism plates, dense star clusters). All plates in this thesis have, however, been measured using the threshold mapping mode (TM). TM is similar to MM but only those pixels whose intensity is greater than a specified percentage (f) above a fitted background (sky) intensity (I_{sky}) are recorded. These pixels are then processed in an off-line pattern analyser which joins pixels together belonging to the same image and calculates a set of parameters for each image. These parameters are listed in table 2.2. As one of these parameters, the machine magnitude (m_{cos}) of an image containing i pixels is defined to be

$$m_{cos} = -2.5\log\sum_{i}\frac{(I_i - I_{sky})}{I_{sky}} \qquad \ldots (2.1)$$

The calibration of this machine magnitude is carried out later using standard star or galaxy sequences (see chapter 2.4).

Use of a percentage cut ($f = (I_{thres} - I_{sky})/I_{sky}$), rather than an arithmetic cut to define the threshold level (I_{thres}) is strictly correct if, as is believed, emulsion sensitivity variations and vignetting are the principal sources of sky background variations (Shanks 1979).

1	X - Unweighted Position
2	Y - Unweighted Position
3	X_{min}
4	X_{max}
5	Y_{min}
6	Y_{max}
7	Area - in pixels
8	T_{min}
9	magnitude - see equation (2.3)
10	I_{sky}
11	X - Intensity Weighted Position
12	Y - Intensity Weighted Position
13	Semi Major Axis)
14	Semi Minor Axis) - Unweighted
15	θ - Orientation)
16	Semi-major axis)
17	Semi-minor axis) - Weighted
18	θ - Orientation)

Table 2.2 COSMOS Image Analysis Parameters

The details of the COSMOS measurements for all plates used in this thesis are given table 2.3. Image analysis marks the final stage of the COSMOS measurement procedure. However, the data is still in a relatively unsophisticated form and has to undergo a number of reduction procedures before it can be used in astronomical applications. This is left to the individual for completion and the description of the procedures followed will form the basis of the next section.

2.4 Reduction of COSMOS data

2.4.1 Bright Images

The COSMOS images analysis software can not deal with very large (> 1 arcminute) images (e.g. stars or galaxies brighter than approximately 10^{th} magnitude, globular clusters), breaking them down into a mosaic of smaller images. Areas including such objects are therefore removed from the COSMOS data and take no further part in the data reduction or subsequent statistical analysis. Each plate has, typically, 4 or 5 such holes 'drilled' in it (see e.g. figure 6.1).

2.4.2 Star-galaxy Separation Techniques

In addition to the automatic discrimination between stellar and galaxian images, various combinations of the COSMOS image-analysis parameters can be used to provide a powerful check on the quality of the data obtained from the machine measurement process. The methods employed here are based on the work of MacGillivray *et al.* (1976) and Shanks *et al.* (1980) and utilise

Plate	Date Measured	Percentage Threshold Cut	m_{obj}
J3721	11/09/79	7	22.65[1]
J1921	5/08/80	7	-
B3499	30/04/84	10	-
U2639	26/04/80	8	-
V3475	30/01/80	10	-
R2775	11/08/80	7	-
I6427	22/04/83	5	-
J6124	12/06/82	10	22.90
J1862	15/01/84	7	21.80
J1891	3/12/83	7	22.10[2]
U3487	18/12/83	7	-
J2672	1/07/84	7	22.10[1]
U8226	21/07/84	7	-
J7674	5/05/84	15	22.20[1]
J9133S	19/01/85	7	21.80[1]
U7714	7/04/84	7	-
V7769	18/02/84	15	-
J5701	5/02/82	7	22.20[1]
U5707	31/12/84	7	-
U9216	6/01/85	7	-
J9108	16/02/85	7	22.55
U7715	25/03/84	7	-
J3390	14/10/82	7	22.15[1]
U1736	6/10/82	7	-
J3585	30/06/84	7	21.90[1]
U7120	19/07/82	35	-

[1] Zero point from Metcalfe (private communication)
[2] Zero point from Ellis (private communication)

Table 2.3 Details of COSMOS Measurements

the image magnitude (m), area (A) and width (σ). The parameter σ is defined to be the standard deviation of a Gaussian fitted to the central intensity and area at threshold of the image. From the parameters listed in table 2.2, it can be calculated as follows:

$$\sigma = 0.302 \sqrt{\frac{A}{\log((I_{max} - I_{sky})/I_{sky}.f)}} \quad \ldots (2.2)$$

where σ is given in pixels.

Regardless of whether or not star-galaxy separation was required, the log A v m and σ v m diagrams were first used to check the quality of the data on each plate. This was done by plotting these diagrams for the images in each of 9 small ($\simeq$ 1 sq. deg.), well separated areas over the plate. Any shift observed for the stellar/galaxian locus in log A v m or σ v m between these areas would then form a strict indication of poor quality data, arising either as a result of non-uniformities in the plate itself (e.g. emulsion variations) or in the measurement process (e.g. defocussing), see Shanks (1979). On any plate displaying these non-uniformities, the usable area was cut down until no shifts were observed over the remaining measured area.

Three plates (J7674, U7714 and U7120) used in this thesis displayed such shifts. On J7674 the non-uniformity was removed by deleting the easternmost and southernmost 1° strips, and the removal of a 2° wide strip from the western edge of U7120 accounted for the non-uniformity seen over this plate. However,

so much of U7714 was affected by these shifts that no reasonably sized area (i.e. < two thirds of the measured area) could be removed to leave a uniform distribution of objects. The poor quality of the data on this plate thus prevented the QNA field from taking part in the 2D clustering analysis discussed in chapter 6. However, since no shifts were observed over the small area in which the stellar calibration sequence and spectroscopic observations lay, this field is still included in the discussion of the UVX survey in chapters 3, 4 and 5.

Having followed the above procedure to remove any existing gradients, star-galaxy separation was then carried out using log A v m and σ v m plots for the images in a central 1 sq. deg. area on each COSMOS J plate listed in table 2.1. Typical diagrams used to define the discrimination lines are given in figure 2.2. The tight stellar locus is clearly visible in these plots, with the extended galaxian images lying above the locus affording a straightforward separation of the stars and galaxies by the solid line. At bright magnitudes (b_J < 19.0 mag - calculated using appropriate zero-point - see table 2.3) log A v m was used as the discriminator between stars and galaxies. At fainter magnitudes log A v m becomes less reliable, and σ v m is used down to a faint limit of b_J = 21.0 mag. Care was taken to ensure that both methods gave the same star and galaxy densities in the magnitude range where they overlapped. Visual checks confirmed the reliability of these automatic procedures; even at b_J = 21.0 mag, the misclassification of stars as galaxies or vice versa was never found to be more than 10%. Since, even on a

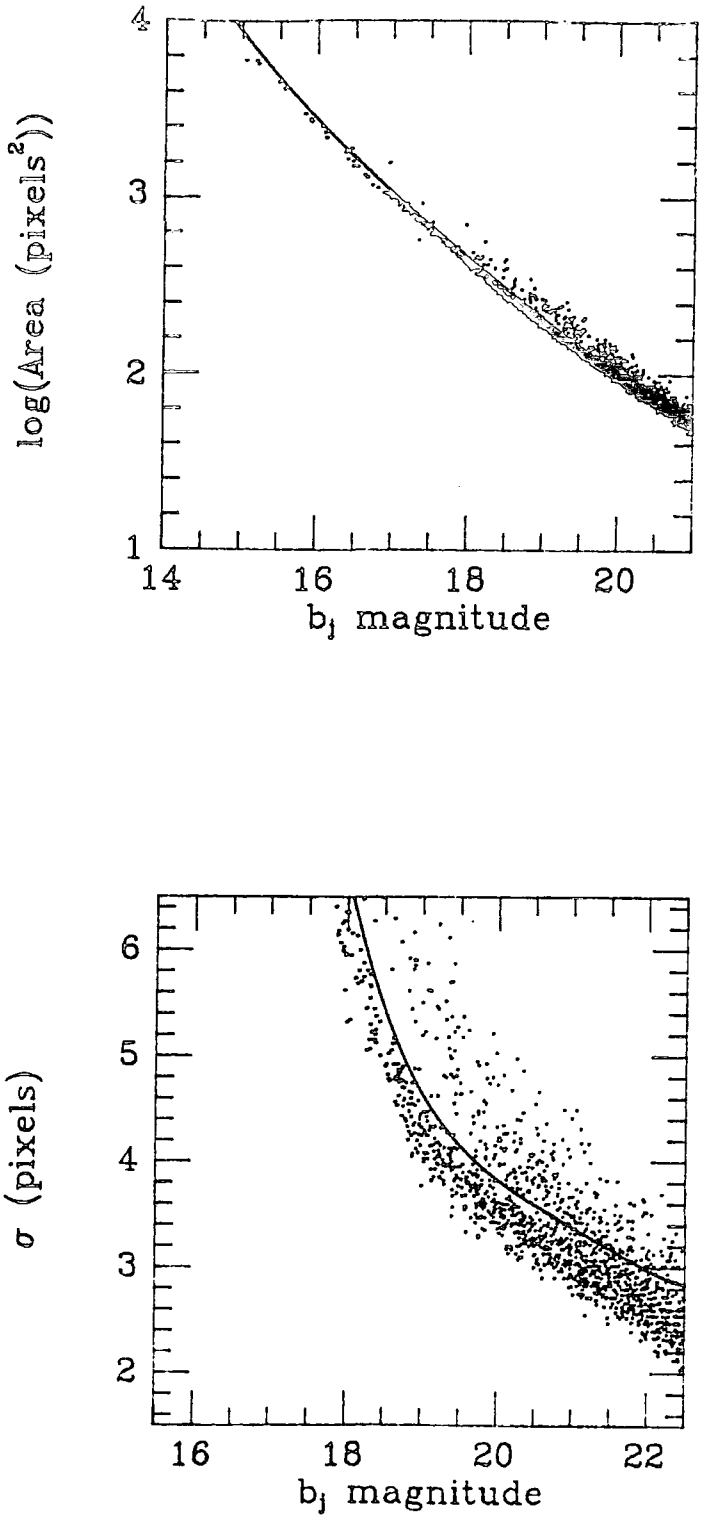

Figure 2.2 Diagrams used to discriminate automatically between stellar and galaxian images.
a) log (Area) v magnitude b) σ v magnitude.

visual inspection, stellar and galaxian images may become difficult to distinguish at $b_J \simeq 21$ mag on a UKST plate, this percentage has been checked (and subsequently verified) on the SGP from a visual inspection of the deeper AAT plate J1888 (Stevenson 1985).

2.4.3 Plate Matching

Typically, a COSMOS measurement for a sky-limited UKST plate contains information for several tens of thousands of stars and galaxies. To obtain colours for all these objects it is therefore necessary to follow a procedure which automatically matches the images from different plates.

The procedure used here is identical for all fields on which plates have been matched. Using the J plate as a 'master', a transformation is found between the COSMOS X and Y coordinates for $\simeq$ 30 bright (13 mag $<$ B $<$ 15 mag) stars on the plate and those for the same stars on a plate which is to be matched to it. This transformation consists of shift and rotation parameters and normally gives residuals of 10 - 20 μm ($\simeq$1") between the positions for the stars on the two plates used to define the transformation. The coordinates for each image on the J plate are then calculated in the frame of the second plate, and if an image is found on this latter plate within a tolerance of 3 arcseconds from the transformed J plate X and Y positions it is paired to the one on the J plate. Image parameters for the second plate are written to tape alongside those for the J plate. However, the XY position and star-galaxy separation parameters

remain as defined on the J plate. If more than one image is found within the tolerance region then the nearest image is matched.

In this way 95% of all images were paired to the J plate down to the corresponding limit of the plate used in the matching process (e.g. U < 20.75 mag, V < 20.5 mag, R < 20.0 mag and I < 18.5 mag). Once the magnitudes on the respective plates have been properly calibrated (see following sections), colours for stars and galaxies can simply be obtained by subtracting the different magnitudes for each matched image.

2.4.4 Stellar Calibration

Because COSMOS has a limited dynamic range, the machine magnitudes for even relatively faint stars (b < 20.0 mag on a sky limited IIIaJ plate) will be saturated and not form a linear relationship with photoelectric magnitude. Calibration of the stellar magnitudes is therefore achieved by fitting a smooth polynomial to the relationship between photoelectric and COSMOS magnitudes for standard stellar sequences on each field. Details of the stellar calibration on all fields are summarised in table 2.4, and representative calibration curves for U and J plates on the fields used in the spectroscopic survey are shown in figure 2.3. On all spectroscopically surveyed fields, accurate B photoelectric, electronographic or CCD photometry exists to at least B = 20.0 mag. The B photometry on three of these fields (SGP, QNB and QNA) goes as deep as B = 21.0 mag, the faint limit of our spectroscopic survey. To maintain consistency from

Field	Plate	Source of Calibration	Number of Stars	Magnitude Range	Symbol
SGP	J3721,J1921 B3499	Hawkins (1981)	28	13.75<B<22.45	•
	U2639,U6380	Cannon (1974)	27	10.20<U<17.50	•
		Hawkins (1981) SGP1: UBV Relation	6	19.29<U<20.29	□
		Hawkins (1981) SGPG2: UBV Relation	11	16.14<U<20.60	×
	V3475	Hawkins (1981)	20	13.20<V<21.14	
	R2775	Hawkins (1981)	18	12.73<R<19.75	
	I6427	Reid & Gilmore (1984)	73	10.79<I<18.33	
QSD	J1891	Savage	37	11.20<B<19.27	
	U3487	Savage	37	9.44<U<19.55	
QSF	J2627	Metcalfe	6	18.28<B<20.40	•
	U8226	Metcalfe	2	19.64<U<20.32	•
QNB	J7674,J9133S	Metcalfe	7	15.62<B<19.46	•
		Peterson	4	15.79<B<21.23	□
	U7714	Metcalfe	4	15.77<U<18.17	•
		Metcalfe: UBV Relation	1	U=18.97	■
	V7769	Metcalfe	7	15.28<V<18.37	
QNY	J5701	Metcalfe	7	12.28<B<20.18	•
		Shanks	5	16.49<B<19.90	□
	U5707,U9216	Metcalfe	6	12.73<U<18.49	•
QNA	J9108	Peterson	4	19.42<B<21.46	•
QSM	J3390	Tritton *et al.* (1984)	13	10.35<B<19.62	•
		Tritton & Morton (1984)	25	14.97<B<19.84	□
		Metcalfe	1	B=20.01	▼
	U1736	Tritton *et al.* (1984)	11	10.37<U<19.99	•
		Tritton & Morton (1984)	21	12.72<U<19.85	□

Note: Name quoted without reference indicates Private Communication

[1] Symbols refer to those plotted in figure 2.3

Table 2.4 Stellar Calibration Details

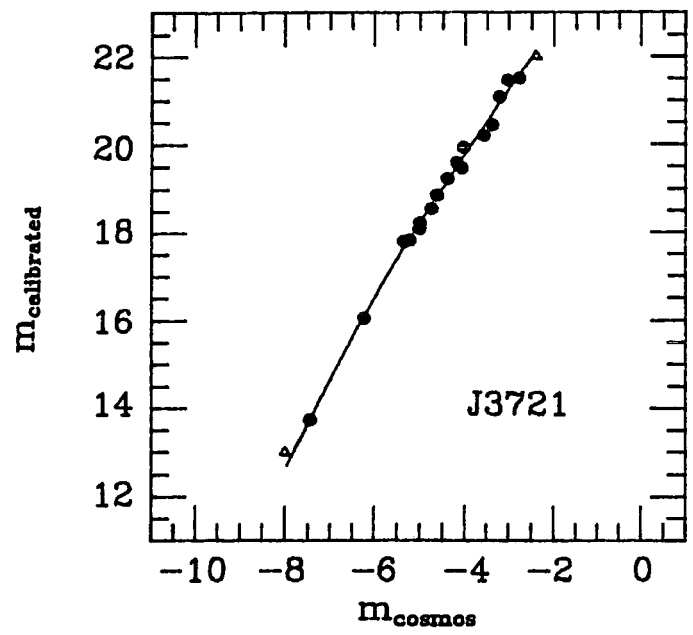

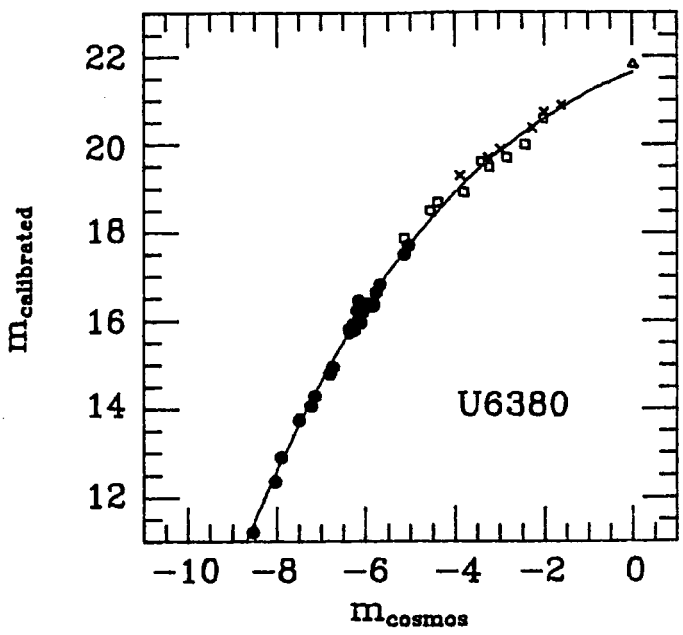

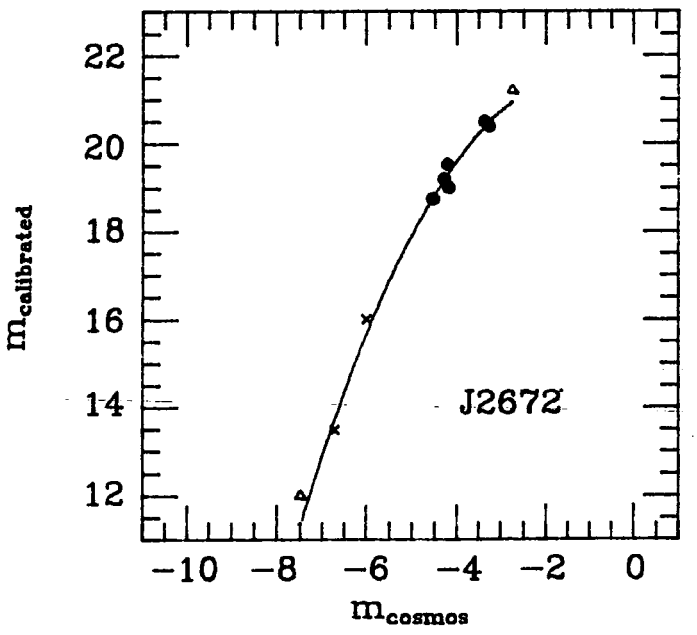

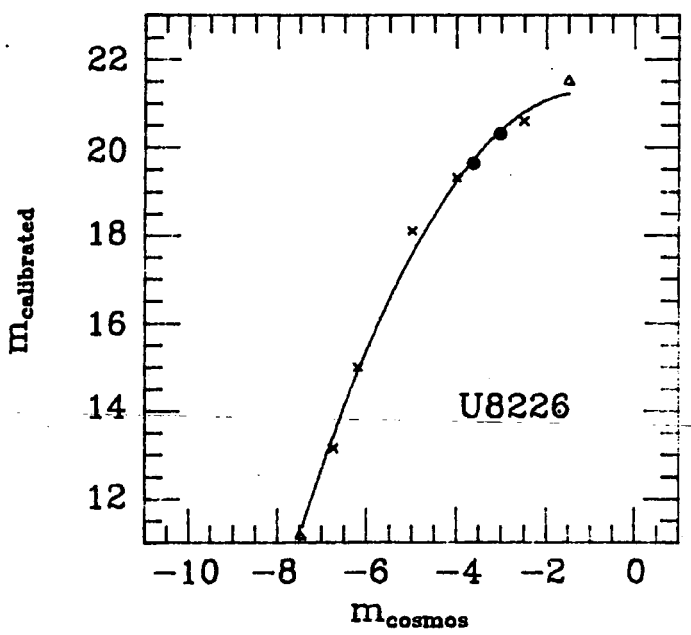

Figure 2.3 Stellar Calibration curves for the U and J plates used to define the UVX samples on the fields in the faint spectroscopic survey. See table 2.4 for key to symbols. Open triangles represent the end points of the polynomial fit.
a) SGP and QNY fields.

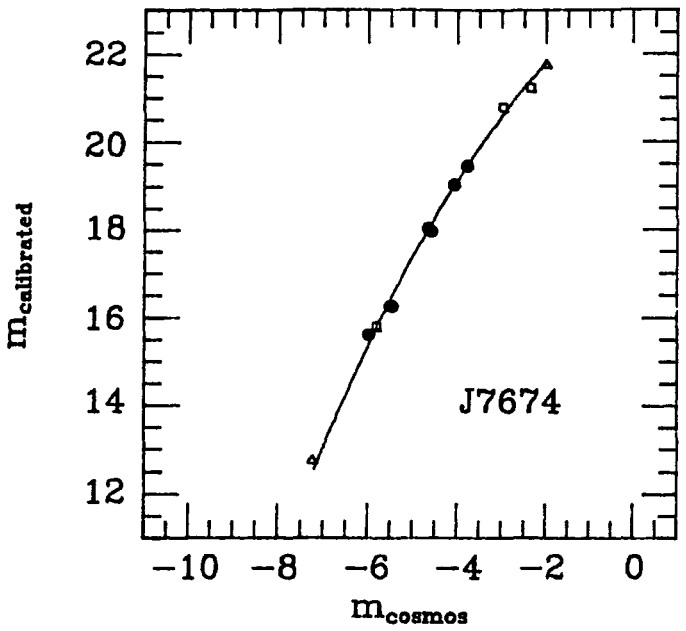

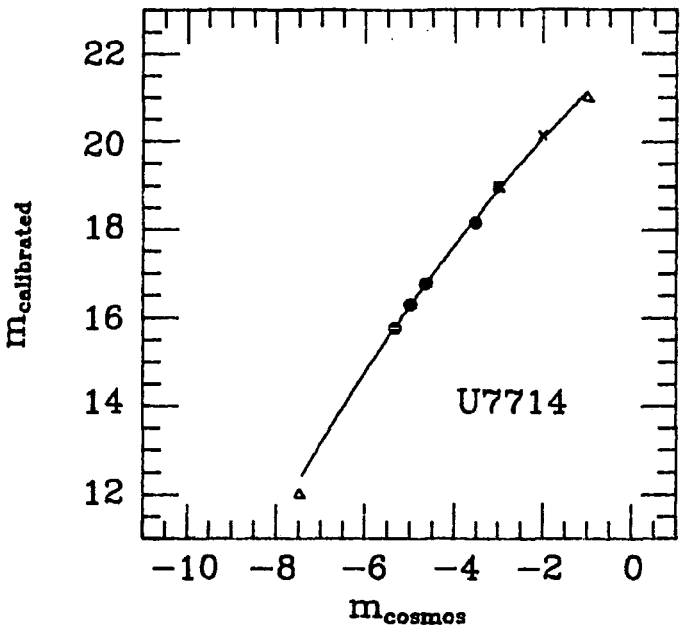

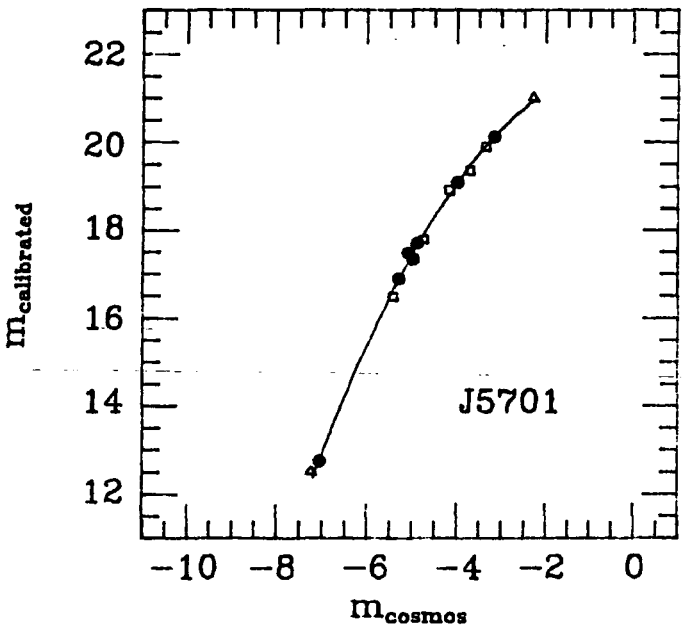

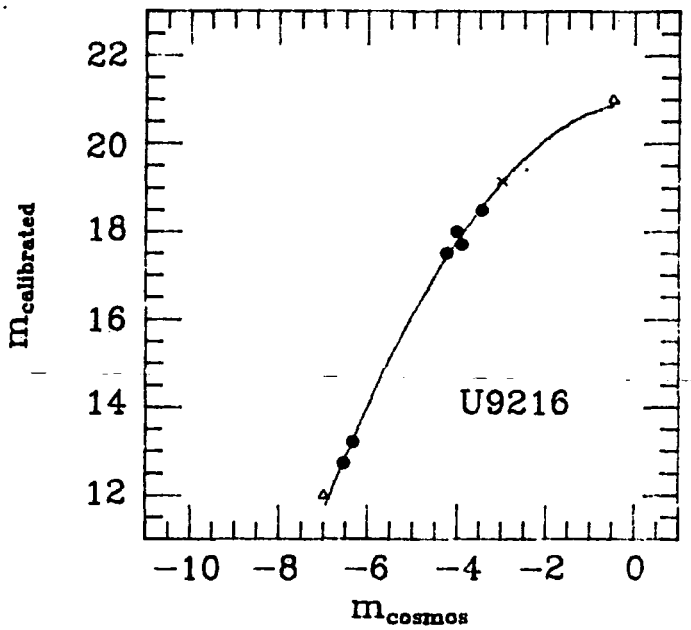

Figure 2.3 continued b) QNB and QNY fields.

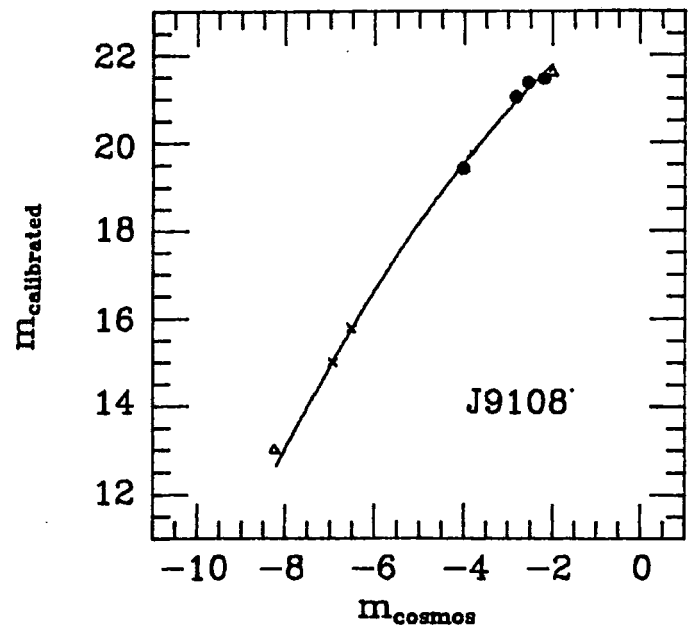

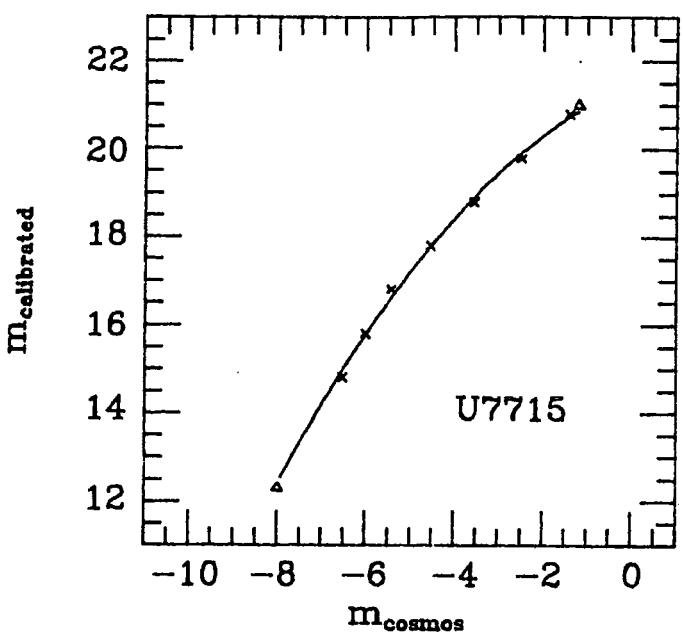

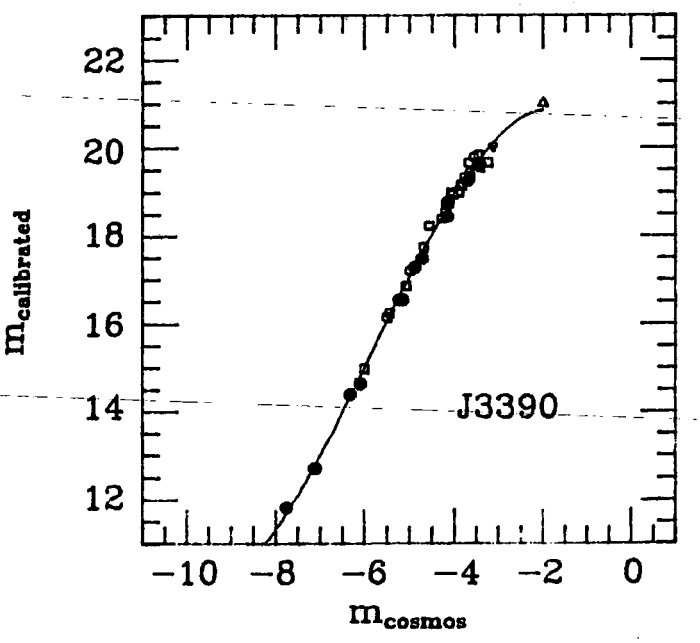

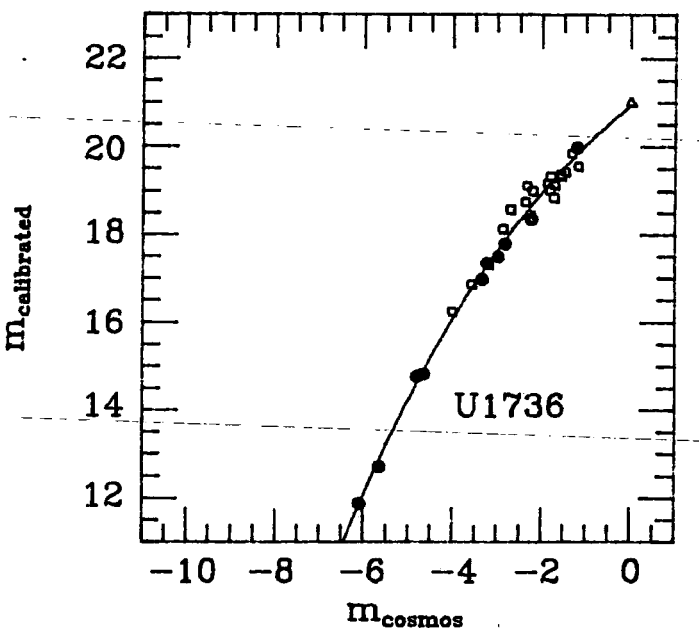

Figure 2.3 continued c) QNA and QSM fields.

field-to-field, all b stellar magnitudes were calibrated using standards given in the Johnson B system. Although standards were quoted directly in this passband for the electronographic sequence of Hawkins (1981) on the SGP and the photoelectric sequences of Shanks (private communication) on the QNY and Tritton *et al.* (1984) on the QSM fields, B magnitudes obtained from the CCD sequences of Metcalfe and Peterson (both private communication) required transformation to the Johnson system using the following relation (Walker 1984):

$$B = B_{CCD} + 0.078(B-V)_{CCD} \text{ mag} \quad \ldots (2.3)$$

While B-V CCD colours were only available for stars on the QNB field, the resulting colour term was so small (B-V $\simeq$ 0.6 mag for stars on the QNB) that equation (2.3) could be approximated on the other fields to

$$B = B_{CCD} + 0.05 \text{ mag} \quad \ldots (2.4)$$

without significant loss of accuracy.

On those fields (QSF, QNY and QSM) where the photometry did not extend to the faint limit of the spectroscopic survey, the calibration polynomials were extended beyond the faintest standard to the survey magnitude limit. This was done by placing a 'pseudo-calibration' point at B > 21.0 mag (triangles in figure 2.3) at a position based on a continuous extrapolation of the polynomial defined at brighter magnitudes by the standard sequence. These extrapolations never exceeded 0.8 mag and while we concede that COSMOS still suffers significant non-linearities

even at faint magnitudes (see e.g. Fong *et al.* 1983), it is unlikely that errors greater than ± 0.2 mag will be introduced by this procedure. We fully recognise, however, the absolute necessity to obtain further faint B photometry on these fields.

Two fields (QSF and QNA) have no bright (B < 18.0 mag) standard stars for calibration. A crude extrapolation to brighter magnitudes was attempted by assigning magnitudes (crosses on relevant calibration curves in figure 2.3) to bright stars (B < 16.0 mag) from the length of their diffraction spikes using the relation given in the UKST handbook. Although this method is extremely unsatisfactory, accounting as it may for the anomalous n(m) counts seen at bright magnitudes on the QNA field in chapter 3.4, it does not significantly affect the magnitudes of QSOs found in the spectroscopic survey, as only 2 surveyed QSOs (both on the QNA field) have magnitudes brighter than the brightest standard available.

While the B photometry on these fields is generally good, the corresponding U photometry is of a much poorer standard. Although good photoelectric and CCD U sequences do exist on some survey fields (e.g QSM and QNY see table 2.4) they do not extend to the faint magnitudes required by the spectroscopic surveys (u < 20.75 mag). On other fields the standards are either too bright (e.g. SGP) or too few in number (e.g. QSF) to provide reliable calibration. In some cases (e.g. QNA) no U sequence exists at all. To achieve a form of calibration for the u magnitudes two methods were therefore employed. The first method made use of the UBVR relation (hence referred to as such in table

2.4) for Galactic stars and hence could only be used on the SGP field where such multi-colour information was available (although a more approximate form of this method involving only UB and V colours was used to give an additional point on the QNB U calibration curve).

The method involved estimating U magnitudes for the stars in the Hawkins' (1981) SGP1 and SGP2 sequences. This was done by first selecting those stars that appeared to be main sequence on the basis of their B-V and V-R colours (thus guarding against the inclusion of extremely metal weak subdwarfs). These stars were then assigned U-B colours using the standard U-B:B-V relation for main sequence stars in the Johnson system (Johnson 1963). The resulting U sequence was then used to calibrate the COSMOS magnitudes on U2639 and U6380.

As a check of this method crude spectrophotometry of the UVX objects in the bright survey was carried out as follows. From the sky-subtracted, fluxed and air-mass corrected spectra for the QSM and SGP UVX survey objects (see chapter 3.2) an approximate u 'spectral' magnitude (u_{spec}) was derived using the total counts in the spectra between 3500Å and 4000Å (I_{3750}) thus:

$$u_{spec} = -2.5\log(I_{3750}) \quad \ldots (2.5)$$

Since accurate U photoelectric photometry is available to U = 20.0 mag on the QSM field (see table 2.4 and above) a zero-point converting spectral magnitude into COSMOS calibrated magnitude was determined from the survey objects on the QSM

field. This zero-point was then added the 'spectral' magnitudes for the SGP objects to give a 'pseudo' u magnitude. Agreement between this magnitude and the U2639 calibrated magnitude was found to be good (figure 2.4) confirming the accuracy of the stellar calibration in U on the SGP at the ± 0.2 mag level down to u = 18.5 mag.

For those fields on which U and J plates alone existed (and indeed for the QNB field at U > 19.0 mag), the lack of additional colours prohibited the method above from being applied. In these cases the u magnitudes were calibrated so that the mean u-b colour of the blue Galactic star population remained constant with b magnitude i.e ensuring that the locus for blue Galactic stars formed a horizontal line in the u-b v b diagram (see figure 2.5). Thus all anomalously blue stellar objects could be selected using a constant u-b cut, regardless of b magnitude. This, of course, will only give a relative calibration in u, and so, if possible, a zero-point for the u calibration was obtained from the bright standards in the field. In figure 2.3 the values used to 'linearise' the u-b v b diagram are shown as crosses with the actual sequence stars signified by filled circles.

The assumption of a constant u-b v b relation has also been employed by a number of other authors (e.g. Hewett *et al.* 1985, Marano *et al.* 1986) in the search for UVX objects. Such a constant relation is observed on the QSM field (see figure 2.5), where deep U (U < 20.0 mag) photometry does exist, thus providing good justification for this technique. Moreover such a constant relation is also seen on the SGP field (where u magnitudes were

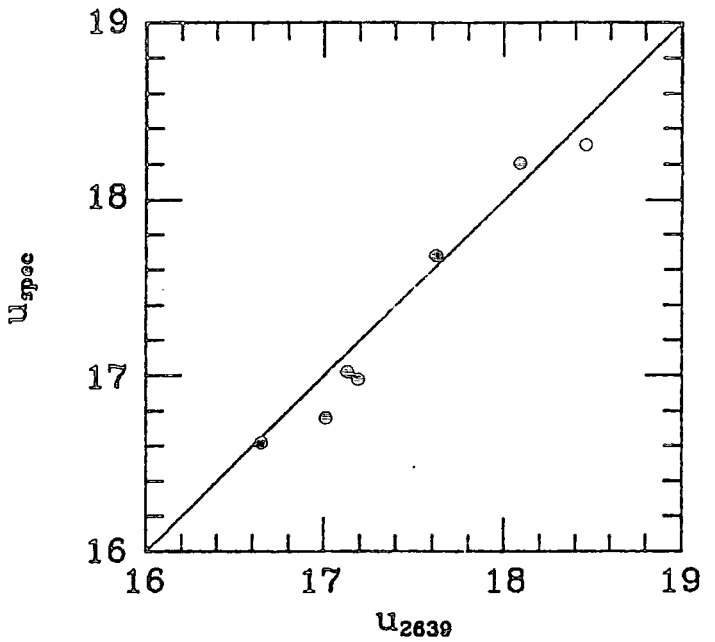

Figure 2.4 Comparison of calibrated u magnitude on U2639 (u_{2639}) with magnitude (u_{spec}) derived from spectrophotometry of bright survey objects on the SGP field.

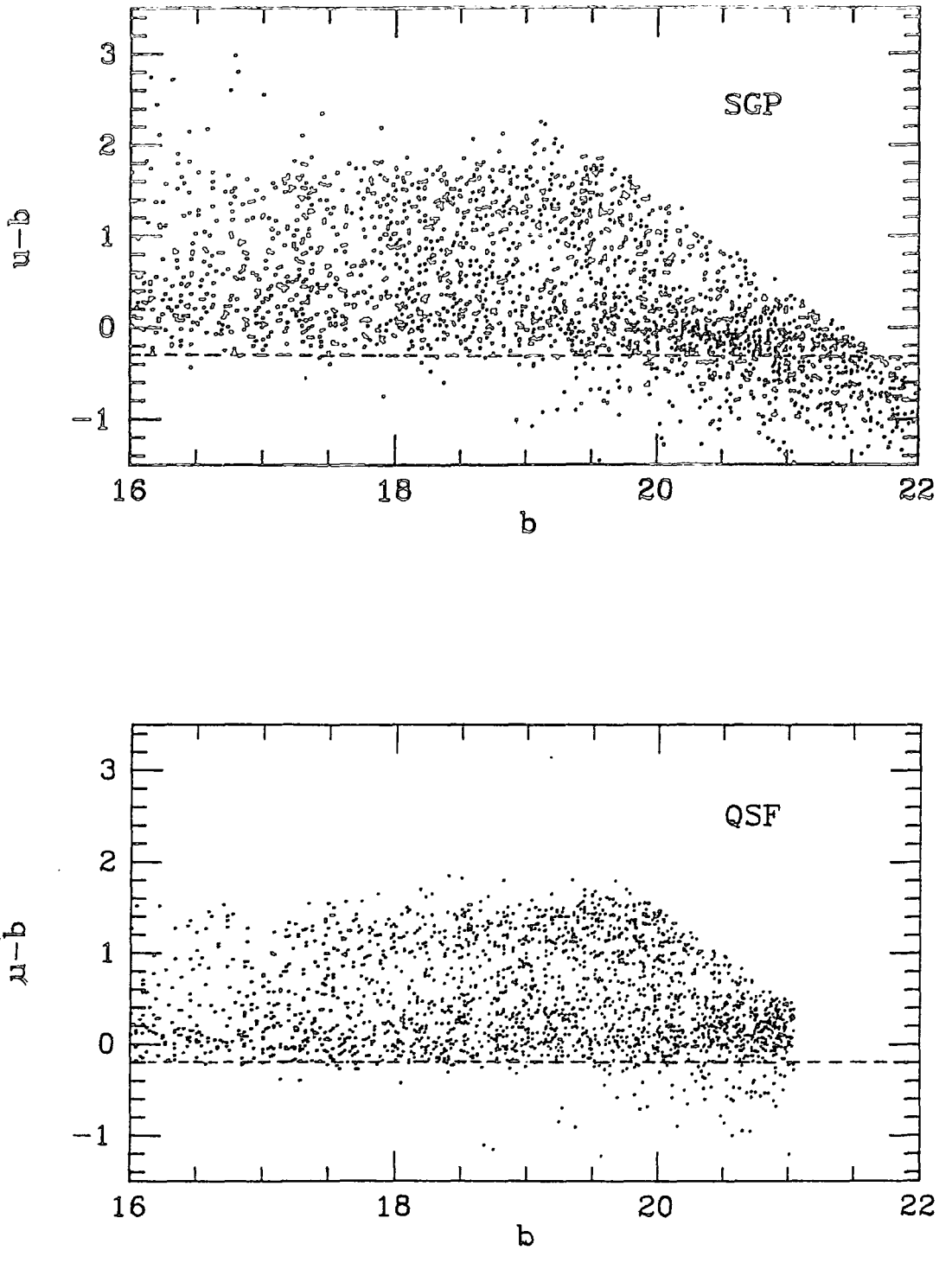

Figure 2.5 u-b v b diagrams for stellar images in central 1 square degree areas on each field observed in the faint spectroscopic survey. Dashed lines indicate UVX limits used for the faint spectroscopic survey. a) SGP and QSF fields.

The 'linearisation' of the u-b v b plots was carried out by ensuring that the 'ridge line' of the blue galactic star population remained at a constant u-b colour as a function of b magnitude.

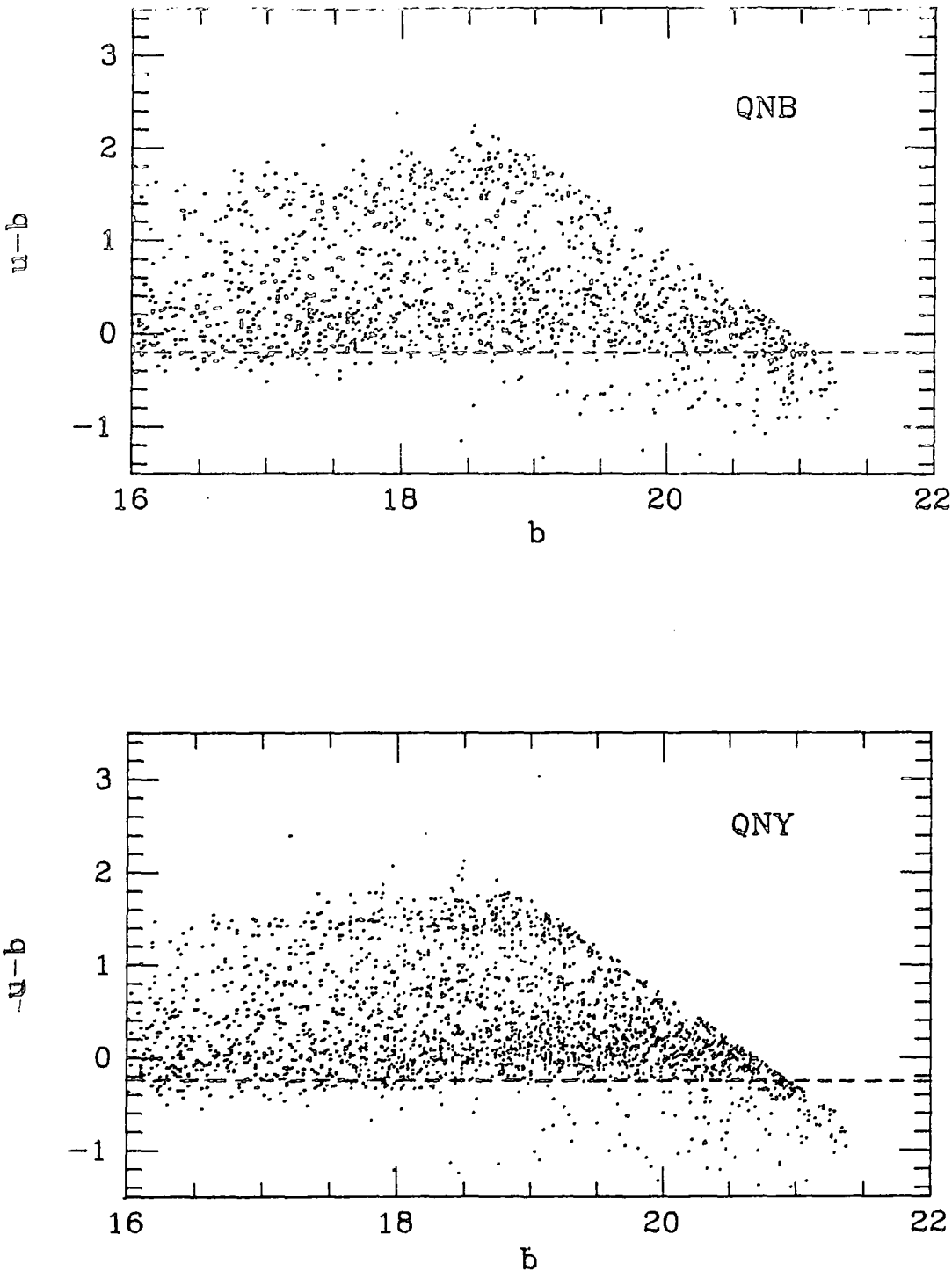

Figure 2.5 continued b) QNB and QNY fields.

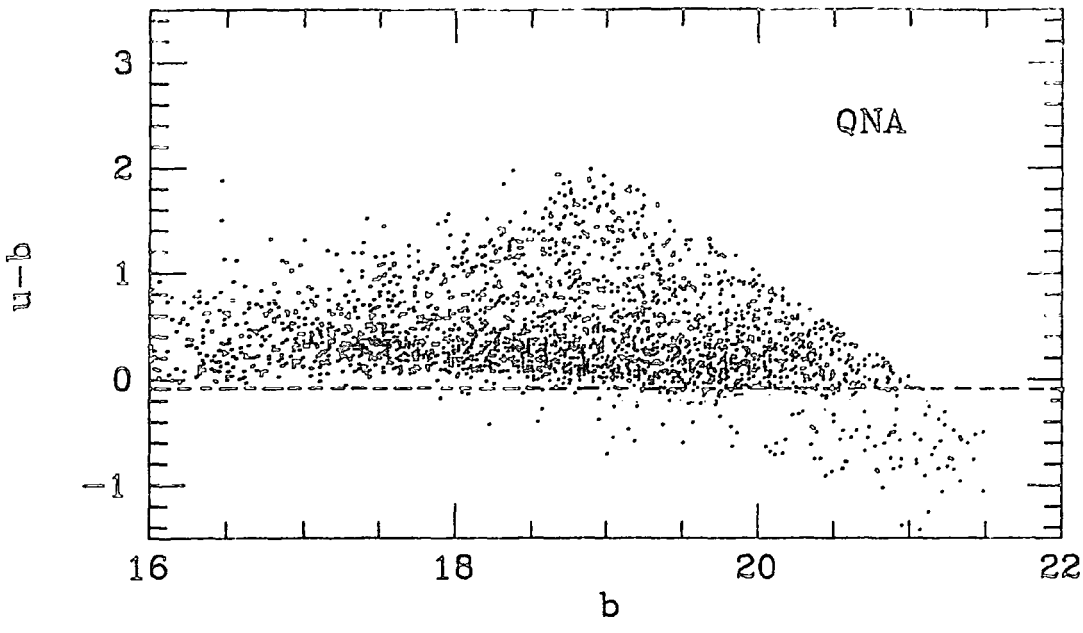

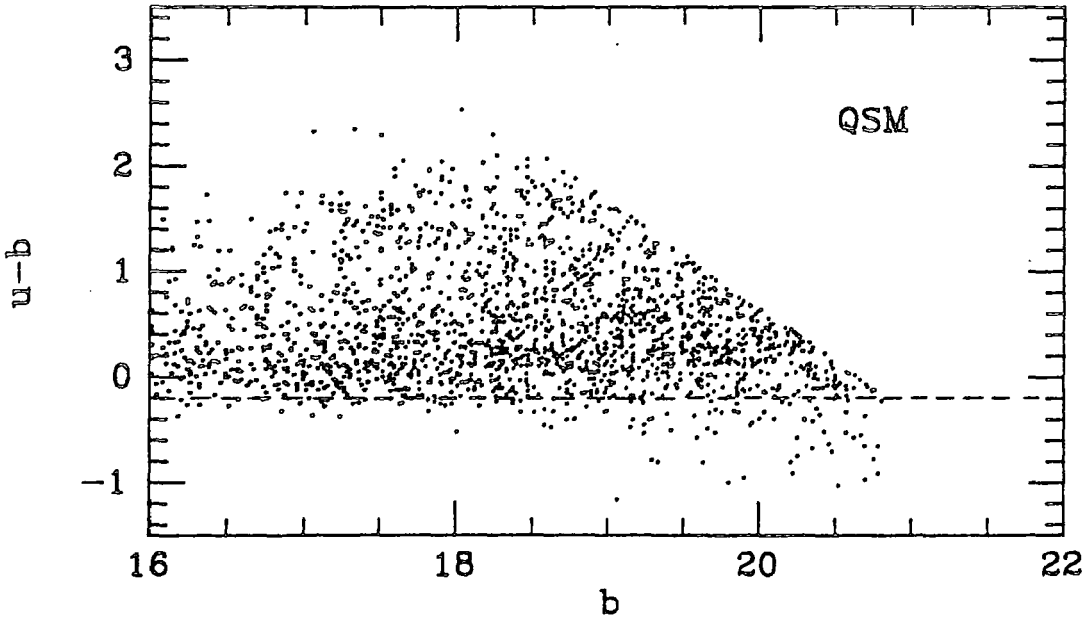

Figure 2.5 continued c) QNA and QSM fields.

calibrated using the UBVR relation). Both these observations vindicate the assumption of a constant u-b colour for blue Galactic stars in the magnitude range 18 mag < b < 21 mag, used to calibrate the u magnitudes on the other fields.

Calibration of the I6427 plate on the SGP was achieved using a sub-beam prism sequence (Reid and Gilmore 1984) based on the Kron-Cousins band (I_{KC}). Later this calibration was checked using data from a CCD I_{KC} frame taken on the AAT (Couch, private communication). From figure 2.6 we can see that, despite a small zero-point shift (0.2 mag), the magnitude scales agree well, with a rms scatter of ±0.1 mag. The stellar magnitudes on the SGP plates V3475 and R2775 were calibrated using the electronographic sequences in Hawkins (1981).

U and J plates on two other fields (QSD and QSI) used for the 2D clustering analysis alone were also calibrated. On the QSD field unpublished U and B photoelectric sequences compiled by Dr. Ann Savage were used, with suitable extrapolation to faint magnitudes using the methods described above. Unfortunately, no stellar sequences exist in either U or B on the QSI field. A relative calibration between the u and b magnitudes was first achieved by 'linearising' the u-b v b diagram on this field as described above. A zero-point for the b magnitude system was then chosen to give agreement between the surface densities of UVX objects found on the QSI field and those on other fields in the range 18 mag < b < 20.5 mag.

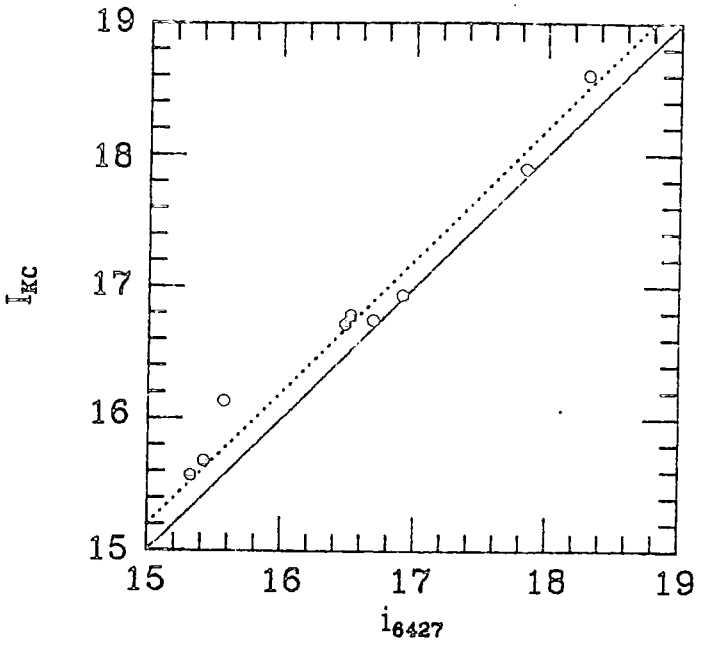

Figure 2.6 Check of I calibration on plate I6427. Plot of CCD I_{KC} magnitudes v calibrated COSMOS i magnitudes, i_{6427}.

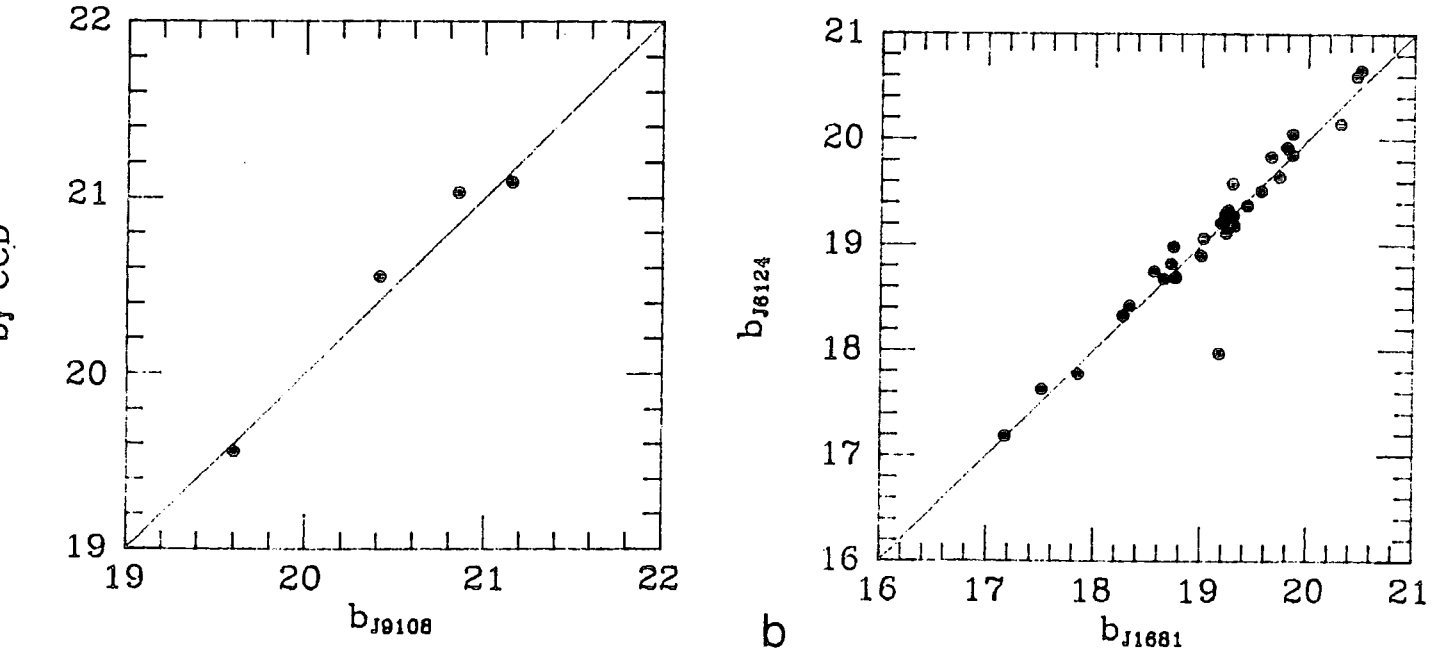

Figure 2.7 Galaxy Calibration
a) QNA field b) QSN field (see text for details).

2.4.5 Galaxy Calibration

In the range 16 mag < b_J < 21 mag, the magnitudes produced by COSMOS for galaxies are linear with calibrated magnitudes to within ±0.2 mag (MacGillivray and Dodd 1982). Calibrated galaxy magnitudes may therefore be calculated from the COSMOS magnitude by the addition of a constant zero-point term. Estimation of the zero-point can be achieved by comparing the photoelectric magnitudes for those galaxies on the measured area with accurate photometry to their COSMOS magnitudes. In this work calibration of the galaxy magnitudes is only carried out on the J plates used for the cross-correlation analysis in chapter 6. The galaxy magnitude in the IIIaJ passband (b_J) is given by

$$b_J = m_{cos} + 5\log(l_{pix}/14.9) + m_{sky} \quad \text{mag} \quad \ldots (2.6)$$

where the first term on the right hand side of equation (2.6) is given by equation (2.1) and the second corrects the sky magnitude (the third term) from magnitudes per pixel into magnitudes per square arcsecond. l_{pix} is the pixel width in the COSMOS scan and 14.9 the UKST plate scale in microns per arcsecond. For all UKST plates measured here l_{pix} = 8 μm. We note that from the definition given in equation (2.6), the value of m_{sky} is only strictly valid within the context of the machine measurements discussed here, and is not necessarily a true m_{sky}.

Table 2.3 lists the values for m_{sky} on all plates which the galaxy catalogues will be used. Most plates have been calibrated previously - the values of Metcalfe were obtained from CCD observations on the South African Astronomical Observatory (SAAO)

1m Telescope, and that of Ellis from a similar observation on the AAT. The plates on which m_{sky} has been directly determined in this work are given below.

a) J9108

CCD observations of four galaxies on this plate have been made in the B_{CCD} passband by B.A.Peterson. To convert their magnitudes into the b_J passband we use equation (2.4) together with

$$b_J = B - 0.23(B-V) \text{ mag} \quad \ldots (2.7)$$

This is the relation given by Kron (1978) , although it is only strictly valid for stars. However, in the absence of an explicit relationship for galaxies it should suffice to an accuracy of ± 0.1 mag.

The subsequent calibration is shown in figure 2.7a, where the calibrated COSMOS magnitudes, b_J , using an m_{sky} = 22.55 mag, show a tight ±0.15 mag, scale-free (45°) relation with those derived from the CCD observations.

b) J6124

A small part (0.5 sq. deg.) of the measured area on this plate overlaps with that on J1681. Since a value of m_{sky} = 22.05 mag is already known for the latter plate (Stevenson 1985), calibration of the galaxy magnitudes on J6124 was achieved by comparing COSMOS magnitudes for the galaxies on the overlap area

(see figure 2.7b). Once again we see a relation with very little scatter (± 0.15 mag) about a 45° line, and $m_{oby} = 22.9 \pm 0.1$ mag.

c) J1862

No galaxy photometry was available on this field so an approximate m_{oby} was chosen to give agreement between the galaxy number magnitude, n(m), counts on this field and those on the SGP.

2.5 Discussion of Passbands

In later chapters we will need to compare surface densities for our QSOs with those found from other sources. To do so we require a transformation from our b magnitudes for QSOs to Johnson B quoted by most other authors. While such transformations do exist for Galactic stars (Blair and Gilmore 1982), QSOs have quite different spectra which may give rise to significantly different colour equations. Using COSMOS measurements of B3499 and J3721, an equation relating b and B magnitudes can, however, be determined quite directly. This is possible because the passband defined by the IIaO/GG395 emulsion filter combination used to take the B plates is much closer to Johnson B than that obtained from the IIIaJ/GG395 combination used to produce J plates. A QSO sample already exists on the SGP (Clowes and Savage 1983) selected from a visual inspection a UKST objective prism plate. The calibrated magnitudes (hereafter referred to as b_{IIao}) for all QSOs on the B plate in this sample with $b_{IIao} < 20.0$ mag (this being the plate limit of B3499) and z

< 2.2 (to avoid possible colour terms - see chapter 7.2) were compared to their corresponding magnitudes on the IIIaJ plate (b_{IIIaJ}), both sets of magnitudes having been calibrated from the Hawkins' (1981) electronographic sequence. The result is displayed in figure 2.8 with the dotted line adopted as the relation between b_{IIIaJ} to b_{I00}, namely:

$$b_{I00} = b_{IIIaJ} - 0.15 \text{ mag} \quad \ldots (2.8)$$

To convert this into B we use the following from Blair and Gilmore (1982)

$$B = b_{I00} + 0.11(B-V) \text{ mag} \quad \ldots (2.9)$$

Again this is only strictly valid for Galactic stars, but, in this case, the correction is so small that QSOs ($B-V \simeq 0.2-0.3$ mag, see e.g figure 7.2) should not be expected to show significant deviations from this relation. For all future use we therefore adopt the following relation (accurate to the nearest 0.05 mag) to convert b magnitudes to the Johnson B passband:

$$B = b - 0.10 \text{ mag} \quad \ldots (2.10)$$

We also note that the u magnitude calibration described in the previous section was not carried out in a consistent fashion from field-to-field. We may therefore expect u magnitude systems on each field to have different zero-points. We will, however, wish to compare UVX limits from field-to-field in the spectroscopic surveys. We therefore obtain an approximate relative u zero-point across the survey fields by normalising the

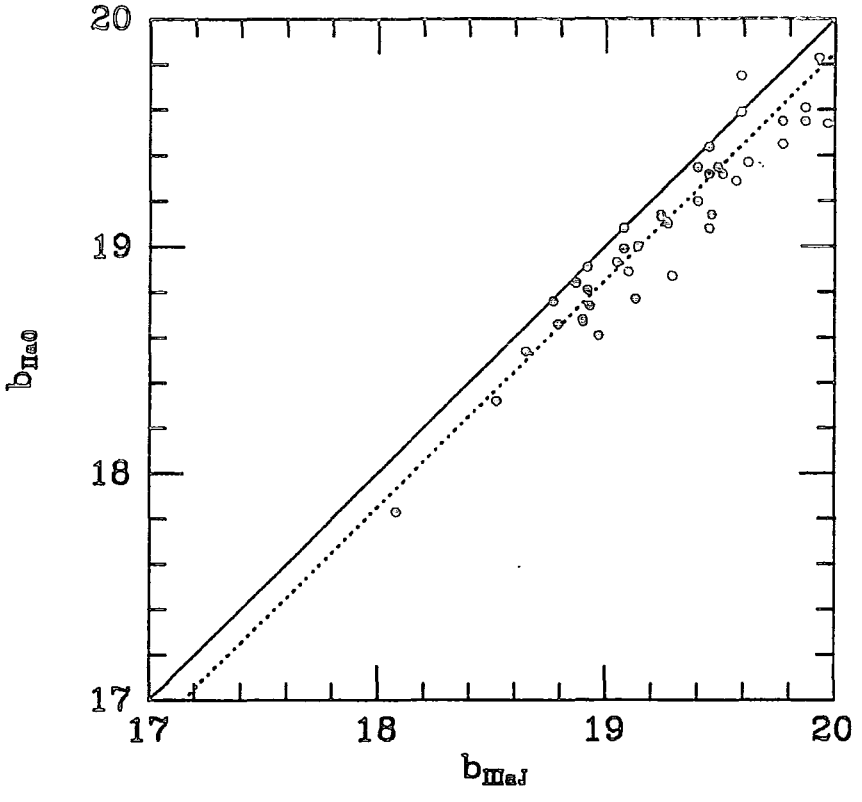

Figure 2.8 Comparison of calibrated magnitudes for Clowes and Savage (1983) $z < 2.2$ QSOs between plates J3721 (b_{IIIaJ}) and B3499 (b_{IIIaO}).
Dotted line denotes relation

$$b_{IIIaO} = b_{IIIaJ} - 0.15 \text{ mag.}$$

u-b colours so that the locus of blue Galactic stars in u-b v b (see figure 2.5) lies at the same u-b colour for all fields as it does on the SGP field. Because much of the u calibration was achieved by straightening out the stellar locus in u-b v b, this normalisation should be more or less independent of the b magnitude at which it is carried out. However we chose to carry out this normalisation in the range 19 mag < b < 20.5 mag, this being the magnitude interval in which the bulk of the QSOs were observed in the spectroscopic surveys. We thus arrive at the following corrections:

QSF: $u' = u - 0.2$ mag ... (2.11a)

QNB: $u' = u - 0.3$ mag ... (2.11b)

QNY: $u' = u - 0.2$ mag ... (2.11c)

QNA: $u' = u - 0.1$ mag ... (2.11d)

QSM: $u' = u - 0.3$ mag ... (2.11e)

where the primed and unprimed indices refer to the corrected and original u magnitudes respectively. All figures in this chapter have been plotted in the original system, but unless otherwise indicated, all future u magnitudes and u-b colours quoted will be the corrected colours. We stress, however, that this is merely a relative calibration for comparative purposes between fields in the UVX survey alone, and, as such, should not be used as an indication of the true U-B colour from which it may show significant discrepancies. The comparison between u-b and U-B colours for QSOs is postponed until spectroscopic information is available to identify precisely the content of the UVX sample (see chapter 3.4).

2.6 Consideration of Errors

As this thesis is based on broadband colour selection techniques, it is vital that due consideration of the errors inherent in the magnitudes used to derive such colours is taken into account. The rms scatter of the photoelectric standards about the calibration curves in figure 2.3 may be used to estimate their size, but since many of the fields have very few such standards (especially at the faint end - where errors are likely to be at their largest), we prefer the more detailed approach given below.

Since the SGP is the only field on which we have two pairs of U and J plates, we can begin this study by computing the rms scatter in the u and b magnitudes for stars between each matched U and J plate pair on this field. From this we will be able to derive errors in the u-b colours on the SGP and, by comparison with the u-b histograms for stars on this and on other fields, devise a procedure to obtain similar errors in u-b in these other fields. The matched pair of U plates on the QNY field can subsequently be used to verify the consistency of this procedure.

We plot in figure 2.9a histograms for $\Delta b = (b_{1921} - b_{3721})$ in 0.5 mag intervals from $b_{3721} = 17.0$ mag to $b_{3721} = 21.0$ mag. In table 2.5 we give the rms scatter (σ) in Δb for each of these intervals. Since J3721 is a better quality plate than J1921 we may expect that the errors associated with b magnitudes on J3721 alone will be no larger than $\sigma/\sqrt{2}$. This gives a error of, at most, ±0.18 mag even in the faintest magnitude bin. Of course,

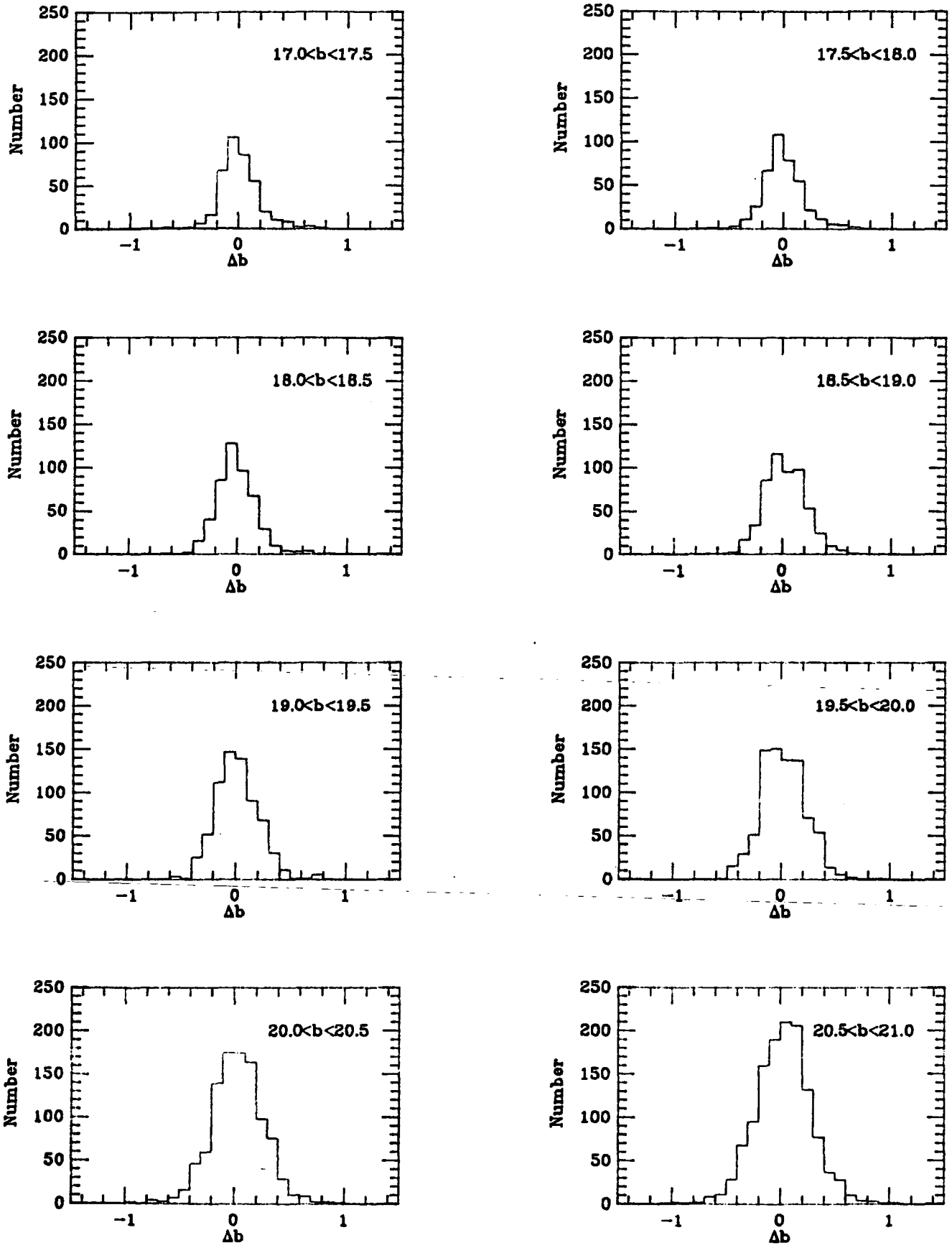

Figure 2.9 Histograms for magnitude differences between stellar images on plate pairs taken in the same passband. a) Number v Δb ($b_{1921}-b_{3721}$): SGP field.

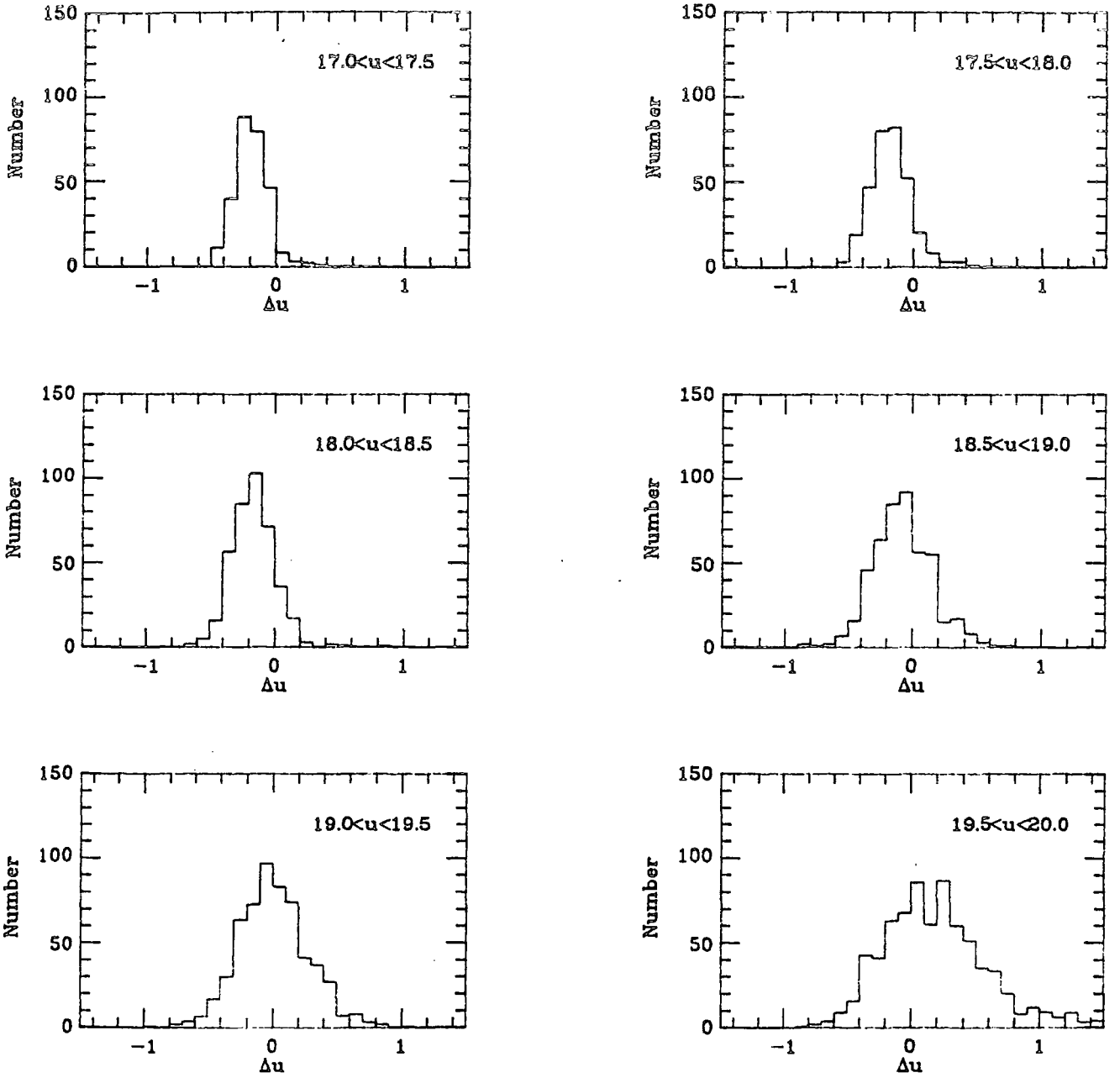

Figure 2.9 b) Number v Δu ($u_{2639}-u_{6380}$): SGP field.

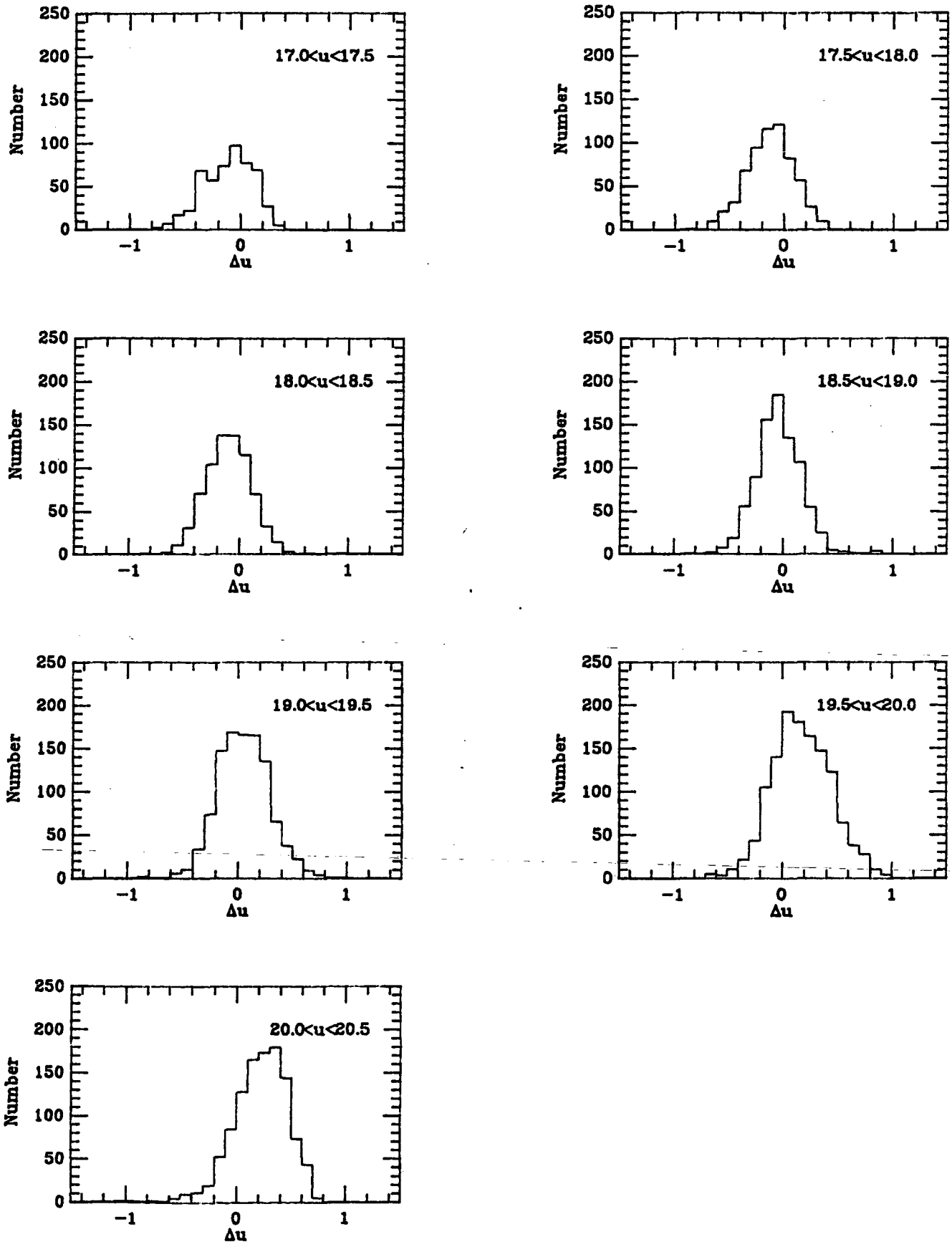

Figure 2.9 c) Number v Δu ($u_{5707}-u_{9216}$): QNY field.

Magnitude Range	$b_{1921}-b_{3721}$	$u_{2639}-u_{6380}$	$u_{6380}-b_{3721}$	$u_{5707}-u_{9216}$
17.0 - 17.5	0.18	0.15	0.16	0.22
17.5 - 18.0	0.20	0.15	0.18	0.21
18.0 - 18.5	0.19	0.18	0.19	0.17
18.5 - 19.0	0.23	0.20	0.22	0.23
19.0 - 19.5	0.20	-	-	0.24
19.5 - 20.0	0.20	-	-	0.27
20.0 - 20.5	0.23	-	-	0.25
20.5 - 21.0	0.25	-	-	-

Table 2.5 Dispersion in magnitudes from Plate Pairs

Magnitude Range	SGP	QSF	QNB	QNY	QNA	QSM
17.0<b<17.5	0.20	0.15	0.20	0.20	0.10	0.15
17.5<b<18.0	0.20	0.15	0.20	0.20	0.10	0.20
18.0<b<18.5	0.20	0.15	0.20	0.20	0.10	0.25
18.5<b<19.0	0.20	0.15	0.20	0.15	0.15	0.30
19.0<b<19.5	0.20	0.15	0.25	0.15	0.15	0.30
19.5<b<20.0	0.25	0.20	0.25	0.20	0.20	0.25
20.0<b<20.5	0.25	0.20	0.20	0.20	0.20	0.30
20.5<b<21.0	0.30	0.25	0.25	0.25	0.25	-

Table 2.6 HWHM of Blue Stellar Peak in u-b distribution

this is only a relative error in the magnitudes defined by COSMOS. Absolute error will depend on the accuracy of the calibration. It would be ideal if this process could be carried out down to a similar magnitude limit with the two U plates available on the SGP, thus obtaining an estimate for the error in u-b colour down to the magnitude limit of the faint spectroscopic survey ($u < 20.7$ mag). Unfortunately, U2639 was taken on IIaO emulsion and consequently does not go very deep. However, we may still obtain an upper limit for the error in the u magnitudes derived from U6380 at bright magnitudes. In figure 2.9b, Δu ($u_{2639}-u_{6380}$) is plotted in 0.5 mag bins from $u_{6380} = 17.0$ mag to $u_{6380} = 20.0$ mag. Beyond $u_{6380} = 19.0$ mag the spread in Δu increases dramatically as the bright plate limit on U2639 comes into play. Table 2.5 therefore lists the rms scatter in Δu down to this magnitude limit, with the errors in u_{6380} being no greater (and probably significantly smaller - due to the much inferior quality of U2639) than ±0.16 mag at u = 19.0 mag. The size of the errors in u-b colours for the SGP can therefore be directly assessed to a magnitude limit of b = 19.0 mag by combining the errors in the u and b magnitudes derived above. Table 2.5 gives the error derived in this fashion for a star with u-b = 0.0 mag at the b magnitude quoted, although the errors for UVX QSOs ($u-b < -0.3$ mag) will be slightly smaller. We therefore derive an upper limit to the size of the error in u-b at b = 19.0 mag to be $\simeq$ ±0.20 mag.

To obtain errors on u-b colours at fainter limits we note that, for $b < 19$ mag, the half width half maximum (HWHM) of the blue peak (calculated on the blueward side of the peak) in the SGP stellar u-b histogram (figure 2.10), is approximately equal in size to the error in u-b for the magnitude bins down to $b = 19.0$ mag (see table 2.6). This equality is not surprising since it reflects the fact that the intrinsic distribution of u-b colours for Galactic stars has a sharp cut-off blueward of $u-b \simeq 0.0$ mag, with the spread in colours to the blue merely reflecting the measurement errors. Such a cut-off arises because the spectral sequence of normal Galactic stars from A to M undergoes a minimum in u-b colour ($\simeq -0.05$ mag) for stars of spectral type F (Allen 1973). Metal-weak subdwarfs, white dwarfs and QSOs will, of course, constitute an intrinsically bluer population than this limit but any error estimated from the HWHM of the blue peak will serve as a useful upper limit to the size of the errors. In table 2.6 we therefore list errors derived in this fashion for all the other 5 survey fields. We see that the errors in u-b vary remarkably little over the magnitude range 17 mag $< b <$ 21 mag, ranging from $\simeq \pm 0.20$ mag at $b = 17.0$ mag to $\simeq \pm 0.30$ mag at $b = 21.0$ mag.

To ensure that the errors derived in this fashion are still true reflections of the real errors involved, we used the two U plates that have been measured on the QNY field to estimate the error associated with the u magnitudes on this field. From figure 2.9c and table 2.5 we arrive at an error $\simeq \pm 0.2$ mag for the faintest u magnitudes. This is not incompatible with the

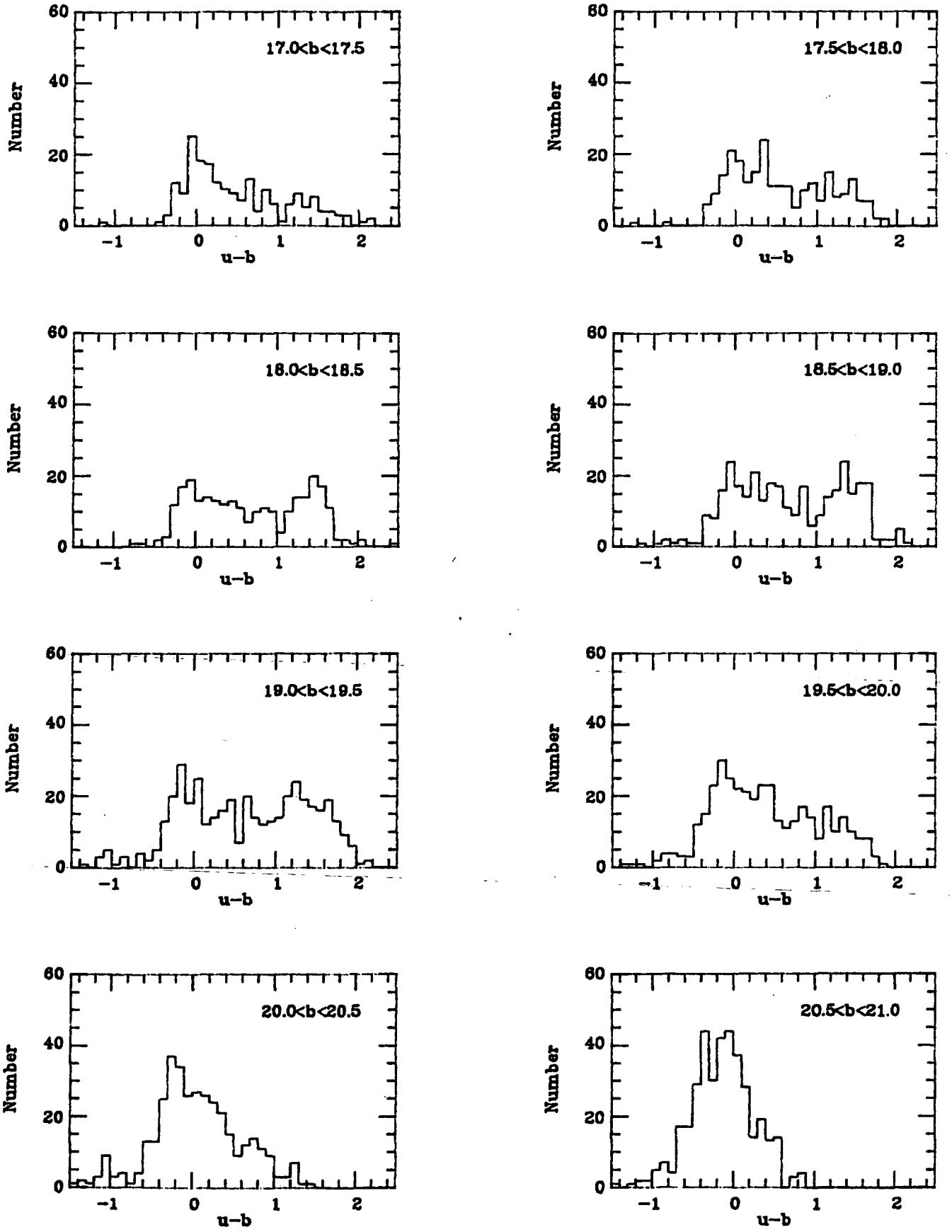

Figure 2.10 u-b histograms for stellar images in a central 2 square degree area on the SGP.

error derived from the u-b distribution on the QNY field (see table 2.6). Indeed, this would imply an error ≃ ±0.15-0.20 mag in the J magnitudes at 20.5 mag < b < 21.0 mag - equal to that derived directly on SGP plate J3721.

We therefore conclude that the errors in the machine measured stellar magnitudes and colours are small, although we stress the need for additional calibration. As such, samples of objects selected by their broadband colours from COSMOS machine measurements of photographic plates can be accurately defined and are therefore well suited to spectroscopic analysis.

CHAPTER THREE

SPECTROSCOPIC OBSERVATIONS OF UVX CATALOGUES

3.1 Introduction

In chapter 1 the power of the UVX technique in finding complete samples of low redshift ($z < 2.2$) QSOs was demonstrated. We now describe spectroscopic observations of UVX catalogues produced from the COSMOS machine measurements of UKST plates detailed in chapter 2.

Two separate spectroscopic surveys were carried out: an initial, bright ($b < 19.0$ mag) survey undertaken using conventional spectroscopic techniques to assess the success of the UVX technique in detecting QSOs, and a further, much larger faint ($b < 21.0$ mag) survey carried out when fibre optic spectroscopy became available at the AAT.

3.2 The Bright UVX Survey

3.2.1 Observations

COSMOS machine measurements of the UKST plates J3721 and U2639, J5701 and U , and J3390 and U1736 were used to define a sample of UVX objects on the SGP, QNY and QSM fields respectively. Small areas on each of these fields were then selected for spectroscopic study (see table 3.1), two areas on the SGP and one each on the QSM and QNY fields. The area at the centre of the SGP field was defined to overlap with that of the AAT plate J1888, and the QSM area was chosen to include the area

Name	Limits of Area				Area Covered (sq. deg.)	Mag. Limits	U-B limit
	RA(1950) (h m s)	-> RA(1950) (h m s)	Dec(1950) (o ' ")	->Dec(1950) (o ' ")			
SGP centre	00 51 43.0	00 57 40.2	-27 21 46	-28 40 26	1.61	17.5<b<19.0	u-b<-0.35
SGP faint	00 46 36.7	01 01 30.0	-26 04 30	-28 43 46	8.17	18.5<b<19.0	u-b<-0.50
QSM centre	21 59 31.5	22 05 10.0	-18 34 05	-19 21 24	1.30	17.5<b<19.0	u-b<-0.50
QSM bright	21 58 40.5	22 08 10.6	-18 00 03	-20 01 50	7.72	17.5<b<18.5	u-b<-0.50
QNY bright	12 28 26.9	12 38 55.6	+01 34 08	-02 10 01	10.06	17.5<b<19.1	u-b<-0.65

Table 3.1 Bright UVX Survey: Areas Chosen and Selection Criteria Applied

surveyed by Morton and Tritton (1982), hereafter MT. On all of these areas, with the exception of the central SGP, the criterion for inclusion in the UVX sample was set to u-b < -0.50 mag (this became u-b < -0.65 mag on the QNY field due to a revision of a zero-point, see Boyle *et al.* 1985). The area at the centre of the SGP plate was defined to have a less strict UVX criterion (u-b < -0.35 mag) than the other areas. At higher Galactic latitudes the contamination of the UVX sample by Galactic stars at a given u-b limit is expected to be smaller than that at lower Galactic latitudes. Thus, on the SGP, we could afford to relax the UVX criterion and still be left with a manageable number of stars to observe. Moreover, this was the UVX criterion used to define the UVX sample in Shanks *et al.* (1983c) and so was included here to allow us to estimate directly the percentage of QSOs in the UVX sample used in that paper. The UVX and limiting magnitude criteria for each spectroscopically surveyed area are also given in table 3.1.

The UVX objects in the samples defined above were observed by Tom Shanks and Fred Stevenson during 12-13 April and 20-22 August 1982 on the 3.9m Anglo-Australian Telescope using the IPCS detector and RGO spectrograph operated at low dispersion (156 Å/mm) with a 2 arcsecond slit. This gave a resolution of 4Å over a spectral range of 3400Å - 7200Å. The integration time for each object (≃ 3000 secs at b = 19.0 mag) was sufficient to obtain approximately 100-150 counts per channel in the objects' spectra. Good signal-to-noise (S/N≃10) was required in order to identify the narrow absorption lines in the spectra of the Galactic stars

and to ascertain whether any of the 'featureless' spectra were produced by unusual objects e.g. BL Lacs. The spectra were reduced on the SERC STARLINK VAX system at the University of Durham using the SPICA software package. The wavelength calibration was carried out using standard Cu-Ar arc spectra taken between each survey object during the observing run, and fluxing of the resultant sky-subtracted, wavelength calibrated spectra was achieved using the spectra of white dwarf standards (Oke 1974) taken throughout the nights of the observing runs. Spectroscopic observations of a few objects in the survey were also carried out by Dr. Arp on the 2.5m telescope at Las Campanas and by Drs de Ruiter and Zuiderwijk at La Silla with the 2.2m telescope (see references below).

3.2.2 The Catalogue

In table 3.2 and figures 3.1, 3.2 and 3.3 we present the UVX catalogue in full. Table 3.2 lists, area by area, the objects in the catalogue together with their (1950) positions, magnitudes, u-b colour, spectroscopic identification and a reference to a note if the object is of particular interest. The positions quoted are based on COSMOS machine measurements converted to R.A. and Dec. using standard astrometric procedures, and are accurate to 1 arcsecond. Where an object had been observed previously, its original identification, and, for a QSO, the original determination for its redshift is given. All the QSO redshifts quoted are based on measurements from slit spectra.

SGP Centre

Name	Position RA(1950) (h m s)	Dec(1950) (o ' ")	b	u-b	Identification	Notes/Reference
S1	00 53 34.6	-28 40 08	17.72	-0.53	Star F6 (A9)	
S2	00 54 28.6	-28 35 57	18.82	-0.36	Star F8 (F7)	
S3	00 56 23.5	-28 37 54	18.01	-0.39	Star F8 (F2)	
S4	00 55 25.1	-28 32 13	17.56	-0.55	Star F7 (A5)	
S5	00 55 38.5	-28 28 23	18.87	-0.35	QSO z=0.648±0.001	MgII(2798) 4612A [NeV](2973)4900 *OIII(3133) 5207A
S6	00 54 49.0	-28 25 20	18.87	-0.44	Star F4 (A4)	
S7	00 54 25.6	-28 25 28	18.00	-0.37	Star G2 (F2)	
S8	00 57 07.5	-28 10 16	18.90	-0.40	Star F3 (A5)	
S9	00 56 25.9	-27 58 44	18.85	-0.71	Star A5 (A5)	
S10	00 56 20.6	-27 56 52	18.79	-0.35	Not observed	
S11	00 54 27.0	-27 52 51	17.76	-0.38	Star G0 (A5)	
S12	00 54 05.1	-27 51 34	17.55	-0.42	Star F8 (F0)	
S13	00 53 34.1	-27 53 00	18.92	-0.55	Star G2 (F2)	
S14	00 55 09.7	-27 44 40	18.77	-0.39	QSO z=2.186±0.003	NV(1240) 3950A 1 SIV(1400) 4468A CIV(1549) 4929A
S15	00 54 06.4	-27 33 36	18.92	-1.20	QSO z=1.26?	CIII(1909) 4308A 2
S16	00 54 46.9	-27 28 25	18.77	-0.68	Star F8 (F0)	
S17	00 54 40.0	-27 26 54	17.55	-0.38	Not observed	
S18	00 51 46.8	-28 11 52	18.97	-0.68	QSO z=2.30	CS
S19	00 51 59.2	-27 48 56	18.80	-0.41	Star F8 (F7)	
S20	00 52 52.3	-27 27 16	17.65	-0.37	Star G0 (F6)	

Table 3.2 Bright UVX Survey: The Catalogue

SGP Faint

Name	Position RA(1950) (h m s)	Dec(1950) (o ' ")	b	u-b	Identification	Notes/Reference
R1	01 00 33.1	-26 10 31	18.70	-0.98	QSO z=2.54	Arp
Q2	00 59 27.7	-26 25 06	18.93	-0.84	QSO z=2.11	CS
P3	00 57 57.4	-26 26 05	18.69	-0.75	White Dwarf DA	Arp
O4	00 55 15.8	-26 13 30	18.57	-0.55	White Dwarf DA	Arp
N5	00 52 58.2	-26 26 26	18.62	-0.58	Star	Arp
TT6	00 49 22.3	-26 17 08	18.54	-0.50	Star	Z
U7	00 47 54.1	-26 47 55	18.79	-0.83	QSO	CT
V8	00 47 07.2	-26 47 21	18.64	-0.77	Star	Z
SS9	00 59 39.4	-27 02 06	18.88	-1.10	QSO	3
L10	00 53 38.5	-27 09 10	18.55	-1.13	QSO z=1.040±0.002	CIII(1909) 3872A 4 MgII(2798) 5717A
M11	00 52 32.0	-27 06 38	18.65	-0.90	White Dwarf DA	
Z12	00 57 56.7	-27 29 46	18.90	-0.78	QSO z=1.20	Z
C15	00 53 05.1	-27 16 39	18.60	-0.58	Star G2 (G0)	
E16	00 51 38.1	-27 26 26	18.90	-0.90	QSO z=0.65	Arp 5
D17	00 51 26.3	-27 35 00	18.72	-0.72	Star	Z
W18	00 48 56.4	-27 29 52	18.85	-0.51	Star	Z
X22	00 47 49.6	-27 59 36	18.52	-0.94	QSO z=2.12	CS
Y24	00 49 10.1	-28 08 53	18.87	-0.66	Star	Z
J26	00 56 14.2	-28 40 34	18.75	-0.79	White Dwarf DA	
I28	00 55 39.9	-28 41 20	18.70	-0.55	Star	Z
H29	00 51 21.8	-28 39 57	18.65	-0.79	QSO	CT

Table 3.2 contd. Bright UVX Survey: The Catalogue

QSM Centre

Name	Position RA(1950) (h m s)	Dec(1950) (o ' ")	b	u-b	Identification	Notes/Reference
T6	22 02 41.8	-19 12 25	18.57	-0.54	Star F8 (F2)	
T8	22 04 32.2	-19 11 39	17.88	-0.87	QSO z=1.067	SBTP
T18	22 02 35.6	-18 32 00	18.81	-0.71	QSO z=1.808	SBTP
T22	21 59 39.8	-19 11 38	18.83	-0.64	Star G0 (A8)	
T25	21 59 36.7	-18 57 30	18.59	-0.51	Star G2 (G0)	
T26	22 00 47.7	-19 00 03	18.80	-0.65	Star F8 (A6)	
T28	21 59 52.7	-18 53 52	18.83	-0.69	Star F8 (F0)	
T31	22 01 16.8	-18 34 15	18.38	-0.75	QSO z=1.829±0.001	SiIV(1400) 3961A *CIV(1549) 4349A NIII(1750) 4950A *CIII(1909) 5397A

QSM Bright

Name	Position RA(1950) (h m s)	Dec(1950) (o ' ")	b	u-b	Identification	Notes/Reference
A1.1	22 05 51.7	-20 01 28	17.95	-0.86	QSO z=1.711±0.003	CIV(1549) 4206A CIII(1909) 5169A
A2.1	22 03 07.9	-20 01 36	18.26	-0.58	Star F7 (A6)	
A3.1	21 59 23.9	-19 26 17	18.18	-0.52	QSO z=1.173	SBTP
A7.1	22 08 09.2	-18 02 38	18.46	-0.52	Star F8 (F0)	
A7.2	22 05 29.1	-18 26 56	18.10	-0.54	Star F6 (A5)	
A9.1	21 59 15.9	-18 13 48	18.30	-0.64	Star F8 (A6)	

Table 3.2 contd. Bright UVX Survey: The Catalogue

QNY Bright

Name	Position RA(1950) (h m s)	Dec(1950) (o ' ")	b	u-b	Identification	Notes/Reference
1A	12 37 35.3	-01 07 50	18.98	-0.52	Not Observed	
1B	12 36 02.8	-01 23 08	19.08	-0.72	"	
2A	12 32 18.4	-01 43 26	18.86	-0.95	Star F8 (?)	
2B1	12 35 47.4	-01 55 44	18.29	-1.31	White Dwarf DG (DC?)	6
3B1	12 30 40.2	-01 11 53	18.97	-0.57	Not Observed	
3C	12 28 39.8	-02 00 31	18.98	-0.76	QSO z=0.274	de Ruiter
5A1	12 37 32.6	-00 20 34	18.53	-0.84	White Dwarf DG	
5B1	12 36 59.0	-00 22 11	19.08	-0.58	Not Observed	
5C1	12 36 02.5	-00 24 14	17.58	-1.49	Star	de Ruiter
5EA	12 37 23.9	-00 49 19	19.06	-1.01	Not Observed	
5EB	12 37 25.9	-00 54 18	18.73	-1.01	QSO z=0.819±0.004	MgII(2798) 5108A NeV(2973) 5412A OIII(3133) 5678A
5D1	12 36 22.2	-00 43 03	18.68	-1.12	Not Observed	
6C	12 32 56.1	-00 25 11	19.08	-0.75	Not Observed	
6A1	12 32 32.1	-00 13 52	18.86	-1.19	QSO z=1.890±0.003	Lyα(1216) 3517A NV(1240) 3592A SiIV(1400) 4043A CIV(1549) 4468A

Table 3.2 contd. Bright UVX Survey: The Catalogue

QNY Bright

Name	Position RA(1950) (h m s)	Dec(1950) (o ' ")	b	u-b	Identification	Notes/Reference
7A	12 31 50.5	-00 22 04	19.01	-0.51	Not Observed	
7B	12 29 14.3	-00 44 25	18.98	-0.42	"	
7C	12 29 21.1	-00 53 28	19.05	-0.87	"	
9A	12 38 34.9	00 39 23	18.41	-1.11	QSO z=1.362±0.001	CIV(1549) 3660A CIII(1909) 4509A
10A	12 33 43.0	00 20 23	18.36	-0.98	White Dwarf DA	
13A	12 36 38.1	01 28 42	17.82	-1.60	QSO z=1.245±0.003	CIV(1549) 3485A CIII(1909) 4279A
13B1	12 38 45.5	01 15 58	19.01	-1.24	Not Observed	
13C1	12 37 37.3	01 07 57	18.35	-1.03	QSO z=1.808±0.002	SIV(1400) 3953A CIV(1549) 4356A CIII(1909) 5356A
13D	12 36 41.5	00 51 57	19.09	-0.91	Not Observed	
14B1	12 32 45.9	01 33 07	18.89	-0.92	"	
15A	12 31 27.5	01 25 22	18.95	-0.58	"	
15B	12 30 46.3	00 45 09	19.06	-0.53	"	
14A1	12 34 38.9	01 39 31	19.03	-0.91	QSO z=0.627±0.001	CII(2326) 3780A MgII(2798) 4555A *OIII(3133) 5142A
14A2	12 34 39.8	01 39 30	19.43	-0.57	QSO z=0.722±0.001	MgII(2798) 4818A OIII(3133) 5399A

Table 3.2 contd. Bright UVX Survey: The Catalogue

Notes

1. S14 shows no Lyα emission. The deep absorption trough shortward of the NV emission may well have absorbed the Lyα emission line. This QSO is also interesting because of its close proximity to a faint cluster of galaxies (see chapter 3.2.4).

2. We regard the redshift determination for this object as being very tentative. Unfortunately the strongest emission line in this spectrum occurs at the blue cut-off in the sensitivity of the IPCS tube. If we take the wavelength of this line to be 3512A, then identifying the line as CIV would give a redshift for QSO of 1.27. This is in fair agreement with the determination of z=1.26 from the emission feature at 4308A attributed to CIII (λ1909). This QSO was also selected by Clowes and Savage (1983) but they failed to derive a redshift from its objective prism spectra.

3. UVX object estimated, from its objective prism spectra, to have a 75% chance of being a QSOs by Dr. Clowes.

4. The CIII] emission line in L10 is heavily cut by absorption so the estimation of the emission line redshift is taken from the observed wavelength of the MgII emission line.

5. The redshift of this QSO is determined from only one, peculiar emission line.

6. Although 2B1 does not have as broad Ca H & K absorption lines as the other DG white dwarf (5A1) we still identify it as a white dwarf on the basis of its continuum slope. There is also the possibility that it could be a DC type white dwarf.

Arp - Arp (Private Communication)

CS - Clowes and Savage (1983)

de Ruiter - de Ruiter (Private Communication)

SBTP - Savage,Bolton,Tritton and Peterson (1976)

CT - Campusano and Torres (1983)

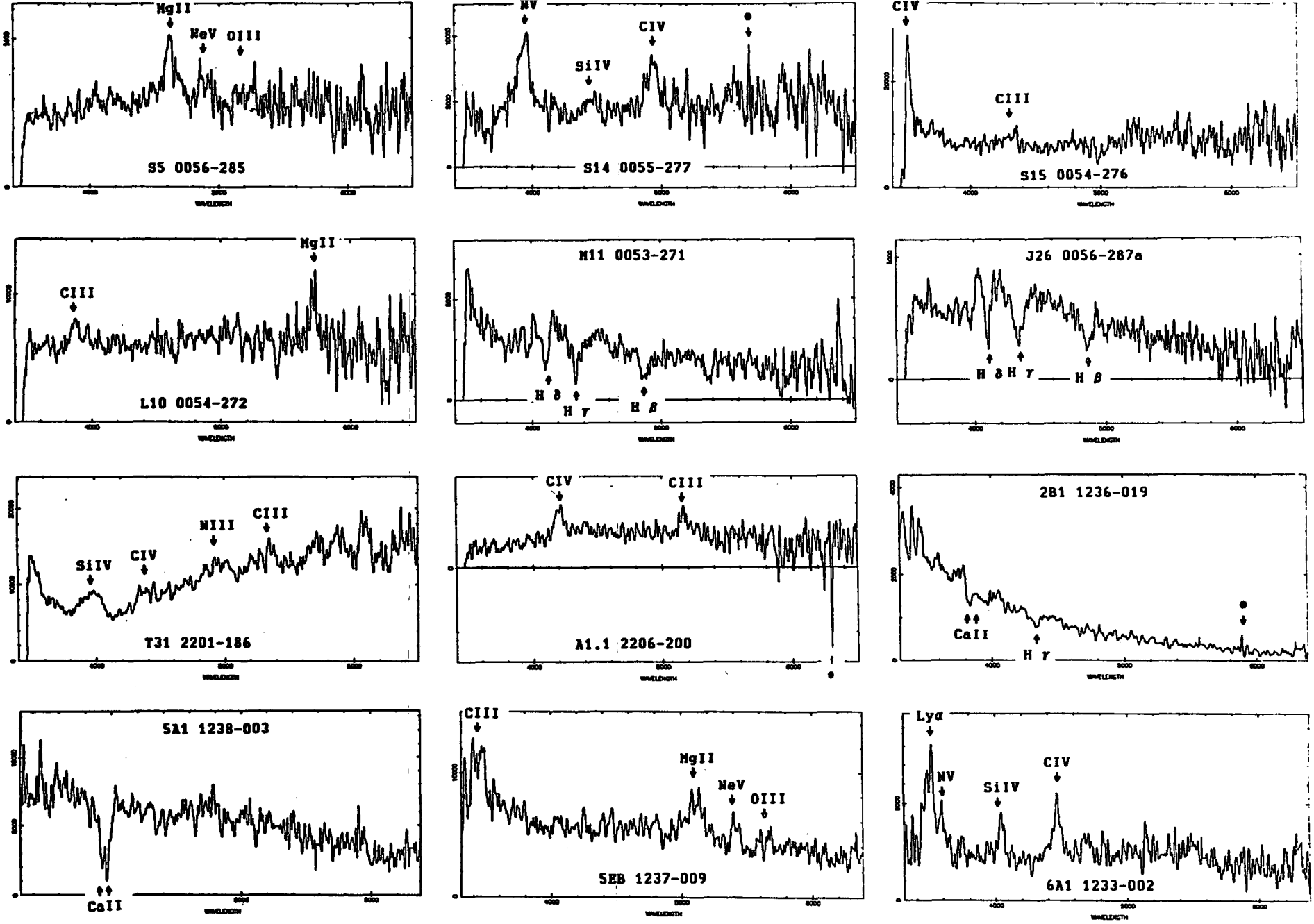

Figure 3.1 IPCS spectra for QSOs and white dwarfs observed in the bright spectroscopic survey. A representative sample of Galactic stars is also shown at the foot of this figure.

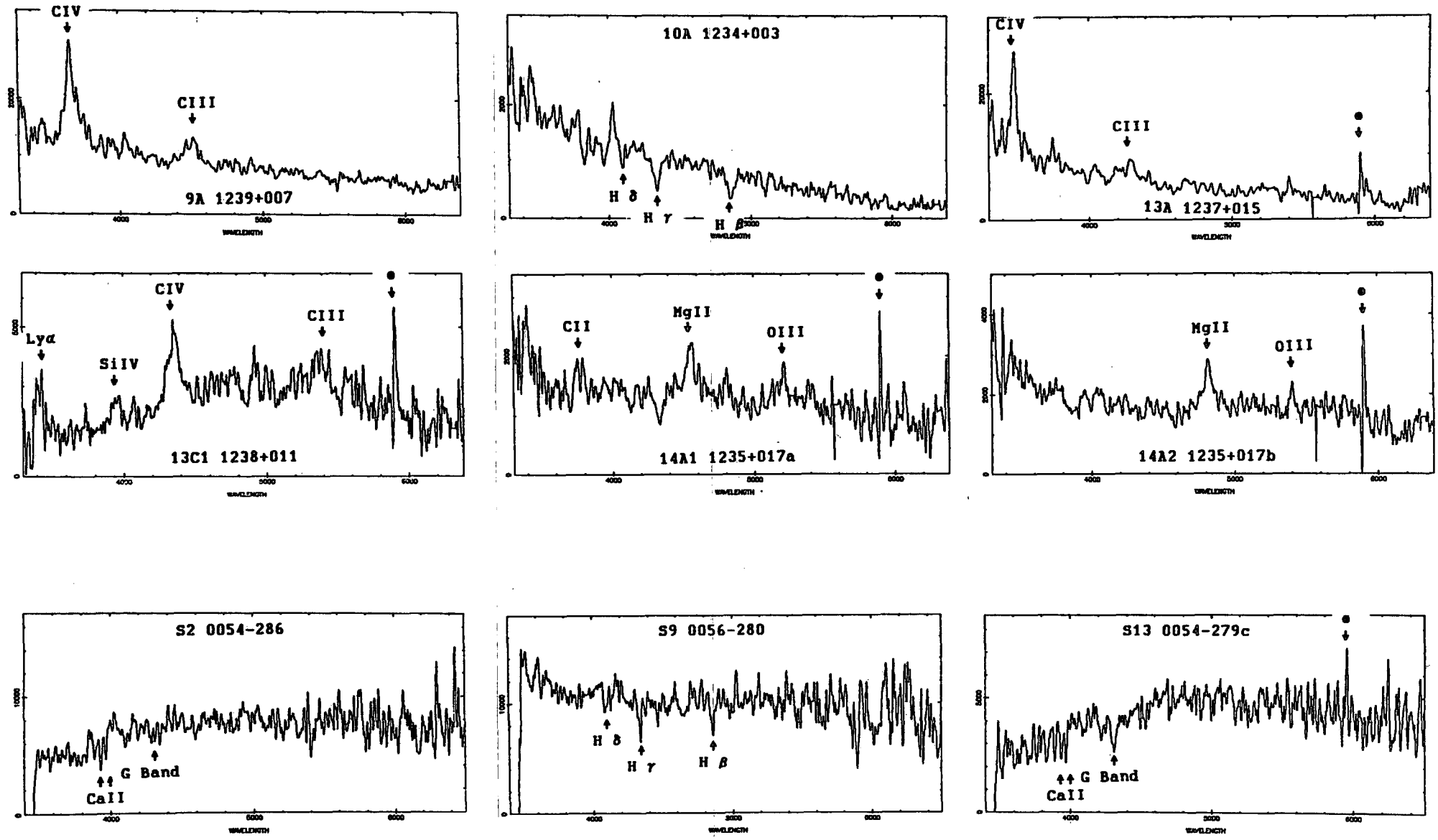

Figure 3.1 continued

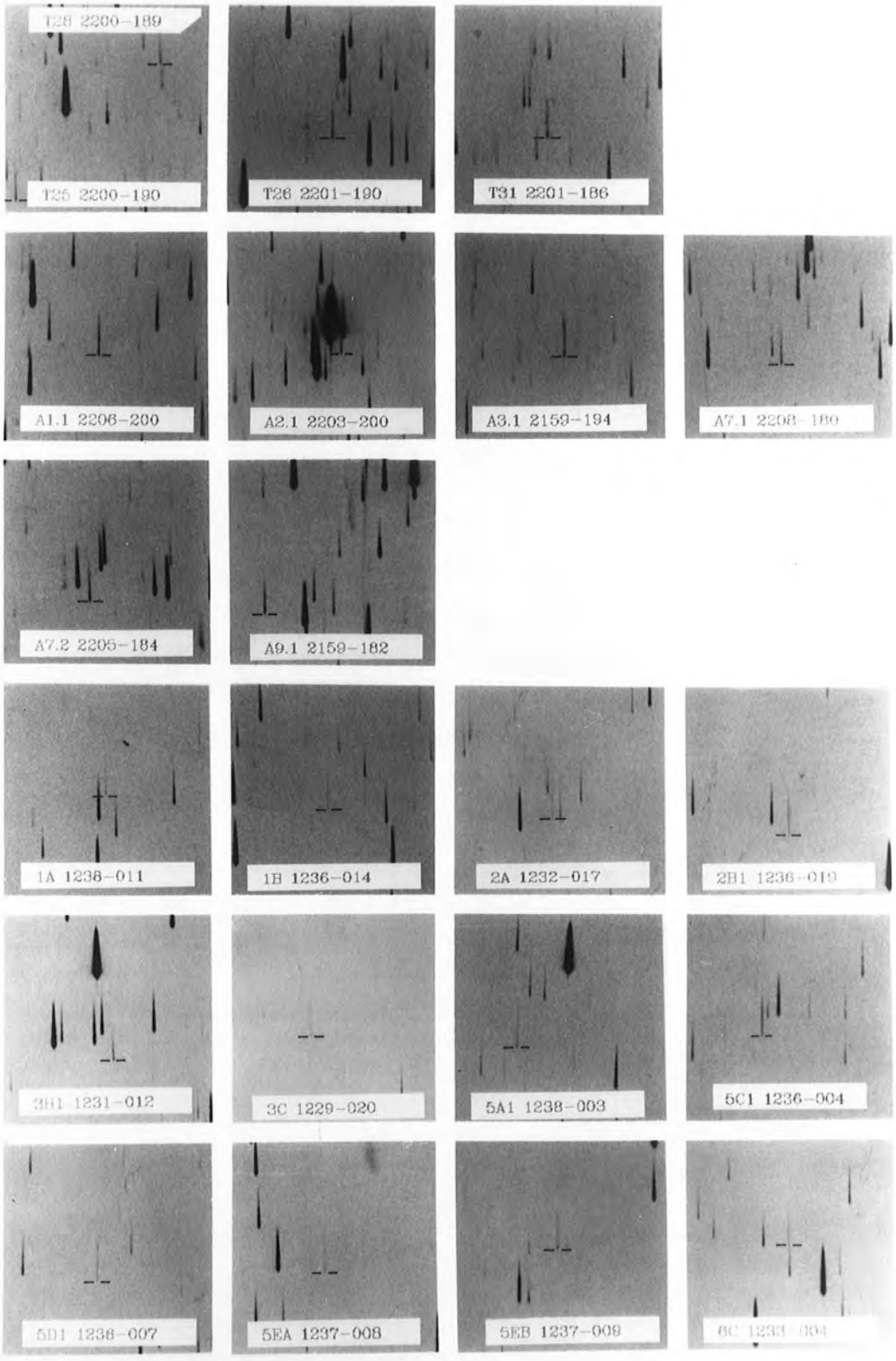

Figure 3.2 continued

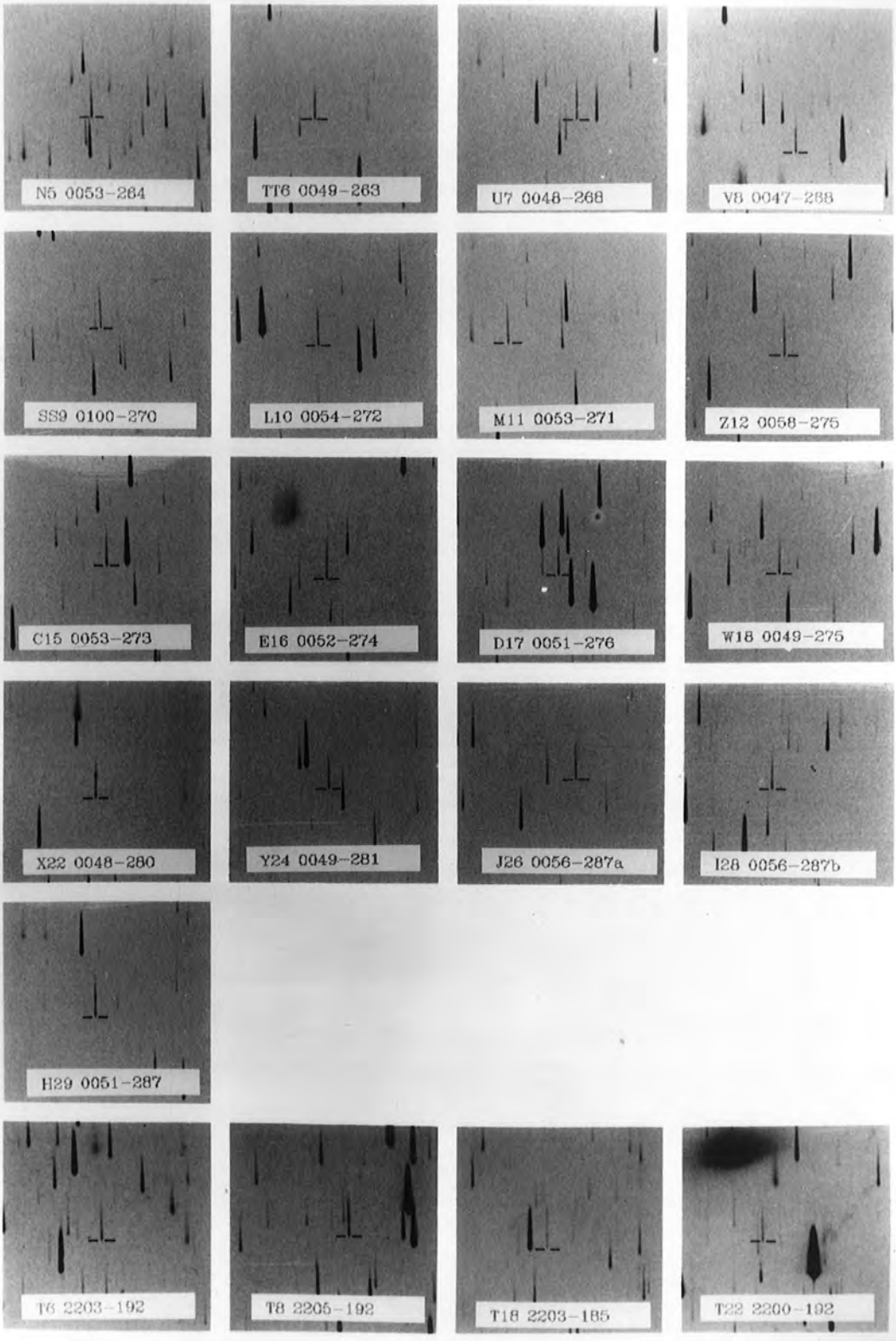

Figure 3.2 continued

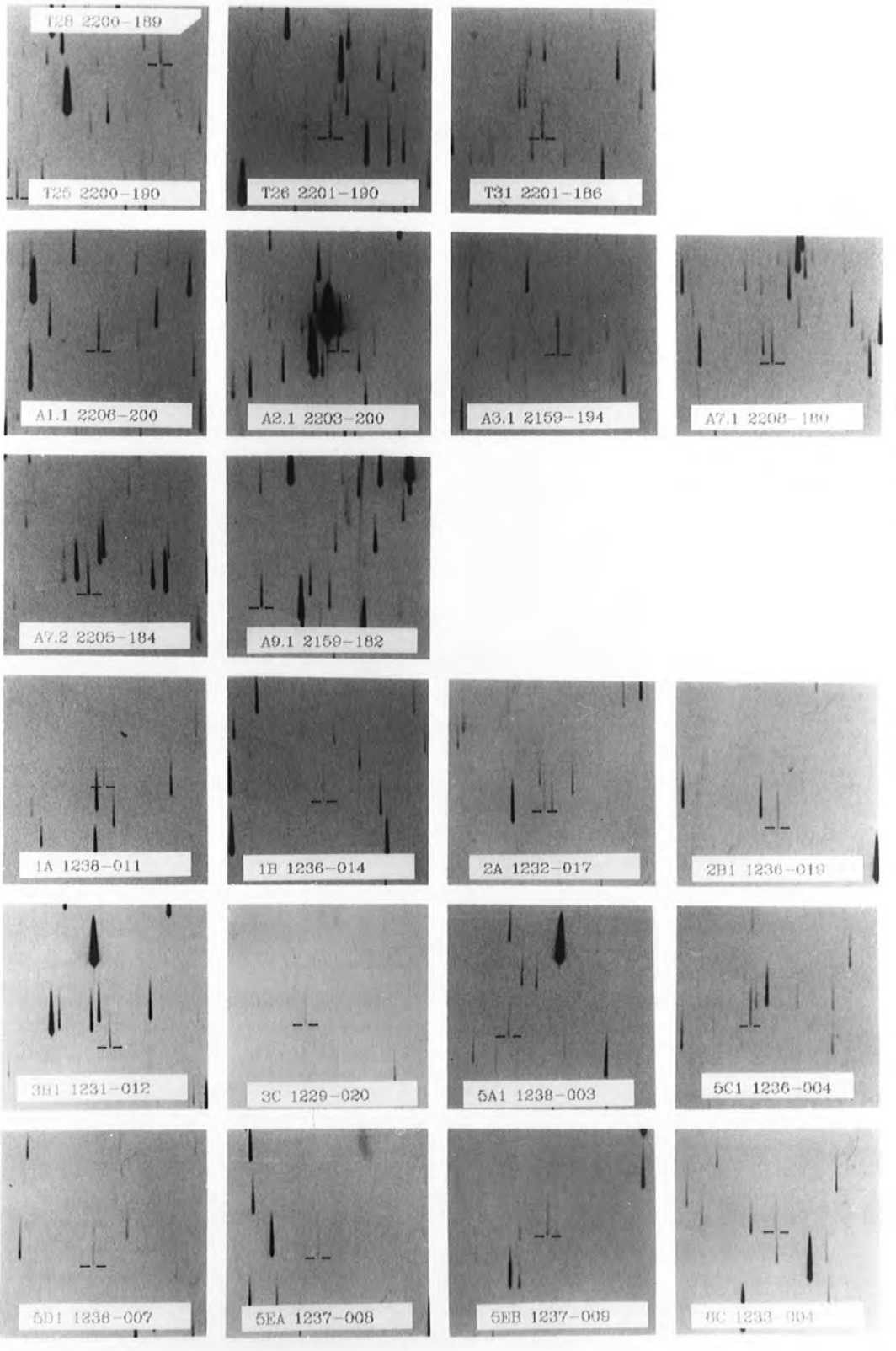

Figure 3.2 continued

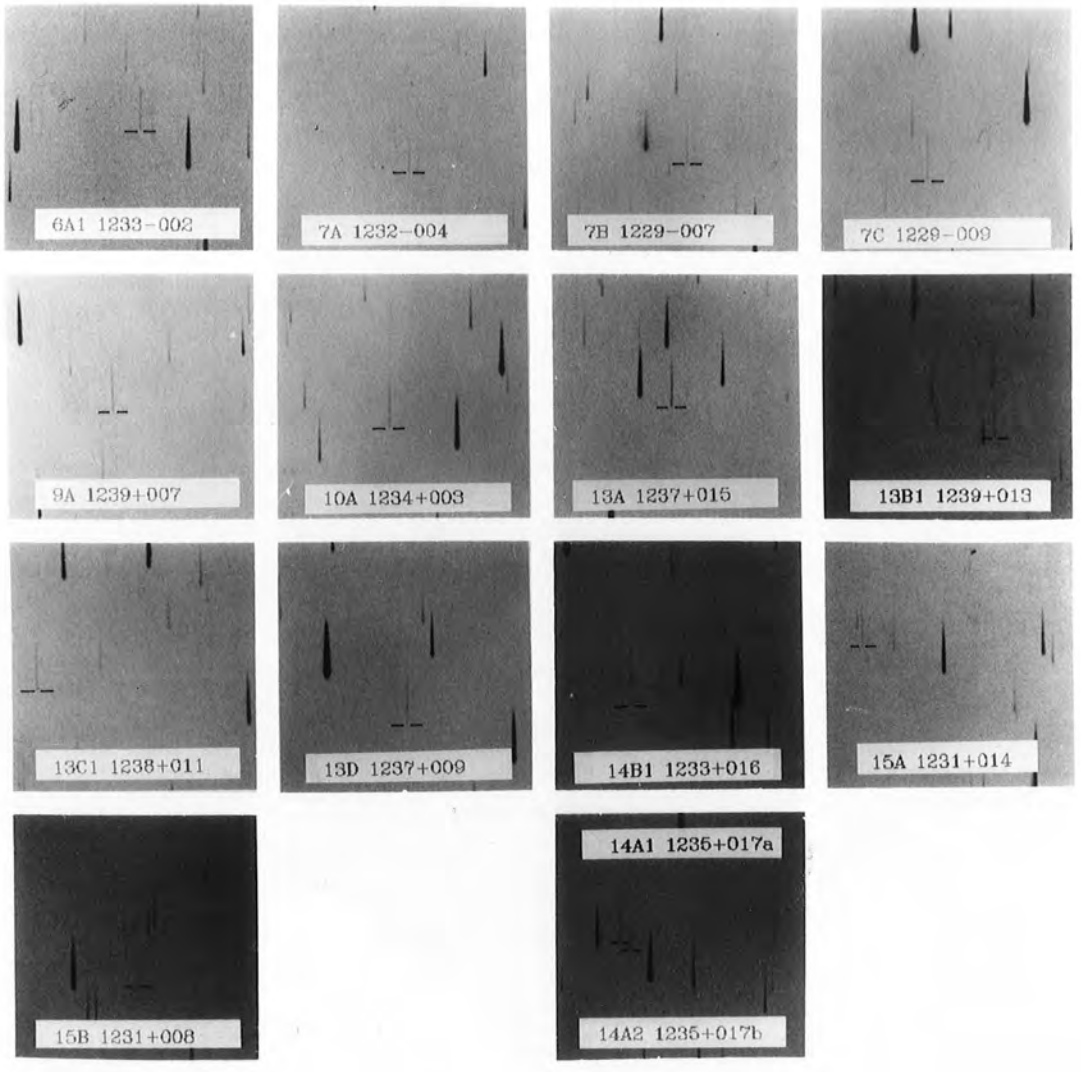

Figure 3.2 continued

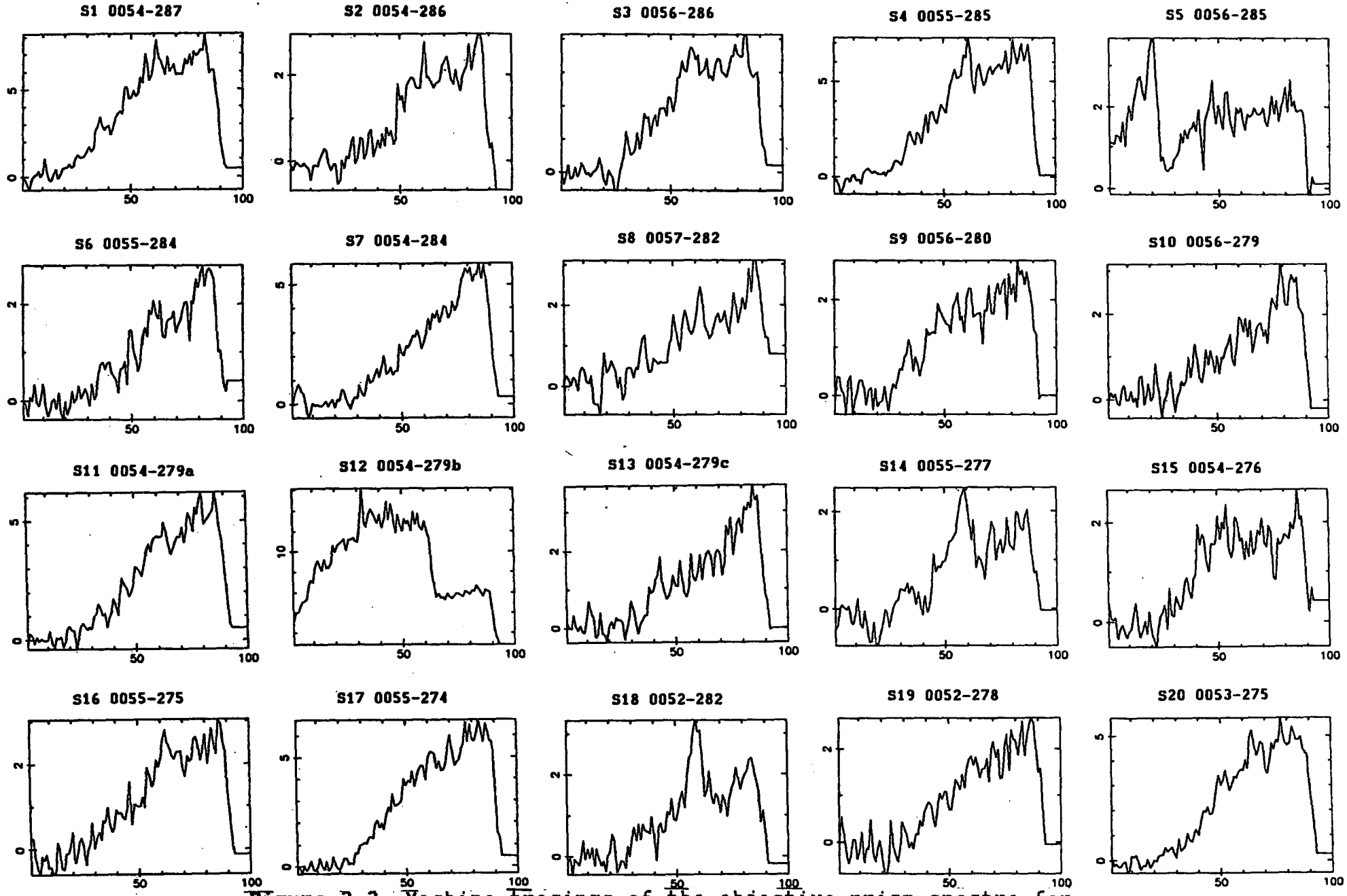

Figure 3.3 Machine tracings of the objective prism spectra for the bright survey objects on the SGP. Channel number 39 corresponds to 3500Å, channel number 61 to 4000Å and 84 to 5000Å. See text for exact conversion

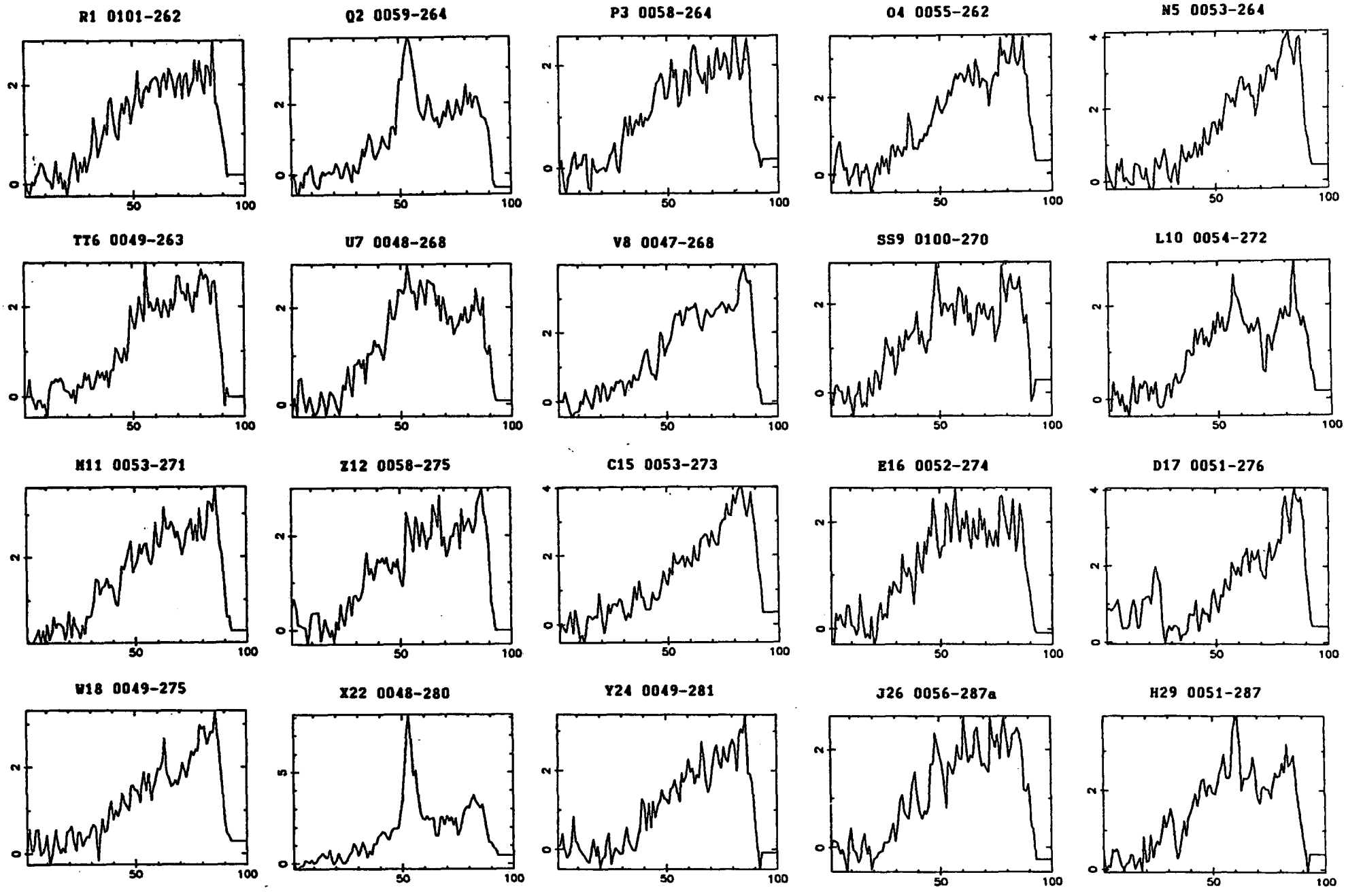

Figure 3.3 continued

Ordinary Galactic stars are given an approximate stellar type. This was estimated from the equivalent widths of the $H\beta$, $H\gamma$ and $H\delta$ absorption lines in their spectra when compared to the same lines in the spectra of standard stars (see figure 3.4) taken during the observing runs. Types are also assigned to white dwarfs found in the survey by referring to standard white dwarf spectra found in Oke (1974) and references therein.

The IPCS spectra for the QSOs and white dwarfs in the various UVX samples are plotted in figure 3.1, the abscissa being the wavelength in angstroms and the ordinate representing an arbitrary flux scale. Poorly subtracted night sky lines are indicated by black dots. As an illustration, at the foot of figure 3.1, we also display spectra which are typical of the Galactic stars found in the survey. In figure 3.2 we present photographs of the objective prism spectra for each object in the UVX sample. For the UVX objects on the SGP the results of a machine scan made by the COSMOS measuring machine of their objective prism spectra (kindly made available to us by Dr. Clowes) are shown in figure 3.3. In the machine scanned spectra, intensity is plotted linearly against distance (channel number) along each spectrum. To convert the channel number to wavelength the following relation may be used:

$$\lambda = 1313 + 3119 \, (\, 2.167 - 0.016X \,)^{-0.8333} \qquad \ldots \; (3.1)$$

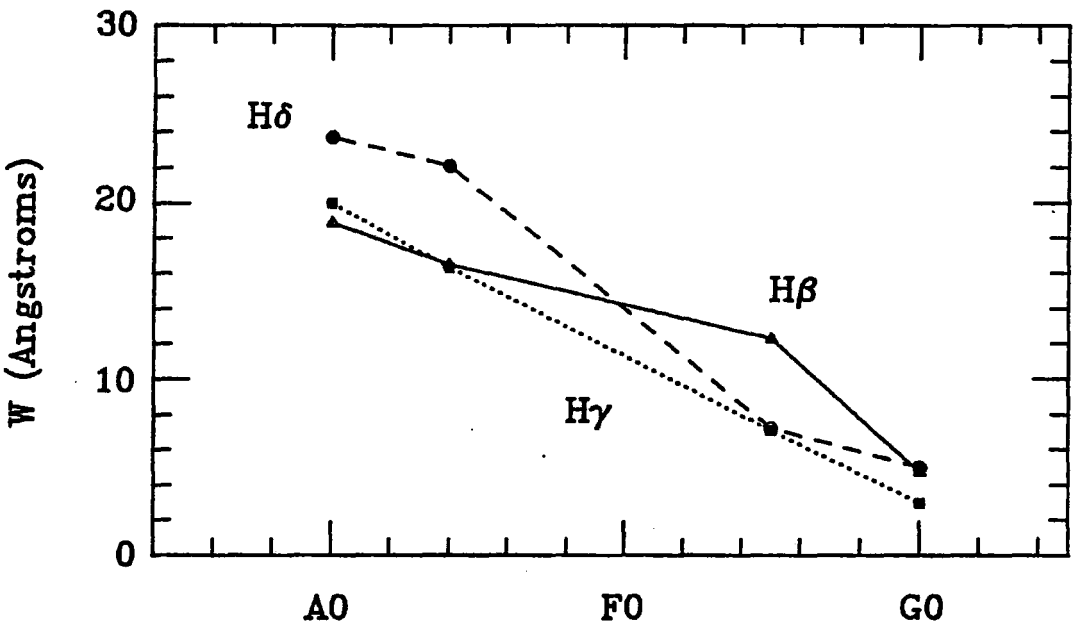

Figure 3.4 Measured equivalent width, W, for Balmer series absorption lines in standard stars.

where λ is the wavelength in angstroms and X is the channel number as plotted on the diagram. For instance, 3500 Å is situated at channel number 40, 4000Å is situated at channel number 61 and 5000Å at channel number 84.

The presentation of the different spectra together is intended to help in the identification of various types of UVX objects from either their appearance to the eye, as used in 'eyeball' searches for QSOs (Clowes and Savage 1983, hereafter CS), or from machine measurements of prism plates used in automated QSO detection (Clowes *et al.* 1984, Hewett *et al.* 1985). We must stress, however, that in no way did the appearance of an object's spectrum on the objective prism plate influence our decision to observe it spectroscopically. We merely observed all the UVX objects within our selected areas regardless of what they looked like on the objective prism plate. In some cases, where observing time was limited, not all the objects in a given sample were observed spectroscopically (see table 3.2 for precise details). However, those objects that were observed were simply selected at random from the parent sample. Thus we were sure not to exclude any particular class of QSO that, while exhibiting UVX, did not possess prominent emission lines.

For all but one QSO (S15 - see note 2 following table 3.2) in the survey, two or more emission lines could be identified in the slit spectrum. For all these objects, therefore, an unambiguous redshift determination was possible. The redshift of each QSO was found by comparing the wavelength ratio of two emission lines in a QSO spectrum with the rest wavelength ratio

of pairs of common QSO emission features such a Lyα/CIV, CIV/CIII] etc. The agreement between the values for the observed and rest line ratios had to be 0.5% or better (corresponding to a maximum allowed shift of $\delta z/z = 0.01$ in the redshifts obtained from the separate emission lines) before the line pairs were positively identified, and thus a redshift assigned to the QSO. The emission line redshift for each QSO is the mean of the redshifts of the individual emission lines, the error quoted being the standard error on this mean.

For some QSOs, in addition to the emission lines used to derive the redshift, other lines in the QSO spectrum could be identified, but were too heavily cut by absorption or too weak to make a reliable determination of the emission wavelength possible, and so give an accurate redshift. Such lines are still marked on the slit spectra, but are indicated by an asterisk in table 3.2.

3.2.3 Stellar Content of Catalogue

As we can see from table 3.2 all of the non-emission line objects picked up by the UVX technique are Galactic stars. Based on their hydrogen line strength, they mostly have late F/early G spectral types. With apparent magnitudes in the range 17.5 mag < b < 19.0 mag, for the SGP field at least, they will lie 4-12 kpc from the Galactic plane and we may expect them to be population II subdwarfs. To investigate their metal poorness we assigned each star a spectral class based on the equivalent widths of their Ca II H and K lines, these being the only metal lines

easily detectable in our low resolution spectra. The resulting spectral types (see the values in parentheses following the Balmer line spectral classification in table 3.2) are generally found to be much earlier than those based on the hydrogen lines and we conclude that the stars are indeed mostly metal weak subdwarfs. It is not possible, however, to explain their excess ultraviolet colours solely on the basis of the metal weakness. Sandage (1969) showed that, even for a star with zero metallicity, the u-b colour is only reddened by 0.3 mag. Thus these late F/early G stars should have a u-b colour no bluer than u-b $\simeq$ -0.2 mag. The most likely explanation of the subdwarfs' apparent UVX colours is that they have been accidentally produced, with the ±0.20 mag rms errors in our u and b magnitudes scattering metal-weak subdwarfs into the UVX region. This, of course, assumes that our (u-b) colours are approximately on the same zero-point as those quoted in the Johnson system. As discussed in chapter 2.5 we have no reason to believe *a priori* that this is so, but the analysis of the u-b colours for QSOs discovered in the faint spectroscopic survey (see chapter 3.4) will demonstrate that this is not an unreasonable assumption.

One of the Galactic stars, S9, deserves further mention. Although it was typed A5 by Boyle *et al.* (1985), subsequent analysis of its spectrum has revealed the presence of the HeI lines at λλ4168,4388 and 4471Å, thus assigning it an even earlier spectral type of B0-B5 from a comparison with the standard stellar spectra in Jacoby *et al.* (1984). This is by far the earliest spectral type found for a star in the bright survey (it

is certainly the only object to exhibit He lines) and its classification is supported not only by its extreme u-b colour but also by its b-v colour which is significantly bluer than those of other stars. Its faint apparent magnitude (b = 18.85 mag) and early spectral type combine to place it at a great distance from the Galactic plane, thus making it a Population II star. The only likely Population II stars to be assigned a spectral type of B are blue stragglers and blue horizontal branch (HB) stars. Since it is well established from studies of globular clusters that blue stragglers only comprise a very small fraction (<1%) of the halo star population, much smaller, indeed, than HB star contribution to the halo population, we conclude that S9 is most likely to be a HB star. We note that the absence of variability seen in S9 (b_{1921}-b_{3721} = 0.1 mag) does not preclude it from being such, as B stars lie well away from the instability strip on the HB. The absolute magnitude for such a star is M_B = + 1, thus putting it 30kpc distant from the Galactic plane.

The remaining Galactic star population consists of white dwarfs. Seven were found in this survey (two DG and five DA) and they comprise ≃10% of our UVX sample. Assuming absolute magnitudes of M_B = +11 for DA white dwarfs and M_B = + 14 for DG white dwarfs (Allen 1973), such objects in our survey will be at distances of between 100pc (for the DG white dwarfs) and 350pc (for the DA white dwarfs) from the sun. Two of the DA white dwarfs observed in this survey (M11 and J26) exhibit unusual Balmer line profiles. We tentatively suggest that the triplet

structure seen is caused by line splitting in a strong magnetic field, i.e. the Paschen-Back effect. From Garstang (1977) we estimate that the size of the magnetic field required to produce the observed splitting is $\simeq 5 \times 10^6$ Gauss (5 MG) and 7 MG in J26 and M11 respectively.

In the literature there are only 15 known magnetic white dwarfs, representing just 1% of all white dwarfs spectroscopically surveyed (Liebert *et al.* 1985), all of which have field strengths greater than $\simeq$ 5 MG. Were these two objects in our survey confirmed to be magnetic white dwarfs it would indeed be a remarkable result, as not only do they represent 25% of our white dwarf sample, though admittedly statistics are poor, but also their fields' strengths are as low as any that have previously been measured. We tentatively conclude that there may be a large population of white dwarfs with magnetic fields of the order of a few megagauss which have either previously escaped detection in the bright magnitude limited surveys (Liebert *et al.* 1983 conclude that this is indeed possible) or which only become numerous at faint magnitudes.

3.2.4 QSO Content of Catalogue

Several interesting QSOs discovered in the survey also merit detailed discussion. One such object is the QSO S14. On the direct, IIIaJ AAT plate of this area (J1888) two faint (B≃22 mag) galaxies are clearly visible a few arcseconds away from the QSO (see figure 3.5). Because of the high redshift of the QSO (z=2.19), it is unlikely that the galaxies are physically

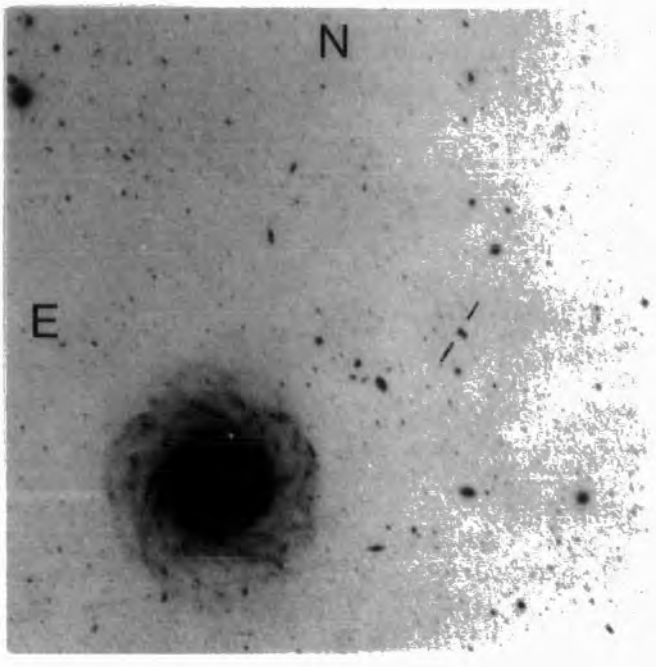

Figure 3.5 The appearance of S14 on the AAT plate J1888.

associated with the QSO. A simple consideration of the surface densities of QSOs at $b < 19$ mag and galaxies at $b < 22.5$ mag, reveals that if QSOs and galaxies are distributed independently over the sky, the probability of finding such a chance superposition is only $\simeq 4\%$. One possible explanation, if the superposition of the QSO and the galaxies is not a statistical fluke, is that the QSO is being lensed by the galaxies.

At the foot of the QNY sample in table 3.2 we also list two UVX objects (14A1 and 14A2) that, while outside the survey limits and thus not included in the complete sample, were a pair of UVX objects observed spectroscopically to check if they formed an interesting grouping such as a QSO cluster or a gravitational lens. The objects are only separated by 15 arcseconds on the sky, have similar u-b colours, and they turned out to have extremely similar spectra. Both QSOs show one strong emission line (displaced by 200Å between the two spectra). We attribute the emission to MgII (λ2798) from the appearance of weaker lines seen in both spectra. This gives 14A1 a redshift of 0.63 and 14A2 a redshift of 0.72. Whether or not these QSOs are located in the same supercluster structure (see e.g. Oort *et al.* 1981) is, however, open to debate as their comoving spatial separation is $200h^{-1}$ Mpc ($q_0 = \frac{1}{2}$), somewhat larger than the currently accepted sizes for galaxy superclusters. In spite of this, this pair merit further observation - especially to investigate the possibility of common absorption line systems and the appearance of absorption line systems in the high z QSO at the emission line redshift of the lower redshift QSO (Shaver and Robertson 1983).

3.2.5 Comparison of QSO search techniques

Two of the fields observed in this survey have been searched for QSOs by other authors. Campusano and Torres (1983), hereafter CT, have compiled a UVX catalogue of stellar objects on the SGP based on searches of Maksutov Schmidt plates. QSOs on the SGP field have also been found by CS from a visual inspection of an objective prism plate. Savage and Bolton (1979), hereafter SB, also used this technique, in conjunction with a UVX criterion, to find QSOs on the QSM field. In addition MT found a number of QSOs in a small area (0.31 sq. deg.) on the QSM field as part of a complete objective prism/spectroscopic survey of all stellar objects in this field down to B = 20.0 mag. We now compare the success rates for finding QSOs between these searches and the UVX technique employed here.

CT detected 4 out of the 13 QSOs found here on the SGP using their UVX technique. This success rate agrees well with their estimate of their survey's completeness at B < 19.0 mag of between 30% and 50%. Conversely, of the 28 QSOs confirmed by slit spectroscopy listed in their paper, 17 were outside our survey regions, 7 were outside the magnitude limits used to define our samples, while the remaining 4 were those picked up in common between the two surveys.

On the SGP central area our UVX technique found both z < 2.2, b < 19.0 mag QSOs found by CS over that area and in addition picked up 2 more QSOs (S5 and S14) that were not discovered in the objective prism search. While S5 shows a reasonably

featureless objective prism spectrum, S14 has a strong emission feature visible in its objective prism spectrum (see figure 3.2). It thus appears that it must have been inadvertently missed in the original visual search of CS. In the SGP faint sample we found that CS detected 6 out of the 9 UVX QSOs contained in that sample. Two of the QSOs missed (Z12 and E16) do exhibit conspicuous emission lines in their objective prism spectra but the other QSO (R1) has a featureless objective prism spectrum.

On the QSM field we discovered no new QSOs in the small area surveyed by MT. In this area MT found 4 QSOs (all fainter than our bright survey magnitude limit), 2 more than had been found by SB on the same area. Although the numbers involved were small, MT proposed that, on the basis of their survey, the SB QSO catalogue appeared to be incomplete. Over a larger area on the QSM field we also find that the SB catalogue is incomplete. We found an extra 2 QSOs - one in the central area (T31) and one in the bright sample (A1.1) - over and above the three QSOs found by SB. Although T31 exhibits an unremarkable objective prism spectrum A1.1 has a conspicuous emission feature in its objective prism spectrum and must have been accidentally overlooked in the objective prism search. Indeed, it has already been noted that the number densities in the SB catalogue are low compared to other catalogues (Veron and Veron 1982).

From the comparisons with the QSO catalogues of CT, CS, and SB we see that, within the magnitude limits used to define our survey, we detected every low redshift ($z<2.2$) QSO that had previously been found by these authors, in addition to doubling

the number of QSOs known on these areas. This provides excellent evidence that the UVX technique is considerably more complete than many methods previously used to search for low redshift ($z < 2.2$) QSOs and establishes UVX surveys from machine measurements of photographic plates as an extremely important method in QSO search techniques. As many of the QSOs in the CS and SB catalogues were found using an independent search technique (e.g. objective prism) to UVX, we may have an indication that our UVX survey is relatively complete for $z < 2.2$ QSOs. However, subtle selection effects amongst optical selection techniques (e.g. weak lined, low redshift QSOs may be non-UVX) may conspire to reduce the independence of such search techniques.

With the vast increase in QSO statistics afforded by the faint UVX survey (see chapter 3.4) we will, however, be able to demonstrate much more accurately the true level of incompleteness in our UVX survey.

It would appear that the 'eyeballed' catalogues made from objective prism plates are substantially (at least 50%) incomplete and it will be interesting to see whether the machine selection of emission line objects from objective prism plates such as the Automated QSO Detection (AQD) of Clowes *et al.* (1984) will remove this incompleteness.

3.2.6 Surface Density of UVX objects

In table 3.3 we present the overall numbers and surface densities for the various types of objects found in the UVX survey. Table 3.3 lists, for each magnitude bin, the area covered by the spectroscopic search, the number of UVX objects, the number for which slit spectra were obtained and the numbers of stars, QSOs and white dwarfs identified from the slit spectra. These numbers are then given as surface densities when due account has been taken of the objects not observed spectroscopically. Table 3.3 can be summarised by the following points:

1. With a u-b < -0.50 mag criterion our UVX sample between 17.5 mag < b < 19.0 mag contains approximately 40% QSOs, 50% Halo Stars and 10% white dwarfs, the surface density of QSOs being 1.70 ± 0.42 per square degree.

2. With the less strict criterion of u-b < -0.35 mag, we find that the percentage of QSOs in the UVX sample drops to ≃ 20% while the surface density of QSOs increases to 2.75 ± 1.23 per square degree. We note, however, that with this UVX cut-off the percentage of QSOs in the faintest 18.5 mag < b < 19.0 mag bin is much higher (≃ 36%). At yet fainter magnitudes the suggestion is that significant numbers of QSOs may also be contained in this u-b range.

u-b < -0.50 SGP and QSM fields

Magnitude Limits	Area	Numbers					Surface Densities (per square degree)			
		UVX stars	Obs[1].	Halo stars	QSOs	WDs	UVX stars	Halo stars	QSOs	WDs
17.5<b<18.0	9.33	4	4	2	2	0	0.43	0.22	0.22	0.00
18.0<b<18.5	9.33	6	6	4	2	0	0.64	0.42	0.22	0.00
18.5<b<19.0	9.47	32	32	16	12	4	3.38	1.69	1.27	0.42
	Totals	42	42	22	16	4	4.45	2.33	1.70	0.42

u-b < -0.35 SGP field

Magnitude Limits	Area	Numbers					Surface Densities (per square degree)			
		UVX stars	Obs[1].	Halo stars	QSOs	WDs	UVX stars	Halo stars	QSOs	WDs
17.5<b<18.0	1.62	6	5	5	0	0	3.70	3.70	0.00	0.00
18.0<b<18.5	1.62	2	2	2	0	0	1.23	1.23	0.00	0.00
18.5<b<19.0	1.62	12	11	7	4	0	7.41	4.72	2.69	0.00
	Totals	20	18	14	4	0	12.35	9.65	2.69	0.00

[1] Objects with spectroscopic confimration

Table 3.3 Numbers and Surface Densities of Objects in the Bright UVX Survey

Further consideration of the QSO surface densities found in this survey will be postponed until the next chapter when we can incorporate the results from the faint survey described in the following sections.

The number density of UVX white dwarfs in the SGP and QSM fields is found to be 0.4 ± 0.2 per square degree for 17.5 mag < b < 19.0 mag. Previously, Sandage and Luyten (1967) found a UVX white dwarf density of 0.6 per square degree down to a magnitude limit of B=17.75 mag (see Green 1980 for a discussion). The surface density of white dwarfs found is therefore in reasonable agreement with this previous observation.

3.3 The Faint UVX Survey

3.3.1 The FOCAP System

The success in detecting complete redshift limited samples of QSOs from the bright UVX survey encouraged us to embark on a much fainter and more comprehensive spectroscopic survey of UVX objects. The primary motivation for such a survey arose from a desire to obtain a complete QSO catalogue suitable for statistical analysis at fainter magnitudes than had hitherto been possible. As stressed in chapter 1, large samples of spectroscopically confirmed QSOs at B > 20.0 mag are essential in order to distinguish between the various forms of QSO evolution postulated and to establish the shape of the QSO luminosity function.

Of course, the prohibitive amounts of telescope time required to obtain spectra for such large numbers of faint objects would render such a survey impractical were conventional spectroscopic techniques to be employed (the reader is referred to the amount of time required to complete our bright UVX survey at b < 19 mag). The introduction of the Fibre Optic Coupled Aperture Plate (FOCAP) system at the AAT has, however, revolutionised faint object spectroscopy, allowing spectra for up to 50 objects to be obtained simultaneously over a wide 40 arcminute diameter field of view. FOCAP is discussed in detail by Gray (1984) and Ellis *et al.* (1984) and only brief details are given here. Basically FOCAP consists of a brass aperture plate and a fibre optic bundle. Holes are drilled into the brass aperture plate at the precise positions (≃0.5") of the objects to be observed. These holes can then be 'plugged up' with the ends of the fibre optic bundle that are mounted in brass ferrules, the collinear arrangement of the other fibre ends forming the entrance slit to the spectrograph. The aperture plate is then secured onto the telescope at the Cassegrain focus and up to 50 objects can be observed simultaneously for every fibre bundle/spectrograph combination used.

FOCAP therefore provides the first opportunity to obtain spectra for large numbers of faint objects quickly and efficiently.

3.3.2 Observations

Samples of UVX objects were selected in 40 arcminute diameter areas from the COSMOS machine produced catalogues on six high Galactic latitude fields. The fields chosen included the SGP, QNY and QSM fields used in the bright survey plus three new fields QSF, QNB and QNA, all selected because of their high Galactic latitude and the availability of good, deep U plates. Different U plates from those employed in the bright survey were used to select the UVX sample on the SGP and QNY fields in these observations. U6380 on the SGP extended to significantly fainter magnitudes than U2639 (see chapter 2.6) and U9216 is of a superior grade to U5707 (see table 2.1). These later plates were not available when the bright UVX survey was undertaken. The UVX criterion on each of these six fields was chosen as close as possible to the locus of Galactic stars (dashed lines in figure 2.5), thus ensuring that as many UVX QSOs as possible were selected whilst keeping the contamination by ordinary Galactic stars to a manageable level.

The faint magnitude limit ($b \simeq 21.0$ mag) for the survey objects was chosen to give approximately 40 - 50 UVX objects in the 40 arcminute diameter FOCAP area, ideally matching the number of UVX objects to the number of fibres available, when due account is taken of $\simeq 5$ sky dedicated fibres in each FOCAP observation. The UVX criteria, magnitude limits and field centres for all FOCAP fields are given in table 3.4.

Field	RA (1950)	Dec	Magnitude Limit	UVX Limit
SGP1	00h 56m 29s.1	-28° 48' 58"	18.0 < b < 21.0	u-b < -0.30
SGP2	00 49 39.4	-29 21 44	18.0 < b < 21.0	u-b < -0.30
SGP3	00 52 34.0	-28 35 58	17.0 < b < 21.0	u-b < -0.30 (b-v < 0.20)
QSF1	03 40 31.5	-45 04 15	17.0 < b < 21.0	u-b < -0.40
QSF2	03 44 54.1	-46 04 20	17.0 < b < 21.0	u-b < -0.40
QNB1	10 39 57.0	01 30 41	17.0 < b < 21.0	u-b < -0.50 (b-v < 0.20)
QNB2	10 41 25.0	00 57 24	17.0 < b < 21.0	u-b < -0.50 (b-v < 0.20)
QNY1	12 33 50.3	-00 38 18	17.0 < b < 21.5	u-b < -0.45
QNY2	12 35 23.8	00 17 56	17.0 < b < 21.5	u-b < -0.45
QNA1	13 36 03.6	00 23 13	17.0 < b < 21.5	u-b < -0.30
QSM1	22 06 56.9	-19 26 23	18.0 < b < 20.75	u-b < -0.50
QSM2	22 07 00.6	-20 05 33	17.0 < b < 20.75	u-b < -0.50

Table 3.4 Faint UVX Survey: Field Centres and Sample Criteria

Additional survey objects were also chosen from their anomalous b-v colours on two fields (SGP and QNB). Objects were selected at random from a sample of stellar images defined by the criteria listed in table 3.4. This extra sample was chosen for two reasons; firstly to see if any high redshift QSOs ($z > 2.2$) could be picked up and secondly to find any $z < 2.2$ QSOs which may have been scattered out of our UVX sample by photometric errors.

Two fields (QNY and QNA) were nominally surveyed to b = 21.5 mag. While neither of the J plates on these fields are complete beyond b = 21.0 mag (see chapter 3.4e), this limit was chosen to obtain spectra for a few ($\simeq$ 3 - 4 per field) extremely blue (u - b $\simeq$ -1.0 mag) objects at very faint magnitudes.

In all, twelve FOCAP fields were observed at the AAT on the nights of 23 September 1984, 20-22 February 1985, 18 April 1985 and 18 July 1985. The equivalent of four clear nights was obtained from these six allocated. As before we used the IPCS with the RGO spectrograph operated at 156Åmm^{-1}. The wider diameter (400μm) fibres were used to observe the survey objects. These fibres have the advantage that, in any conditions other than those experienced in excellent seeing (i.e. in conditions where the seeing is > 2") their efficiency is higher than that of the smaller diameter (200μm) fibres. Since the effective slit width at the entrance to the spectrograph is dictated by the diameter of the fibres, the larger fibres do have the disadvantage that the resolution of the system is decreased, in this case to 15Å. However, we are concerned with merely identifying and obtaining redshifts for broad emission line

objects and the decreased resolution was not considered to be too great a drawback. Based on the results of the bright survey, where integration times of 3000 secs were sufficient to obtain a S/N of $\simeq$ 10 for b = 19.0 mag objects, we estimated that 8000 secs would be long enough to give a S/N $\simeq$ 4-5 for b = 21.0 mag QSOs, taking into account the overall transmission (70%) of the FOCAP system (Gray 1984). This reduced S/N was considered high enough to identify the broad QSO emission lines. On all but four FOCAP fields this integration time was achieved (see table 3.5). As a result the sample on the QNA1 field was restricted to b $<$ 20.5 mag. Another of these fields (QSM1) was limited to b $<$ 20.75 mag anyway because of the U plate limit. However, on two of the shorter exposure fields (SGP1 and QSF1) we appeared to have no problem in identifying faint QSOs (i.e. there is no fall off in their surface density beyond b $\simeq$ 20.5 mag - see appendix B) and we consider them to be complete to b = 21.0 mag. That good signal-to-noise is obtained on these fields despite their short integration times, may well be the result of the good seeing conditions prevalent during these exposures.

3.3.3 Data Reduction

Reduction of the data was carried out using the SPICA software package on the Durham University node of the SERC STARLINK VAX system. With data obtained from FOCAP observations it is first necessary to select the $\simeq$ 40 - 50 spectra from the IPCS data. The IPCS introduces significant S-distortion into many of these spectra, causing each spectrum to lie over several

Field	Date Observed	Seeing (arcsec)	Integration Time (seconds)
SGP1	23/09/84	1.5	5851
SGP2	23/09/84	2.0	9000
SGP3	18/07/85	2.5	9000
QSF1	20/02/85	0.8	6000
QSF2	21/02/85	3.5	4250
	22/02/85	1.5	5558
QNB1	21/02/85	3.5	4217
	22/02/85	2.0	6000
QNB2	20/02/85	1.5	9000
QNY1	20/02/85	3.5	8000
QNY2	22/02/85	2.0	8750
QNA1	18/04/85	3.7	5340
	18/07/85	3.0	2305
QSM1	23/09/84	1.5	6000
QSM2	18/07/85	4.0	9000

Table 3.5 Faint UVX Survey: Observational Details

cross-sections in the IPCS data frame. The spectra were therefore extracted from the data frame using the FOLLOW and EXTRACT programs written by R.M. Sharples. FOLLOW uses a polynomial fit to define the shape of each spectrum from the co-added object frames for each FOCAP field. Two cross-sections either side of each fitted line were EXTRACTed and summed to give the individual spectra.

Extracted spectra were then wavelength calibrated using the Cu-Ar, He and Hg arc spectra taken after every 3000 second integration on the survey fields. For each fibre field it was found that the arc lines shifted by half a channel or less throughout the observation (see table 3.6). In addition the fibre to fibre sensitivity did not change by more than 5%, as estimated from the 3 - 5 sky offset frames taken during each FOCAP observation (see figure 3.6). Thus each arc, sky offset and object frame could be co-added within any particular FOCAP observation, with wavelength calibration and sky subtraction being carried out using the co-added frames. Normally $\simeq$ 15 arc lines would be used to define the wavelength calibration polynomial. The wavelengths of the lines extended from 3650Å (Hg arc) to 7227Å (Cu-Ar arc). Residuals for these lines in the fit were never more than 4Å. The accuracy of the calibration was checked from the wavelengths of the night sky lines λ5577 and λ6300, which were always found to be within $\pm$3Å from their true position. The sky offset frames were used to normalise the transmissions of the individual fibres in the object frame, whereupon sky subtraction could be achieved using the 4 - 10

Arc Number	λ6678 (Channel No.)	λ5876 (Channel No.)	λ3889 (Channel No.)
1	124.5	396.2	832.6
2	124.0	395.8	832.6
3	124.4	396.0	832.8

Table 3.6 Shifts in He Arc Lines during FOCAP Observation of SGP3

Name	RA (1950) (h m s)	Dec (o ' ")	b	u-b
QNY1:04	12 33 24.2	-00 54 56	19.48	-1.01
QNY2:04	12 35 25.5	00 21 08	20.00	-1.02
QSM2:45	22 06 49.5	-20 13 15	20.01	-1.17

Table 3.7 Survey Objects Located on fibres with Poor Transmission

Magnitude Range	Number Observed	Number Unidentified (Classes: Q?,NL?,CONT,?)
17.0 < b < 18.0	29	0
18.0 < b < 19.0	67	0
19.0 < b < 19.5	57	0
19.5 < b < 20.0	72	5
20.0 < b < 20.5	105	12
20.5 < b < 21.0	127	25

Table 3.8 Magnitude Distribution of Unidentified Objects in Faint UVX Survey

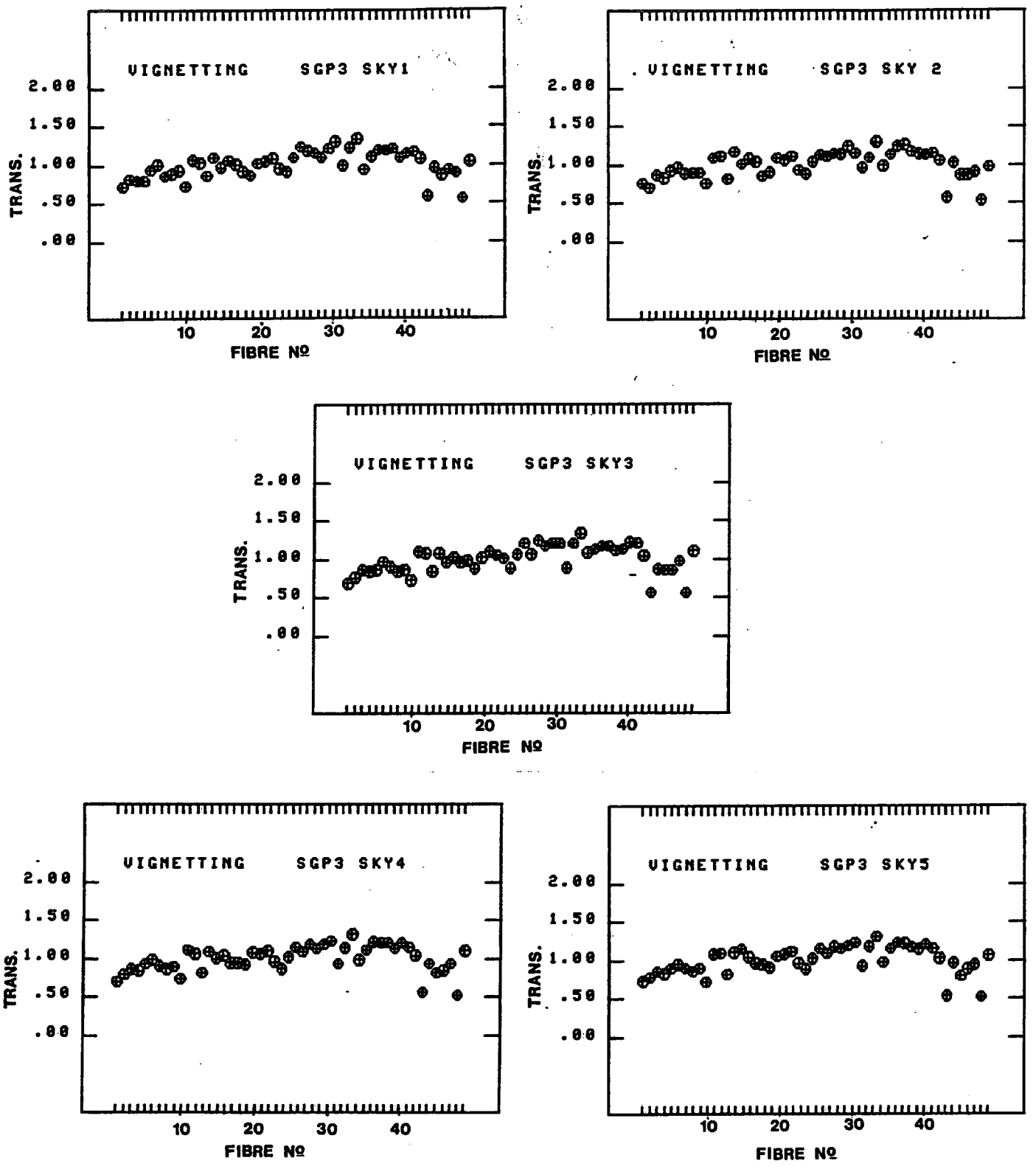

Figure 3.6 Normalised fibre transmissions for sky offset frames taken during FOCAP observation of the SGP3 field.

sky-dedicated fibres in this frame.

3.3.4 The Catalogue

Appendices A,B,C and D contain the faint UVX survey in full. Spectra for all emission line, bright (b < 20.5 mag) Galactic stars and unidentifed objects are plotted in appendix A. The spectra presented are not fluxed, thus facilitating the identification of lines at the extreme blue or red ends of the IPCS spectra. The wavelength scale is plotted in angstroms, while the 'counts' ordinate is, in fact, plotted in units of 0.1 counts. The names for the objects represent the FOCAP field in which it was found, followed by the fibre number in that field. Three survey objects (see table 3.7) fell on fibres where the transmission was so low that the spectra of the objects were degraded to the extent where identification was impossible. While their UVX colours makes them strong QSO candidates, these three objects are ignored in any further analysis. A representative sample of sky subtracted sky fibres are plotted at the foot of appendix A to illustrate the success of the sky subtraction and the level of noise associated with the spectra. Appendix B lists details for all the emission line objects (QSOs and narrow line objects). Data for each object is provided in the following columns:

1. Name: See text above

2. R.A. and Dec.: 1950 coords, accurate to 1"

3. b: Calibrated COSMOS magnitude

4. u-b: Colour obtained from calibrated COSMOS magnitudes

5. ID: Identification of object.

   a. Q - QSO with broad emission lines

   b. BQ - Broad absorption line QSO

   c. NL - Narrow emission line object

6. z: Emission line redshift, determined for all spectra in an identical fashion to that indicated in chapter 3.2.2. The error (derived from the rms spread in the emission redshifts for each line) ranged between 0.001 and 0.005 for redshift class 1 and 2 objects.

7. Class: Goodness of Redshift

   1. Certain redshift - Two or more strong lines identified in the spectrum.

   2. Probable redshift - Usually obtained from one strong line and additional weaker lines.

   3. Uncertain redshift - Only 1 strong line seen or weak lines alone visible.

These are only general guidelines to the redshift classification, as the shape of the emission lines and surrounding continuum also provides many clues as to the likely redshift of the QSO even when only one strong line is visible (e.g. broad FeII emission around the MgII line).

8. Lines: Emission lines identified in the spectrum, with measured wavelength (in Angstroms)

Details for the non-emission line objects are given in appendix C. Columns 1. - 5. are the same as for appendix B, with the identification of the objects falling into one of four classes.

1. WD - White Dwarf, as identified from its broad absorption lines. Apart from two rare DAB white dwarfs found on the QSF field (QSF2:1 and QSF2:7), all white dwarfs identified were of the DA type.

2. B,A,F,G - Approximate stellar type (based on the Balmer series line strengths and reference to standard stellar spectra in Jacoby *et al.* 1984).

3. BIN - Binary Star (see below)

4. '-' - Faint stellar objects not classified. While the stellar absorption features of CaII H and K, G band and Balmer series are seen in these faint stars, the poor S/N obtained at these faint magnitudes (b > 20.5 mag) precludes

the assignment of reliable spectral types to these objects.

Appendix D contains a list of all those objects that remain unidentified in the faint UVX survey, usually due to poor S/N. Columns are as for appendices B and C with identification as follows:

1. Q? - Possible QSO

2. NL? - Possible narrow emission line object

3. CONT - Objects with no recognisable absorption or emission features. This class is only assigned to objects with sufficient signal-to-noise in their spectra to allow them to be easily distinguishable from ordinary Galactic stars.

4. ? - Insufficient S/N to attempt any classification

Table 3.8 presents the numbers of these unidentified objects in the survey as a function of magnitude.

3.3.5 Content of Stellar Catalogue

In table 3.9 we present the surface densities in each field for the various types of Galactic stars listed in appendix C. For consistency from field-to-field we ignore the objects picked up in the b-v selected sample on the SGP and QNB fields. From this table we see that, as in the bright survey, most of the Galactic stars found are halo stars, outnumbering the white dwarfs by 10:1.

	SGP			QSF			QNB		
Magnitude Range	Halo Stars	WD	Total	Halo Stars	WD	Total	Halo Stars	WD	Total
17.0<b<17.5	-	-	-	1.4	-	1.4	11.4	-	11.4
17.5<b<18.0	-	-	-	7.1	-	7.1	2.9	-	2.9
18.0<b<18.5	1.9	-	1.9	7.1	-	7.1	5.7	-	5.2
18.5<b<19.0	3.8	1.0	4.8	4.3	1.4	5.7	7.1	-	7.1
19.0<b<19.5	3.8	1.0	4.8	1.4	4.3	5.7	-	-	-
19.5<b<20.0	10.5	-	10.5	2.9	-	2.9	4.3	-	4.3
20.0<b<20.5	8.6	1.0	9.5	5.7	5.7	11.4	7.1	-	7.1
20.5<b<21.0			30.5			11.4			22.9
b<20.5	28.6	2.9	31.4	30.0	11.4	41.4	38.6		38.6

	QNY			QNA			QSM		
Magnitude Range	Halo Stars	WD	Total	Halo Stars	WD	Total	Halo Stars	WD	Total
17.0<b<17.5	5.7	-	5.7	-	-	-	11.4	-	11.4
17.5<b<18.0	2.9	-	2.9	-	-	-	1.4	-	1.4
18.0<b<18.5	4.3	-	4.3	5.7	-	5.7	12.9	-	12.9
18.5<b<19.0	1.4	-	1.4	-	-	-	11.4	-	11.4
19.0<b<19.5	2.9	1.4	4.3	17.1	5.7	22.9	14.3	-	14.3
19.5<b<20.0	2.9	-	2.9	5.7	-	5.7	12.9	-	12.9
20.0<b<20.5	4.3	-	4.3	25.7	-	25.7	2.9	-	2.9
20.5<b<21.0			15.7						
b<20.5	25.7	1.4	27.1	54.3	5.7	60.0	61.4	-	61.4

Table 3.9 Surface Densities (per square degree) for Galactic Stars found in faint UVX survey

All Fields

Magnitude Range	Halo Stars		White Dwarfs		Total	
	No.	Surface Density (/sq deg)	No.	Surface Density (/sq deg)	No.	Surface Density (/sq deg)
17.0<b<17.5	17	5.4	0	0.0	17	5.4
17.5<b<18.0	10	3.2	0	0.0	10	3.2
18.0<b<18.5	25	6.0	0	0.0	25	6.0
18.5<b<19.0	21	5.0	1	0.2	22	5.2
19.0<b<19.5	23	4.3	7	1.7	30	7.1
19.5<b<20.0	29	6.9	0	0.0	29	6.9
20.0<b<20.5	32	7.6	5	1.2	37	8.8
20.5<b<21.0					67	21.3
b<20.5	157	38.3	13	3.1	170	41.4

Table 3.9 contd. Surface Densities (per square degree) for Galactic Stars found in faint UVX survey

A total of 13 ($b < 20.5$ mag) UVX white dwarfs were detected in this survey, giving an average surface density of 3.1 ± 0.9 / sq. deg. However, eight of these white dwarfs were found on the QSF field alone. Thus the surface density on the QSF field (11.4 / sq. deg.) is significantly in excess of that determined over the other five fields (1.4 ± 1.1 / sq. deg.). It is unlikely that this anomalous density can be attributed to a redder UVX criterion on the QSF field, as the QSF limit is similar to those on the other fields. We therefore conclude that this enhanced density of QSOs on the QSF field is likely to be real. The white dwarf population on the QSF field is also anomalous in one other respect. Two white dwarfs on the QSF2 field (QSF2:1 and QSF2:7) exhibit broad HeI λ4471 absorption, in addition to the broad absorption lines of the Balmer series. Both these objects belong to the rare, DAB class of white dwarfs.

With apparent magnitudes in the range 19.0 mag $< b <$ 20.5 mag, the white dwarfs discovered in our faint survey lie at distances between $\simeq$ 300 - 800 pc from the sun. Thus the enhanced surface density of white dwarfs on the QSF field is unlikely to signify a 'white dwarf cluster' as such, since even if the cluster extended over the full 25 square degrees of the Schmidt plate, its angular size would only correspond to a distance of $\simeq$ 30 pc, some 10 times less than its line of sight extent. We note, however, that the distances for the white dwarfs are based on the assumption of an average luminosity of $M_B = +11$ for the DA and $M_B = +10.5$ for the DAB white dwarfs respectively. Increased S/N will be needed on many of these white dwarf spectra

before more accurate luminosities can be defined and thus the possibility of a 'white dwarf cluster' firmly ruled out. However, it is difficult to understand why there should be an enhanced density of the UVX white dwarfs in the direction of the QSF field (l^{II} = 250°, b^{II} = -50°) when many other fields (e.g. QSM, QNB and QNA) in the UVX survey have similar Galactic latitudes. Indeed the QSF field is closer to the Galactic *anti*centre than any of the other survey fields. The white dwarf population on this field thus remains an enigma.

Although many of the white dwarf spectra obtained in this survey have considerably poorer S/N than those obtained in the bright survey, we again note that a surprisingly large fraction (SGP1:13, QSF1:2 and QSF1:14) appear to exhibit the same splitting in their Balmer lines as did the white dwarfs (M11 and J26) in the bright survey. As before, we tentatively interpret this to be due to the presence of a magnetic field with a strength of a few megagauss. The high percentage of such white dwarfs in our faint survey (despite the decreased resolution in this survey) reinforces our conclusions on the nature of these objects reached in chapter 3.2.3. We stress, however, that such conclusions are still tentative and increased signal-to-noise will be required on many of these spectra before the magnetic properties of these white dwarfs can be firmly established.

The survey will, of course, be substantially incomplete for the other types of Galactic subdwarfs and cooler white dwarfs (e.g. DF, DG etc.), most of which will have redder colours than the UVX limits used in the survey. This is evidenced by the

numbers of Galactic stars picked up with such colours in the b-v selected sample on the SGP and QNB fields. We can however establish that, even in our survey, significant numbers of early type (B/A) stars are found at high Galactic latitudes (there may indeed be more B stars than we can identify, as the signal-to-noise obtained in most of the faint stellar spectra prohibits the identification of the weak HeI lines). As discussed in the case of S9, such objects are likely to be blue HB stars at large distances from the Galactic plane ($\simeq$ 50kpc for SGP3:14). For these stars there is also the possibility that they may be white dwarfs with weak absorption lines and therefore much closer. However, in the faint survey many of the objects assigned a spectral class of A or B were found in the b-v selected samples on the SGP and QNB fields (e.g. SGP3:14, QNB2:12) and hence have u-b colours incompatible with their being white dwarfs (e.g. SGP3:14 u-b = -0.14 mag c.f. DA white dwarf U-B = -0.8 mag). The strong Balmer limit seen in many of these objects (see spectra of QNB2:12) also precludes them from being (hot) white dwarfs. We note in passing, that although provisionally typed as a B star, QNB2:12 has an unusual spectrum. The width of the Balmer series lines and the size of the Balmer jump are consistent with it being a late B/ early A star. However, QNB2:12 also exhibits the HeII λ4200 line, usually only seen in O stars. This is all the more unusual when we consider that it does not show any trace of HeI lines we might expect to see if it were a O/B star with anomalously strong H lines.

We conclude therefore that significant numbers of field HB stars (along with perhaps some considerably more exotic varieties) do exist at substantial distances from the Galactic plane. Further investigations of their properties will, however, have to wait until increased resolution and/or better signal-to-noise are obtained for their spectra.

Five objects in the survey are listed as having no identifiable emission or absorption line features. These objects may belong to the BL Lac class but again increased signal-to-noise and higher resolution is also needed on their spectra.

Three other stars deserve special mention, namely QSF1:35, QNB2:27 and QSM1:10. These stars exhibit a composite spectrum: at wavelengths greater than 5500Å their spectra exhibit the broad TiO bands ($\lambda\lambda$5862, 6159) characteristic of M stars, while at shorter wavelengths they display blue spectra characteristic of either F stars (e.g. QSM1:10) or an almost featureless continuum (as in the other two cases), similar to those found in very hot stars. Such spectra are thought to be caused by binary systems where the light from the two stars involved, usually a late-type dwarf and a early-type star, combine to give the unusual spectrum seen. Ferguson *et al.* (1984) also find a number of such objects in their UVX survey, although the cool companion is normally earlier than spectral type M.

3.3.6 Content of Emission Line Catalogue

In all, 169 QSOs with broad emission lines have been identified, with class 1 or 2 redshifts obtained for 85% of the sample.

Five of these QSOs were identified as belonging to the broad absorption line (BAL) class of QSOs (as defined by Weymann and Foltz 1983). Thus BAL QSOs represent ≃3% of all QSOs identified in this survey. This number agrees well with other estimates of the frequency of BAL QSOs; Weymann *et al.* (1981) estimate that BAL QSOs constitute between 1 - 10% of the QSO population and Hazard *et al.* (1984) arrive at a similar figure of between 3 - 10%. The percentage found by Hazard *et al.* (1984) was derived for QSOs with higher redshifts ($2.2 < z < 2.4$) and brighter magnitudes ($B < 18.5$ mag) than those in our survey ($z < 2.2$, $B < 20.9$ mag). Thus we find no support for the claim by Hazard *et al.* (1984) that BAL QSOs are found preferentially at higher redshifts and higher luminosities, although we do note that, within our own survey, the BAL QSOs were found preferentially at bright magnitudes (only one was identified with $b > 20.0$ mag). However, we recognise that the lack of faint BAL QSOs found in our survey may merely be due to the lower S/N at faint magnitudes preventing their identification here. Moreover, our figure for the number of BAL QSOs is likely to be a lower estimate, as some BAL QSOs may fail the UVX criteria when a broad absorption trough is present in the U band (the BAL QSO SGP3:35 has an anomalously 'red' UVX colour - see chapter 3.4d - for precisely this reason).

If confirmed, the redshift for the BAL QSO QNB1:49, z = 0.49, will be the second lowest yet seen for this particular class of QSO, being at a much lower redshift than PG0946+301, z=1.216 (Wilkes 1985), currently the second lowset redshift BAL QSO, and much closer to the redshift of the lowest PG1700+518, z=0.288 (Wampler 1985). At present the redshift of QNB1:49 is based on the identification of the strong emission line seen as MgII with a weaker HeII feature seen redward of this emission line. The discovery of such a low z BAL QSO would have important consequences for the evolution and nature of the BAL phenomenon in QSOs (Turnshek *et al.* 1985), but further comment is judiciously postponed until a red spectrum is obtained for QNB1:49 to identify further lines.

In addition to the broad emission line QSOs, a further 23 narrow emission line objects were identified. All these objects are at low redshifts ($z < 0.42$) and hence have low luminosities ($M_B > -21.0$). These objects have also been detected in other UVX or broadband surveys for QSOs (Koo 1983, Marano *et al.* 1986) and are identified as galaxies with bright nuclei, giving them a stellar appearance on the photographic plate. Indeed only 3 of the emission line galaxies found in our survey show extended structure on a close visual inspection of the relevant J plate. Their increasing prominence in the UVX sample at fainter magnitudes and their relatively red UVX colours are general features of this population (Koo 1986) which is well reflected in this survey (see table 3.10). No further identification of the type of nucleus is attempted as most classification schemes rest

	u-b colour						
Magnitude	<-.8	-.75	-.65	-.55	-.45	-.35	Total
19.0<b<19.5	-	-	-	-	0.6	-	0.6
19.5<b<20.0	-	-	-	-	0.6	-	0.6
20.0<b<20.5	0.2	-	0.2	0.3	-	1.0	1.7
20.5<b<21.0	-	0.3	1.0	1.3	1.1	1.9	5.6
b<21.0	0.2	0.3	1.2	1.6	2.3	2.9	8.4

Table 3.10 Surface Densities (per square degree) for Narrow Emission Line Objects discovered in faint UVX survey

on the strengths of such lines as Hα and [NII] λ6583 (Osterbrock 1984), well beyond the wavelength sensitivity of this survey. We do note, however, that the relative weakness of the Hβ line in SGP1:10 makes it a likely Seyfert II type nucleus - one of the most distant yet discovered (see Veron-Cetty and Veron 1984). From their weak UVX colours it is clear that the survey will be substantially incomplete for such objects and, as such, no further statistical analysis of their properties is made. However, their effect on 2D clustering studies of the UVX sample is discussed further in chapter 6.

As indicated in chapter 3.2.5 a number of the fields in this survey have been searched by other authors for QSOs. A complete list of those QSOs found in the faint survey that have been previously listed as candidate or spectroscopically confirmed QSOs is given in table 3.11. Within the magnitude limits of our survey areas we find that we missed no QSOs found by other authors, whether selected by UVX, objective prism or even radio observations. The increasing incompleteness of the CS sample at faint magnitudes (b > 19 mag) is amply demonstrated in table 3.12 where we present, as a function of magnitude, the percentage of UVX QSOs found in our SGP survey fields (both bright and faint surveys) also detected by CS.

We also plot, in figure 3.7, the u-b v z relation for all CS QSOs for which we have a broadband u-b colour from the COSMOS measurements. From this we see that every low z (z < 2.2) QSO detected by the emission line search of CS is also contained within our UVX sample on the SGP.

This Survey			Other Surveys			
Name	ID	z	Ref.	Method	Spectroscopic Confirmation?	z
SGP1:03	QSO	0.662	CT	UVX	NO	
SGP1:25	STAR	-	CT	UVX	NO	
SGP1:45	QSO?	1.366	CT	UVX	NO	
SGP2:01	QSO	2.370	CS	O/P	NO	1.68*
SGP3:02	QSO	2.181	CS	O/P	NO	
SGP3:10	QSO	2.350	CS	O/P	YES	2.29
SGP3:14	STAR	-	CS	O/P	NO	
SGP3:21	STAR	-	CT	UVX	NO	
SGP3:23	QSO	1.574	CS	O/P	NO	
SGP3:25	QSO	1.338	CS	O/P	NO	1.35*
SGP3:27	QSO	1.920	CT	UVX	YES	?
SGP3:48	QSO	2.097	CT	UVX	NO	
SGP3:49	QSO	1.402	CT	UVX	NO	
QSM1:19	QSO	1.940	SB	UVX	NO	1.97*
QSM1:26	QSO	1.525	SB	UVX	NO	1.55*
QSM1:38	QSO	1.285	SB	UVX	YES	1.282
QSM2:07	QSO	1.098	SB	UVX	NO	1.11*
QSM2:09	QSO	2.577	SB	RADIO	YES	2.555
QSM2:22	QSO	2.062	SB	UVX	YES	2.070
QSM2:27	CONT	-	SB	UVX	NO	0.065*
QSM2:31	QSO	1.978	SB	UVX	NO	0.98*

*Redshift estimated from Prism Spectrum

Table 3.11 Survey QSOs Previously Detected in other Surveys

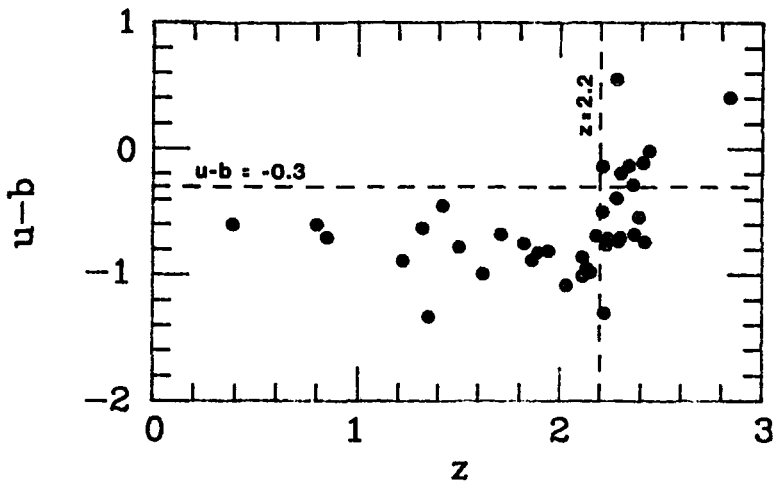

Figure 3.7 u-b v z for Clowes and Savage (1983) QSOs on SGP.

Magnitude Limit	Number of QSOs on SGP		%age
	Picked up in UVX surveys	Also selected by CS	
18.5 < b < 19.0	16	9	56
19.0 < b < 19.5	9	3	33
19.5 < b < 20.0	8	1	12
20.0 < b < 20.5	16	1	6
20.5 < b < 21.0	11	0	0

Table 3.12 Completeness of Clowes and Savage (1983) Sample

Table 3.12 and figure 3.7 provide further evidence for the completeness of our UVX technique. However, to obtain an accurate estimate for the precise level of completeness, we must consider the many subtle selection effects to which our UVX survey may be prone.

3.4 Completeness of UVX Technique

a) UVX Limit

One of the most straightforward ways to lose QSOs from a UVX survey is to set too blue a UVX limit, thereby missing those QSOs that exhibit only a moderate UVX. It is well known (e.g. Veron 1983, see figure 1.1) that QSOs exhibit a tight U-B v z relation, with their U-B colours reddening significantly in the ranges $0.6 < z < 0.8$ and $z > 2$. For $0.6 < z < 0.8$ this reddening is due to the appearance in the B passband of the broad Balmer continuum emission feature at 3000A in the QSO rest frame (Grandi 1982). Such an effect has been cited (Wampler and Ponz 1985) as being responsible for the low numbers of QSOs found at $0.6 < z < 0.8$ in major UVX surveys (Schmidt and Green 1983). At $z > 2.0$ the Lyman alpha forest becomes increasingly prominent in the U passband, thus decreasing the flux at these wavelengths and once again reddening the QSO (see chapter 7).

In *radio* selected QSOs there should be no selection effect operating to systematically bias the *optical* U-B colours towards any particular colour. Thus the U-B v z relation obtained by Veron (1983), see figure 1.1, for radio as well as optically selected QSOs should represent the intrinsic U-B v z distribution

for QSOs, and, as such, may be used to estimate the incompleteness in our survey due to the UVX limits applied. To do so we plot, in figure 3.8, the individual field u-b v z relations for QSOs with redshift classes 1 and 2 (thus excluding QSOs whose redshifts could be completely wrong) found in our surveys. The u-b colours plotted are those obtained after the re-zero-pointing procedure carried out for the u magnitudes in chapter 2.5. As all the u-b colours on different fields will therefore be on the same zero point relative to one another, we can combine the u-b v z plots to give the composite diagram (figure 3.9) for all redshift class 1 and 2 QSOs in the survey. In these diagrams filled circles represent QSOs with $b < 20.0$ mag, and open circles those with $b > 20.0$ mag. Similarly, filled and open squares represent bright and faint BAL QSOs respectively.

On inspection of figures 3.9 and 1.1 we note how closely our u-b v z relation follows the U-B v z relation found by Veron (1983). Indeed, from such a comparison we also note that our u-b colour appears to be on approximately the same zero-point as the Johnson U-B colours plotted by Veron (1983). The well defined nature of this relation augers well for the accuracy of the stellar calibration techniques employed in chapter 2. In particular, the observation that the u-b colours of faint QSOs show no systematic shift with respect to those for the brighter QSOs confirms that our method of u calibration by straightening the u-b v b locus for Galactic stars (see chapter 2.4.4), has not introduced significant magnitude dependent errors.

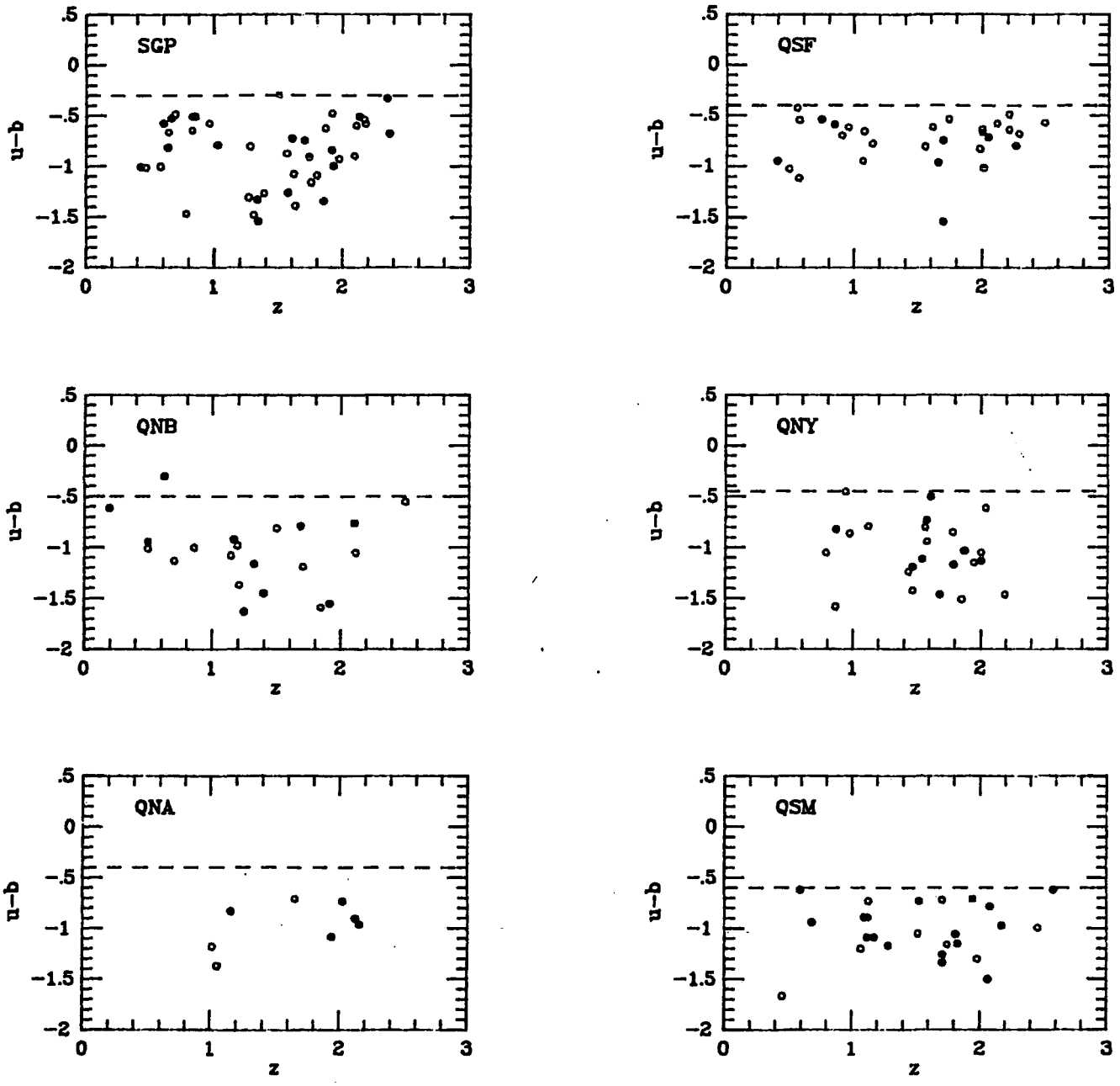

Figure 3.8 u-b v z for redshift class 1 and 2 QSOs discovered in the faint UVX survey. Dashed lines denote the UVX limits applied on each field.
• denote b < 20 mag QSOs, ○ b > 20 mag QSOs,
■ b < 20 mag BAL QSOs, □ b > 20 mag BAL QSOs.

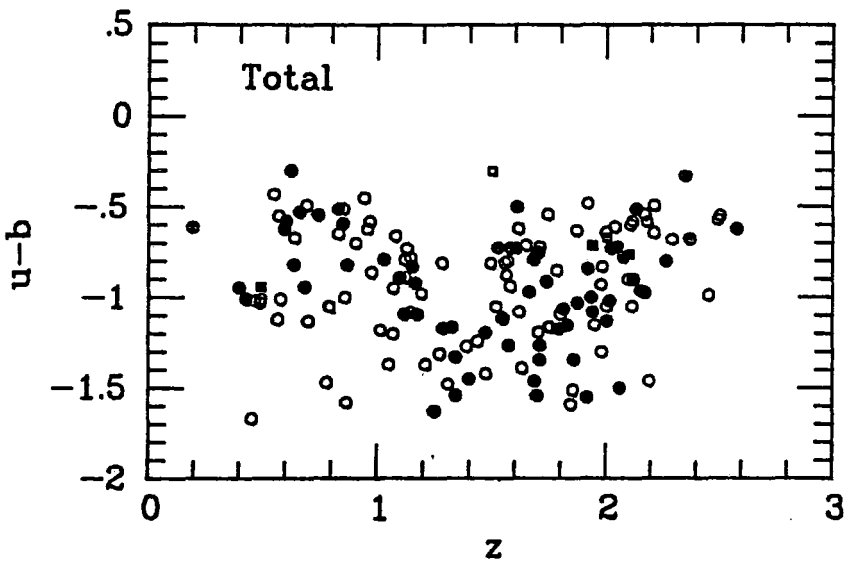

Figure 3.9 Composite u-b v z diagram for redshift class 1 and 2 QSOs discovered over all fields in the faint UVX survey. Symbols as for figure 3.8.

Having established that our colours are sufficiently accurate to give the Veron (1983) U-B v z relation for QSOs, we may use this relation to determine the completeness of our survey in the following manner. At each redshift we estimate the number of QSOs that would be found redder than the survey limit on each field, assuming that the U-B colours of QSOs form a Gaussian distribution about the mean U-B v z Veron (1983) relation. The standard deviation of this Gaussian is taken to be 0.25 mag, arising from the combination of the intrinsic scatter in QSO colours about this relation (±0.15 mag as estimated from the plot of Veron 1983) and the errors in our u-b colours (found to be ≃ ±0.20 at b = 20.0 mag, see chapter 2.6). We also assume that the u-b colours derived from the re-zero-pointed u magnitudes (see chapter 2.5) are equivalent to the U-B colours given by Veron (1983). In table 3.13 we give the percentages of QSOs thus lost to the UVX sample as defined on each field in 0.1 redshift intervals. At the foot of table 3.13 we also give the total percentage of $z < 2.2$ QSOs lost on each field by summing over all redshift bins at $z < 2.2$, using the observed n(z) relationship (see figure 4.7) to normalise the percentage losses in individual bins. Similarly the percentage of $z < 2.2$ QSOs lost to the entire sample is determined by normalising the total percentage losses on each field to the number of FOCAP areas observed on that field.

From table 3.13 we note that, while at specific redshifts (e.g. $0.6 < z < 0.8$) on particular fields (e.g. QNB and QSM) losses due to the 'blue' UVX criterion can be quite large (≃

z	U-B (Veron Relation)	Percentage of QSOs Redder than UVX limit SGP,QNA < -.3	QSF < -.4	QNY < -.45	QNB,QSM < -.5	Total
0.15	-.90	1	2	3	5	2.8
0.25	-.85	1	3	5	8	4.2
0.35	-.80	2	5	8	12	6.8
0.45	-.75	3	8	12	16	9.8
0.55	-.70	5	12	16	21	13.5
0.65	-.60	12	21	27	34	23.5
0.75	-.65	8	16	21	27	18.0
0.85	-.70	5	12	16	21	13.5
0.95	-.75	3	8	12	16	9.8
1.05	-.80	2	5	8	12	6.8
1.15	-.85	1	3	5	8	4.2
1.25	-.90	1	2	3	5	2.8
1.35	-.90	1	2	3	5	2.8
1.45	-.80	2	5	8	12	6.8
1.55	-.75	3	8	12	16	9.8
1.65	-.70	5	12	16	21	13.5
1.75	-.80	2	5	8	12	6.8
1.85	-.85	1	3	5	8	4.2
1.95	-.90	1	2	3	5	2.8
2.05	-.80	2	5	8	12	6.8
2.15	-.75	3	8	12	16	9.8
2.25	-.50	21	34	42	50	36.8
%loss z < 2.2		2.9	6.9	9.9	13.8	8.4

Table 3.13 Losses on each Field due to UVX Criterion Applied

20-30%), averaged over all fields these losses become quite small, although still redshift dependent. As a result of the UVX limits applied, we therefore estimate our survey to be $\simeq$ 8% incomplete for $z < 2.2$ QSOs.

b) Variability

Most of the U and J plates used to define the UVX samples in the faint survey were taken at least a year apart (see table 2.1). Thus variability may cause a QSO to fail the UVX criteria if, for example, it was undergoing a brighter phase when the J plate was taken. Because the CS sample will not be systematically biased against variable objects, we chose to estimate the percentage of variable QSOs from this sample. A QSO was defined here to be variable if the difference it its b magnitudes, as determined from J3721 and J1921, was greater than 2.5 times the rms scatter in stellar magnitudes between these plates at the b_{3721} magnitude of the QSO (see table 2.5). Although we note that a larger percentage of QSOs are likely to exhibit variability at levels smaller than $\pm$ 0.50 mag, at such levels the effect of variability will become indistinguishable from the rms errors encountered in our colours, the losses for which have already been accounted for above. Moreover, we may also find that more QSOs are variable at the 2.5σ level if we were to inspect many more, different epoch plates. However, the problem here is to determine how many QSOs are lost to the UVX sample because they have varied significantly over the time interval between which the relevant U and J plates were taken,

and, as such, the use of only two J plates to estimate this fraction is justified. QSOs thus identified as variables (all have $\Delta b > 0.50$) are listed in table 3.14. They comprise less than ≃5% of the CS sample which fall on the measured areas of both J plates. On average, variabilty is just as likely to manifest itself by making the QSO bluer rather than redder from the definition of our colours. We therefore conclude that, at most, variability will account for 2-5% incompleteness in the survey. From the small numbers involved it is impossible to tell if variability is magnitude dependent, but no strong evidence for this has been found in any of the more comprehensive studies of variabe QSOs (see e.g Usher *et al.* 1983).

c) Misclassification of Stellar Images

All objects in each FOCAP area were visually inspected on the corresponding J plate before the spectroscopic observation. Over the entire magnitude range, only 3 - 5 % of all stellar images had been misclassified as galaxies, with only a slight trend towards an increase in misclassification at the faintest magnitudes (≃ 5 - 10 % at 20.5 mag < b < 21.0 mag). Inspection of the corresponding U plate on each field revealed no trend for this misclassification to occur preferentially amongst UVX objects.

Name	b_{3721}	b_{1921}	Δb	σ
CS46	19.87	20.38	-0.51	2.6
CS126	20.09	19.51	0.58	2.5
CS137	18.79	17.60	1.19	5.0

Table 3.14 Variable QSOs in Clowes and Savage (1983) Catalogue

d) BAL QSOs

In figure 3.8, we note that, on the SGP, the BAL QSO SGP3:13 (open square) exhibits an anomalous u-b colour with respect to the well defined u-b v z relation seen on this field. This is due to the appearance, in the U passband, of the absorption trough associated with CIV λ1549 emission. The anomalous reddening which results thus implies that a number of BAL QSOs may be missed in a UVX survey when such a broad line falls in the U band. To estimate the percentage of QSOs thus lost from the survey we must first estimate the true percentage of BAL QSOs amongst normal QSOs. We note that the three BAL QSOs observed with $1.8 < z < 2.2$ in the UVX survey (filled squares in figure 3.9) exhibit the same u-b colours as normal QSOs and we may therefore assume that the ratio of such BAL QSOs to normal QSOs seen within this redshift range ($\simeq$ 5%) is close to the true value (although we concede that some QSOs with extreme BAL properties may still be missed). At worst, we assume that all BAL QSOs (representing $\simeq$ 5% of the QSO population) will be missed in the UVX survey between redshifts of $1.3 < z < 1.7$, i.e. when broad CIV absorption is present in the U band. At lower redshifts it is unlikely that any further BAL QSOs will be missed as, of the two broad emission lines visible in the optical at these low redshifts (CIII] and MgII), only MgII is seen to have associated broad absorption, and even then it is only rarely seen (see e.g. Wampler 1985).

We conclude, therefore, that even if we have missed the bulk of the BAL QSOs in the redshift range $1.3 < z < 1.7$ this will only account for $\simeq$ 1% of all QSOs seen in the survey at $z < 2.2$.

e) Plate Limit

In figure 3.10 we plot the number magnitude, n(m), counts for stellar images in u and b for each of the fields used in the spectroscopic survey. The u counts are plotted using the u magnitudes before they were re-zero-pointed (see chapter 2.5). With the exception of the QNA field, all counts show the same steady increase at least up to the magnitude limits used in the faint spectroscopic survey (dotted lines in figure 3.10). The fact that all plates, exhibit the same general n(m) relation at b $<$ 21 mag and u $<$ 20.7 mag as the SGP, therefore provides good evidence that each plate is complete up to the magnitude limit of the survey. At the very least the smooth nature of these counts implies that the feature seen in the QSO n(m) counts at b $\simeq$ 19.5 mag (chapter 4.2) can not be attributable to the plate limit on any of the fields used in the spectroscopic survey.

The anomalous form of the u and b n(m) counts on the QNA field may be more the result of poor calibration at bright magnitudes (see chapter 2.4.4) than incompleteness at faint magnitudes. However, particular attention will be paid to the QSO n(m) counts on this field in chapter 4.2 to ensure that they do not exhibit significant differences from those observed on other fields.

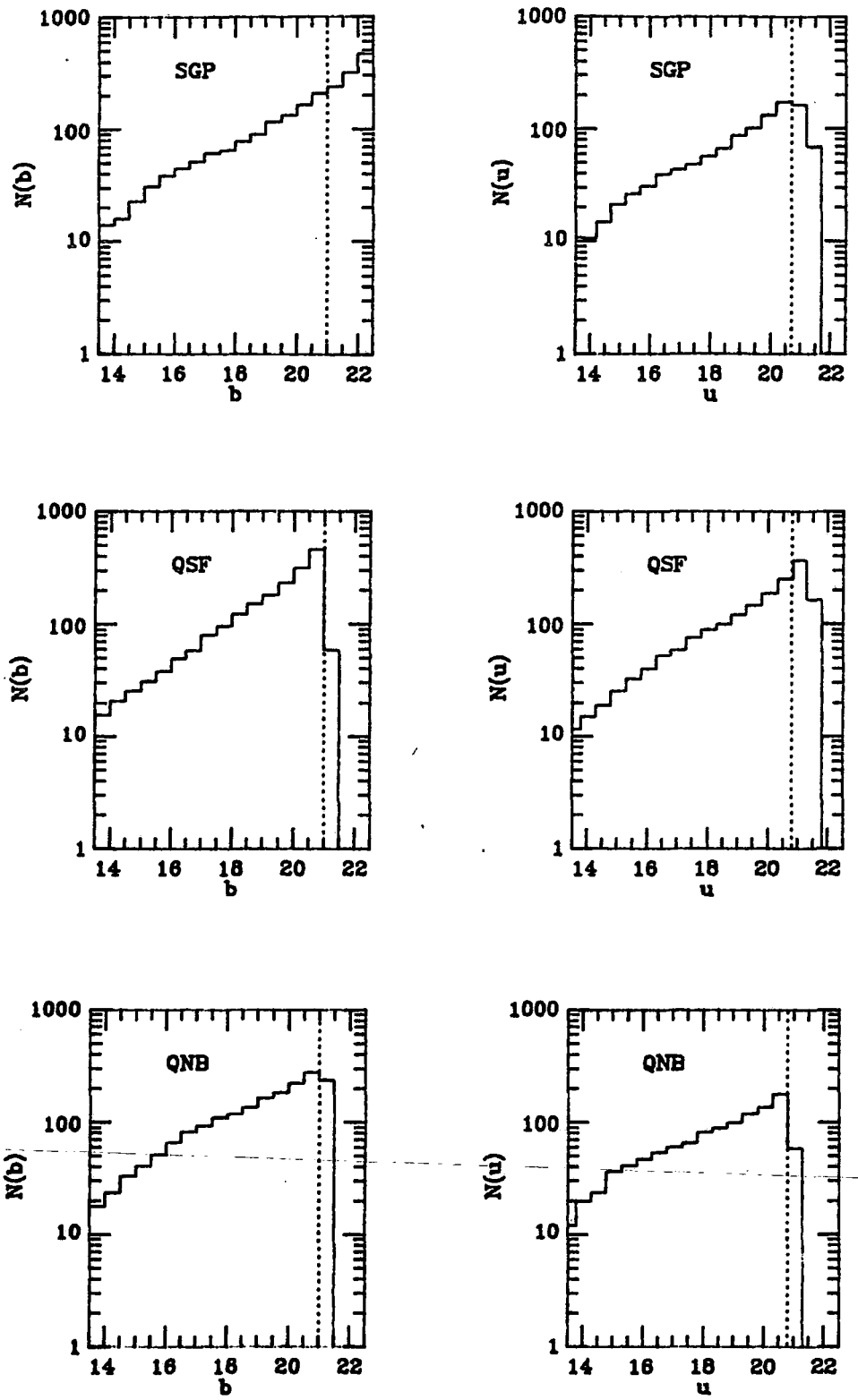

Figure 3.10 Differential n(m) counts (per square degree per magnitude) for stellar images on U and J plates used in the faint spectroscopic survey. Dotted lines indicate the survey limits. a) SGP, QSF and QNB fields.

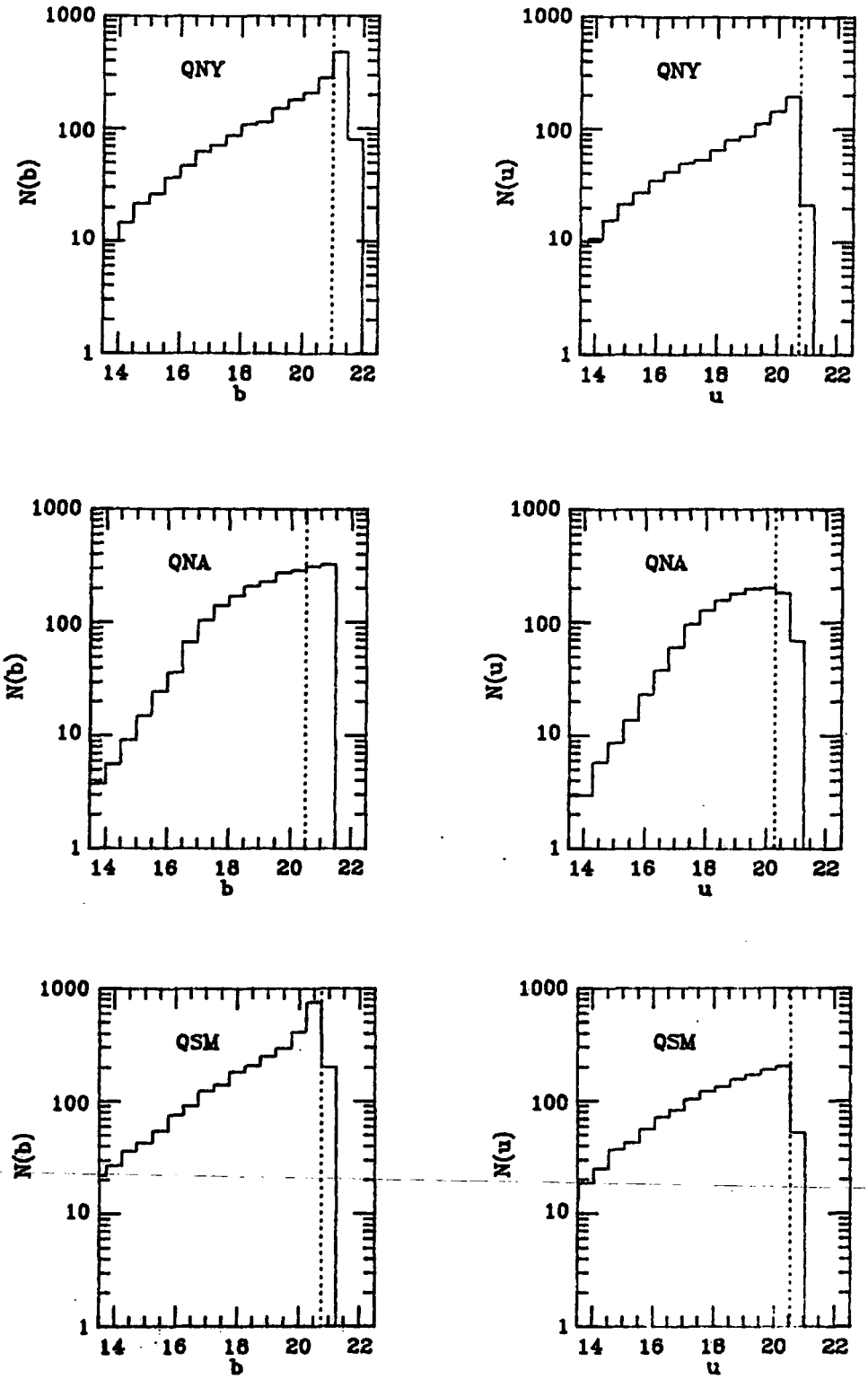

Figure 3.10 continued b) QNY,QNA and QSM fields.

f) QSOs with weak lines

Although we have obtained sufficient signal-to-noise at the b = 21.0 mag faint limit to identify unambiguously the strong lined QSOs (see e.g. the spectrum of SGP2:11, b = 20.98 mag), we may wonder whether faint QSOs exist with weak lines that have proven difficult to identify. We can obtain an upper limit to the number of such QSOs in our survey as follows. From table 3.8 we note that only 10% of all survey objects with 20.0 mag < b < 20.5 mag and 20% with 20.5 mag < b < 21.0 mag remain without a positive identification. Thus the numbers of QSOs with weak, unidentified emission lines in the spectroscopic survey can amount to no greater fraction than this. As we shall see in chapter 4.2, such losses can not account for the break in the observed QSO n(m) counts beyond b $\simeq$ 19.5 mag.

g) 'Non-stellar' QSOs

It is well established (see e.g. Veron 1983) that low redshift, low luminosity QSOs may exhibit extended structure (due to the increased visibility of the underlying host galaxy) on a photographic plate which would cause their exclusion from a survey, such as ours, based on the selection of UVX stellar objects. We concede that our survey could also suffer from this selection effect. However, most of the conclusions arrived at in chapters 4 and 5 will be largely independent of the consideration of z < 0.5 QSOs, i.e. those QSOs which might appear extended on a UKST plate.

h) Low Luminosity QSOs

It has been suggested (see e.g. Marshall 1985) that as QSOs become intrinsically fainter the background light from their host galaxies becomes progressively more and more dominant, with the result that, at sufficiently faint magnitudes, $M_B > -23$, QSOs may become non-UVX.

If this was a strong effect we would expect to see this reflected in figure 3.9, with the open circles ($b > 20.0$ mag QSOs) showing a systematic redward (upward) shift in u-b with respect to the filled circles ($b < 20.0$ mag QSOs) in the u-b v z diagram. As this seems not to be the case we conclude that such an effect is not large and does not result in significant losses of QSOs from our survey, although, as we shall see in chapter 4, conclusions regarding the evolution of the QSO luminosity function do not depend on such faint QSOs.

In this section we have considered a number of possible selection effects to which our UVX survey may be susceptible. From those that are directly quantifiable (e.g. UVX limit, misclassification, varibility and BAL QSOs) we conclude that this survey is unlikely to be more incomplete than $\simeq$ 15%. This precise fraction will be slightly redshift dependent with relatively more QSOs being lost in the redshift ranges $0.6 < z < 0.8$ and $1.6 < z < 1.8$ (due to UVX criterion) and $1.3 < z < 1.7$ (due to BAL QSOs being missed). Other biases, which are less directly quantifiable, either have little effect on the properties of QSOs observed in our survey (e.g. reddening of low

luminosity QSOs) or will have no significant influence on the conclusions derived in the following chapters (e.g. loss of low redshift extended QSOs).

3.5 Conclusions

In this chapter we have demonstrated the power of the UVX technique in the detection of low redshift QSOs when applied to machine measurements of photographic plates. The enormous advance in spectroscopic techniques represented by the FOCAP system at the AAT has enabled the potential of the UVX technique to be realised to the full. The large QSO catalogue produced exhibits a high level of completeness (85%), greater than that observed in other catalogues, particularly those selected by objective prism searches. Our QSO catalogue is therefore ideally suited for the statistical analysis which will form the basis of our next two chapters.

CHAPTER FOUR

THE EVOLUTION OF QSOs AT $z < 2.2$

4.1 Introduction

The increase in QSO statistics which our surveys afford is easily seen in figure 4.1, where we have plotted the Hubble diagram for all QSOs obtained from complete spectroscopic surveys of UVX catalogues. The open circles represent the data for QSOs observed in the surveys listed in table 4.1 and the filled circles denote the QSOs observed in our survey. We see that the bulk of the QSOs discovered in our UVX survey lie 1-2 magnitudes fainter than those previously observed. As stressed in chapter 1, it is at precisely these magnitudes where the QSO number counts may first begin to show significant deviations from their pure power law behaviour established at bright magnitudes. Such a result would, in turn, imply that discrimination between the various evolutionary models introduced in chapter 1 may be possible.

In the light of this, the statistical analysis presented below will be divided into two different approaches.

1. Establishing the form of the QSO number magnitude, n(m), relation down to B = 20.9 mag, thus verifying the reality or otherwise of the break proposed in the n(m) relation at B $\simeq$ 20.0 mag.

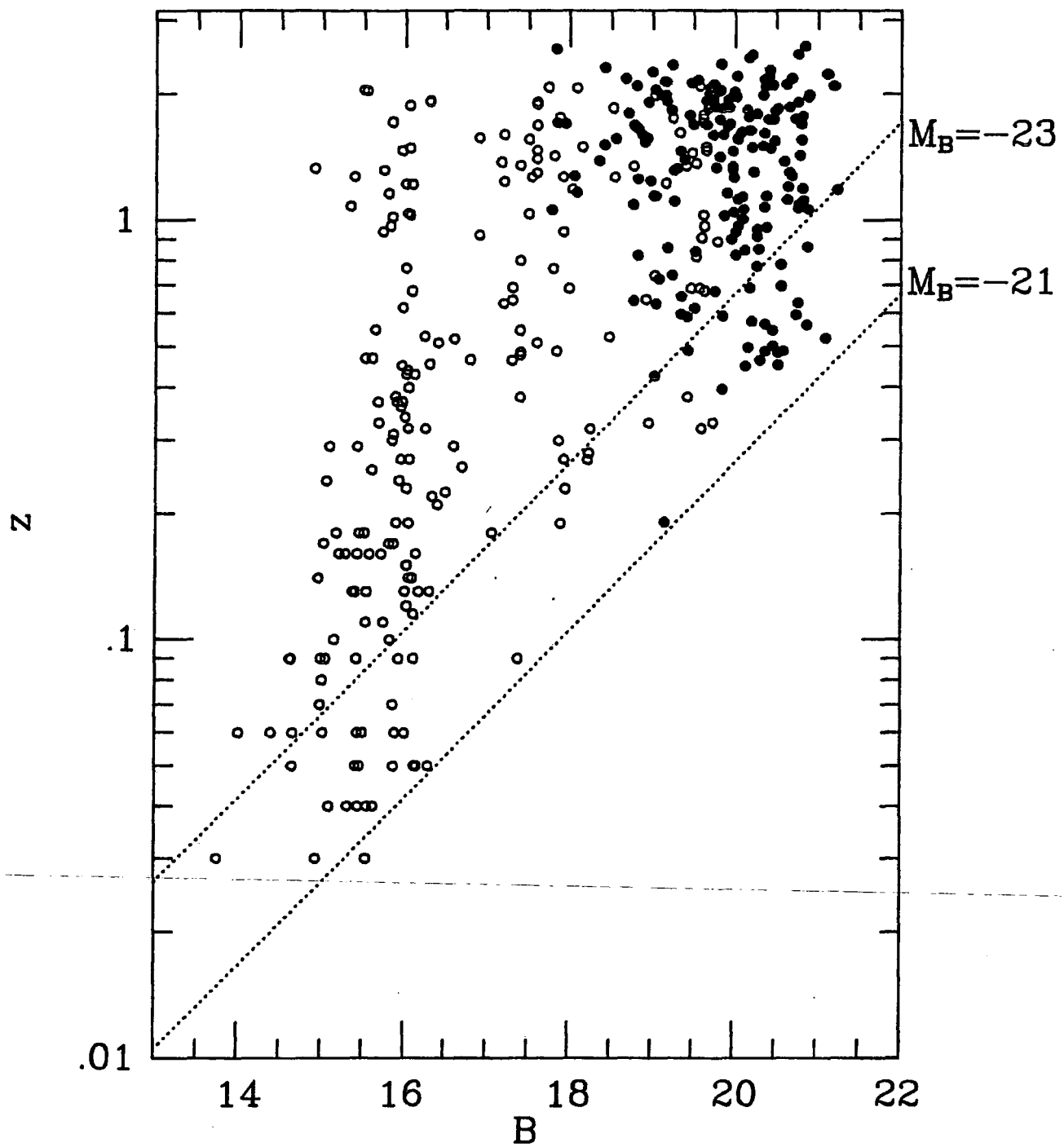

Figure 4.1 Hubble diagram for all spectroscopically observed QSOs in complete UVX surveys.

Reference	Magnitude Limits	Area Searched (square degrees)	Number of QSOs found
Schmidt and Green (1983)	B < 16.16	10716.0	116
Mitchell *et al.* (1984)	B < 17.25	108.6	14
	B < 17.65	87.3	18
Marshall *et al.* (1983b)	B < 18.25	37.2	20
Marshall *et al.* (1984)	B < 19.80	1.72	35

Table 4.1 Previous UVX Surveys With Complete Spectroscopic Coverage

	Survey UVX Criteria				Restricted UVX Criteria			
Field	UVX Limit	Q+Q?	NL	Stars	UVX Limit	Q+Q?	NL	Stars
SGP	-0.3	51	6	66	-0.5	47	1	15
QSF	-0.4	38	6	32	-0.6	24	1	10
QNB	-0.5	25	4	34	-0.7	25	-	8
QNY	-0.45	31	4	24	-0.65	23	1	5
QNA[1]	-0.3	9	-	21	-0.6	9	-	1
QSM[1]	-0.5	22	-	42	-0.7	17	-	10
Totals:		172	20	219		145	3	49
%ages:		42	5	53		74	2	25

[1] All numbers quoted for the magnitude range 18 mag < b < 21 mag with the exception of QNA (18 mag < b < 20.5 mag) and QSM (18 mag < b < 20.75 mag) fields.

Table 4.2 Comparison of UVX Criteria

2. Explicit calculation of the QSO luminosity function (LF) as a function of redshift. In particular, the determination of the QSO LF at the faint absolute magnitudes represented in our deep survey will help in the discrimination between models proposed for the evolution of the QSO LF.

These two topics will be covered in separate sections and we begin with the number magnitude counts.

4.2 The Number Magnitude Relation

4.2.1 Normalisation

The spectroscopically observed areas in our survey constitute only a small part of the entire measured area on the plates over which the UVX catalogue was defined. We therefore wish to ensure that, on each Schmidt field, the surveyed regions do not exhibit anomalously low or high surface densities of UVX objects in comparison with the rest of the measured area. Because we are primarily interested in the 'normalisation' of the QSO surface density across each field we first redefine our UVX sample in order to obtain minimal contamination from Galactic stars. Further motivation for reducing this contamination will be encountered in chapter 6 when we investigate the 2D clustering properties of the UVX samples. The method by which this is achieved is detailed below.

In figure 4.2 we plot the u-b histograms for the stars and QSOs discovered in each of the faint survey fields. With the exception of the QSM ($b < 20.75$ mag) and QNA ($b < 20.5$ mag)

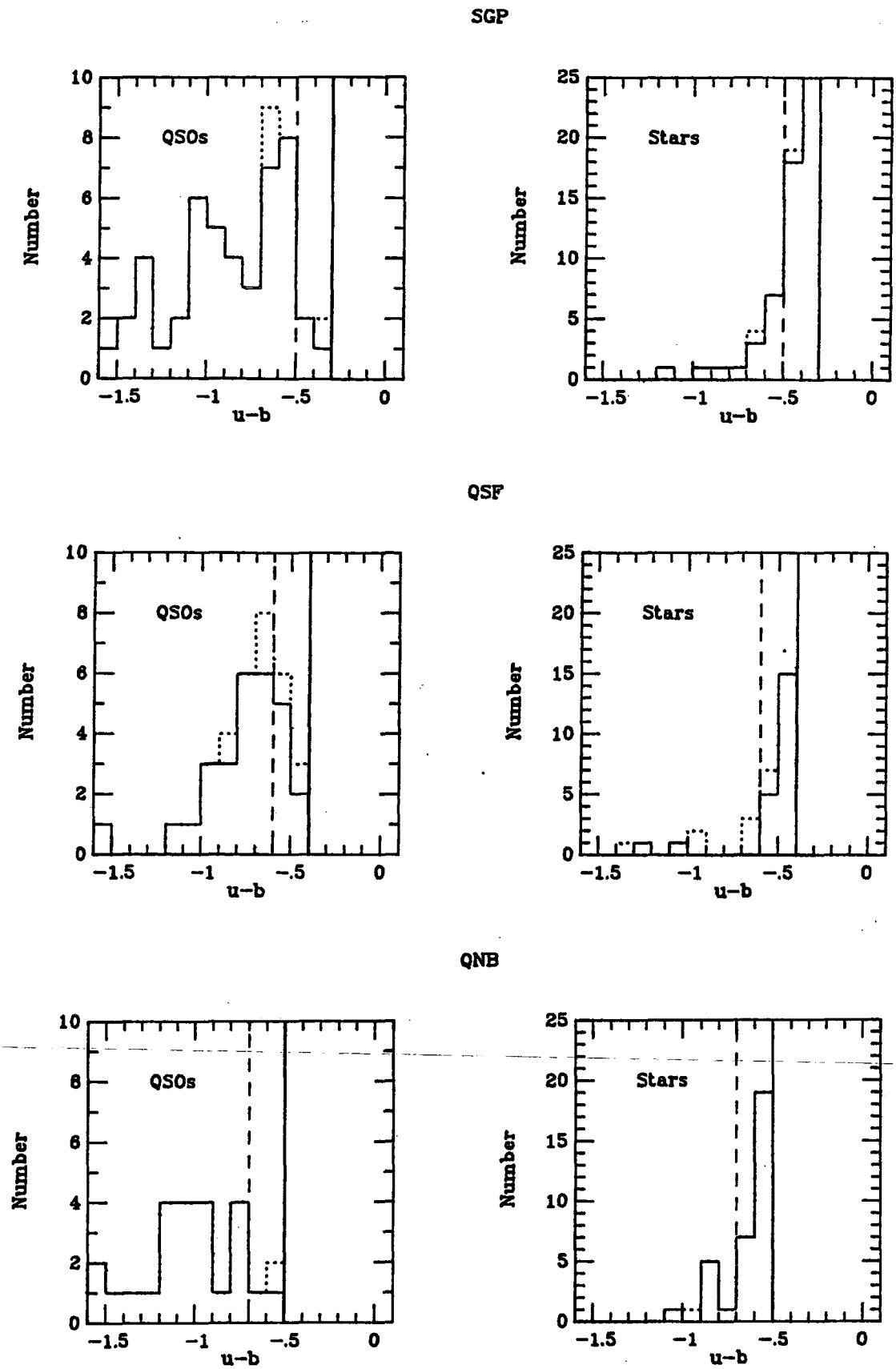

Figure 4.2 u-b histograms for QSOs and Galactic stars observed in the faint UVX survey. Dotted lines indicate the additional contribution from z > 2.2 QSOs and white dwarfs in the QSO and star histograms respectively. a) SGP, QSF and QNB fields.

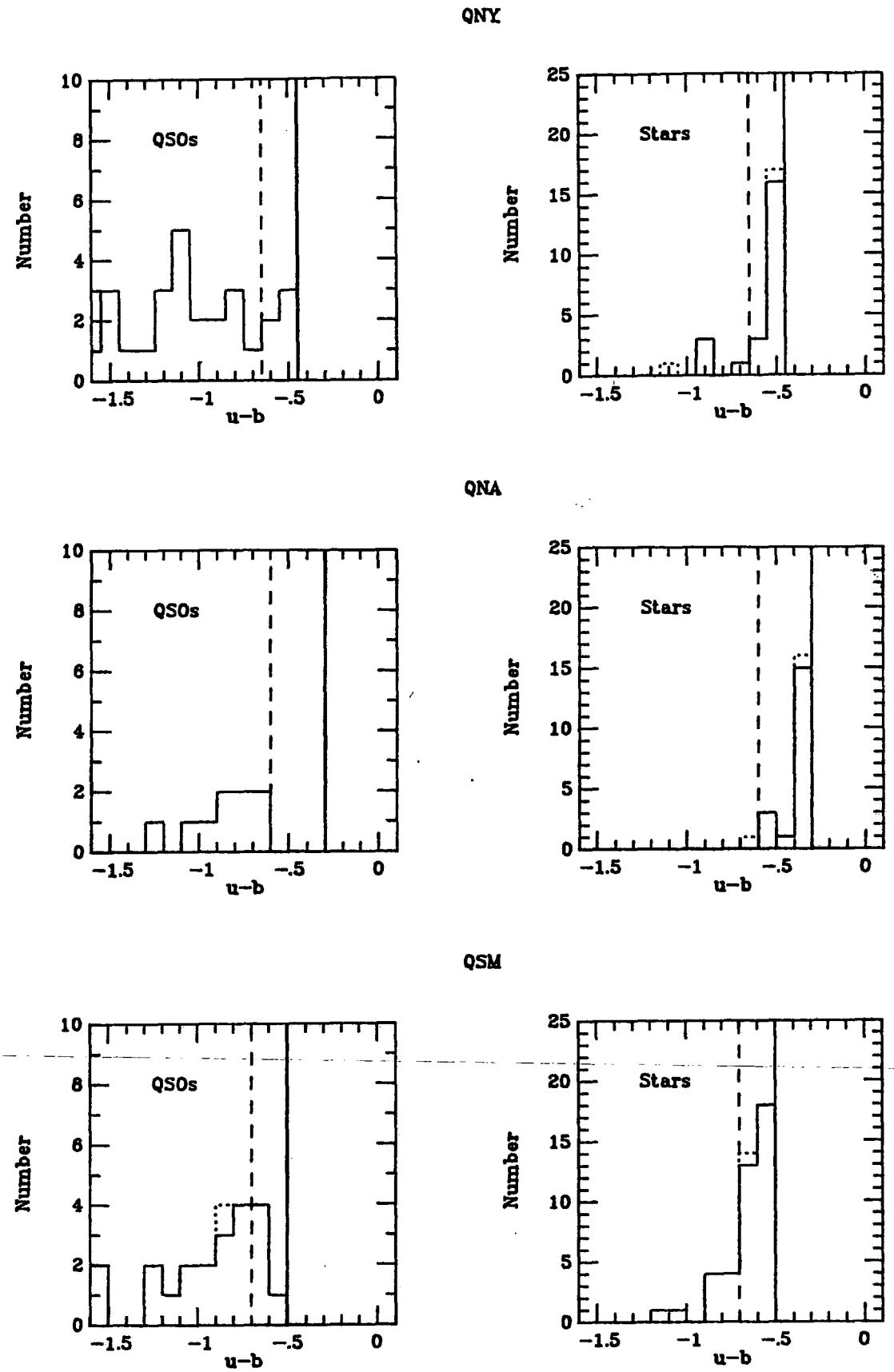

Figure 4.2 continued b) QNY,QNA and QSM fields.

fields, the histograms plotted include all stars and QSOs with b < 21.0 mag. The dotted lines in these plots represent the additional contribution from white dwarfs and z > 2.2 QSOs in the stellar and QSO histograms respectively. From these histograms we see that, whereas the bulk of the Galactic stars were discovered with u-b colours within 0.1 - 0.2 mag of the UVX limit (solid line) on each field, the majority of the QSOs lie with u-b colours much bluer than this limit. This separation in u-b colour between the two classes of object allows us, from visual inspection of the histograms, to redefine the UVX criterion (dashed line in figure 4.2) on each field so as to minimise the contamination by Galactic stars whilst retaining the vast majority of QSOs. The efficacy of these new 'restricted' UVX limits are clearly illustrated in table 4.2, where we see that, in the surveyed areas, the Galactic star contamination has dropped from 55% to 25% with the introduction of the new 'restricted' UVX criteria, whilst a large fraction of the z < 2.2 QSOs (85 - 90%) have been retained.

In table 4.3 we compare the surface density of the objects thus redefined as UVX in the areas surveyed with FOCAP to those found over the matched area of the U and J plates on each field observed in the faint spectroscopic survey. The surface densities are compared over the magnitude range 18 mag < b < 21 mag (the faint limit becomes b < 20.75 mag on the QSM field), this being the interval over which the vast majority of the QSOs were found in the faint survey. Because of the strong gradients seen in the distribution of UVX objects over the QNA Schmidt

Field	UVX Limit	Magnitude Limit	Surface Densities (per square degree) Survey Area	Whole Plate
SGP	< -0.5	18.0 < b < 21.0	60.0	51.2
QSF	< -0.6	18.0 < b < 21.0	50.0	53.5
QNB	< -0.7	18.0 < b < 21.0	47.2	44.4
QNY	< -0.65	18.0 < b < 21.0	41.4	38.6
QSM	< -0.7	18.0 < b < 20.75	38.6	35.8

Table 4.3 Comparison of UVX Surface Densities

field (see e.g. figure 6.1), comparison of the UVX star densities on this field was not attempted. We see that in general the surface densities of UVX objects in the FOCAP areas are approximately the same as those observed over the whole measured areas. Although there may be a slight trend in some fields (in particular the SGP) towards a higher surface density ($\simeq$ 5 - 15%) in the surveyed areas we choose not to correct for this, as not only is this a relatively small effect but it may well compensate (at least in terms of number density) for those QSOs lost from the UVX survey by the 10 - 15% incompleteness noted in the last chapter.

4.4.2 Surface Densities

In table 4.4 we give, field by field, the numbers and surface densities for the QSOs observed in the spectroscopic surveys in 0.5 magnitude bins between 17 mag < b < 21 mag. We exclude any QSO with z > 2.2 from this table , to ensure we only obtain surface densities for QSOs for which the UVX technique is complete. All FOCAP fields have been incorporated in this table, along with the three bright survey areas (SGP centre, QSM bright, QSM centre) for which we have complete (or near complete) spectroscopic identification. We have included the QNA field in this analysis, although we have previously noted that the calibration for stellar magnitudes at b < 19 mag on the field may be significantly in error (see chapter 3.4). However, this area represents only 1 out of the 12 FOCAP fields and its inclusion makes no significant difference to the results obtained.

Magnitude Range	SGP	QSF	QNB	QNY	QNA	QSM	Total
17.0<b<17.5	-	-	-	-	-	-	-
17.5<b<18.0	-	-	-	-	-	2	2
18.0<b<18.5	-	-	1	-	-	3	4
18.5<b<19.0	6	2	2	1	-	3	13
19.0<b<19.5	7	2	4	5	2	2	22
19.5<b<20.0	7	6	5	4	4	5	31
20.0<b<20.5	16(18)	12(13)	4	7	3	6	48(51)
20.5<b<21.0	11(13)	7(8)	9(11)	9(12)	-[1]	4	40(48)

Numbers in parentheses include contribution from Q? objects.
[1] Number for magnitude range 20.5 mag < b < 21.0 mag.

Table 4.4a Numbers for z < 2.2 QSOs

Magnitude Range	SGP	QSF	QNB	QNY	QNA	QSM	Total
17.0<b<17.5	-	-	-	-	-	-	-
17.5<b<18.0	-	-	-	-	-	2.86	0.17±0.12
18.0<b<18.5	-	-	1.43	-	-	1.15	0.56±0.28
18.5<b<19.0	2.66	2.86	2.86	1.43	-	1.50	1.83±0.51
19.0<b<19.5	6.67	4.29	5.71	7.14	5.71	2.86	5.24±1.12
19.5<b<20.0	6.67	8.57	7.14	5.71	11.43	7.14	7.38±1.33
20.0<b<20.5	15.24	17.14	5.71	7.14	8.57	8.57	11.43±1.90 (12.14±2.23)[2]
20.5<b<21.0	10.48	10.00	12.86	12.86	-	(5.71)[1]	11.43±1.90 (13.51±2.10)[2]
b<20.5	31.24	32.86	22.85	21.24	25.71	24.08	26.31±1.90

[1] Surface Density Quoted for magnitide range 20.5 mag < b < 20.75 mag
[2] Surface Density Including Q? Objects

Table 4.4b Surface Densities (per square degree) for z < 2.2 QSOs

Moreover, the surface densities of QSOs found on this field at b < 20.5 mag (the magnitude limit of the QNA field) are in good agreement with those obtained on other fields.

At b < 20.5 mag the mean QSO surface density over all fields is 26.3 ± 1.9 per square degree, the error representing the rms field-to-field variation in this mean. Although inhomogeneity in the QSO surface density from field-to-field may arise in our UVX survey because of the poorly defined (in absolute terms) UVX limit applied on each field, the fact that we have complete spectroscopic identification for the UVX sample thus selected has allowed us to put strict limits on the amount to which this will affect the numbers of QSOs found in each field (see chapter 3.5). As such, we view the agreement found between the QSO surface densities on each field as good evidence for the large scale homogeneity of the QSO distribution over the sky. This is in contrast to claims put forward by other authors (see e.g. Arp 1984) that the surface density of QSOs can vary by as much as 400% over different areas of the sky.

The surface densities averaged over all fields are plotted as filled dots in the number magnitude, n(m), diagram presented in figure 4.3, the error bars representing either the rms field-to-field variation in the surface density or $\sqrt{n}$ (where n is the number of QSOs contributing to the surface density value at that point), whichever is the larger.

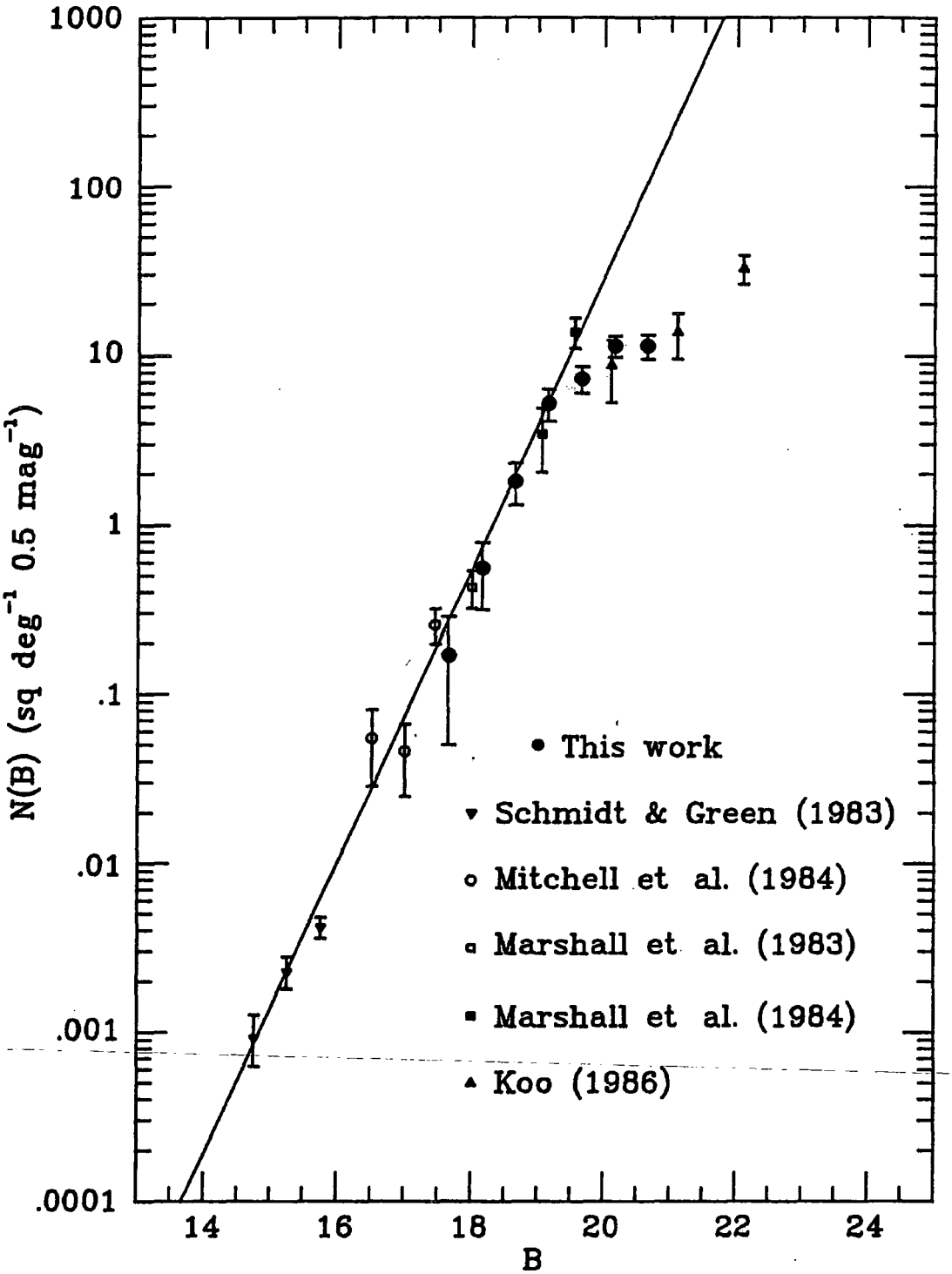

Figure 4.3 Differential number magnitude counts for z < 2.2 QSOs. Solid line indicates Braccesi *et al.* (1980) power law relation.

We note that in composing this diagram the b magnitudes for the survey QSOs have been converted into the Johnson B magnitude system using equation (2.10) to enable comparison with the counts of UVX QSOs found from the other complete spectroscopic surveys (see table 4.1), also shown in figure 4.3.

The solid line in figure 4.3 represents the Braccesi *et al.* (1980) power law relation found to reflect accurately the UVX QSO n(m) counts at bright magnitudes (B < 20.0 mag). In differential form it can be expressed as follows:

$$\log (N(B)) = 0.864 (B - 18.31) \quad \ldots (4.1)$$

where N(B) is the number of UVX QSOs per square degree in a 0.5 mag bin centred on B. Table 4.5 gives the QSO surface densities determined explicitly from this relation and compares them with those observed in our survey. From figure 4.3 and table 4.5 we note the following.

At bright magnitudes (B < 19 mag) our counts are in good agreement with the values of Marshall *et al.* (1983b,1984) and Mitchell *et al.* (1984), following the Braccesi *et al.* (1980) relation. As we go to fainter magnitudes (B ≃ 19.5 mag), however, discrepancies arise between our observations and those of Marshall *et al.* (1984). Furthermore the observed surface density at B = 19.65 mag lies 5σ (4σ if 10% incompleteness is assumed) from the power law slope. In the magnitude range of interest here (19.5 mag < b < 20.0 mag) all fields are covered by accurate photoelectric photometry, and there should be no problems identifying QSOs in the spectroscopic survey, as all

Magnitude Range	N(m) observed	N(m) predicted	Significance of Discrepancy
17.4<B<17.9	0.17±0.12	0.27	0.83σ
17.9<B<18.4	0.56±0.28	0.73	0.61σ
18.4<B<18.9	1.83±0.51	1.97	0.27σ
18.9<B<19.4	5.24±1.12	5.32	0.07σ
19.4<B<19.9	7.38±1.33	14.38	5.26σ
19.9<B<20.4	11.43±1.90	38.88	19.70σ
20.4<B<20.9	11.43±1.90	105.14	49.32σ
'Worst possible case' (see text)			
19.7<B<20.2	14.28±2.62	26.12	4.52σ
20.2<B<20.7	15.89±2.47	70.63	22.16σ
'Flattest Slope' (see text)			
19.4<B<19.9	7.38±1.33	10.01	1.98σ
19.9<B<20.4	12.14±1.90	24.32	5.46σ
20.4<B<20.9	13.51±2.10	59.02	21.67σ

Table 4.5 Comparison of Number Counts with Braccesi *et al.* (1980) power law relation

objects with b < 20 mag will have signal-to-noise in their spectra greater than 10. We therefore view the observed discrepancy as highly significant. In addition, the discrepancy between our value for the QSO surface density at B = 19.5 mag and that of Marshall *et al.* (1984) is all the more significant when we consider that, using essentially identical search techniques as those employed here, Marshall *et al.* (1984) obtained a UVX (U-B < -0.4) sample which contains 95% QSOs at B = 19.8 mag. Were we to obtain such a minimal contamination from Galactic stars we would lose about 30% of the QSOs. If we do not accept the hypothesis that the area surveyed by Marshall *et al.* (1984) has an anomalously high QSO surface density (see above) then either the B photometry of Marshall *et al.* (1984) is incorrect and they are surveying to fainter magnitudes than they believe or many of the objects identified as QSOs in their survey are in fact simply Galactic stars. Unfortunately, no spectra have been published to enable this hypothesis to be tested.

At the faintest magnitudes the observed surface densities begin to show gross deviations from the Braccesi *et al.* (1980) relation, but agreeing well with the counts found for z < 2.2 QSOs by Koo (1986). At B = 20.15 mag the surface density is a factor of four down on that predicted from the extrapolation of the 0.86 power law and at B = 20.65 mag a factor of 10. We regard the surface density in the range 19.9 mag < B < 20.4 mag to be secure as not only have the b magnitudes in 8 of the 12 FOCAP fields been calibrated using accurate photoelectric photometry down to the magnitude limit of this bin (the QSO

surface density in these 8 fields alone is 12.5 ± 2.7 per square degree, not significantly different from that observed over all fields), but the objects here are sufficiently bright to enable the vast majority of all QSOs to be identified (with a S/N ≃ 7 for 9000 seconds).

However, as an example of what little effect possible errors will have on these discrepancies let us consider a 'worst possible case' in which we correct for all inaccuracies in such a way as to make the observed values in these faint bins as large as possible. From table 4.5 we see that, even allowing for 15% incompleteness, including all the dubious (Q?) QSOs and brightening the magnitude limit up by ≃ 0.2 mag (the size of the rms error in our b magnitudes at this limit), the surface densities in the faintest bins are still factors of 2 - 5 lower that those predicted from the power law relation.

It may be that the slope derived for the power law relation by Braccesi *et al.* (1980) is too steep at 0.86, although we note that the values found by other authors allow for very little freedom in changing the slope. We can, however, make an independent estimation of the reality of any break by deriving the slope of the power law n(m) relation at bright magnitudes using our survey data alone. Moreover, we take the flattest possible slope that could be drawn through the surface densities found in our four brightest bins. This gives a relation of the form:

$$\log (N(B)) = 0.77 (B - 18.45) \quad \ldots (4.2)$$

The comparisons between the predictions for the surface densities at faint magnitudes from equation (4.2) and those observed are given at the foot of table 4.5. We see that, even with the inclusion of the Q? objects, the observed surface densities at B > 19.9 mag are still 2 - 5 times lower than predicted.

We conclude, therefore, that the low QSO number counts at B > 19.5 mag seen in our survey are consistent with the break in the power law form for the n(m) counts first suggested by the observations of Koo and Kron (1982). We note that Braccesi *et al.* (1980) have explicitly demonstrated that, for a pure density evolution (PDE) model (see chapter 1), the n(m) relation for UVX ($z < 2.2$) QSOs is a pure power law from the very brightest magnitudes ($B \simeq 14$ mag) to magnitudes fainter than $B = 22.0$ mag. The deviations from such a power law behaviour observed in both our survey and those conducted by Koo and Kron (1982) and Koo (1986) thus imply that PDE is not an adequate parameterisation for the evolution of the QSO LF. As such we can deduce indirectly that the QSO LF must exhibit a feature at correspondingly faint absolute magnitudes (Cavaliere *et al.* 1983) and that this feature can be used to trace the form of QSO evolution. We now go on to investigate the nature of this evolution by explicitly determining the QSO LF in discrete redshift intervals from our data.

4.3 The QSO Luminosity Function and its Evolution

4.3.1 Calculation of Absolute Magnitude

The luminosity function, $\Phi(M_B, z)$, for any class of astronomical objects (in this case QSOs) simply expresses their space density as a function of absolute magnitude, M_B, and distance (in this case represented by their redshift, z). From Schmidt and Green (1983) the absolute magnitude for a QSO can be calculated as follows:

$$M_B = B - 5\log d_L + 2.5\,(1+\alpha)\log(1+z) - 25 \qquad \ldots\ (4.3)$$

where $d_L(z)$ is the luminosity distance for a QSO at a redshift z. In Friedmann cosmologies this can be expessed (Weinberg 1973) as

$$d_L = \frac{c}{H_0 q_0^2}\left(zq_0 + (q_0 - 1)(\sqrt{(1+2q_0 z)} - 1)\right) \qquad q_0 > 0 \qquad \ldots\ (4.4a)$$

$$= cz/H_0(1+z/2) \qquad q_0 = 0 \qquad \ldots\ (4.4b)$$

Ideally we would like to measure the QSO's absolute magnitude at the same wavelength in the rest frame of each QSO. In practice, however, we observe QSOs in a fixed passband over a wide range in redshifts and so this is generally not possible. The third term on the right hand side of equation (4.3) therefore represents the magnitude (or k) correction resulting from the change in the observed wavelength back to the fixed rest wavelength for each QSO. The form of this correction is based on an assumed spectral energy distribution for QSOs of $f_\nu \propto \nu^\alpha$ derived from observations of optically selected QSOs by Richstone

and Schmidt (1980). After Richstone and Schmidt (1980) we take α = -0.5. No correction has been made for emission lines, broad absorption lines or other deviations from a pure power law behaviour (see e.g. Grandi 1982). At redshifts z < 2.2 such effects give rise to less than ±0.1 mag variation in the B magnitude for QSOs, as explicitly calculated in Marshall *et al.* 1983b and Veron 1983 (see also chapter 7). These effects are therefore small when compared to the uncertainties regarding the spectral index for QSOs. For example, it is quite common for QSOs to have a spectral index as steep as -1.0 (see Richstone and Schmidt 1980), and thus, with the assumption that α = -0.5, the magnitude assigned to such a QSO at z = 1.5 will therefore be in error by 0.5 mag. The effect which the resulting uncertainty in the k-correction will have on the evolution derived for the QSO LF will be discussed in chapter 4.3.4.

Compared to these uncertainties the size of the correction for Galactic obscuration is small. All QSOs observed in this survey are located above a Galactic latitude of of b^{II} = 45°. The two most commonly used laws for absorption within our own Galaxy are

$$A_B = 0.12\ (\mathrm{cosec}\ b^{II} - 1) \qquad b^{II} < 50° \qquad \ldots (4.5a)$$

$$= 0 \qquad b^{II} > 50° \qquad \ldots (4.5b)$$

from Sandage (1973) and

$$A_B = 0.2\ \mathrm{cosec}\ b^{II} \qquad \ldots (4.5c)$$

given by de Vaucouleurs and Buta (1983). Both these laws give rise to relative differences across our survey fields of less

than 0.1 mag. Bearing in mind the small size of these corrections (and uncertainties regarding their form see e.g Burstein and Heiles 1982) we make no correction for obscuration in our Galaxy.

4.3.2 Derivation of the QSO Luminosity Function

Although many sophisticated statistical techniques have developed over the years to determine the QSO LF and its evolution with redshift (e.g. the C-method of Lynden-Bell 1970 and the applications of maximum likelihood techniques by Marshall *et al.* 1983b), they have mainly been born out of the necessity to obtain information from small samples of QSOs. Indeed, Schmidt and Green (1983) have noted, that with sufficient numbers of QSOs, it would be straightforward to construct the LF at any given redshift by simply 'reading off' from the Hubble diagram (figure 4.1) the distribution of QSOs, n(B,z), in a horizontal redshift strip thus:

$$n(B,z)dBdz = \Phi(M_B,z)dM_B\,dV \qquad \ldots (4.6)$$

where dV is the comoving volume element.

However, Schmidt and Green (1983) found that the Hubble diagram then available had only patchy coverage, especially in the region B > 18 mag, z < 1.8, and they had to construct a LF based on an initial assumption about the form of the evolution.

Now that we have 'filled up' this region with QSOs from our surveys, (see figure 4.1), we can approach the problem of constructing the LF using the simple method which Schmidt and Green (1983) were frustrated in applying.

From equation (4.6) we have that the LF can be obtained from observations of n QSOs as follows:

$$\Phi(M_B, z) = \sum_{z_j \varepsilon \Delta z} (V_a^j)^{-1} \delta(M_B^j - M_B) \quad \ldots (4.7)$$

where V_a is the accessible comoving volume as defined by Avni and Bachall (1980). This estimator was introduced as a more natural way of combining data from surveys with different magnitude limits, redshift limits or conducted over separate areas of the sky. V_a is simply the total volume within which a QSO, selected from any of the surveys making up the QSO catalogue, could have been observed over all surveys in the catalogue. As such it does not assume any *a priori* knowledge of the particular survey in which the QSO originally appeared and thus makes more efficient use of the data to hand (Avni and Bachall 1980). For a catalogue consisting of m different surveys, each observed over ω_m steradians and to an apparent limiting magnitude $B_{lim,m}$, V_a is given by

$$V_a = \sum_m \omega_m / 4\pi \int dV/dz \, dz \quad \ldots (4.8)$$

where the integration is performed over the redshift range for the particular bin of interest, unless $z_{max,m}$, given by

$$B_{lim,m} - 5\log d_L(z_{max,m}) + 2.5(1+\alpha)\log(1+z_{max,m}) - 25 = M_B \quad \ldots (4.9)$$

is less than the upper limit of the bin, in which case integration proceeds up to $z_{max,m}$. When $z_{max,m}$ is less than the lower limit of this bin the contribution from this integral to the summation in equation (4.8) is zero. In principle the value of $z_{max,m}$ can be found from equation (4.9) by iteration. It was found, however, that substitution for $d_L(z)$ using equation (4.4) yielded an equation that was difficult to iterate and a much easier iterative formula was obtained with an expression for $d_L(z)$ given by Terrell (1977):

$$d_L(z) = \frac{cz}{H_0}\left[1 + \frac{z(1-q_0)}{(\sqrt{(1+2q_0 z)}+1+q_0 z)}\right] \quad \ldots (4.10)$$

In equation (4.8) the comoving volume, dV/dz, of a shell at redshift z, width dz, can be obtained from Phillipps *et al.* (1978) to be:

$$dV/dz = 4\pi f^2(z)g(z)(1+z)^3 \quad \ldots (4.11)$$

where

$$f(z) = d_L(z)/(1+z)^2 \quad \ldots (4.12)$$

is the angular diameter distance, and

$$g(z) = c/(H_0(1+z)^2\sqrt{(2q_0 z+1)}) \quad \ldots (4.13)$$

is the derivative of proper distance with respect to redshift.

4.3.3 Results

The QSO LF was calculated at intervals of 1 magnitude in four separate redshift bins for the following combinations of surveys:

a. Those fields in our bright and faint spectroscopic surveys which were used to derive the n(m) relation in chapter 4.2 (i.e. all FOCAP fields and the SGP centre, QSM bright and QSM centre fields in the bright survey). The dubious QSOs (Q? objects in the faint survey) were not included in the derivation of the LF, it having been checked explicitly that, even with their inclusion, no significant change was observed in the LF. As many of these objects may well not be QSOs it was thought best to exclude them from the analysis. QSOs with redshift class 3 were, however, included in the estimation of the LF. From the n(z) distributions for the faint survey QSOs both with and without the inclusion of the redshift class 3 objects (see e.g. figure 4.7) we see that the uncertain redshifts are not preferentially assigned to one particular redshift range, and although individual redshifts may be incorrect the overall effect does not seriously bias the redshift distribution.

b. As above but with the inclusion of the Marshall *et al.* (1983b,1984) QSOs.

c. As case b) but incorporating the Schmidt and Green (1983) QSOs. As the Schmidt and Green survey was conducted at such bright apparent magnitudes, the majority of the QSOs found therein are at low redshifts. This survey will therefore be strongly subject to the selection effect mentioned in chapter 3.5g, namely that low redshift, low luminosity QSOs may appear non-stellar on photographic plates and are therefore rejected from a UVX stellar sample. Indeed Schmidt and Green (1983) themselves concluded that such a selection effect did play a strong part in the selection of their catalogue. To account for this we reject all QSOs in the Schmidt and Green (1983) catalogue with $z < 0.55$ (i.e. the extent of our lowest redshift bin and the redshift beyond which galaxies are unlikely to be recognised on Palomar Sky Survey plates) and $M_B > -24$. This is the magnitude which Peacock *et al.* (1986) conclude marks the transition between host galaxy types for QSOs, with QSOs fainter than $M_B = -24$ lying in spiral galaxies (and therefore easier to see as extended objects) and those brighter lying in elliptical galaxies (and consequently more difficult to detect as extended sources).

d. The restricted Schmidt and Green (1983) catalogue as described above and the Marshall *et al.* (1983b,1984) surveys.

The redshift bins in which the LFs are calculated were formed by merely splitting the redshift range over which the UVX technique is complete into 4 bins of equal width in redshift. Although dependent on precisely which combinations of catalogues

were chosen, this division was made to obtain approximately equal numbers of QSOs in each redshift interval, averaging out at ≃ 50 for combination b.

The LFs calculated for an Einstein-de Sitter universe in which H_0 = 50 km s^{-1} Mpc^{-1} are plotted in figure 4.4. This value of H_0 was used to facilitate comparison with other authors who most frequently use this value for H_0 in the determination of their LFs. The lines plotted in figure 4.4 represent the LFs predicted from the evolutionary model which will be derived in the following section. For the present, however, they may be used as fiducial marks with which to compare the LFs derived from the various combinations of surveys a - d.

From Marshall (1985) the error bars (σ) on the estimates of the LF can be expressed as

$$\sigma = (\Sigma V_a^{-2})^{\frac{1}{2}} \qquad \ldots (4.14)$$

They were found to be an accurate reflection of the uncertainties involved in the calculation of the LF when the QSO catalogues were split into two and errors derived from the rms variation in the values for the LF in each half.

From figure 4.4 we immediately note the following points:

1. There is good agreement between the LFs derived from the different surveys in the magnitude regions in which they overlap.

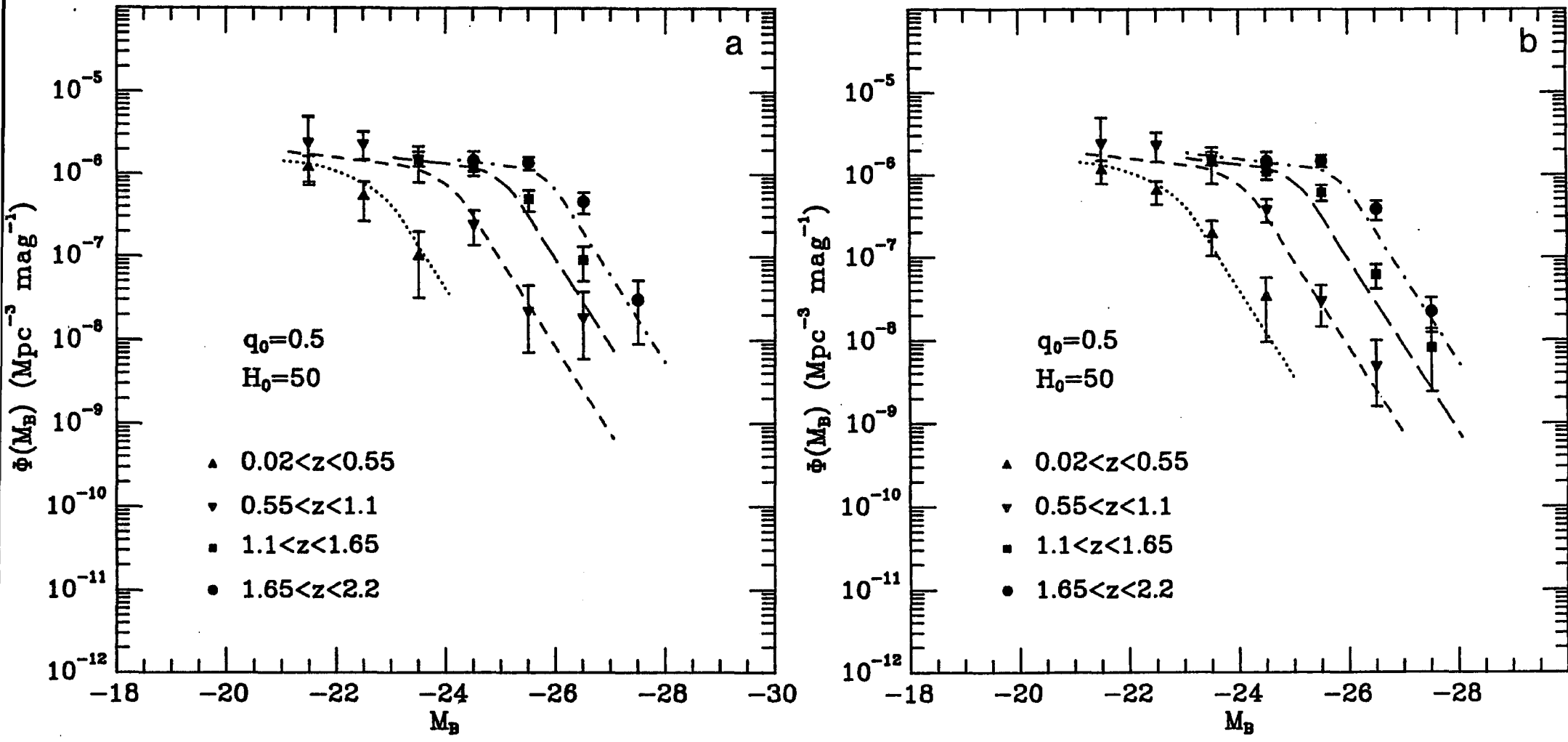

Figure 4.4 QSO luminosity functions for the survey combinations a - d given in the text. Lines indicate prediction of the standard evolution model.

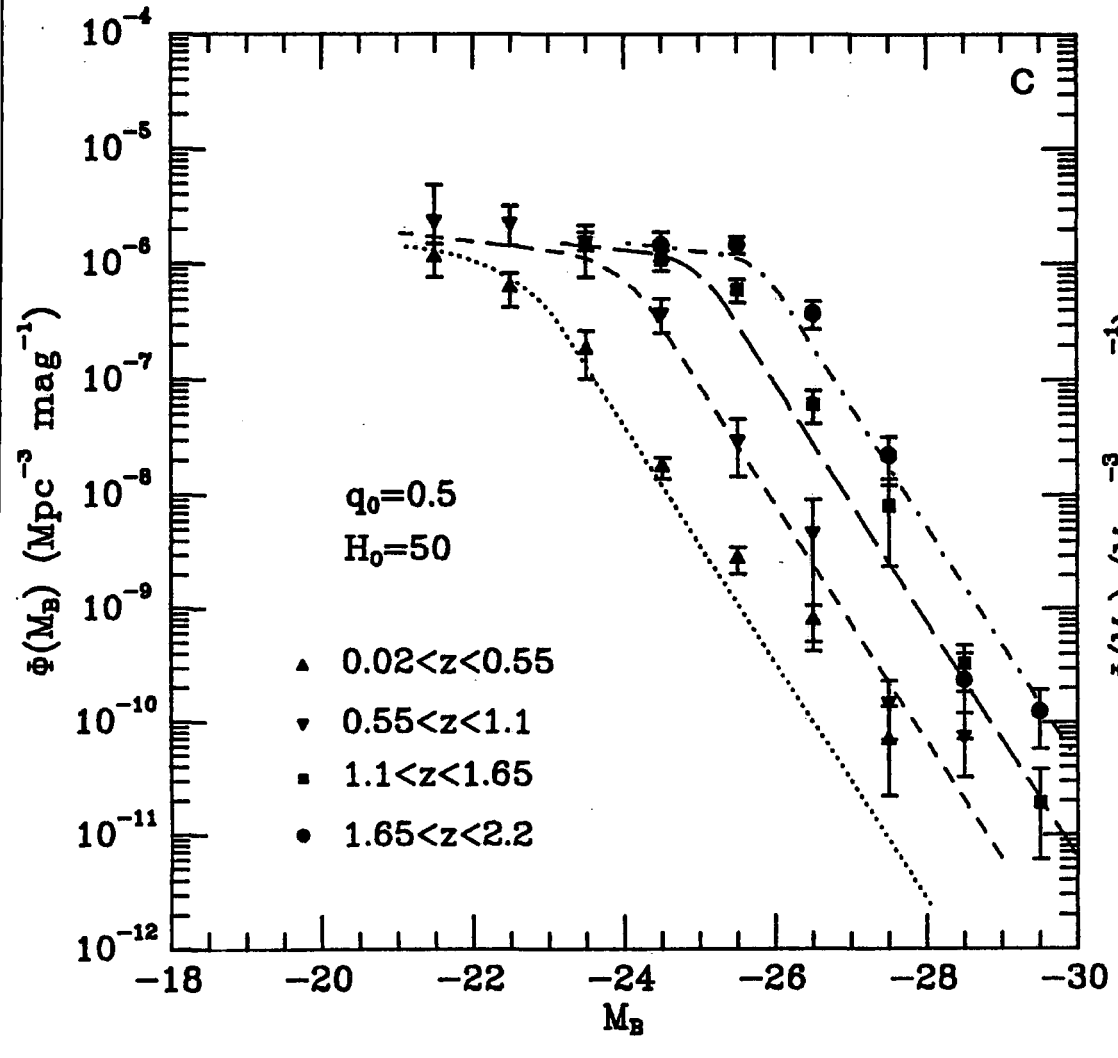

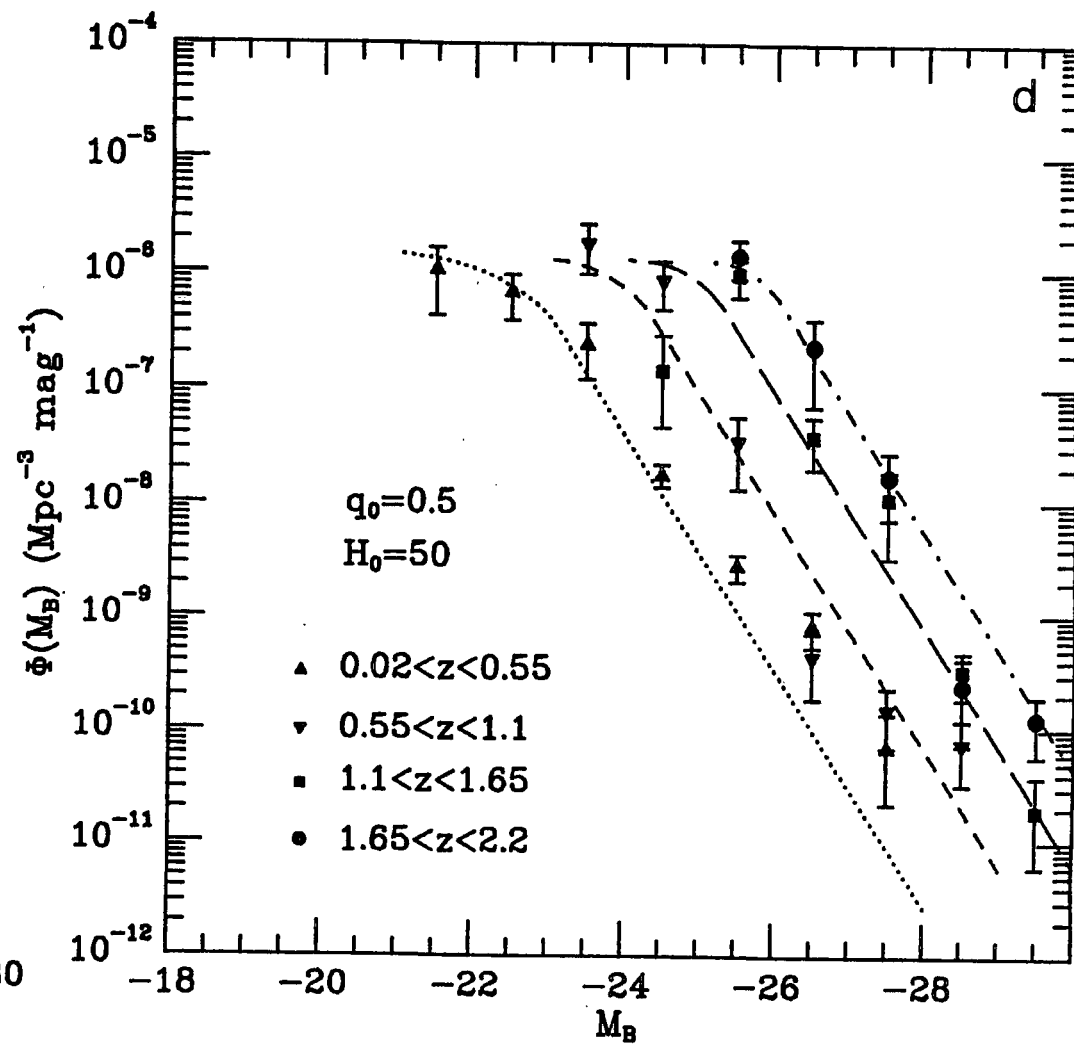

Figure 4.4 continued

2. As indicated by the break in the n(m) counts the LF does indeed exhibit a feature at faint absolute magnitudes. Evidently this feature is only clearly apparent when our faint QSO surveys are included. Although there may be a slight indication of a turn-over in the QSO LF in the lowest redshift bin from the surveys of Marshall *et al.* (1983b,1984) and Schmidt and Green (1983) alone, it is not reproduced at higher redshifts. Not only does the inclusion of the QSOs from our surveys make such a feature visible in all redshift bins, but it also defines the LF for at least two magnitude bins fainter than this feature for $0.55 < z < 2.2$. Thus this turn-over in the steep power law from the LF at bright absolute magnitudes is confirmed by QSOs with apparent magnitudes at least as bright as b = 20 mag, the magnitude to which our survey should represent a complete sample with accurate B calibration. This is consistent with the break in the QSO n(m) counts observed at $B \simeq 19.5$ mag for our data. With this feature the general form of the QSO LF appears to be, at its simplest, a two power law model, with a steep slope at bright magnitudes and a much flatter one at faint magnitudes.

3. By tracking the movement of this feature with redshift, we note that the evolution of the QSO LF appears to manifest itself predominantly as a uniform shift towards higher luminosities in the past, with no corresponding shift in density space. As such, it is most similar to the pure luminosity evolution (PLE) described in chapter 1.

4. The conclusions reached in 2 and 3 above are unaffected by the possible biases in the UVX selection technique described in chapter 3.5g and 3.5h. Firstly, even ignoring the LF for QSOs at $0 < z < 0.55$ (see chapter 3.5g), the two power law form for the LF and its luminosity evolution is still well represented in the three higher redshift bins. Secondly, PLE and the bent LF are still readily apparent when we discount all QSOs with $M_B > -23$ (see chapter 3.5h). Indeed, if anything, the space densities of the faint ($-21 < M_B < -23$) QSOs in the $0.55 < z < 1.1$ redshift bin may even be slightly higher than those of their brighter ($M_B < -23$) evolutionary equivalents (under the assumption of PLE) in the higher redshift bins.

Using the b) combination of surveys (thereby retaining information on the bright end of the QSO LF, whilst excluding the 'incomplete' Schmidt and Green survey), we plot in figure 4.5 the effect of varying q_0 on the shape of the LF. We see that the choice of q_0 does not significantly alter the pure luminosity evolution derived for the QSO LF.

4.3.4 Parameterisation of the QSO LF and its Evolution.

From the appearance of the LFs in figure 4.10 we choose to parameterise the QSO LF as a two power law function which we may express as

$$\Phi(M_B, z) = \Phi^* \mathrm{dex}(0.4(M^*(z)-M)(\beta+1)) \quad \ldots (4.15)$$

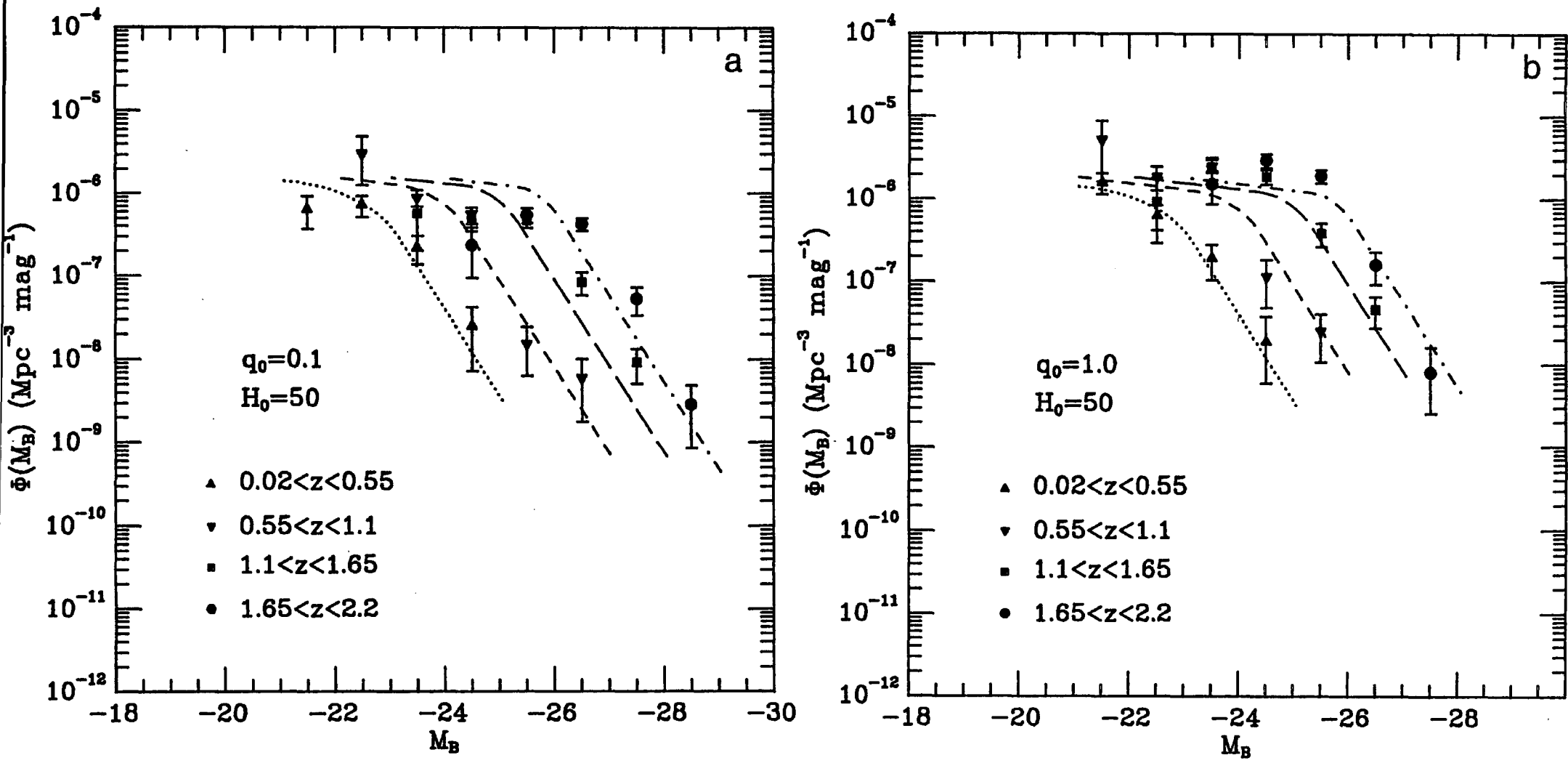

Figure 4.5 QSO luminosity functions for the survey combination b.
a) Open universe, q_0 = 0.1
b) Closed universe, q_0 = 1.0
Lines as for figure 4.4.

The index β (the slope of the LF) assumes one of two values depending on whether M (the absolute magnitude for the QSO) is greater than or less than $M^*(z)$. We also, however, test a model in which the LF is represented by a single power law. Φ^* is the normalising factor in this equation and will be expressed in terms of number mag^{-1} (comoving $Mpc)^{-3}$. $M^*(z)$ represents the position of the break and its evolution with redshift is assumed to be purely in the direction of increasing luminosity towards higher redshift. To facilitate comparison with other commonly used parameterisations for PLE (see e.g. Mathez 1976 and Marshall *et al.* 1983b) we choose two models whose dependence on redshift can be expressed in the following manner:

1. As a power law with redshift

$$L^*(z) = (1+z)^{k_L} L_0^* \qquad \ldots (4.16a)$$

with $L^*(z)$ and L_0^* being the luminosity equivalents of $M^*(z)$ and M_0^*. In terms of magnitudes this becomes:

$$M^*(z) = -2.5k_L \log(1+z) + M_0^* \qquad \ldots (4.16b)$$

This power law form is representative (Marshall 1985) of a homologous evolution i.e. one in which all QSOs are in the same evolutionary state, dimming or brightening without a characteristic time scale.

2. As an exponential in look back time (τ)

$$L^*(z) = \exp(k_L \tau) L_0^* \qquad \ldots (4.17a)$$

where, from Sandage (1961), τ can be expressed as a fraction

of the Hubble time in a $q_0 = \frac{1}{2}$ Universe as follows:

$$\tau = 1 - 1/(1+z)^{-1.5} \qquad \ldots (4.17b)$$

Again expressing this in magnitudes (4.17a) becomes:

$$M^*(z) = -1.08 k_L \tau + M_0^* \qquad \ldots (4.17c)$$

We may interpret this exponential form as evolution with a characteristic time scale (e.g. $1/\tau$), such as is obtained (Cavaliere *et al.* 1985) when the rate at which the QSO evolves is dependent on its luminosity.

Parameterising the LF and its evolution thus, we have four free parameters, namely M_0^*, k_L and two for β; Φ^* being determined from the normalisation of the counts (there will only be two free parameters in the case of the single power law LF model - β and k_L). To obtain the best estimates for these parameters we proceed as follows. Firstly, using initial estimates for the values of β, M_0^* and k_L, we predict the numbers of QSOs expected in each bin of the luminosity function, $n(M_B, z)$, for a particular combination of surveys. This can be found using a generalisation of equation (4.6) e.g.

$$n(M_B, z)dBdz = \Phi(M_B, z)\Omega(M_B, z)(dV/dz)dMdz \qquad \ldots\ldots (4.18)$$

where $\Omega(M_B, z)$ is the fractional area of sky over which QSOs with absolute magnitudes M_B and redshifts z could be observed over all the surveys used (see Marshall *et al.* 1983b). The normalising constant Φ^* is obtained from

$$\Phi^* = \frac{N_Q}{\int\int \Phi(M_B, z)/\Phi^* \, dB dz} \quad \ldots (4.19)$$

N_Q being the total number of QSOs in the surveys. By then comparing the numbers predicted to those observed in each magnitude and redshift bin used to calculate the LFs, we can compute a χ^2 statistic (employed here to maintain consistency with the binning procedure used to derive the LF in the previous section) for the particular choice of parameters used. The parameters can then be varied to give the smallest χ^2 value, these 'best-fit' values being quoted with errors corresponding to the amount by which these individual parameters can be varied before we can reject the fit at the 95% confidence level.

While we were able to obtain 'best-fit' values for M_B^*, k_L and the slope of the LF at faint magnitudes from our survey alone, we have too few QSOs in our survey with absolute magnitudes brighter than the break in the QSO LF to permit an accurate determination of the slope here. We therefore fixed the value of this slope to be that obtained by Marshall (1985) from analysis of the Schmidt and Green (1983) and Marshall *et al.* (1983b,1984) surveys.

Table 4.6 gives the resultant best-fit values, together with their errors (where applicable), for the parameters determined from the χ^2 analysis for a q_0 = ½ universe. The probability that the fit is acceptable (i.e. $P(>\chi^2)$) to both the LFs derived for our survey QSOs alone (i.e. those used to obtain the best fit parameters in the first place) and the LFs determined from the QSOs in survey combination b is given in the last two columns of

Model	β		k_L	Φ^*	M^*	$P(>\chi^2)$ (a)	(b)
$q_0 = 0.5$							
$\exp(k_L t)$	-3.6	-1.2	4.9	1.7×10^{-6}	-21.0	0.0029	4.4×10^{-6}
$(1+z)^k$	-3.6	-1.2±0.2	3.7±0.1	1.5×10^{-6}	-21.4±0.2	0.39	0.089
Single Power Law	-2.4		3.9	0.3×10^{-6}	-21.4	1.7×10^{-4}	1.1×10^{-9}
LDDE	-5.7	-3.7	2.18	4.0×10^{-11}	-26.0	1.0×10^{-6}	1.9×10^{-9}
$q_0 = 0.1$							
$\exp(k_L t)$	-3.5	-1.3	5.8	4.7×10^{-7}	-21.2	0.0041	3.8×10^{-5}
$(1+z)^k$	-3.5	-1.1±0.2	3.9±0.1	6.1×10^{-7}	-21.9±0.1	0.23	0.11

Table 4.6 'Best Fit' Parameters for Evolutionary Models

table 4.6. From table 4.6 we note that the single power law model and the exponential evolution law can both be rejected at a high level of confidence (errors are not quoted on the 'best-fit' parameters in these cases as the 'best-fit' parameters are themselves rejected at the 95% confidence level). This latter result confirms the unacceptability of the exponential luminosity model first remarked upon by Marshall (1985) from consideration of the QSOs in the Schmidt and Green (1983) and Marshall *et al.* (1983b,1984) surveys. However, the power law luminosity evolution model is found to be a good fit to the data and, in the spirit of this analysis in which we accept the simplest model to fit the data, is considered as our standard evolution model (SEM).

Similar results are obtained when we consider the evolution of QSOs in a $q_0 = 0.1$ universe (see foot of table 4.6). Again the exponential model is rejected at a high level of confidence, while the power law PLE model is consistent with the data.

We note that the form of this evolution remains unchanged under the assumption of a different value for α, the spectral index of the QSO. The magnitude of a QSO at any redshift, M(z), exhibits the same log(1+z) dependence on spectral index as it does for evolution. Thus the only effect that a specific increase in the value for the spectral index will have on the SEM will be to decrease the value of k_L by the same amount.

As a check on the consistency of the SEM we use equation (4.6) to predict the n(m) and n(z) relations based on this model. The n(m) counts discussed in chapter 4.2.2 are reproduced in figure 4.6, but this time the solid line represents the SEM predictions. We see an excellent fit to the counts at all magnitudes 14 mag < B < 22 mag. In the very faintest bin the model appears to predict too low a surface density when compared to the Koo (1986) value. However, Koo (private communication) concedes that this point may be an overestimate. In fairness, we must also concede that the actual slope for the faint end of the QSO LF may be steeper than the value derived here as a result of incompleteness in our survey at faint magnitudes. In deriving these number counts we have assumed that the QSO LF continues smoothly on, with slope β = -1.2, beyond the faintest absolute magnitudes observed here (M_B = -21). Under such an extrapolation of the LF we predict that at faint apparent magnitudes (B > 24 mag) the bulk of the objects contributing to the counts of low redshift (z < 2.2) QSOs will be just such faint objects, more akin to the Seyfert galaxies and low luminosity active galactic nuclei (LLAGNs) seen at low redshift. The justification for such a smooth extrapolation of the QSO LF to faint magnitudes arises not only from our 'simplest possible model' ethic but also, as we shall see in the following section, from the shape of the Seyfert and LLAGN LF which displays such a smooth form to magnitudes as faint as $M_B \simeq -12$.

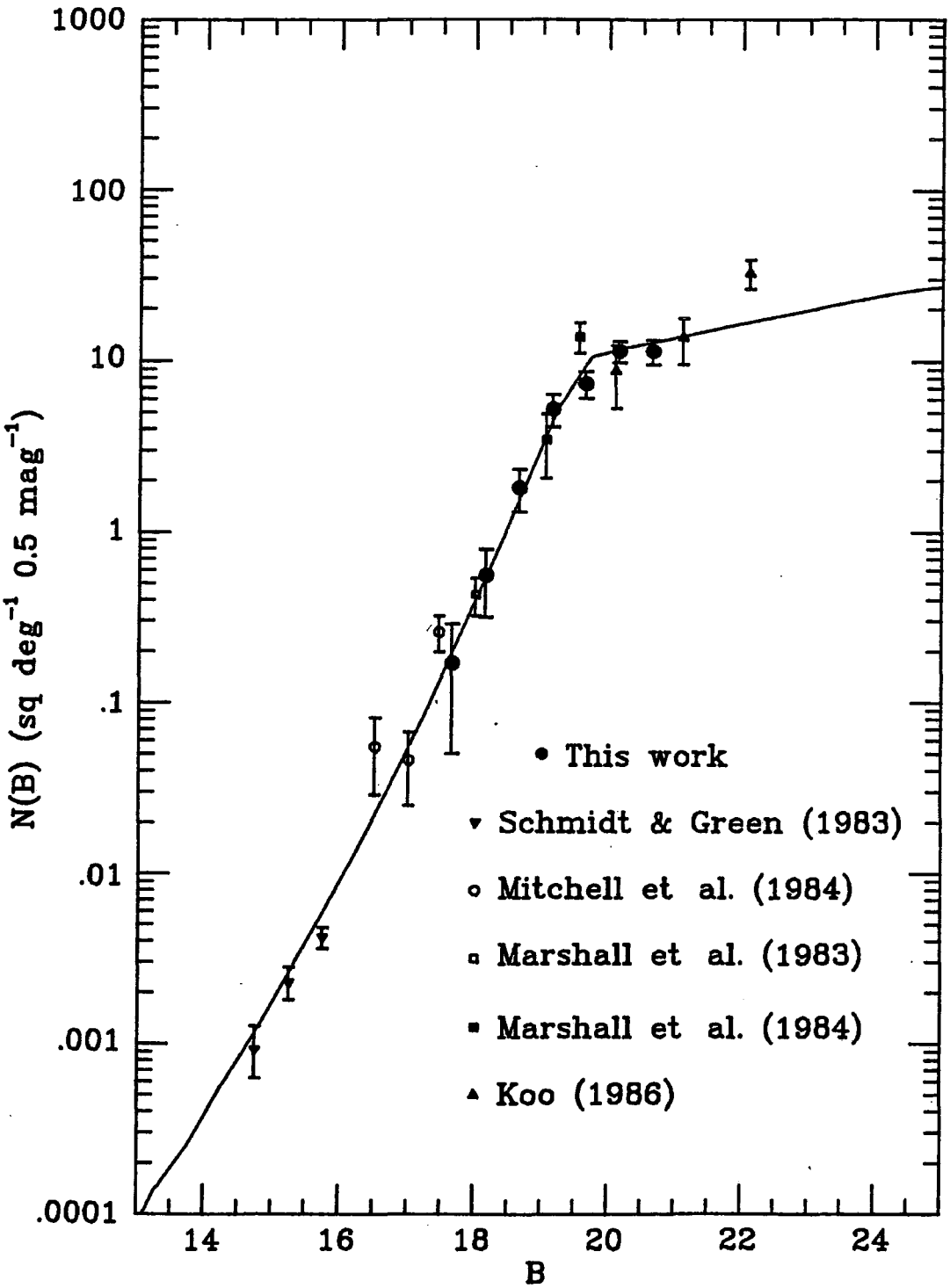

Figure 4.6 Differential number magnitude relation for z < 2.2 QSOs. Solid line indicates prediction of the standard evolution model (see text).

We also note that the SEM predictions are consistent with the observed n(z) distributions for both redshift class 1 and 2 QSOs (figure 4.7a) and all redshift class QSOs (figure 4.7b) in our survey. The absence of low redshift ($z < 0.4$) QSOs can therefore be explained as a natural consequence of the sharp break to a flat slope at faint absolute magnitudes seen in the QSO LF and the fast rate witnessed for the evolution of this LF.

4.3.5 Comparison with the Seyfert and Galaxy Luminosity Functions

It has long been known (see e.g. Weedman 1976) that QSOs, Seyfert galaxies and LLAGNs exhibit a continuous range in their observed properties (e.g. luminosities, line widths) and that the 'botanical' distinction between QSOs and other forms of active galactic nuclei (AGNs) merely arose because QSOs exhibited stellar images while AGNs were observed in galaxies. Now that deep CCD imaging of QSOs has revealed extended structure (see e.g. Malkan 1984) around many low redshift ($z < 0.5$) QSOs, even this distinction is beginning to be eroded. However, the evolutionary link between Seyferts and QSOs has been more difficult to establish with so few high redshift QSOs being observed at the luminosities of low redshift Seyferts. With our faint survey we may go some way towards resolving this problem.

To do so, we first evolve our QSO LF back to $z = 0$ and compare its form (solid line in figure 4.8) with those for LFs derived from observations of Seyferts and other LLAGNs. Weedman (1986) has derived a composite LF for the nuclear magnitudes of active galactic nuclei culled from a variety of sources and

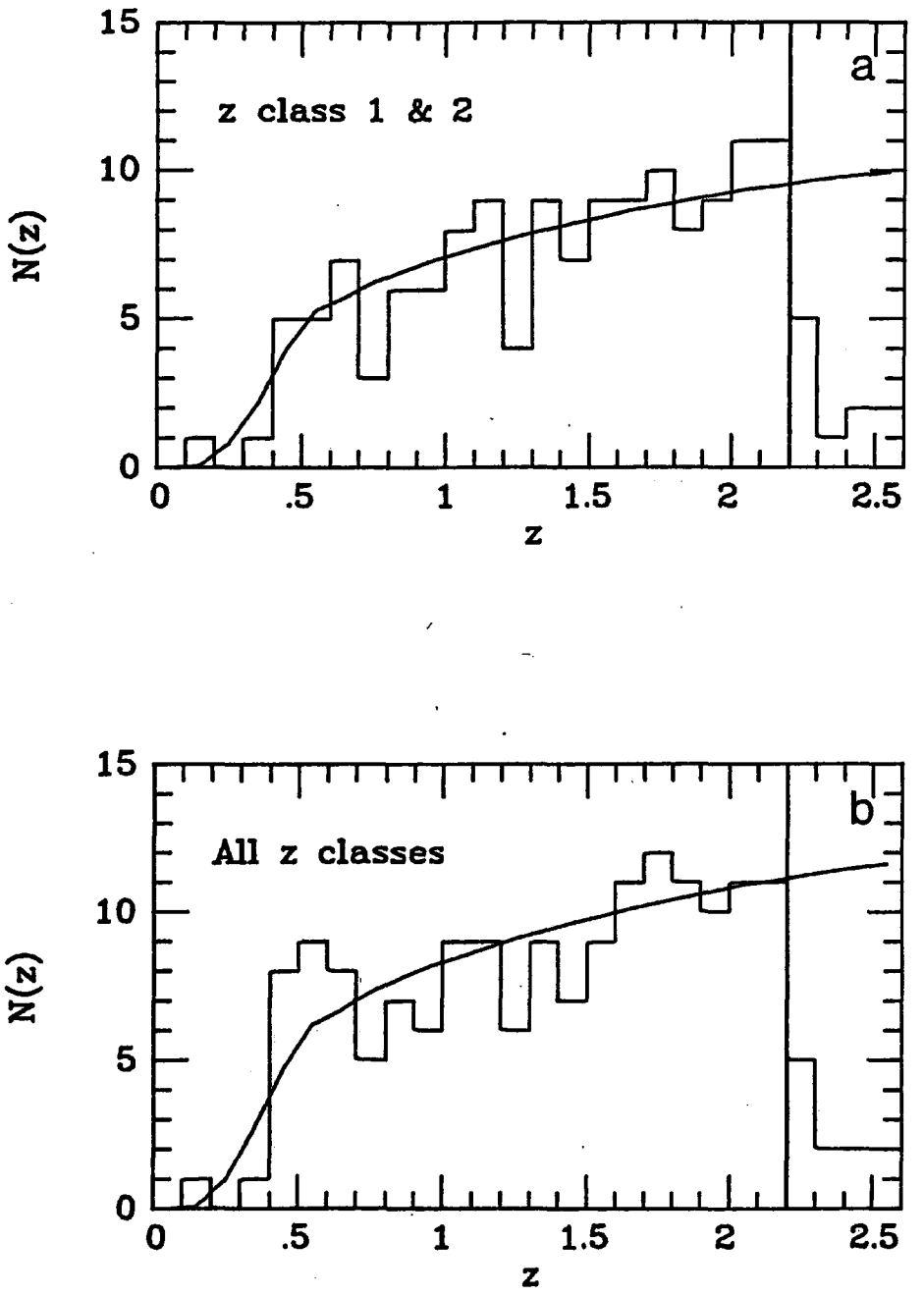

Figure 4.7 Number redshift relation for a) redshift class 1 and 2 and b) all redshift class QSOs discovered in the faint spectroscopic survey. Solid line indicates prediction of the standard evolution model (see text).

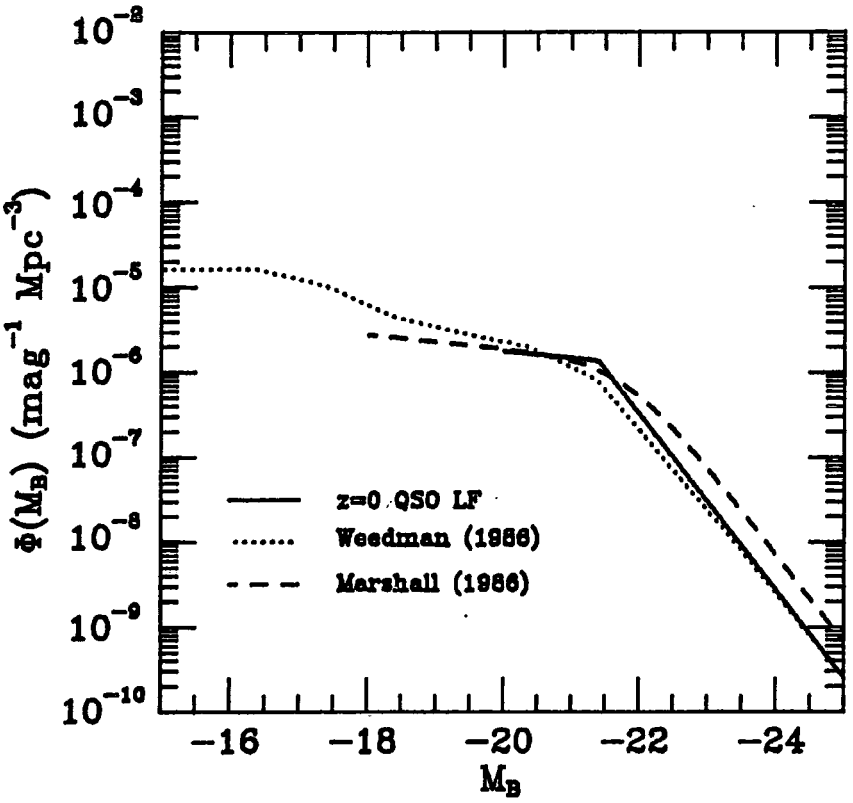

Figure 4.8 Comparison of the z=0 QSO luminosity function, derived from extrapolation of the standard evolution model, with those luminosity functions explicitly calculated for the nuclear magnitudes of Seyfert galaxies and low luminosity active galactic nuclei.

encompassing a wide range ($-12 < M_B < -24$) in magnitude. The final form of the average LF given explicitly in Weedman (1986) is plotted as the dotted line in figure 4.8. In addition the dashed line in figure 4.8 represents the parameterisation of the Seyfert LF (again in terms of nuclear magnitudes) obtained by Marshall (1986) from observations of Seyferts in the CfA survey. Bearing in mind the considerable uncertainties in the estimation of Seyfert LFs (e.g. problems in deriving nuclear magnitudes from subtraction of the galaxian component), we view the observed agreement in density and shape between the LFs determined explicity for Seyferts and that LF extrapolated from the observations of our QSOs as highly suggestive that Seyferts and LLAGNs are the evolutionary equivalents of QSOs at the present day. Whether Seyferts and LLAGNs represent the end-points of long lived QSOs or the present day population of a short lived QSO phenomenon is a more subtle distinction, which we shall discuss further in chapter 8.

We also note how similar the shape of the QSO LF is to that obtained for cluster galaxies. It is well known (see e.g. Abell 1975) that the LF for galaxies in rich clusters is well represented by a two power law function (i.e. the form used here to describe the QSO LF) and does not obey the standard Schechter (1976) form. Godwin and Peach (1977), with later corrections by Metcalfe (1983), find the LF for galaxies in the Coma cluster to follow a steep ($\beta = -2.6$, in the notation employed here) slope at bright magnitudes, flattening out to a slope of $\beta = -1.4$ beyond $M_B^* = -20$. The values of these parameters are remarkably

similar to those found for the QSO LF, although the space density of galaxies is ≃ 100-1000 times that observed for QSOs (Koo 1986, Marshall 1986)

Because the galaxy luminosity function is calculated using extended magnitudes while the QSO LF is derived from nuclear magnitudes, the observed agreement in shape may be viewed as somewhat fortuitous. However, there is some evidence from deep CCD imaging studies of QSOs (Gehren *et al.* 1984) that the nuclear luminosities of QSOs (L_{NUC}) may be closely related to the luminosities of their extended components (L_{EXT}) in the form $L_{NUC}/L_{EXT} \simeq 2$. In such a case the observed agreement between the shapes for the galaxy and QSO LF would assume a greater significance, possibly suggesting that the mechanism whereby, at any particular epoch only a small fraction of galaxies have been 'triggered' to form QSOs, occurs relatively independently of magnitude. Further discussion of the implication of such an observation must, however, wait until any relationship between L_{NUC} and L_{EXT} is more firmly established.

4.3.6 Comparison with Other Parameterisations

a) Pure Density Evolution

Although we have discounted this form of evolution in chapter 4.2, it is instructive to compare the n(m) predictions for $z < 2.2$ QSOs in a PDE model in which the LF assumes the two power law form derived above. To obtain the steep slope at bright magnitudes we require a density evolution of the form (see e.g. Marshall *et al.* 1984):

$$\Phi(M_B, z) = \Phi(M_B, 0)\exp(14.8\tau) \quad \ldots (4.20)$$

The predicted n(m) relation for the two power law LF is shown in figure 4.9 and once again we see that the high number counts predicted beyond B = 19.5 mag rule out this model. Moreover, we note that the n(m) counts predicted using our two power law LF still exhibit the same steep power law behaviour at all magnitudes, whatever other parameterisations for PDE (e.g. density increasing as a power law with redshift) are chosen.

b) Pure Luminosity evolution

PLE has most recently been championed by Marshall *et al.* (1983b,1984) and Marshall (1985). However, as has been made clear from previous sections, their information on QSOs did not extend to sufficiently faint magnitudes to pick up the break in the QSO LF. To arrive at the low counts seen by Koo and Kron (1982), they merely assumed that the QSO LF had an epoch dependent cut-off (L_{min}) at faint luminosities below which no QSOs existed. However, from the differential n(m) counts plotted in figure 4.10, we can see that such a parameterisation is far too 'brutal' in that it predicts no QSOs at all fainter than B ≃ 21.0 mag. Its predictions do not, however, look nearly as bad when plotted on an integral n(m) diagram - see figure 6 of Marshall *et al.* (1984)! The only model parameter obtained here that we can directly compare with those given in Marshall *et al.* (1983b,1984) and Marshall (1985) is k_L. For model G of Marshall (1985) (q_0 = 0.5, α = -0.5), k_L = 3.2 ± 0.1, lower than our value of 3.7 ± 0.1, and hence less evolution is required by

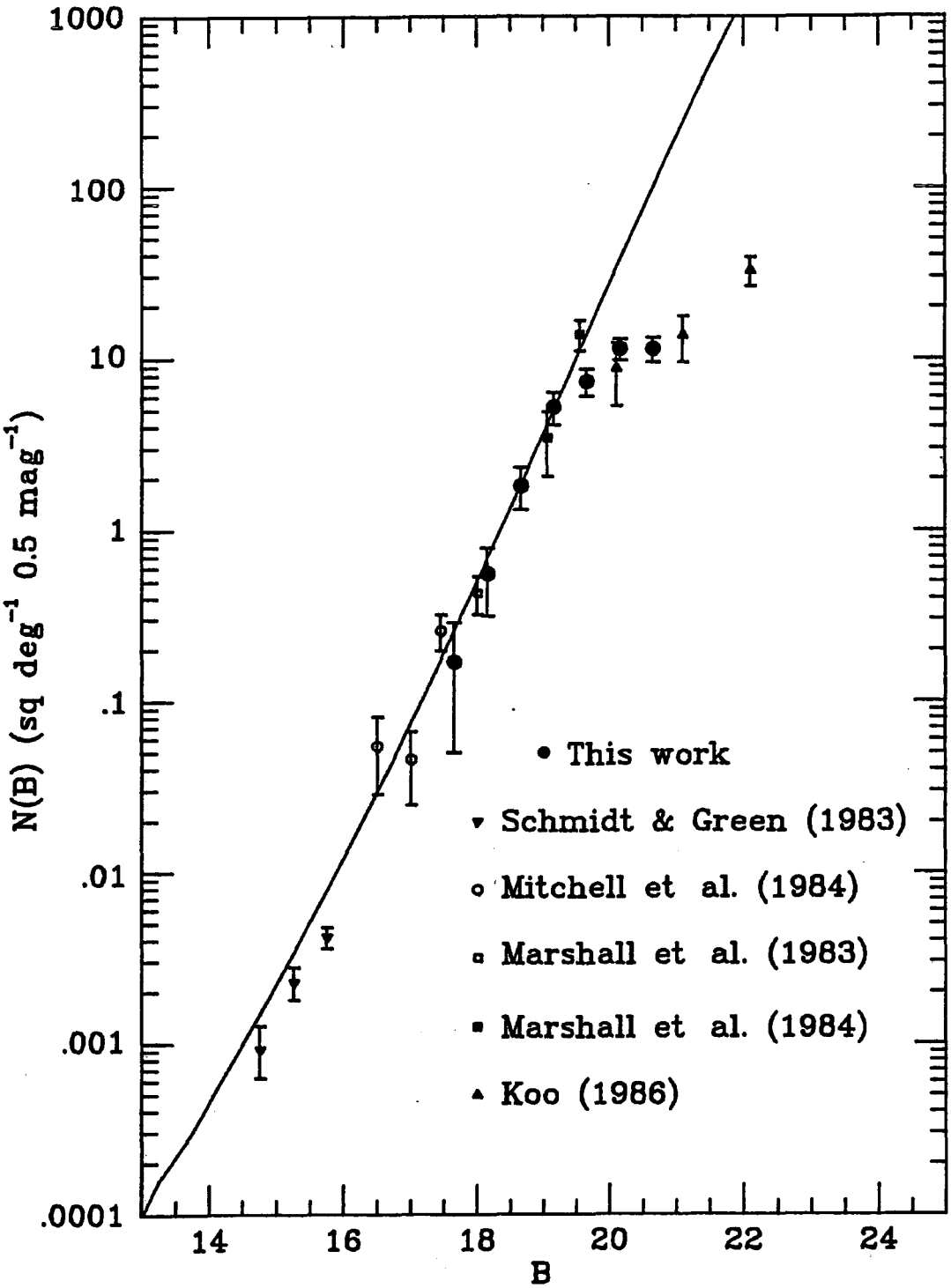

Figure 4.9 Differential number magnitude counts for z < 2.2 QSOs. Solid line indicates prediction from pure density evolution model (see text).

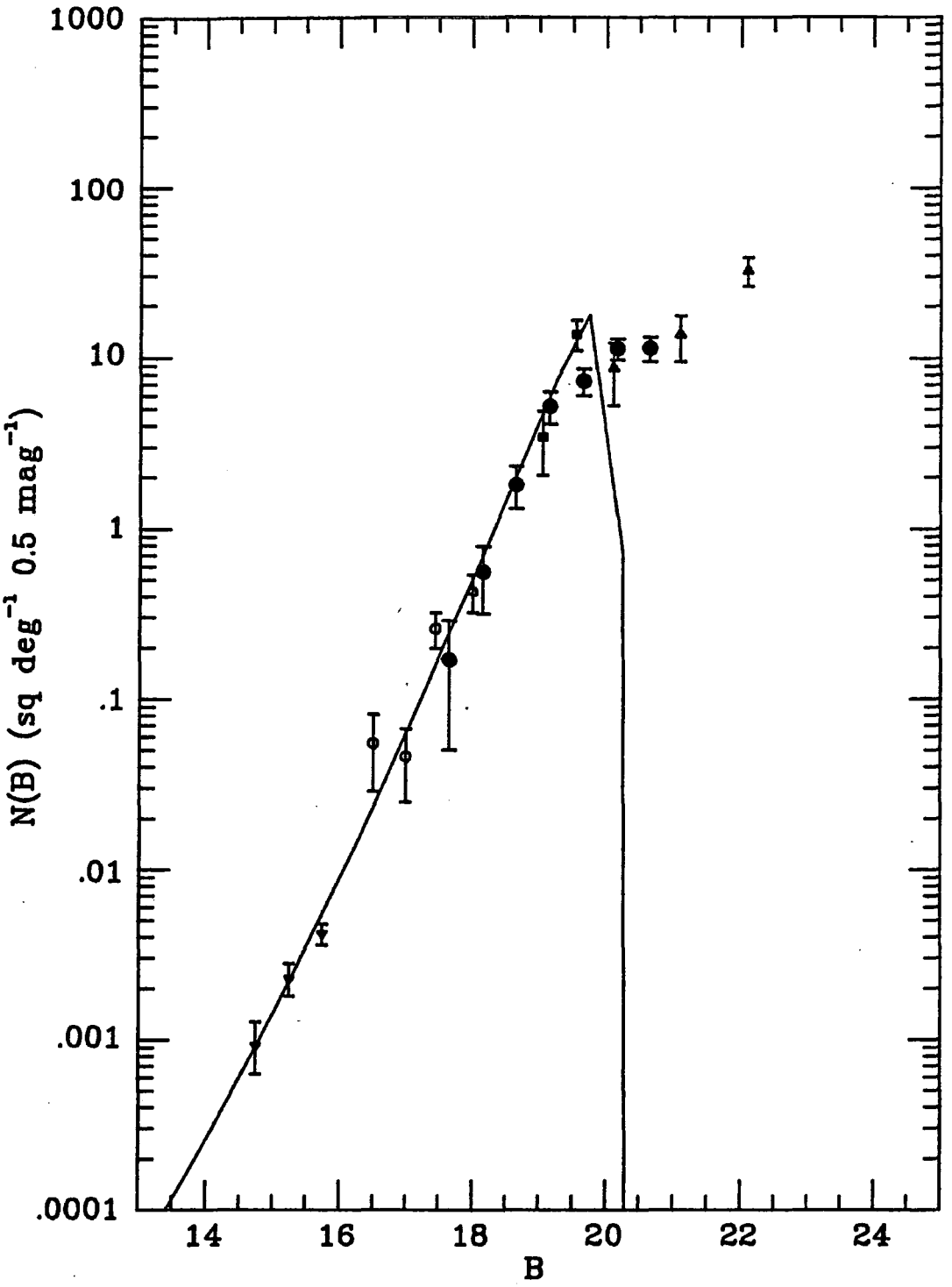

Figure 4.10 Differential number magnitude counts for z < 2.2 QSOs. Solid line indicates Marshall (1985) prediction. See figure 4.9 for key to symbols.

Marshall (1985) to fit his data than is necessary here. This difference may, in part, be attributable to the inclusion of the bright QSOs in the Schmidt and Green (1983) catalogue by Marshall (1985) in his estimation of k_L. From figure 4.5 we note that, although statistics here are poor, at the brightest magnitudes the LFs show marginally less evolution than at the fainter magnitudes where we determined our evolutionary parameters. Their inclusion in the derivation of the evolutionary parameters for the QSO LF by Marshall (1985) may well have influenced the values of k_L obtained.

c) Luminosity Dependent Density Evolution

This is the form of evolution advocated by Schmidt and Green (1983). To test its applicability to the data, we use their HH5 model (i.e. the evolutionary model obtained for a $q_0 = 0.5$ universe with the assumption that the surface density of QSOs at B = 21 is 50 per square degree). The zero age LF was taken to be

$$\Phi(M_B,0)=\Phi^*(\mathrm{dex}(0.4(M-M^*)(\alpha+1))+\mathrm{dex}(0.4(M-M^*)(\beta+1))) \quad \ldots (4.21)$$

where $\alpha = -5.7$, $\beta = -3.7$, $M^* = -26$ and $\Phi^* = 4 \times 10^{-11}$ Mpc^{-3} mag^{-1} gave the best re presentation to the binned LF given in Schmidt and Green (1983). The evolution with redshift is parameterised as follows:

$$\Phi(M_B,z) = \Phi(M_B,0)\exp(k(-20.12-M_B\tau)) \quad \ldots (4.22)$$

where k=2.18 for $M < -20.12$ and k=0 for $M > -20.12$. We compare the predictions of this model to the observations by the χ^2 test

(see table 4.6) and by plotting out the LFs explicitly (see figure 4.11). In both cases we see poor agreement, although admittedly the bulk of the discrepancies occur for the faintest bins. In fairness to Schmidt and Green (1983) we should really re-compute the parameters for their model using the new faint data at our disposal. However, we may wonder about the necessity to parameterise the LF in this more complex manner when a much simpler PLE model has already been shown to be a perfectly good fit to the data. It appears that Schmidt and Green (1983) chose LDDE to reflect the dependence of $\langle V/V_{max} \rangle$ (see Schmidt 1968), obtained for QSOs in their survey, on absolute magnitude (QSOs at brighter magnitudes had higher $\langle V/V_{max} \rangle$ values). However $\langle V/V_{max} \rangle$ is merely an indicator of evolution and does provide information *a priori* on the form this evolution takes. Indeed, Petrosian (1973) has demonstrated that $\langle V/V_{max} \rangle$ increases with absolute magnitude for many forms of PDE, where no luminosity dependence exists. We therefore see no need to invoke LDDE with the data on QSOs presently available.

d) Density and Luminosity Evolution

We find no indication from our data to suggest that the LF also evolves in the sense of decreasing density toward higher redshift as found by Koo (1983).

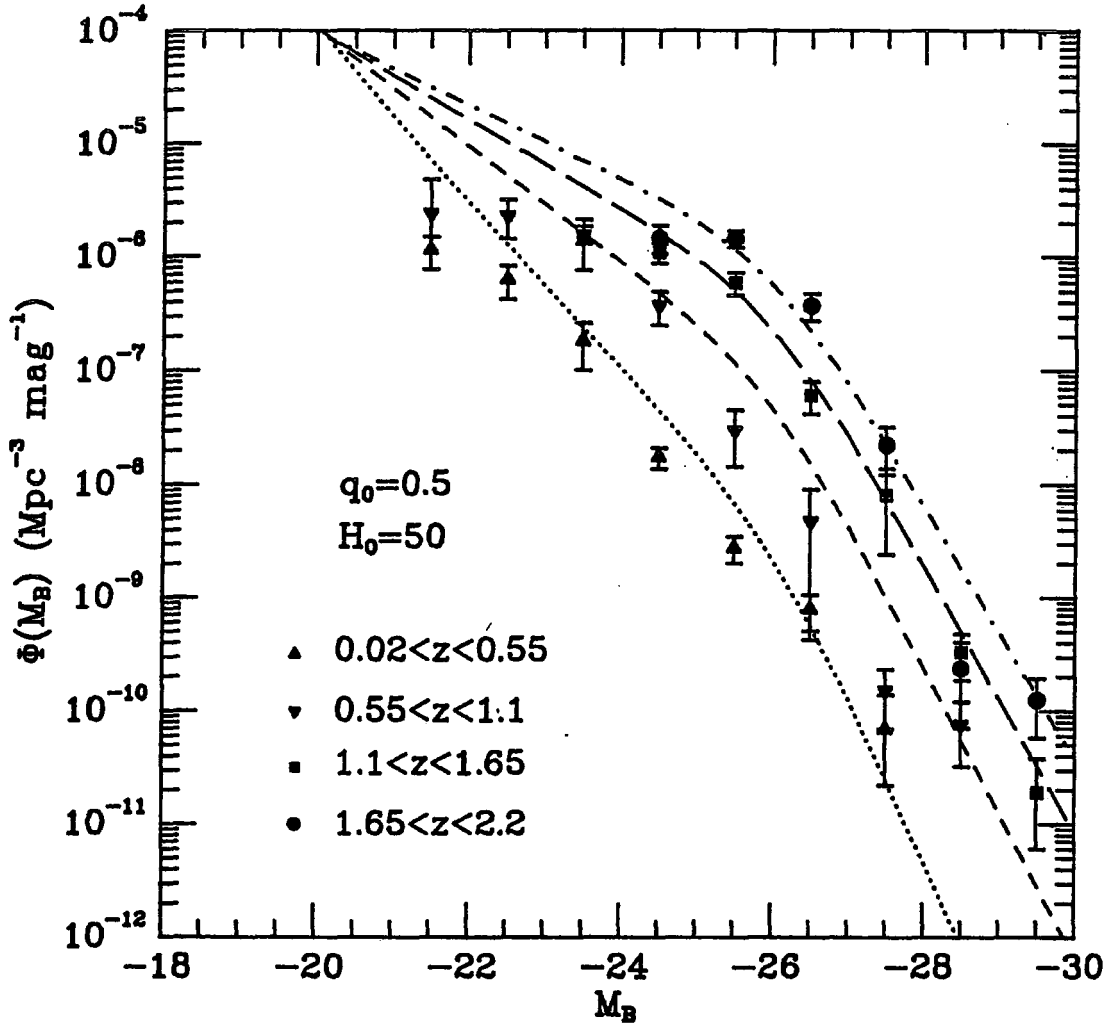

Figure 4.11 Differential QSO luminosity function for the survey combination d. Lines indicate prediction of Schmidt and Green's (1983) HH5 model.

We conclude, therefore, that out of all the possible parameterisations considered for the evolution of the QSO LF, the PLE model proves to be the simplest one which still gives a good fit to the observations. Density evolution is strongly ruled out as it predicts far too many QSOs at faint magnitudes, and more complex forms are unnecessary to describe the data.

CHAPTER FIVE

THE SPATIAL CLUSTERING OF QSOs

5.1 Introduction

As discussed in chapter 1, previous attempts to study the physical clustering of QSOs have been thwarted by poor statistics or inaccurate redshifts. Our large, spectroscopically surveyed QSO catalogue therefore provides an opportunity to tackle the problem of QSO clustering more effectively than has hitherto been possible.

5.2 Estimation of $\xi(r)$

In this analysis we shall employ the statistic most commonly used to study the clustering of galaxies (see Peebles 1980 and references therein) and QSOs (Osmer 1981, Chu and Zhu 1983), namely the two point correlation function, $\xi(r)$. The correlation function can be defined (Peebles 1980) through the joint probability

$$\delta P(r) = n^2(z)[1+\xi(r)]\delta V_1 \delta V_2 \qquad \ldots (5.1)$$

of finding a pair of objects (in this case QSOs) in the comoving volume elements $\delta V_1 \delta V_2$, separated by comoving distance r at redshift z, where the space density of QSOs is n(z). As QSOs are observed over a wide range of redshifts, we choose to work in a comoving coordinate system in which distances will remain unchanged with epoch. For a random spatial distribution the

number of QSOs in any comoving volume element (δV) will be given by $n(z)\delta V$. Thus $\xi(r)$ will be positive at scales where QSOs are clustered amongst themselves, zero where QSOs are randomly distributed with respect to one another and negative where they exhibit anti-clustering.

Before we can find an estimator for $\xi(r)$ we must first establish a method for calculating the comoving distance, r, between QSOs observed at redshifts z_1 and z_2 and separated by an angular distance θ. In standard Friedmann cosmologies it has long been known (Sandage 1961) how to calculate such distances in the limit of small redshift separations, Δz, or small angular separations, $\Delta\theta$, e.g.

$$r = c/H_0 \, s\Delta\theta \qquad \text{at constant } z \qquad \ldots (5.2a)$$

$$r = c/(H_0(1+z))\Delta z \qquad \text{at constant } \theta \qquad \ldots (5.2b)$$

$$s = \frac{(zq_0+(q_0-1)(\sqrt{(1+2q_0 z)}-1))}{(1+z)q_0^2} \qquad q_0 > 0 \qquad \ldots (5.2c)$$

$$= \frac{z(1+z/2)}{(1+z)} \qquad q_0 = 0 \qquad \ldots (5.2d)$$

where s is the dimensionless comoving coordinate. However such approximations do not hold in the case of QSOs where Δz is large. Osmer (1981) has therefore devised a method to calculate the distances between QSOs separated by arbitrary large redshifts or angular distances. In doing so, he utilises the expression given by Weinberg (1973) for transforming from one coordinate system to another in the Robertson-Walker metric.

$$X' = X + a\{\sqrt{(1-kX^2)} - [1-\sqrt{(1-ka^2)}](X.a/a^2)\} \qquad \ldots (5.3)$$

where **X'** and **X** are the comoving vectors to a particular QSO from the transformed and original origins respectively. The transformation vector **a** is expressed in the frame of the transformed coordinate system and k is the curvature term in the Robertson-Walker metric (k=1,0,-1 for $q_0 < 0.5$, 0 or > 0.5 respectively).

The problem of finding the distance between two QSOs simply reduces to the task of transforming from the coordinate system in which we observe the QSOs to one in which one QSO in the pair lies at the origin. The distance is then given by the magnitude of the transformed vector **X'**, when **X** is the coordinate vector of the second QSO in the original system.

As demonstrated by Osmer (1981), the simplest way to use equation (5.3) is to locate each pair of QSOs in the observer's (x,y,z) coordinate frame at $(0,0,s_1)$ and $(s_2 \sin\theta, 0, s_2 \cos\theta)$, where s is given by equation (5.2c or d) and the subscripts refer to the individual QSOs in the pair. The transformation vector therefore has components $(0,0,s_1)$ and, from equation (5.3) the transformed vector **X'** becomes:

$$\mathbf{X'} = (s_2 \sin\theta, 0, s_2 \cos\theta) + C(0,0,-s_1) \quad \ldots (5.4a)$$

$$C = \{\sqrt{(1 \pm s_2^2)} + s_2/s_1 \cos\theta - s_2/s_1 \cos\theta \sqrt{(1 \pm s_1^2)}\} \quad q_0 \lesseqgtr \tfrac{1}{2} \ldots (5.4b)$$

$$C = 1 \quad q_0 = \tfrac{1}{2} \quad \ldots (5.4c)$$

The distance between the QSOs, r, is then found from the magnitude of the vector **X'**:

$$r = c/H_0 \int ds/\sqrt{(1-ks^2)} \quad \ldots (5.5)$$

For $q_0 = \frac{1}{2}$ the equations (5.4a,c) and equation (5.5) reduce to the standard Euclidean cosine rule:

$$r = c/H_0 \, (s_2^2 + s_1^2 - 2 s_1 s_2 \cos\theta)^{0.5} \qquad \ldots (5.6)$$

Using the above method to calculate distances between QSOs an estimator for $\xi(r)$ can be defined as follows (Peebles 1980):

$$\xi(r) = N_{QQ}/N_{QR} - 1 \qquad \ldots (5.7)$$

N_{QQ} is merely the number of catalogue QSO pairs found at separations $r-\Delta r/2$ to $r+\Delta r/2$. N_{QR} is the number of QSO/random point pairs found (after appropriate normalisation for the respective numbers of objects in the QSO and random point catalogues and correction for double pair counting) over the same range in separations. The latter catalogue was obtained by randomly distributing points on the plane of the sky over the surveyed areas, with redshifts assigned to each QSO, by random selection from the observed QSO n(z) distribution (figure 4.7). The smooth n(z) distributions for the survey QSOs illustrated in that figure indicate that the QSO catalogue is not seriously biased towards particular redshift ranges. Such a biased distribution could have occured had either the UVX technique been seriously incomplete (see chapter 3.4a) or had a large number of QSOs been preferentially assigned the incorrect redshift from a single line identification. As this appears not to be the case our QSO catalogue is well suited to this clustering analysis.

While the overall n(z) distribution may be smooth, we note from figure 5.1 the apparent 'clumpiness' of the redshift distribution for QSOs on individual fields. In particular, we observe several 'clusters' of QSOs i.e 3-4 QSOs with similar redshifts ($\Delta z < 0.1$) separated by a few arcminutes. A good example of such a 'cluster' is to be found on the QNY2 field. The 4 QSOs (QNY2:07,15,21 and 22) which make up this group all have redshifts in the range $1.95 < z < 2.03$ and are separated by less than 20 arcminutes on the sky. Their spectra are re-plotted in figure 5.2. The following analysis will ascertain the significance of such associations.

In our estimation of $\xi(r)$ from the catalogue QSOs, 'cross-FOCAP field' pairs have only been taken into account when the FOCAP fields lie on the same Schmidt fields. The different Schmidt plates on which the survey areas were defined lie at least 25 degrees away from each other, corresponding to separations of $1000h^{-1}$ Mpc at $z = 1.5$ ($q_0 = \frac{1}{2}$). However $\xi(r)$ will not be calculated for distances greater than this value.

5.3 Results from the faint QSO survey

We now calculate $\xi(r)$ for the QSOs in our faint survey using the method defined above. In doing so we will explicitly take into account the dependence of $\xi(r)$ on the cosmological model chosen by calculating the correlation function for both a closed ($q_0 = \frac{1}{2}$) universe and an open ($q_0 = 0.1$) universe.

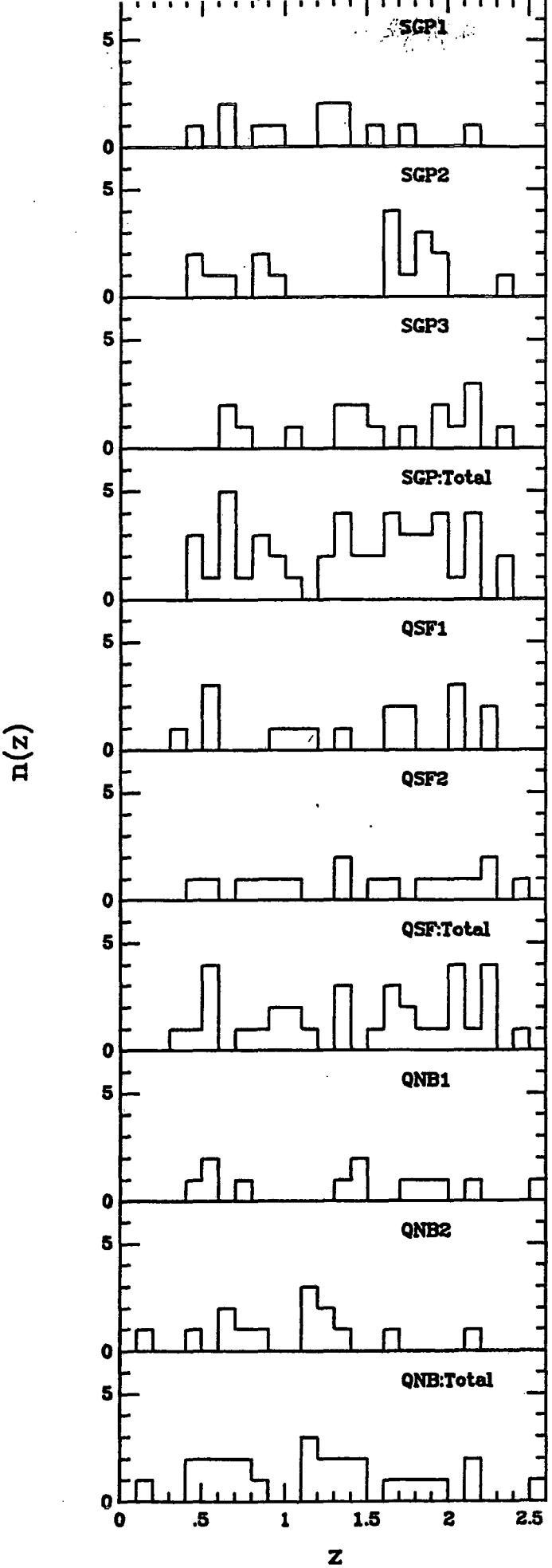

Figure 5.1 Number redshift relation for QSOs (all redshift classes) on individual fields in the faint spectroscopic survey.
a) SGP, QSF and QNB fields.

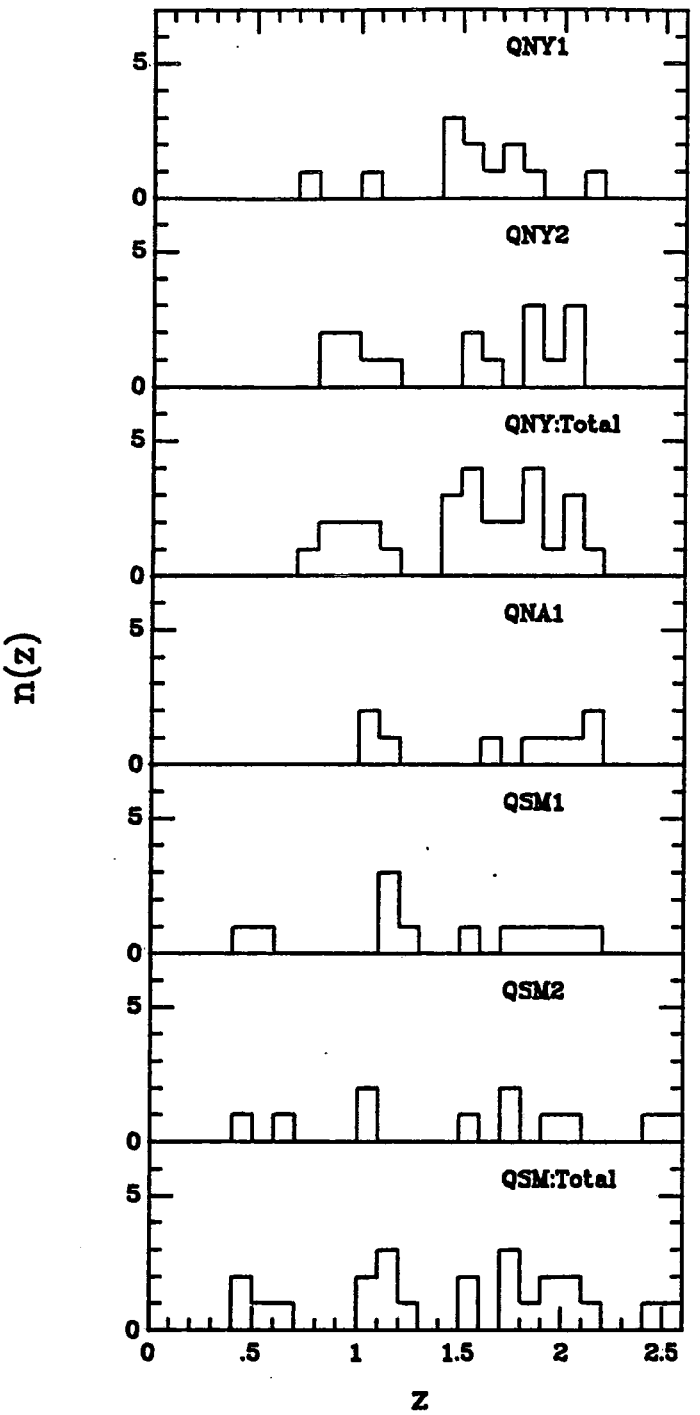

Figure 5.1 continued b) QNY, QNA and QSM fields.

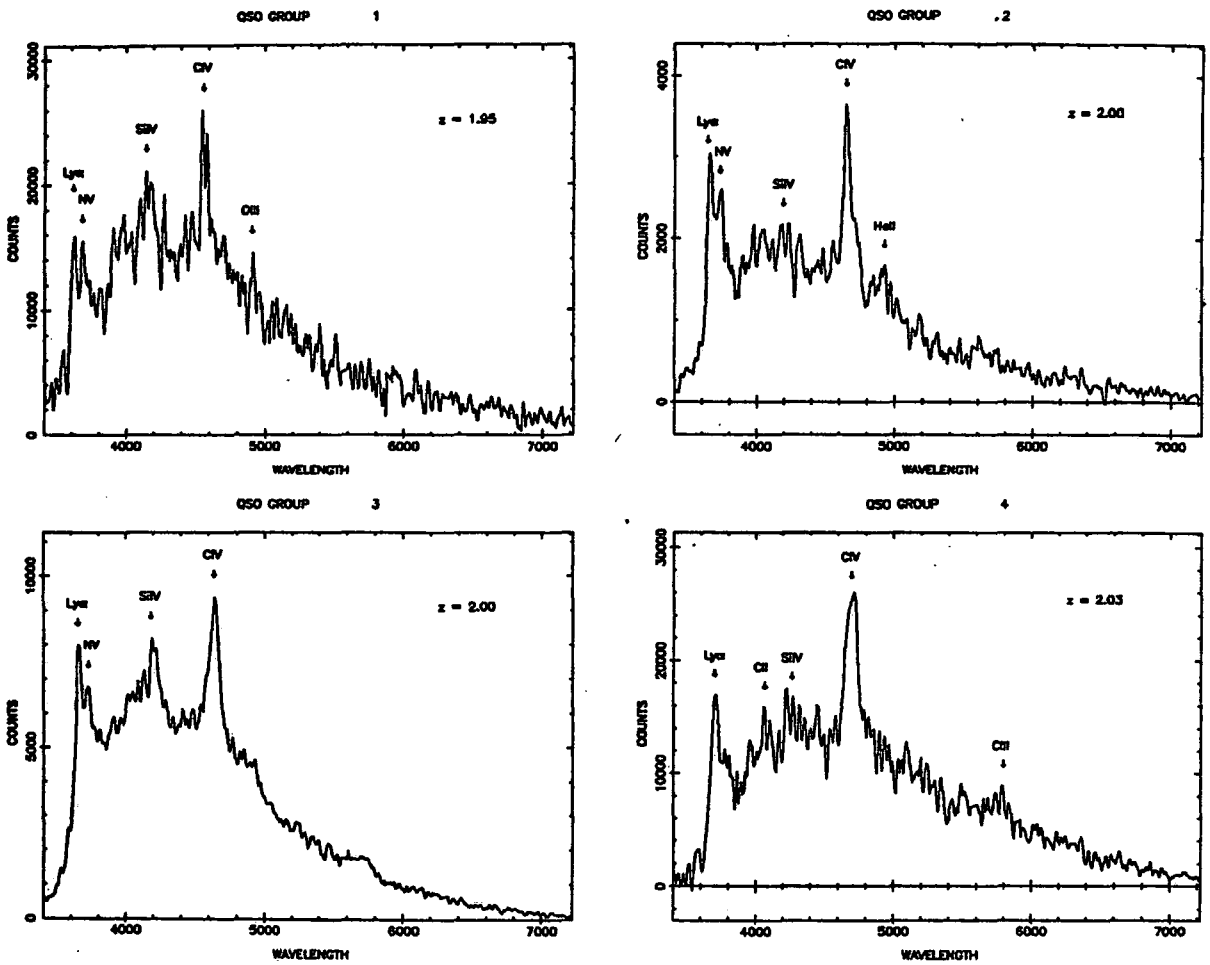

Figure 5.2 An unusual QSO grouping. Spectra of 4 QSOs discovered on the QNY field within a 20 arcminute radius.

Initially we determined $\xi(r)$ using only the QSOs with $0.4<z<2.2$ and redshift classes 1 and 2. The lower limit of $z = 0.4$ was imposed to avoid the strong discontinuity seen in the $n(z)$ distribution (figure 4.7). Thus the smoothed fit to this distribution used in the construction of the random point catalogue could be approximated by a straight line. It was found, however, that $\xi(r)$ was insensitive to small changes in the fit, as more complex polynomials used to define the $n(z)$ relation between $0.4<z<2.2$ (and even $0<z<2.2$ when the two lower redshift QSOs were included) made no significant change to $\xi(r)$.

Moreover, the inclusion of redshift class 3 objects, originally excluded for fear that their uncertain redshifts may be preferentially assigned towards one particular redshift range, thus biasing $\xi(r)$, also made no significant difference to the estimate of $\xi(r)$. This is demonstrated explicitly in figure 5.3, where the estimate of $\xi(r)$ (calculated for a $q_0 = \frac{1}{2}$ universe) is plotted both with and without the inclusion of redshift class 3 objects. Henceforth, estimates of $\xi(r)$ will include all classes of redshift (by rejecting redshift class 3 QSOs we might equally well be biasing $\xi(r)$ against redshift ranges in which QSOs have only one strong line visible in their IPCS spectrum). Using the QSO sample thus defined we plot $\xi(r)$ for a $q_0=0.1$ universe in figure 5.4.

Table 5.1 lists the number of QSO pairs on which the above estimates of $\xi(r)$ were based. In this analysis $\xi(r)$ was calculated in logarithmic bins over the scales $1h^{-1}<r<1000h^{-1}$ Mpc. The error on our spectroscopic redshift ($\Delta z \simeq 0.003$), however,

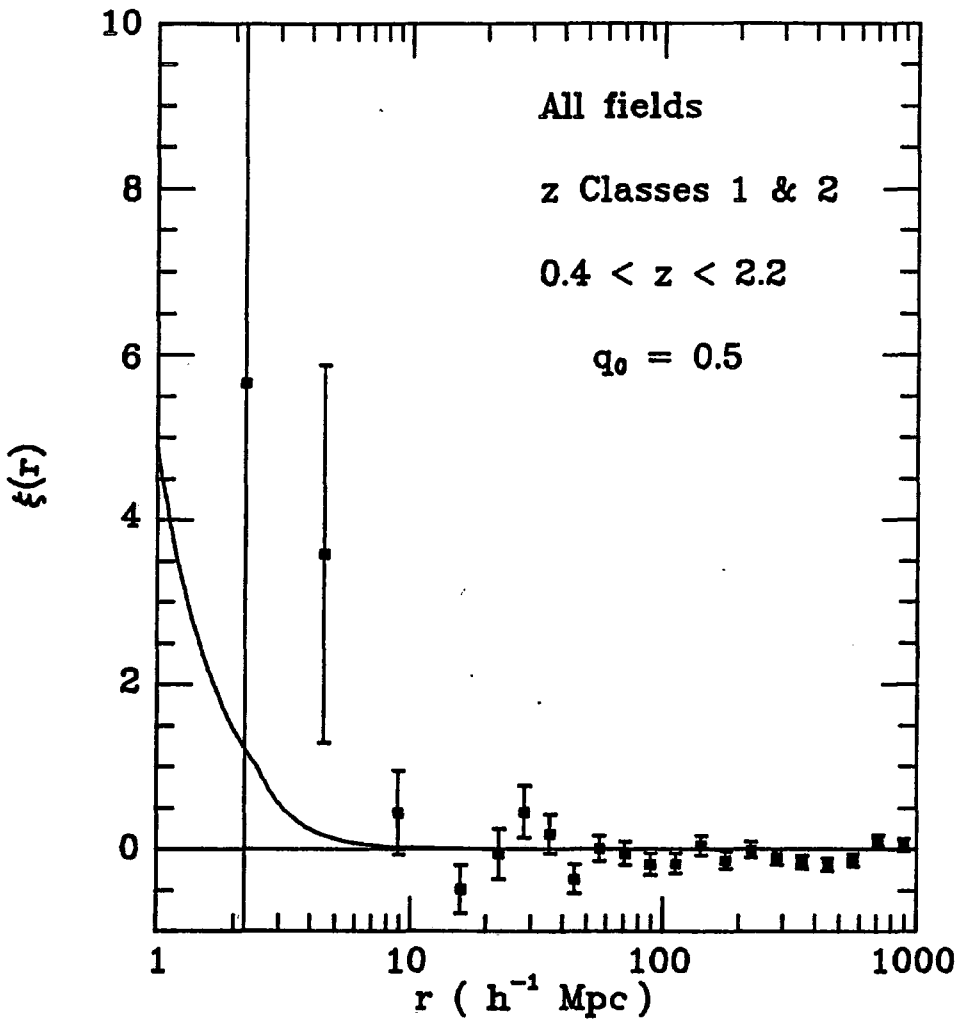

Figure 5.3 Correlation function, ξ(r), for QSOs in the faint UVX survey, calculated for a q_0 = 0.5 universe. Solid line indicates predicted galaxy ξ(r) at z=1.5.
a) Redshift classes 1 and 2 only.

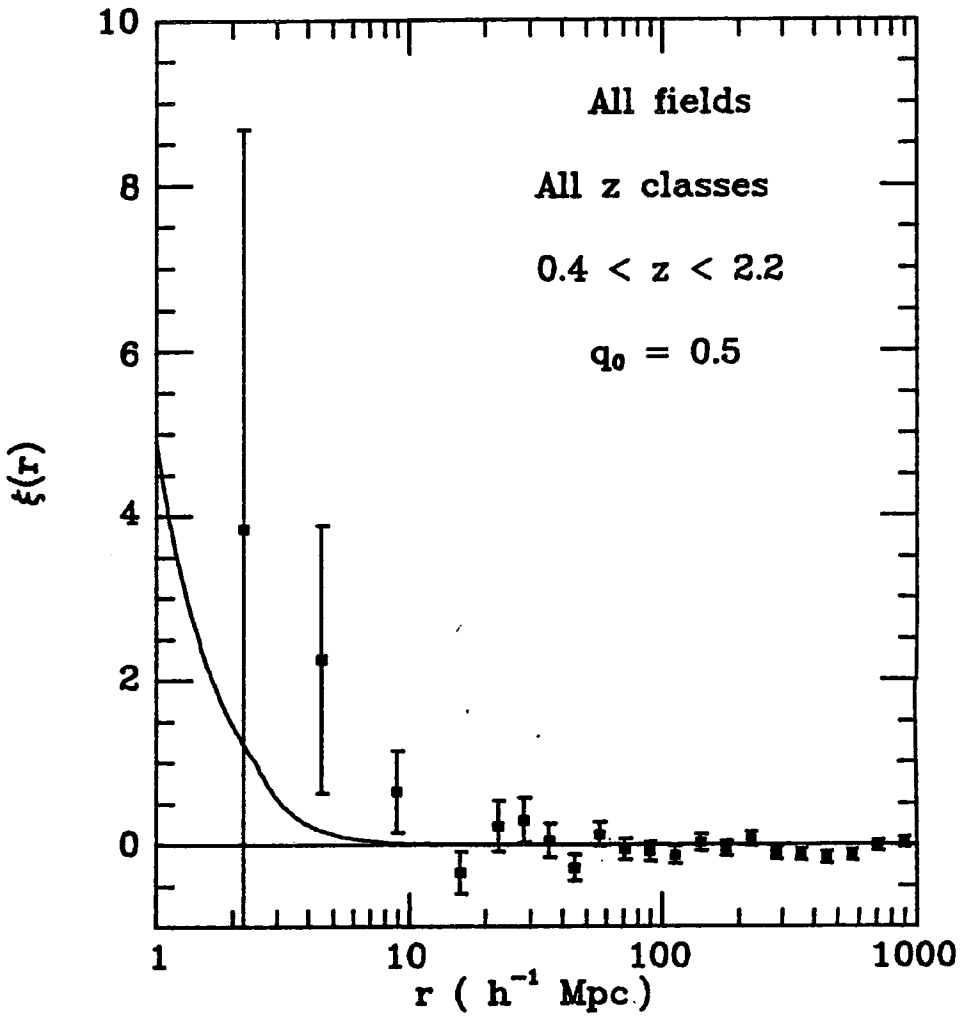

Figure 5.3 continued b) All redshift classes.

r (h^{-1} Mpc)	$q_0 = 0.5$ Number of QSO pairs	$q_0 = 0.5$ $\xi(r)$	$q_0 = 0.1$ Number of QSO pairs	$q_0 = 0.1$ $\xi(r)$
2.2	1	3.84	1	7.58
4.5	5	2.52	1	0.68
8.9	5	0.65	6	1.17
15.8	10	-0.33	8	0.35
22.4	16	0.23	5	-0.40
28.2	23	0.30	6	0.12
35.5	27	0.06	15	0.24
44.7	28	-0.28	19	0.30
56.2	59	0.13	36	-0.33
70.8	60	-0.05	24	-0.06
89.1	68	-0.08	40	0.01
112.2	75	-0.12	56	-0.09
141.3	104	0.03	50	-0.04
177.8	114	-0.04	72	-0.07
223.9	151	0.07	91	-0.04
281.8	150	-0.10	99	0.11
354.8	165	-0.12	139	-0.04
446.7	172	-0.15	160	-0.16
562.3	198	-0.12	159	-0.16
707.9	240	-0.01	195	-0.10
891.3	249	0.03	203	0.02

Table 5.1 Pair Counts and $\xi(r)$ Estimate for Open and Closed Models (all redshift classes included).

represents a fundamental limit for the accuracy of the distances calculated between QSOs in the catalogue ($\simeq 5h^{-1}$ Mpc). Although we have plotted the correlation function at smaller values than this, because of the noise at these small separations, any conclusions drawn from the form of $\xi(r)$ at small scales will only involve the total number of pairs seen at separations less than $10\text{-}15h^{-1}$ Mpc.

The error bars plotted in figures 5.3 and 5.4 are derived from

$$\sqrt{(1+\xi(r))/N_{qq}} \qquad \xi(r) > 0 \qquad \ldots (5.8a)$$

$$1/\sqrt{N_{qq}} \qquad \xi(r) < 0 \qquad \ldots (5.8b)$$

representing the statistical significance of the fluctuations from the Poisson hypothesis for $\xi(r)$. The validity of these error bars were checked by ensuring that they were of the same magnitude as those defined by the variation in the values for $\xi(r)$ derived from North and South Galactic latitude subsamples (plotted in figure 5.5 for a $q_0 = \frac{1}{2}$ universe).

5.4 Discussion

We now discuss the main features of the correlation functions derived in the previous section, commenting in turn on 3 different scale lengths in $\xi(r)$. The scale lengths quoted will refer explicitly to the estimate of $\xi(r)$ in the $q_0 = \frac{1}{2}$ model, the equivalent separations in the $q_0 = 0.1$ model being some 50% larger.

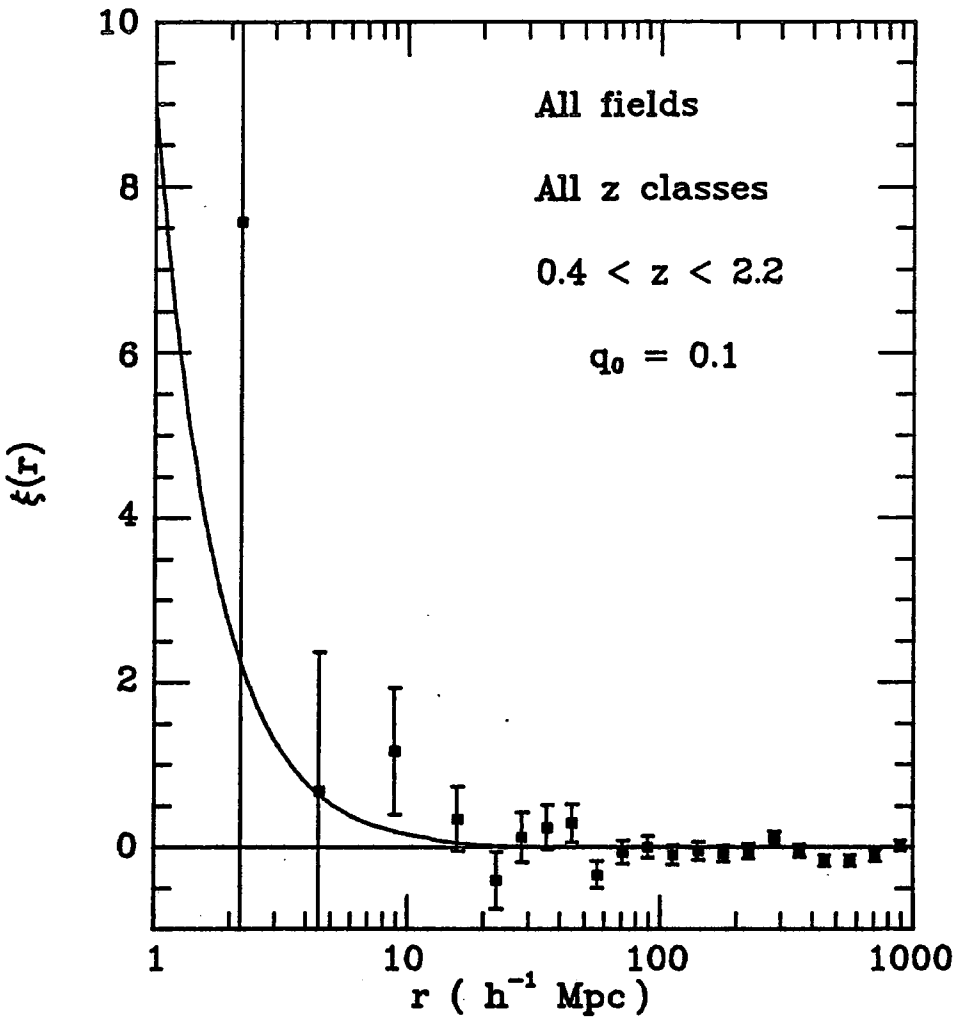

Figure 5.4 Correlation function, ξ(r), for QSOs in the faint UVX survey, calculated for a q_0 = 0.1 universe. Solid line indicates the predicted galaxy ξ(r) at z=1.5 All redshift classes included.

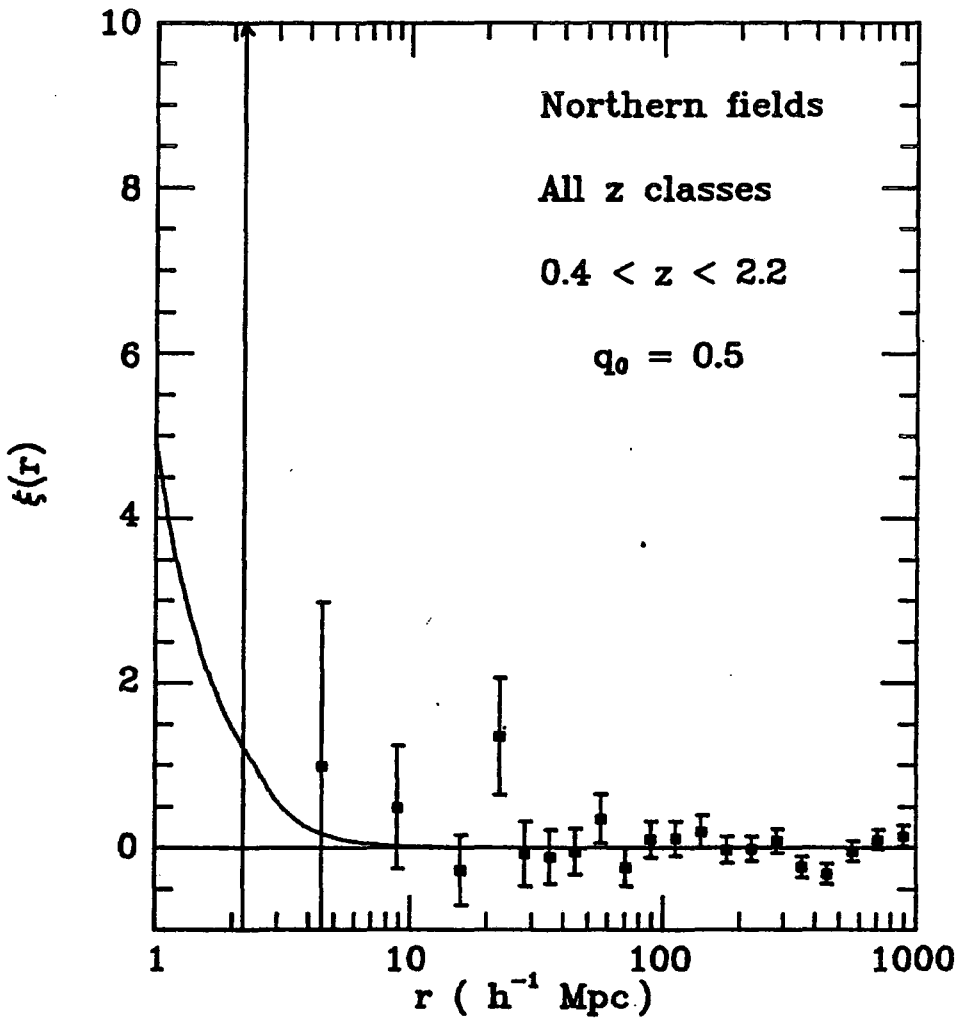

Figure 5.5 a) ξ(r) calculated in a q_0 = 0.5 universe for the north Galactic latitude subsample of the faint UVX QSO survey.
Solid line indicates the predicted galaxy ξ(r) at z=1.5.

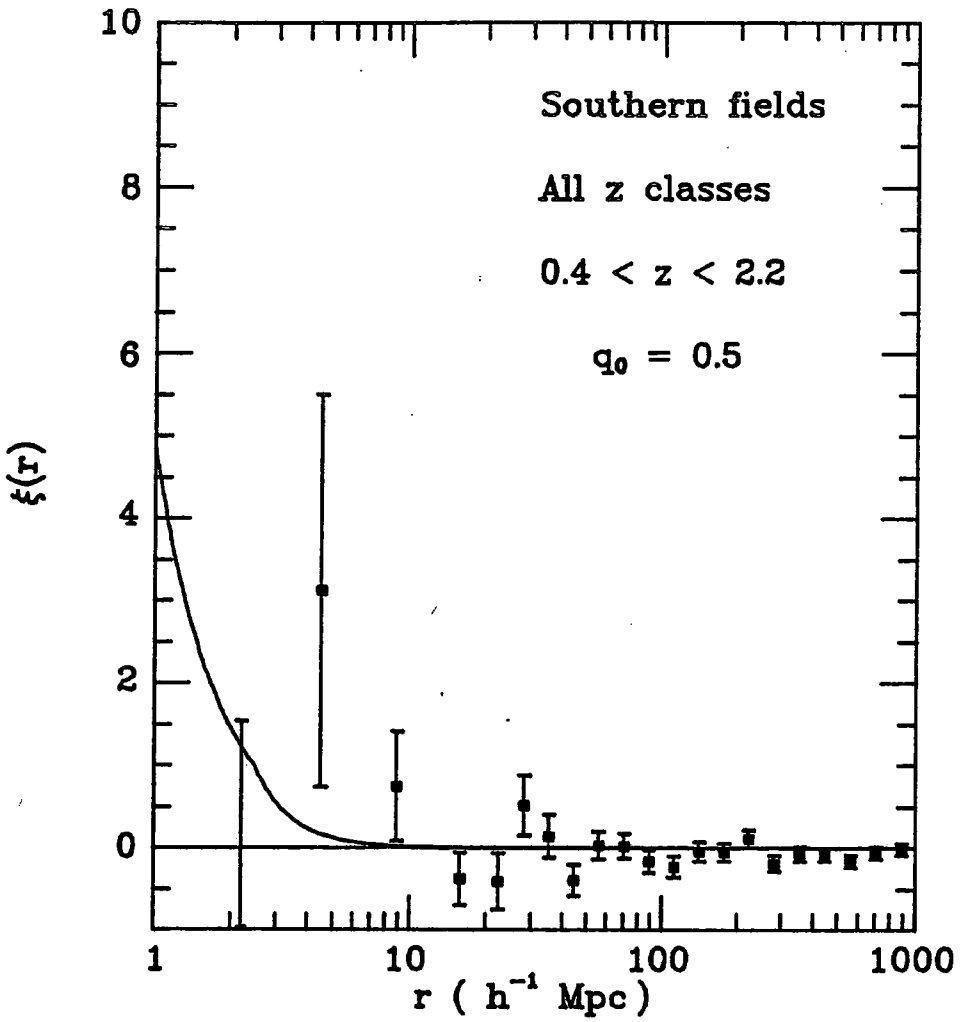

Figure 5.5 b) ξ(r) calculated in a q_0 = 0.5 universe for the south Galactic latitude subsample of the faint UVX QSO survey.
Solid line indicates the predicted galaxy ξ(r) at z=1.5.

a) $r < 10h^{-1}$ Mpc

As these are the scales at which we observe galaxies to be strongly clustered at the present epoch, we first compare the amplitudes of the galaxy and QSO correlation functions within this range.

The galaxy correlation function has a well established power law form below $5h^{-1}$ Mpc which can be represented by (Peebles 1980 and references therein):

$$\xi(r) = ((r/r_0)h)^{-1.8} \quad \ldots (5.9a)$$

$$r_0 = 4h^{-1} \text{ Mpc} \quad \ldots (5.9b)$$

This function reflects the clustering of galaxies in regions where the over density of matter has become so high ($\delta\rho/\rho \simeq 1$) that they have ceased to take part in the general expansion of the universe and have become bound units. Above $5h^{-1}$ Mpc a break to an even steeper power law is clearly seen in the galaxy correlation function (see Shanks *et al.* 1983a). Such a feature implies that density inhomogeneities on these scales have not become bound units and are, in the main, still expanding with the Hubble flow. In this 'linear' regime the correlation function will be given by

$$\xi(r) \propto (rh)^{-(3+n)} \quad \ldots (5.10)$$

where n is the power of the spectrum of mass density fluctuations (Peebles 1980). In a hierarchical clustering model the value of n is reflected in the slope of the correlation function in the bound regime e.g. (Peebles 1980)

$$\xi(r) \propto r^{-(9+3n)/(5+n)} \propto r^{-1.8} \qquad \ldots (5.11)$$

Equation (5.11) therefore suggests a value of n = 0. Certainly n is unlikely to be less than -1 (otherwise the break in $\xi(r)$ would not be so conspicuous). We therefore take n = 0 in equation (5.10) to provide a useful upper limit to the amount of clustering at large scales.

Because scales smaller than the break at $5h^{-1}$Mpc are no longer expanding freely with the universe, we can not directly compare the QSO and galaxy correlation functions at the same comoving separations. We therefore evolve the galaxy correlation function back to z=1.5 (corresponding to the average QSO redshift in our survey) and perform the comparison at that epoch. The form of this evolution is, however, dependent on the cosmological model adopted and so we will consider separately the open and closed universe models adopted here.

i) Closed, $q_0 = \frac{1}{2}$

In a closed universe, 'seed' perturbations continue to grow gravitationally from decoupling until the present epoch. In terms of proper distance the break scale in the correlation function will therefore evolve as (Peebles 1980)

$$r_0(t) \propto t^{2/\gamma} \qquad \ldots (5.12)$$

where γ is the slope of the galaxy correlation function and t is the age of the universe ($t=1-\tau$, where τ is given by equation (4.17b)). By ensuring that the break still occurs at an

amplitude of $\xi=1$, we obtain, in comoving coordinates the galaxy correlation function at z = 1.5:

$$\xi(r) \simeq 4(rh)^{-1.8} \qquad r < 2.7h^{-1}\,\mathrm{Mpc} \qquad \ldots (5.13a)$$

$$\xi(r) \simeq 10(rh)^{-3} \qquad r > 2.7h^{-1}\,\mathrm{Mpc} \qquad \ldots (5.13b)$$

The solid lines plotted in figures 5.3 and 5.5 correspond to this correlation function. Because of the noise in the QSO correlation function at these separations, we choose not to draw conclusions from the comparison of the general form of these correlation functions but rather from the comparison between the observed and predicted number of pairs for the QSO and galaxy correlation functions respectively.

For a population of objects with a correlation function $\xi(r)$, Peebles (1981) has shown that, at scales less than r, the fractional number of pairs, $\delta N/n$, expected in excess of that for a uniform (Poisson) distribution is given by:

$$\delta N/N = 3/r^3 \int_0^r \xi(r')r'^2\,dr' \qquad \ldots (5.14)$$

At scales $<10h^{-1}$Mpc, the number of galaxy pairs thus predicted for the correlation function given by (5.13) can be compared in table 5.2 to the number of QSO pairs actually observed. From this we see that, in a closed universe at least, QSOs are more strongly clustered than galaxies at the 2.7σ level. Moreover we note that the average value for the galaxy correlation function at these scales (also given in table 5.2) is well below that observed for QSOs. These conclusions are

		Observed			Predicted					
					Galaxy		Cluster			
							No Stable Regime		Stable at $r < 10h^{-1}$ Mpc	
Model	Scale	N_{qr}	N_{qq}	ξ_{obs}	N_{gg}	ξ_{gal}	N_{cc}	ξ_{clus}	N_{cc}	ξ_{clus}
$q_0 = .5$	$<10h^{-1}$ Mpc	4.6	11	1.39	4.9	0.06	83.3	17.1	22.8	3.96
$q_0 = .1$	$<15.8h^{-1}$ Mpc	7.8	16	1.05	9.2	0.18	-	-	-	-

Table 5.2 Correlation Function Comparison

relatively independent of the break scale chosen. Even with the break in the galaxy $\xi(r)$ at $10h^{-1}$Mpc (see Peebles 1980 and references therein), only 5.2 QSO pairs would be expected in our survey on the hypothesis that QSOs cluster like galaxies, still a 2.5σ discrepancy from the observed value.

ii) Open, $q_0 = 0.1$

In an open universe, growth of the initial perturbations from decoupling stops by a redshift of $z = 1/(2q_0 - 1)$, which, for a $q_0 = 0.1$ universe, will occur at a redshift of 4. Thus the non-linear regimes which we observe today will have been 'frozen in' at the same proper diameters since that epoch. In comoving coordinates this will result in the size of the break between non-linear and linear regimes increasing with redshift as $(1+z)$. It is, however, difficult to see how such a large break scale ($12.5h^{-1}$Mpc comoving) could arise at $z = 1.5$ in the standard gravitational instability model dicussed here. Indeed, the break scale length currently observed in the galaxy correlation function has been used as an argument against a low q_0 universe (Peebles 1980). The following treatment must therefore be viewed as purely empirical, with the predictions providing a useful upper limit on the number of QSO pairs expected at small separations in an open universe.

In proper coordinates, the density in the non-linear regions will stay constant with redshift while the background density will increase as $(1+z)^3$. The amplitude of $\xi(r)$ in comoving coordinates will therefore decrease as $(1+z)^{1.2}$ and the galaxy

correlation function at z = 1.5 will be given by:

$$\xi(r) = 9(rh)^{-1.8} \quad r < 12.5h^{-1}\,\mathrm{Mpc}. \quad \ldots (5.15a)$$

$$\xi(r) = 180(rh)^{-3} \quad r > 12.5h^{-1}\,\mathrm{Mpc}. \quad \ldots (5.15b)$$

As distances are $\simeq$ 50% larger in a $q_0 = 0.1$ universe compared to those in an Einstein-de Sitter universe, we choose to compare the predicted number of QSO pairs from equation (5.15) with those observed in the first four bins plotted for $\xi(r)$ in figure 5.4, corresponding to scales $< 15.8h^{-1}$Mpc. At these scales we once again find moderately significant (2.2σ) evidence that QSOs are clustered more strongly than galaxies, with the average value for the galaxy $\xi(r)$ being well below that observed for QSOs.

We note that Shaver (1984) has also calculated $\xi(r)$ for those QSOs with accurate spectroscopic redshifts in the Veron-Cetty and Veron (1984) catalogue. While the correlation function presented there is extremely noisy, it appears (from inspection of Shaver's figure 2) to be in qualitative agreement to that found here. Although Shaver (1984) concludes that the amplitude of the QSO $\xi(r)$ is indeed consistent with the present day galaxy correlation function it appears that he has not taken into consideration the dynamical evolution of the galaxy correlation function discussed here.

We can also compare the amplitude of the QSO $\xi(r)$ to that obtained from the Abell cluster correlation function (Bachall and Soniera 1983):

$$\xi(r) = 360(rh)^{-1.8} \quad \ldots (5.16)$$

Unfortunately, both the form of this correlation function and its evolution are subject to strong uncertainties. In particular, the nature of the evolution is critically dependent on which scales we may consider to be 'stable' at the present epoch. We therefore attempt to predict the form of the cluster correlation function at $z = 1.5$ for the closed model only, merely as an illustration of the approximate numbers we may expect to see were QSOs to cluster like Abell clusters of galaxies. Any conclusions drawn from this analysis will therefore be extremely tentative.

We consider two cases for the evolution of the cluster correlation function in a closed universe. Firstly, all scales are assumed to be still expanding with the universe (i.e. in the linear regime). $\xi(r)$ will therefore retain the same form at $z = 1.5$ as it does at the present day. The numbers of pairs and the average value for $\xi(r)$ predicted from such a model are, however, much larger than the numbers of QSOs observed (see table 5.2) and it appears that we can rule out this model at a high level of significance. A more realistic approach, however, will be to assume that clusters have begun non-linear collapse below at least some small scale. Guided by the shape of the galaxy correlation function it would appear that a choice of $10h^{-1}$ Mpc for this scale would not be unreasonable. The correlation function will then evolve in the same manner as the galaxy correlation function in the $q_0 = \frac{1}{2}$ universe detailed above. The cluster correlation function at $z = 1.5$ will therefore be given by:

$$\xi(r) = 120(rh)^{-1.8} \quad r < 5.4h^{-1}\text{Mpc} \quad \ldots (5.17a)$$

$$\xi(r) = 910(rh)^{-3} \quad r > 5.4h^{-1}\text{Mpc} \quad \ldots (5.17b)$$

From table 5.2 we see that a much reduced number of pairs is now expected, although there is still a 2.5σ discrepancy with the observed number of pairs. This illustrates well the strong model dependence on the form of the cluster $\xi(r)$ at $z = 1.5$.

From the amplitude of the QSO correlation function at scales $< 10h^{-1}$Mpc we tentatively conclude that QSOs are more strongly clustered than galaxies. While uncertainties still exist over the precise form and evolution for the Abell cluster correlation function, we also conclude, albeit even more tentatively, that QSOs do not cluster as strongly as rich clusters. Further observations will be necessary before these conclusions can be based on a firmer footing. It is interesting to note that Yee and Green (1984), from direct imaging of low redshift QSOs, find QSOs preferentially associated with small clusters or groups of galaxies and not in the field or in large, Abell-type clusters. The amplitude of our QSO correlation function may then be providing us with information on the environment of QSOs, in turn indicating the scale (i.e 'local' galaxy or 'external' cluster) of the effects necessary to initiate the QSO phenomenon. We discuss this more fully in chapter 8.

b) $10h^{-1} < r < 50h^{-1}$ Mpc

In contrast to the relatively high amplitude of the QSO correlation function observed at small scales above, $\xi(r)$ for QSOs in the range $10h^{-1} < r < 50h^{-1}$ Mpc is close to zero. However, within this range considerable structure may exist in the correlation function.

Comparison between the number of QSO pairs observed at these separations and the numbers predicted from the cluster correlation function yields no additional information on the similarity or otherwise of the QSO $\xi(r)$ to the cluster $\xi(r)$. For example 136 pairs would be expected in our survey at separations $< 50h^{-1}$ Mpc on the assumption that QSOs clustered like Abell clusters (with an assumed break at $10h^{-1}$ Mpc) whereas 116 were observed, a discrepancy of only 1.6σ.

We do note however that we find no evidence for strong clustering on the scales at which we observed the apparent QSO 'clusters' commented on in chapter 5.2. In particular, of the group of 4 QSOs on the QNY2 field discussed there, only 2 (QNY1:20 and QNY1:25) are observed at separations ($r = 8h^{-1}$ Mpc) where we find a significantly positive value for the QSO $\xi(r)$. The separations between the other members of this 'group' are 30 - $40h^{-1}$ Mpc, where no strong clustering is observed in the QSO $\xi(r)$. Many such QSO clusters, which appear remarkable on first inspection, may therefore be simply chance associations.

Although the average value of $\xi(r)$ at these scales may be close to zero, we can not rule out the fact that there could be significant structure over small ranges in separation within this region. In particular, we note that the QSO $\xi(r)$ may exhibit (although at present seen at low signal-to-noise) a characteristic 'trough-peak-trough-peak' relationship over this range. Such recurrent behaviour in the amplitude for the correlation function is most naturally predicted for baryon dominated universes (Peebles 1981) and not for universes dominated by weakly interacting particles (Peebles 1982). This is because, unlike the particle case where all fluctuations up to the Jeans mass scale are damped prior to the epoch when the relevant particles decouple form the photons, in baryon dominated universes damping only occurs for perturbations smaller than the Silk mass scale. Between this and the Jeans mass scale perturbations oscillate acoustically until the baryons decouple from the radiation, giving rise to 'peaks' in $\xi(r)$ at scales determined by the cosmological model.

It is interesting to note that such peaks are also observed in the galaxy correlation function of Shanks (1986) at scales of $28h^{-1}$ Mpc and $56h^{-1}$ Mpc. Any feature observed at these scales will still be taking part in the general expansion of the universe, and so its comoving scale length will remain unchanged with cosmic epoch. Thus the identification of such peaks in the QSO $\xi(r)$ would not only suggest a baryon dominated model, but also provide a powerful q_0 test as the difference between QSO separations calculated in open ($q_0 = 0.1$) and closed ($q_0 = 0.5$)

models amounts to some 50% at $z = 1.5$. If confirmed, the appearance of the 'peaks' at $\simeq 30h^{-1}$ Mpc and $55h^{-1}$ Mpc in the QSO $\xi(r)$ for a $q_0 = \frac{1}{2}$ universe (i.e. at the sames scales as in the galaxy $\xi(r)$) would therefore indicate a closed universe. However many uncertainties still exist. In particular, biasing (Kaiser 1984) would almost certainly be required to enable these 'peaks', observed to have $\xi(r) \simeq 0.1$ in the galaxy correlation function, to be observable in the QSO $\xi(r)$. Further comment is therefore postponed until increased signal-to-noise is available on the estimates of the QSO $\xi(r)$ at these scales.

c) $r > 50h^{-1}$ Mpc

At these scales $\xi(r)$ is compatible with a Poisson process, providing strong evidence for the homogeneity of the Universe at high redshifts. This confirms the more tentative results of Osmer (1981) and Webster (1982a) who also found no significant clustering of QSOs at these large separations. It is interesting to note that we find no evidence for clustering at scales $\simeq 100h^{-1}$ Mpc and, as such, groups of QSOs seen at these scales (e.g. Oort *et al.* 1981, Webster 1982a) are unlikely to be representative of the clustering properties of the QSO population as a whole. We note in passing that the zero amplitude for the QSO $\xi(r)$ at these scales is consistent with the homogeneity of the QSO n(m) counts observed over our survey fields in chapter 4.2.

The homogeneity discussed above is only strictly valid to within the noise level on our estimates for $\xi(r)$ at these large scales. Futher observations will be necessary to set stronger constraints on the homogeneity of the universe, and, as such, may reveal features in the correlation function at small amplitude corresponding to large scale fluctuations in the early universe e.g. Jeans scale (see Peebles 1980).

5.5 Conclusions

We have seen how the QSO correlation function can be used as a powerful probe of the structure of the universe at large redshifts. Convincing evidence has been found for the homogeneity of the universe at scales greater than $50h^{-1}$Mpc. Although as yet based on a relatively small number of QSO pairs, we also conclude that, at small scales ($r < 10h^{-1}$Mpc), QSOs appear to cluster more strongly than galaxies and less strongly than rich clusters but, especially in the case of clusters, any conclusions drawn are also strongly dependent on the cosmological model adopted and evolution assumed for the correlation functions. Further observations are therefore required to increase the numbers of surveyed QSOs suitable for clustering analysis. Such an increase would help to drive the noise down on the estimates of $\xi(r)$ at all scales, thus achieving better discrimination between the predictions of the galaxy and cluster correlation functions at small scales, and obtaining verification for other low S/N features in the QSO correlation function. Moreover, it would also enable calculation of the QSO $\xi(r)$ at

discrete redshift intervals between $0 < z < 2.2$, thereby affording an explicit demonstration of the evolution of the QSO correlation function.

CHAPTER SIX

TWO DIMENSIONAL ANALYSIS OF QSO CATALOGUES

6.1 Introduction

In the previous chapters we have used only a small fraction of the UVX sample (i.e. that part for which we have spectroscopic information) to study the clustering and evolution of QSOs. However, the spectroscopic surveys confirmed that the UVX sample does indeed contain a large fraction of QSOs and, in applications where redshift information is not essential, the large UVX samples can be used to provide a statistically powerful basis from which to investigate many important features of the QSO population.

One such application is the objective assessment of the significance of associations seen between high redshift QSOs and low redshift galaxies. Such observations have fuelled speculation about a non-cosmological interpretation for the QSO redshift (see chapter 1). As exemplified by Nieto and Seldner (1982), the success of any statistical approach is dependent on the unbiased nature of the QSO and galaxy catalogues employed. As such, our large, machine measured UVX catalogues are ideally suited to this task.

In this chapter, therefore, we apply standard statistical techniques to the UVX samples and galaxy catalogues obtained from COSMOS machine measurements in order to investigate the clustering properties of UVX objects amongst themselves, and with

respect to galaxies. For comparison, the clustering properties of catalogues of emission line objects are also analysed. Initial results from these clustering studies have previously been reported in Shanks *et al.* (1983c) and Boyle *et al.* (1983,1984).

6.2 Statistical techniques

6.2.1 The 2-point Cross-correlation Function

Following Seldner and Peebles (1979), we use the 2-point cross-correlation function to investigate QSO/galaxy associations. As pointed out by Seldner and Peebles (1979), the method has the advantage that statistical tests of such associations are possible even with incomplete QSO samples. The 2-point cross-correlation function is obtained from suitable galaxy and QSO catalogues by firstly centring on catalogued QSOs and making counts of galaxies in annuli (radius θ, width $\Delta\theta$) around each one in turn ($N_g(\theta)$). Secondly, the total number of galaxies expected on the basis of a Poisson model in each annulus is computed ($N_r(\theta)$), using a random catalogue (containing typically 10 times as many points as the galaxy catalogue) normalised to the average density of galaxies used in the correlation analysis. Because the random catalogue is 'laid down' over precisely the same area over which the galaxies were selected, any 'holes' (see chapter 2.4.1) in the galaxy catalogue are naturally taken into account. The 2-point cross-correlation function, $w_{qg}(\theta)$, is then defined by

$$w_{qg}(\theta) = N_g(\theta)/N_r(\theta) - 1 \qquad \ldots (6.1)$$

The normalising constant, -1, ensures that $w_{qg}(\theta)$ is zero on the Poisson hypothesis, positive if QSOs cluster around galaxies and negative is there is an avoidance of galaxies by QSOs.

Since $w_{qg}(\theta)$ depends only on the number of QSO-galaxy pairs, ideally $w_{qg}(\theta)$ should be the same whether we centre on QSOs and count galaxies or vice versa. However, since the construction of the UVX catalogue involves the measurement of 2 plates, rather than the single plate measurement required for the galaxy catalogue, any gradients on the plates used to compile the catalogues are twice as likely to be introduced into the UVX sample as into the galaxy sample. In addition, the subjective selection of emission line objects may also introduce gradients into the catalogues produced from visual inspection of objective prism plates. We therefore choose the objects in the UVX or emission line catalogues as centres, since any gradients in the population of objects chosen as centres will not affect the cross-correlation result (Seldner and Peebles 1979), as long as the distribution of objects to be counted around these centres (i.e. galaxies) is uniform. However, subsequent study of the UVX objects in the 'restricted' (see chapter 4.2.1) samples has revealed no strong gradients in their distribution across any of the fields used in the cross-correlation analysis, see e.g. figure 6.1. Indeed, the only UVX field (QNA) that did exhibit any non-uniformity was rejected from inclusion in this study (see chapter 2.4.2 and figure 6.1). As such we could afford to replace UVX objects with cluster galaxies as centres when the latter were used in the cross-correlation analysis, since, by

their very nature, cluster galaxies will exhibit strong non-uniformities over the plate.

6.2.2 The 2-point Auto-correlation Function

To analyse the clustering of QSOs amongst themselves we employ the 2-point auto-correlation function, $w_{qq}(\theta)$. An estimator for this function can be defined as follows (Shanks 1979):

$$w_{qq}(\theta) = N_p(\theta)/N_r(\theta) - 1 \qquad \ldots (6.2)$$

where $N_p(\theta)$ is the total number of QSOs found in half annulus bins of width $\Delta\theta$, distance θ away from each other QSO in the sample and $N_r(\theta)$ is the number of objects found in these bins from a random distribution of objects. Approximately 10-20 times as many random points as QSOs were chosen to estimate w_{qq}, $N_r(\theta)$ being normalised using the respective number of objects in each catalogue. This correlation function is extremely sensitive to small gradients in the data set used (Shanks 1979).

6.3 Data

6.3.1 The Combined Data Set

Table 6.1 lists all fields used in the clustering analysis together with the catalogues available on each field. UVX and galaxy catalogues were obtained from a total of 7 of these fields on which UK Schmidt U and J plate pairs have been measured by COSMOS. Five of these fields were covered in the faint spectroscopic survey - the additional survey field (QNA) was

Field	UVX Sample	Emission Line Catalogue
SGP	YES	Clowes and Savage (1983)
QSN	NO	Savage *et al.* (1984)
QSC	NO	Chen (1984)
QSD	YES	Savage and Bolton (1979)
QSF	YES	-
QNB	YES	-
QNY	YES	-
QSM	YES	Savage and Bolton (1979)
QSI	YES	-

Table 6.1 QSO samples used on fields in 2D correlation analysis

Name	b	u-b*	z
0154-512U	17.66	-0.47	1.660
0155-495	18.68	-0.26	1.298
0155-501U	19.01	-1.19	1.978
PKS0203-520	17.57	-1.14	1.42
0203-497U	17.59	-0.71	1.42
PKS0208-512	17.12	-0.51	1.001
0213-484	17.99	-0.34	0.169

Table 6.2 Spectroscopically Confirmed QSOs on QSD field

excluded because gradients in the U plate on this field (chapter 2.4.2) gave rise to large variations in the UVX surface density over the matched U and J plate area (see figure 6.1).

J plates alone on a further two fields (QSN and QSC) were used to provide the positions of faint galaxies, with which catalogues of emission line objects already available on the fields could be cross-correlated. Emission line catalogues also existed on three of the UVX fields (SGP,QSM and QSD) on which a similar analysis could be carried out.

6.3.2 The UVX Sample

Whilst machine based UVX samples are unbiased, they suffer from the disadvantage that, without spectroscopic observations, the amount of contamination by Galactic stars and even galaxies is unknown. Since Galactic stars are distributed randomly amongst themselves (Shanks 1979) and with respect to galaxies, contamination of the UVX sample by Galactic stars will only serve to reduce any non-Poissonian result seen for the UVX/UVX or UVX/galaxy associations. More importantly, however, contamination of the UVX sample by galaxies will greatly affect any clustering results as normal galaxies are not only strongly clustered amongst themselves but also many compact blue galaxies (which can form a considerable fraction of the UVX sample, see chapter 3.6) may exhibit a marked anti-correlation with respect to clusters of galaxies (Fairall 1976). It is therefore vital to ensure that the contamination by objects other than QSOs (especially galaxies) in the UVX sample is kept to a minimum.

Fortunately, in this case, the fact that many of our UVX fields intended for use in the clustering analysis have already been observed spectroscopically allows us to do just that.

The contamination of the UVX sample by Galactic stars on 5 out of the 7 fields (SGP,QSF,QNB,QNY and QSM) can immediately be reduced by using, as a UVX criterion, the 'restricted' u-b limits derived in chapter 4.2.1 on these fields. These limits were chosen to cut the contamination by Galactic stars in the UVX survey from 55% down to 25%. Most of the remaining contaminating stars are white dwarfs and early type stars with u-b colours approximately equal to the mean QSO u-b colour. Thus further reduction of the stellar contamination would require UVX limits so blue that a great many QSOs (≃50%) would also be lost from the UVX sample. As it stands, the restricted UVX criteria defined on these five fields selects 85% of all the UVX QSOs (see table 4.2). Knowledge of the precise level of contamination by Galactic stars further allows us to make direct quantative comparisons between the results obtained for the UVX sample and those obtained for the emission line catalogues, whose contamination is also known (see chapter 6.3.4).

The other two UVX fields (QSI and QSD), were not included in the spectroscopic survey and so we do not know directly the level of contamination of UVX samples on these fields. The UVX criterion on the QSD field was therefore chosen to give a similar surface density of UVX objects at b=20.0 mag to that found on the five survey fields. Although B photometry on the QSD field was not available to as faint magnitudes as on the survey fields (see

chapter 2.4.4), we can confirm (see table 6.2) that the UVX sample defined for the correlation analysis on this field contains all the spectroscopically confirmed low redshift ($z < 2.2$) QSOs (Savage *et al.* 1985) listed in the emission line catalogue of Savage and Bolton (1979). We do note, however, that a number of $z < 2.2$ objective prism QSO candidates (5 out of 26) in the Savage and Bolton (1979) catalogue have u-b colours significantly redder than our UVX limit on this field. Originally this was thought to be due to large errors in our colours on this field and so QSD was not included in our faint spectroscopic survey. However, de Ruiter (private communication) finds that, on obtaining slit spectra for these objects, they are either misidentified Galactic stars or high redshift ($z > 2.2$) QSOs.

As discussed in chapter 2.4.4 the calibration on the QSI field is poor. The UVX limit chosen here is dictated by the method chosen to calibrate the b magnitudes on this field. Finally, table 6.3 gives the u-b limits and surface densities for the UVX samples on all 7 fields.

In addition to removing most of the Galactic stars, the use of the more severe 'restricted' UVX criteria in this analysis also removes all but two (QSF1:33 and QNY2:39) of the compact, narrow emission line galaxies identified in the UVX spectroscopic survey down to a magnitude limit of b=20.75 mag. One of these galaxies (QNY2:39) has a u-b = -1.81 mag, a value so blue that we can set a lower limit for all the UVX samples of u-b > -1.75 mag, which will remove such objects whose u-b has arisen from

Field	Area (sq. deg.)	UVX limit	Surface Density (/square degree) b < 20.00	b < 20.75
SGP	11.33	< -0.5	13.2	31.1
QSD	18.29	< -0.15	11.1	21.1
QSF[1]	21.29	< -0.55	13.1	30.5
QNB[2]	25.40	< -0.25	11.5	25.4
QNY[1]	9.01	< -0.60	13.3	23.8
QSM	16.74	< -0.70	14.4	26.7
QSI	12.96	< -0.10	10.3	26.4

[1] UVX limits slighty different (0.05 mag) to the restricted limits defined in section 4.2.1.
[2] UVX limit employed on J9133S to give same surface density as restricted UVX limit on J7674 (see chapter 4.2).

Table 6.3 UVX Star Surface Densities

misclassification of the image on the J plate, without removing any QSOs from the UVX sample (the bluest QSO QNB2:01 has a u-b = -1.63 mag). The removal of the narrow emission line galaxies in this manner, by setting both a red and a blue limit for the UVX sample, will therefore ensure that any clustering seen between the UVX objects and the galaxy sample is not due to the contamination of the UVX sample by such compact galaxies.

From the complete UVX catalogue we defined two sub-samples. One sample (hereafter referred to simply as the UVX sample) contained all UVX stars with 18 mag < b < 20 mag, while a faint UVX sample contained all UVX stars with 18 mag < b < 20.75 mag. The bright magnitude limit of b = 18 mag was chosen because, while only one QSO was observed in the faint spectroscopic survey with b < 18 mag, a large number of stars were. The faint magnitude limit of b = 20.75 mag was decided upon to prevent contamination of the UVX sample by the significant number of UVX emission line galaxies observed beyond this magnitude limit (see chapter 3.3.6) which could not be removed by using the 'restricted' UVX limits described above.

Plots showing the XY distribution of the objects in the UVX and faint UVX samples on all fields are shown in figures 6.1 and 6.2. The extent of these plots represent the measured areas of the J plates on each field. The dashed lines signify the areas over which the clustering analysis took place. In most cases this area corresponds to the overlap between the U and J plates on the respective field, although in the case of the QSI field the clustering analysis took place over the smaller area, chosen

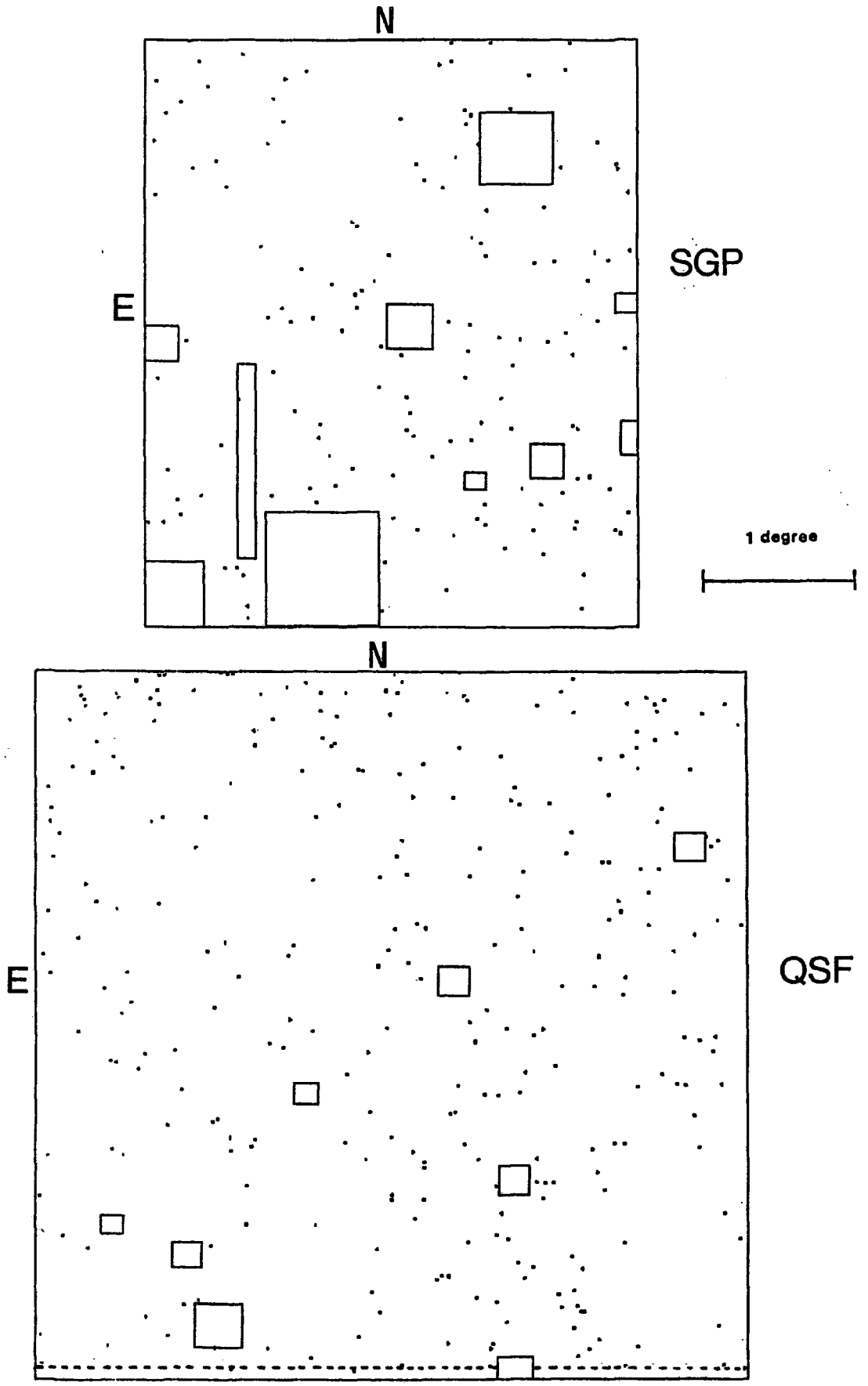

Figure 6.1 Distribution of UVX objects (18 mag < b < 20 mag) on all fields used in the correlation analysis. Dashed lines indicate the areas over which clustering analysis took place.

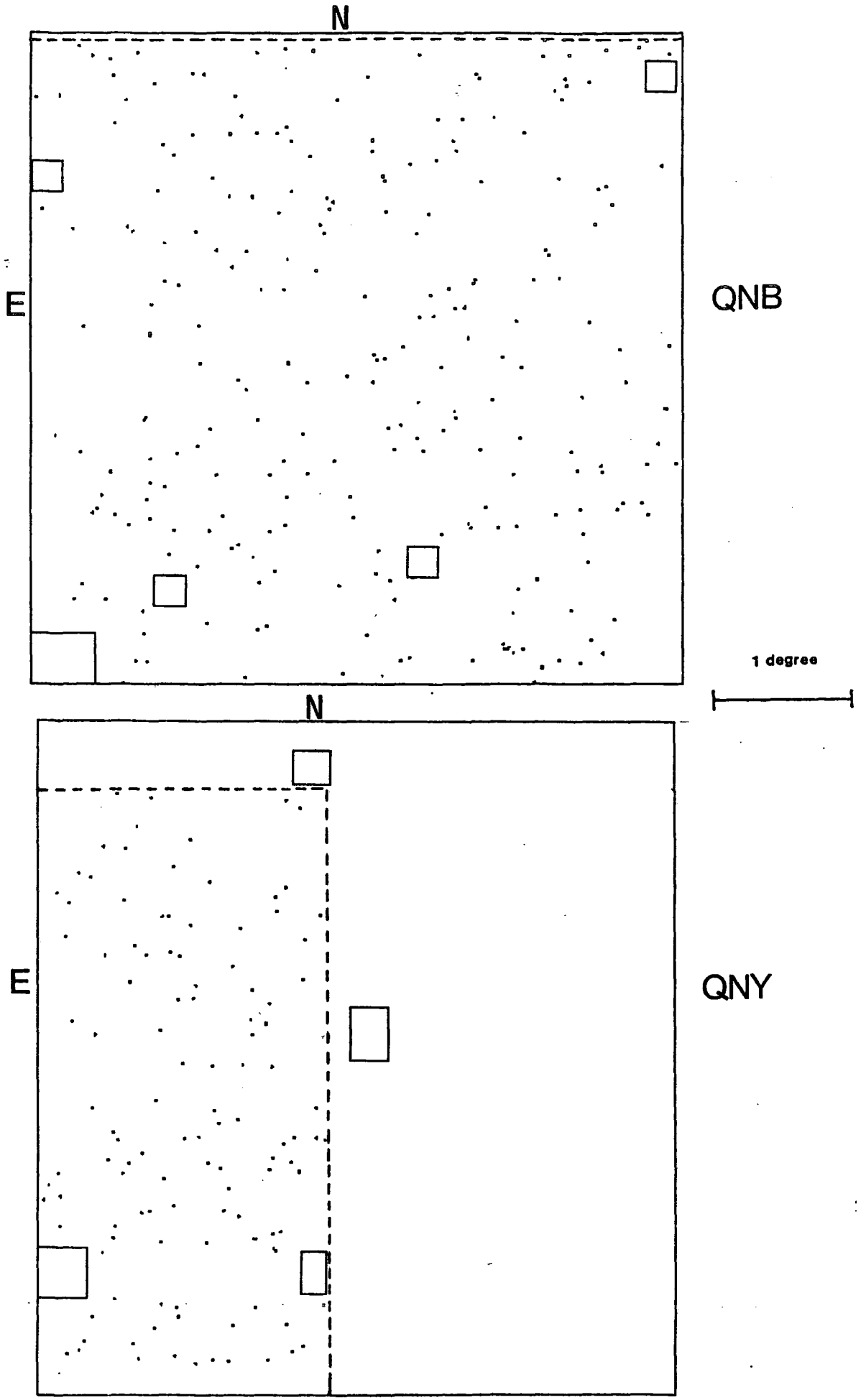

Figure 6.1 continued

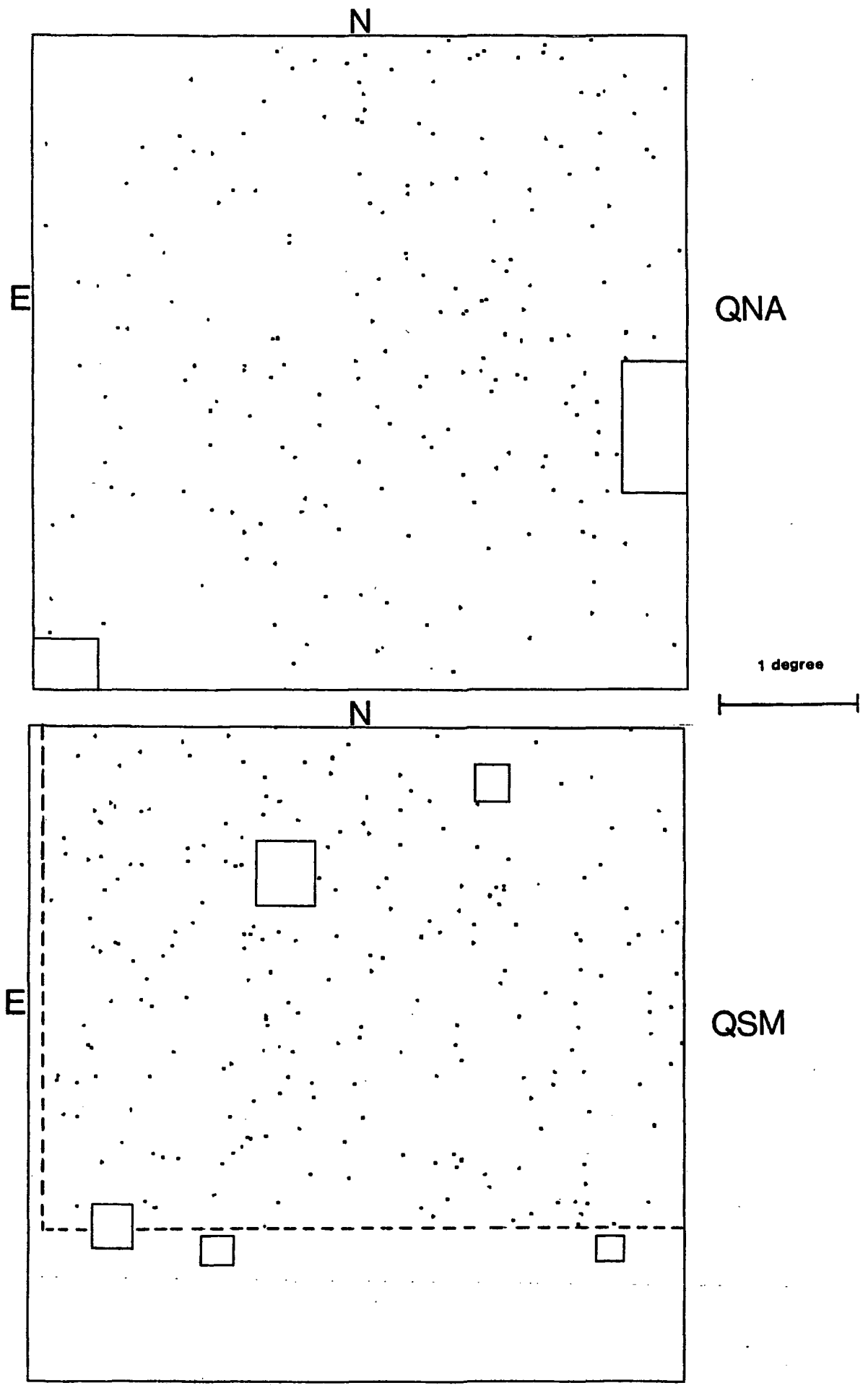

Figure 6.1 continued

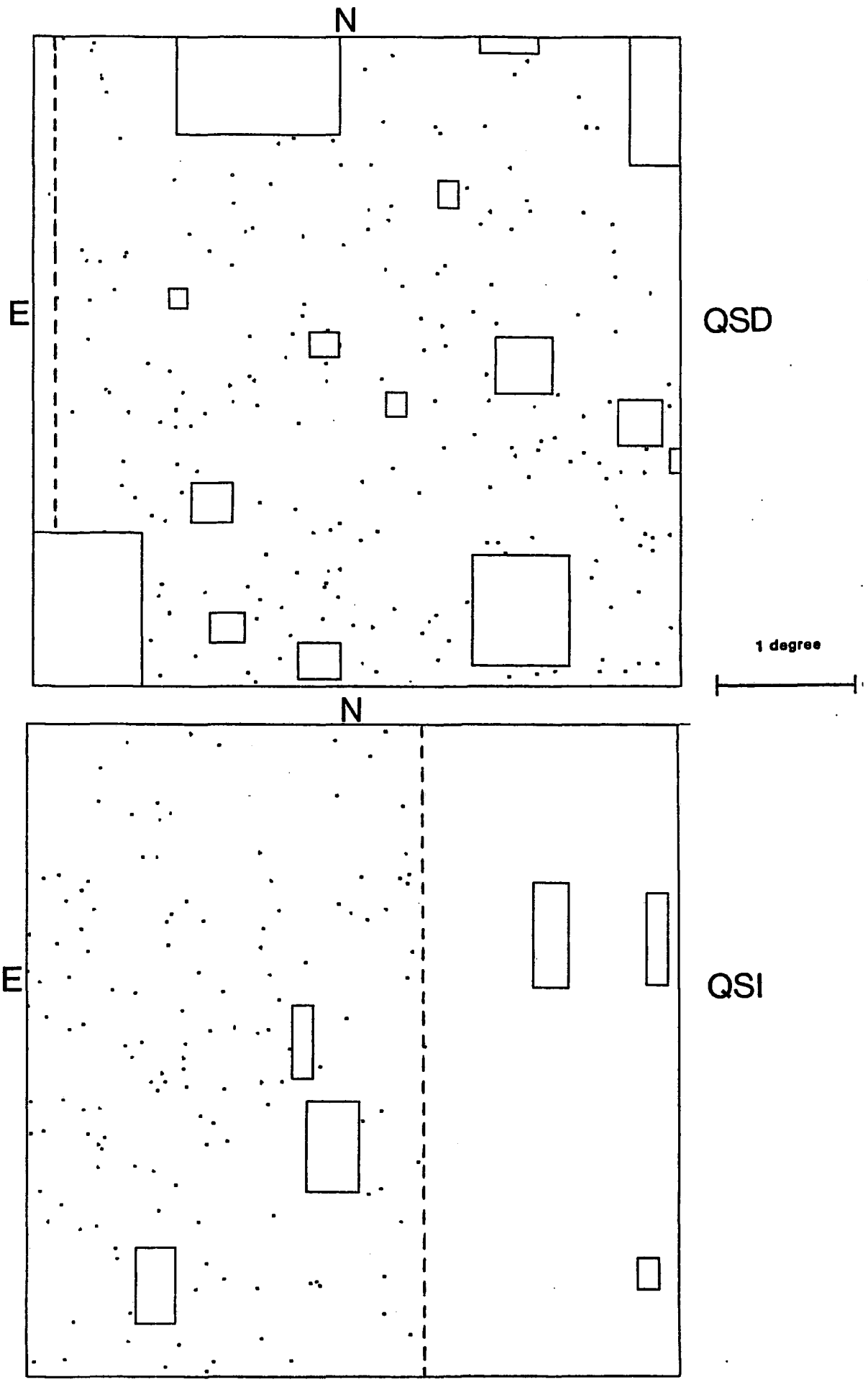

Figure 6.1 continued

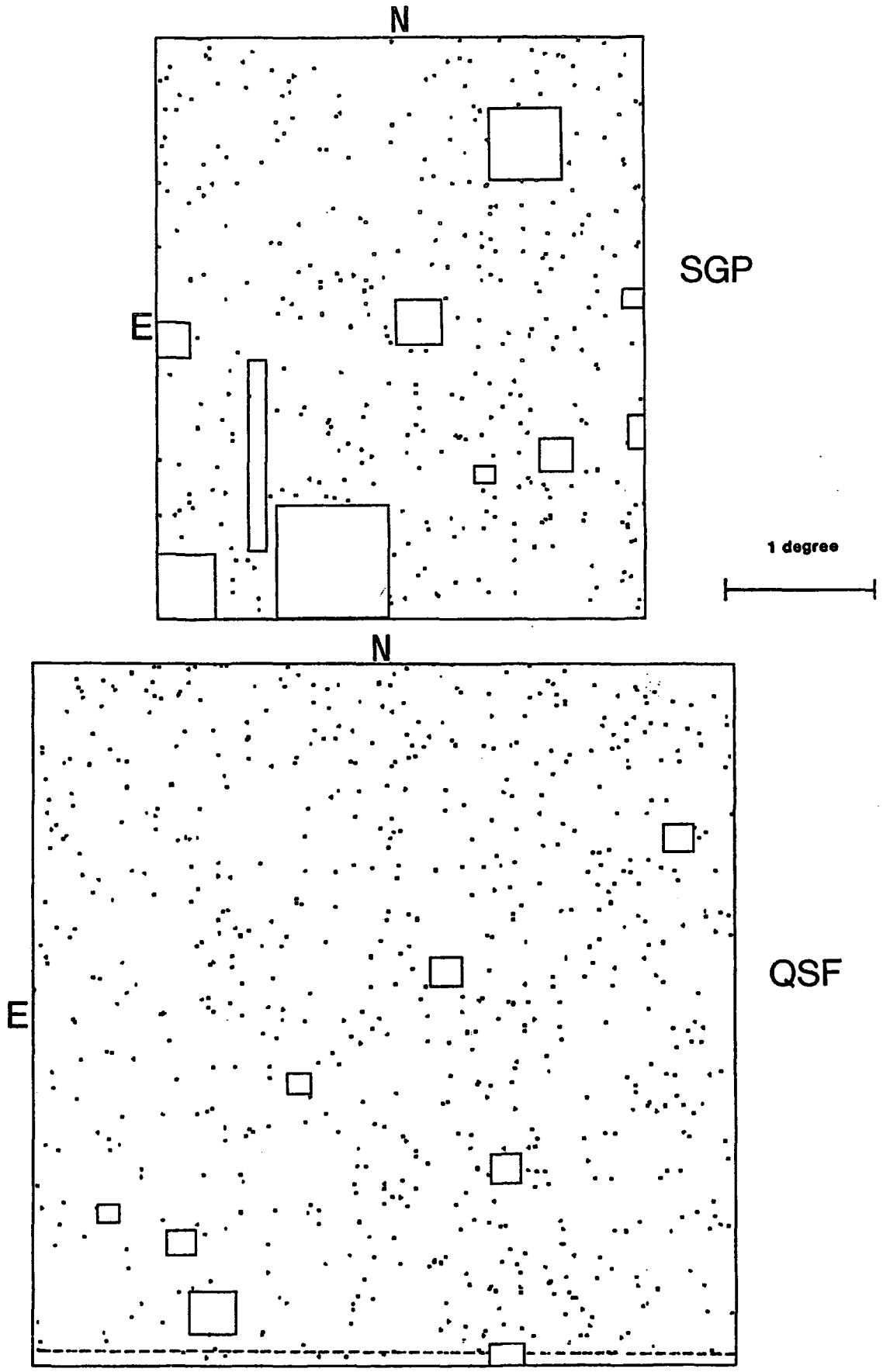

Figure 6.2 As figure 6.1 but for the faint (18 mag < b < 20.75 mag) UVX sample.

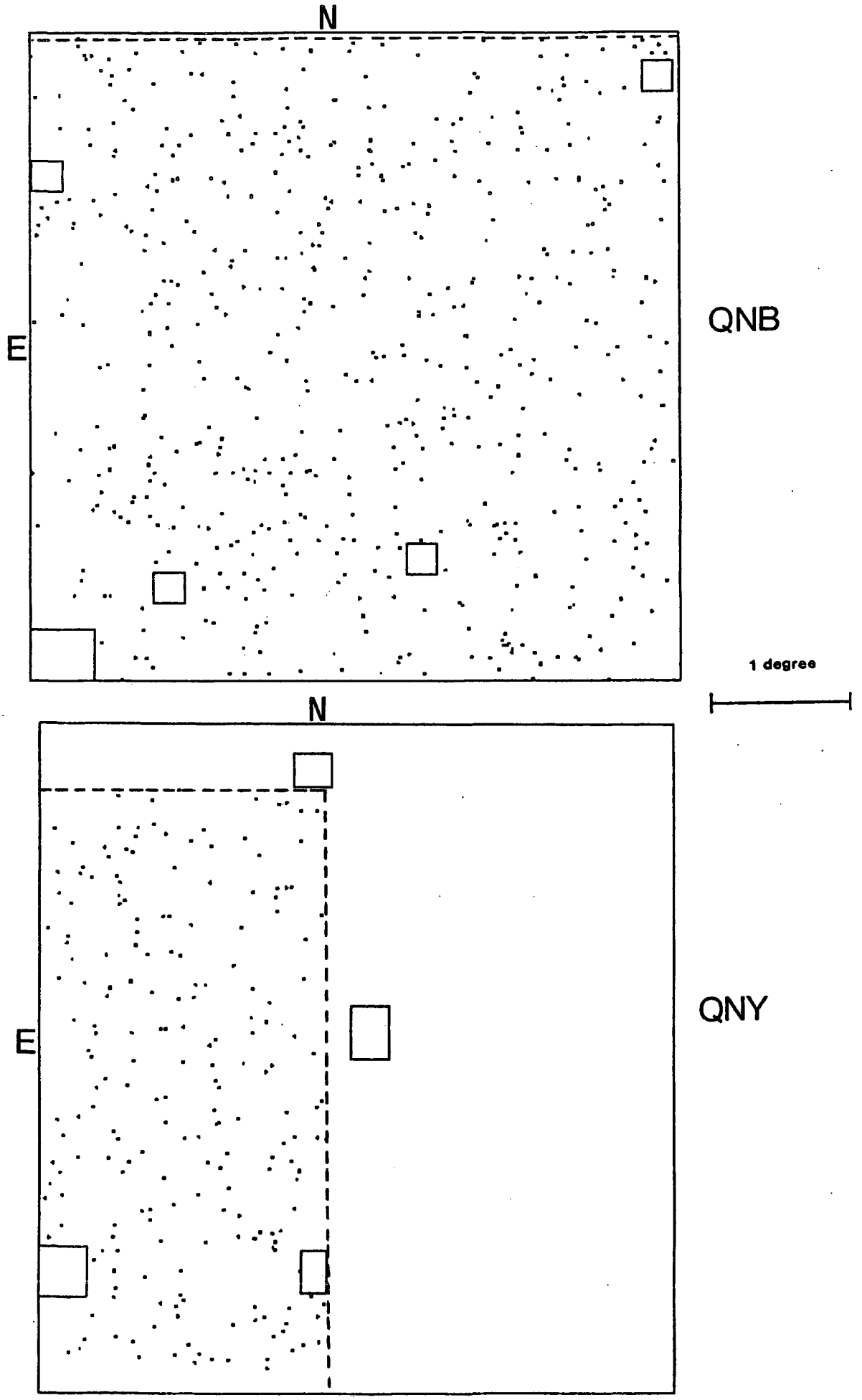

Figure 6.2 continued

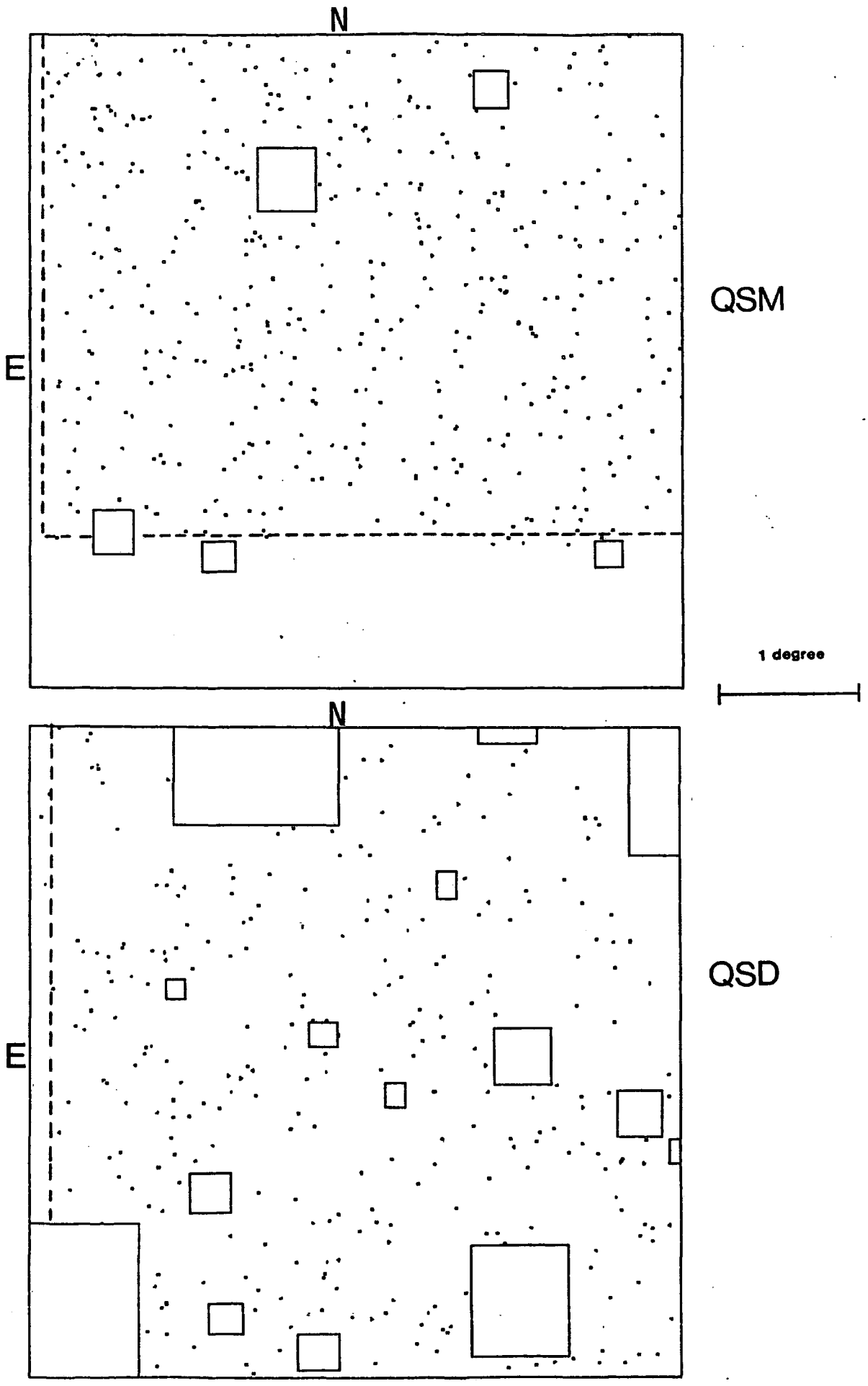

Figure 6.2 continued

to be free of the gradient detected on U7120 (see chapter 2.4.2) As also discussed in chapter 2.4.2, J7674 (the J plate used for the spectroscopic survey on the QNB field) exhibits gradients over ≃ one third of its measured area, cutting down the usable area on this plate. However, an additional J plate on the QNB field, J9133S, which became available after the spectroscopic survey had been made, exhibited no such gradients and was therefore included in the correlation analysis in place of J7674.

Figure 6.1 also displays the UVX sample at b < 20.0 mag on the QNA field. The large gradients across this field are clearly reflected in the anomalous distribution of UVX objects, demonstrating why this field was not considered in the clustering analysis.

6.3.3 The Galaxy Sample

The complete galaxy catalogue consists of all galaxies brighter than b_j = 20.0 mag over all fields listed in table 6.1. In addition we also selected a sub-sample of 'cluster' galaxies. This was done to establish the source of any clustering seen. The cluster galaxies were selected from the main galaxy catalogue using an algorithm written by Dr. P.R.F.Stevenson based on the multiplicity technique of Gott and Turner (1977). The application of this algorithm to COSMOS data is fully detailed in Stevenson (1985). Galaxies found in groups of 5 or more, where the density of galaxies within the group was greater than 8 times that of the average galaxy density over the whole plate, were taken to be cluster members. The magnitude limit of the cluster

galaxy sample was chosen to be b_J = 20.16 mag (see Stevenson 1985). With this technique 10% of galaxies were identified as belonging to clusters. Figure 6.3 displays the cluster galaxy sample over all seven fields.

6.3.4 The Emission Line Sample

The five catalogues of emission line objects used in this analysis are listed in table 6.1 above. All catalogues were obtained from visual searches of UK Schmidt objective prism plates. Full details of the compilation of these catalogues are given in the references listed. The RAs and Decs listed for the objects on these fields were transformed to the XY coordinate system in which the corresponding J plate was measured using the standard astrometric programs available on the SERC STARLINK VAX system at the University of Durham. The nearest stellar image (within a tolerance of 10 arcseconds) on the J plate was then identified as being the emission line object. This removed any emission line object identified as a galaxy, which may have biased the correlation analysis (see chapter 6.3.2), and those objects which lay in holes 'drilled' in the COSMOS data (see chapter 2.4.1). The distribution of the emission line objects thus included in the clustering analysis are shown in figure 6.4. On all but one field the clustering analysis was performed over the whole measured area of the J plate. The exception, the QSM field, is where the objective prism plate is centred 1 degree north of the J plate centre, and the area chosen for the clustering analysis is shown by dotted lines in figure 6.4.

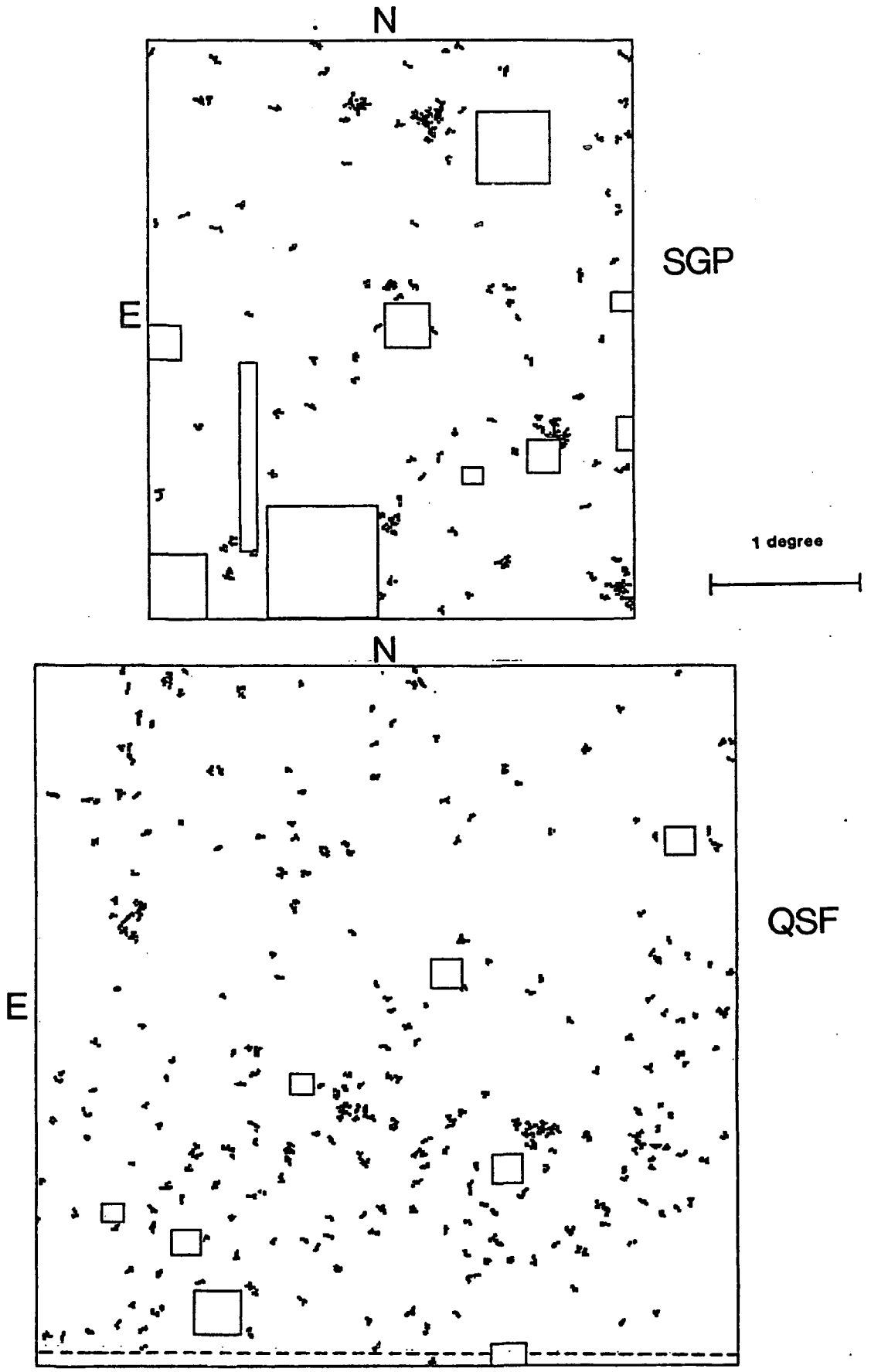

Figure 6.3 As figure 6.1 but for the cluster galaxy sample.

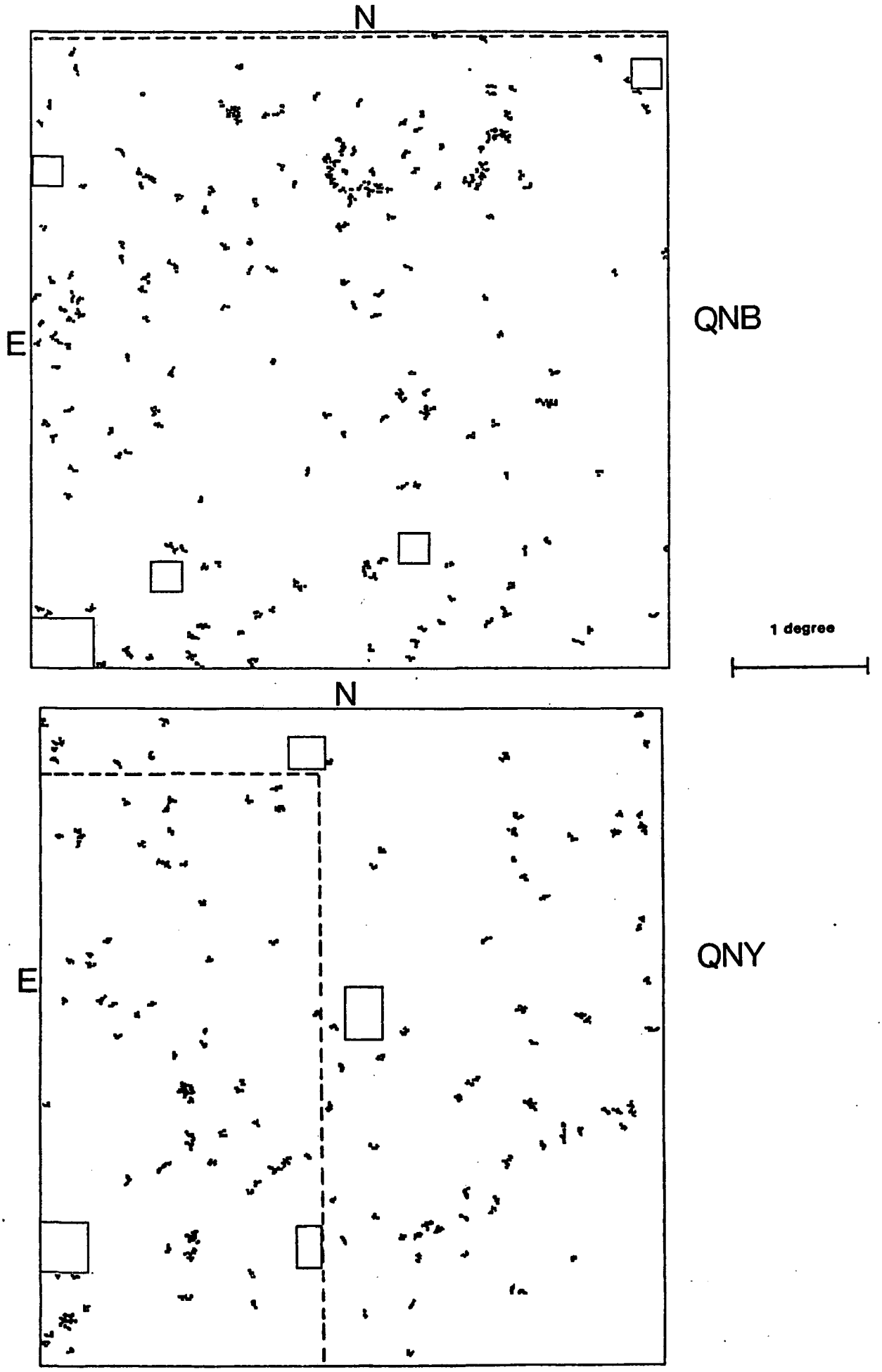

Figure 6.3 continued

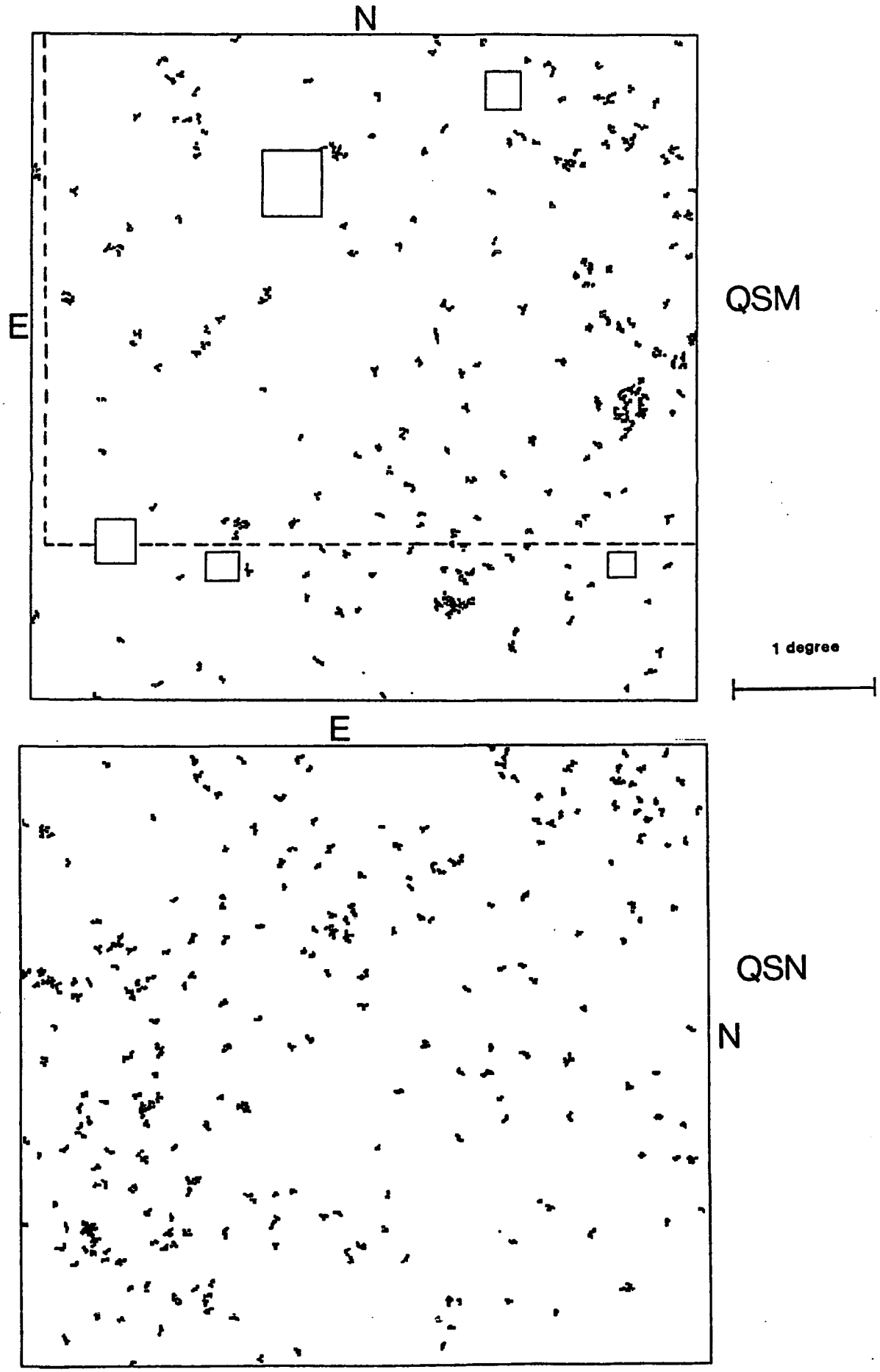

Figure 6.3 continued

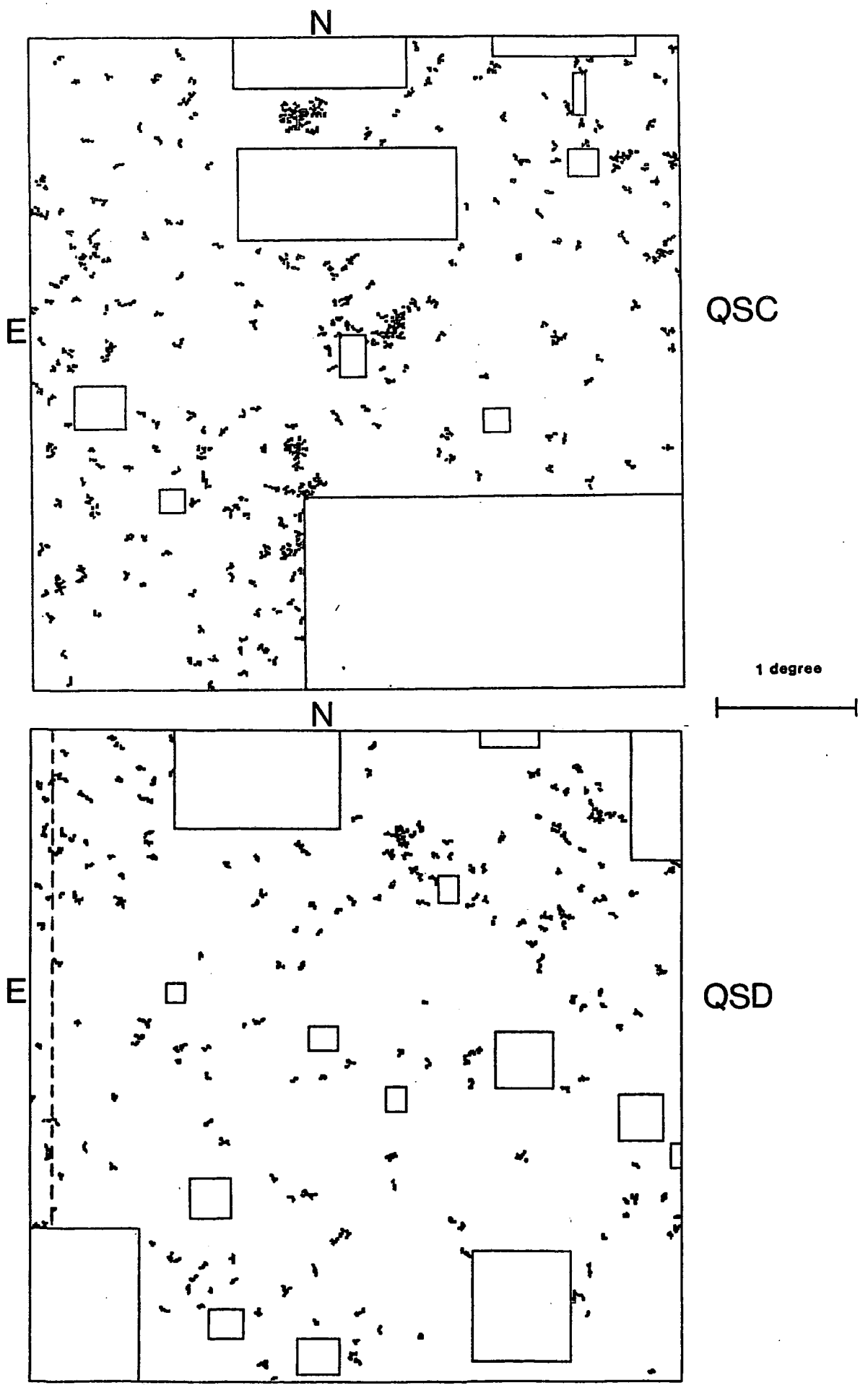

Figure 6.3 continued

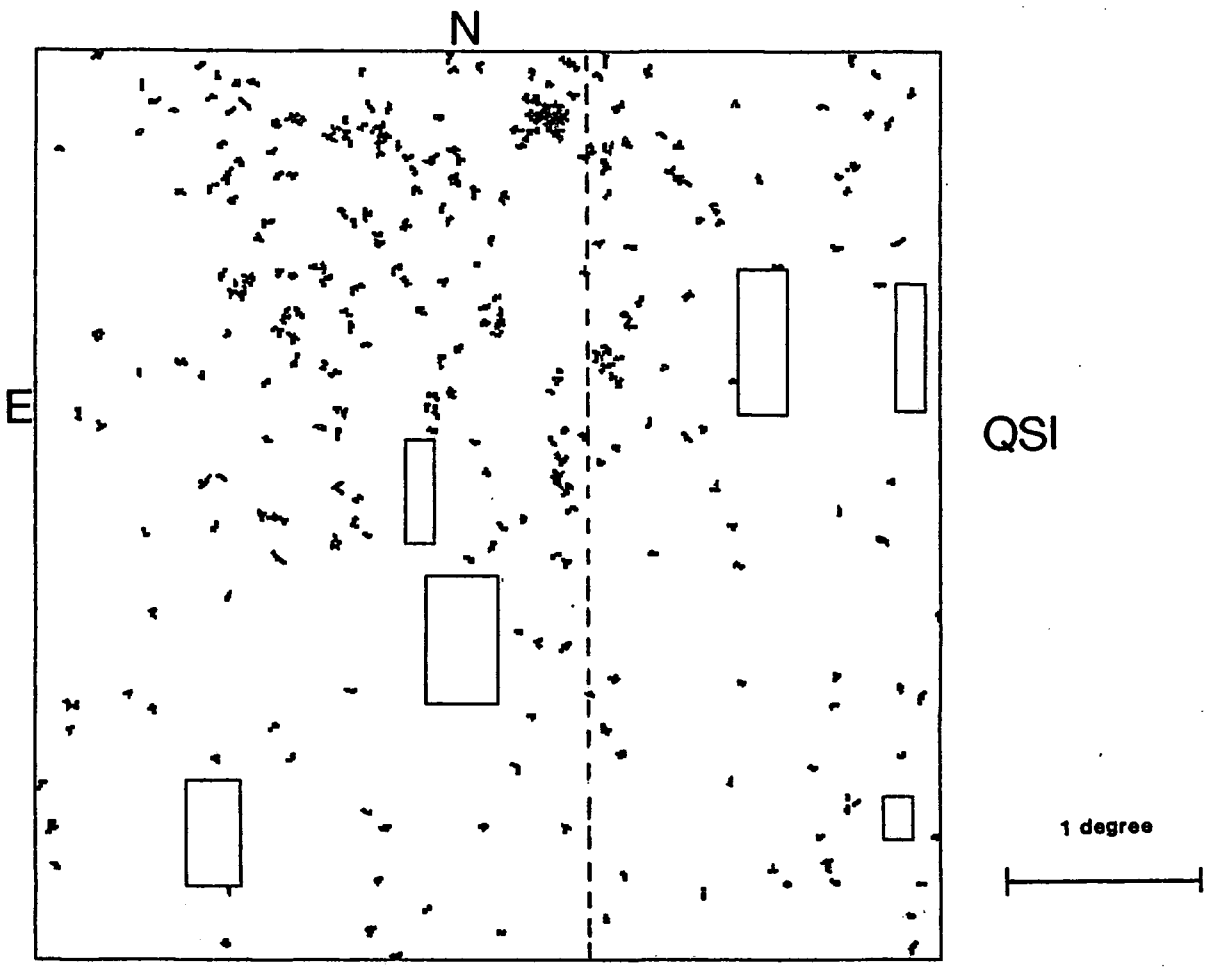

Figure 6.3 continued

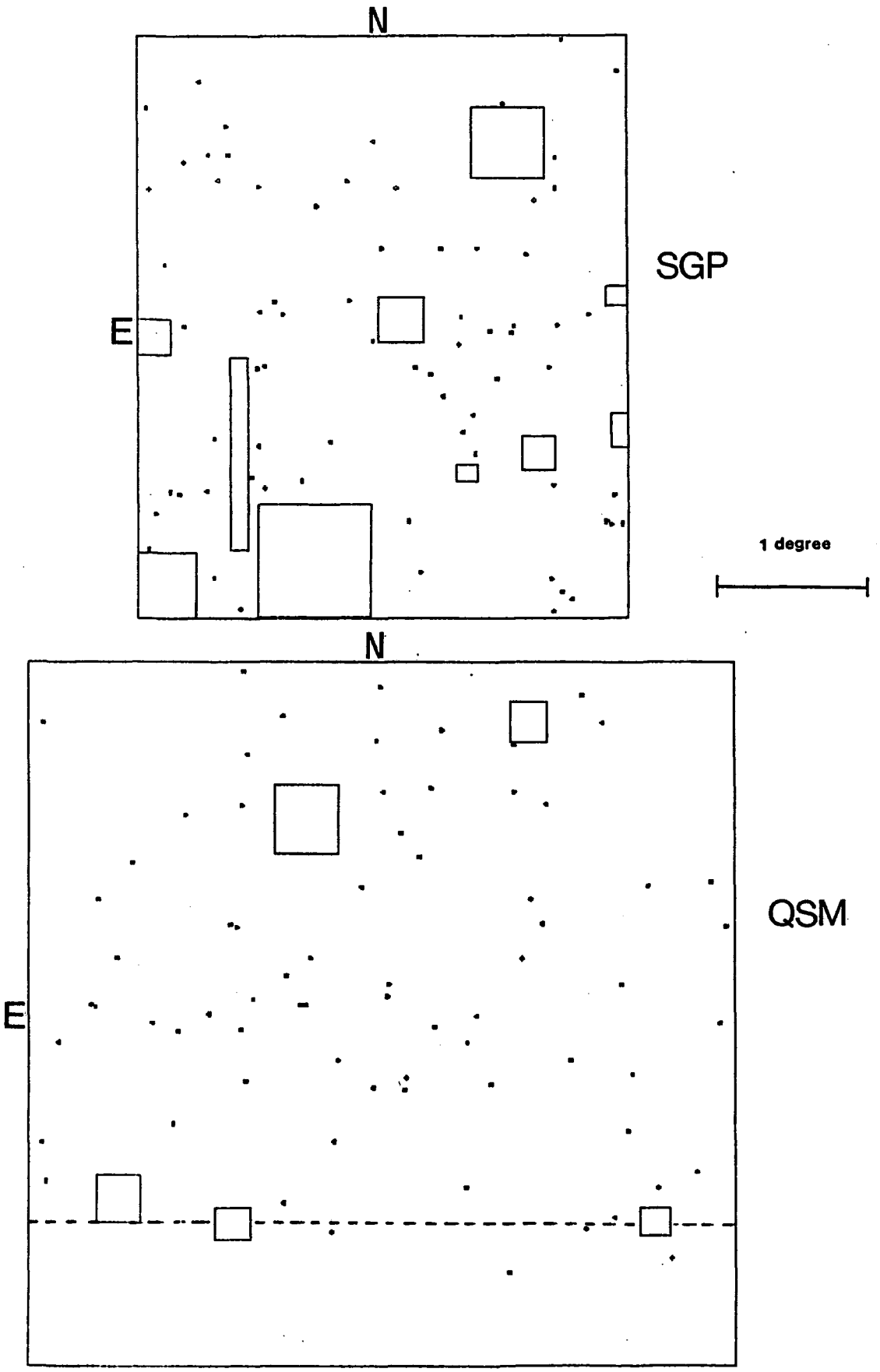

Figure 6.4 As figure 6.1 but for the emission line sample.

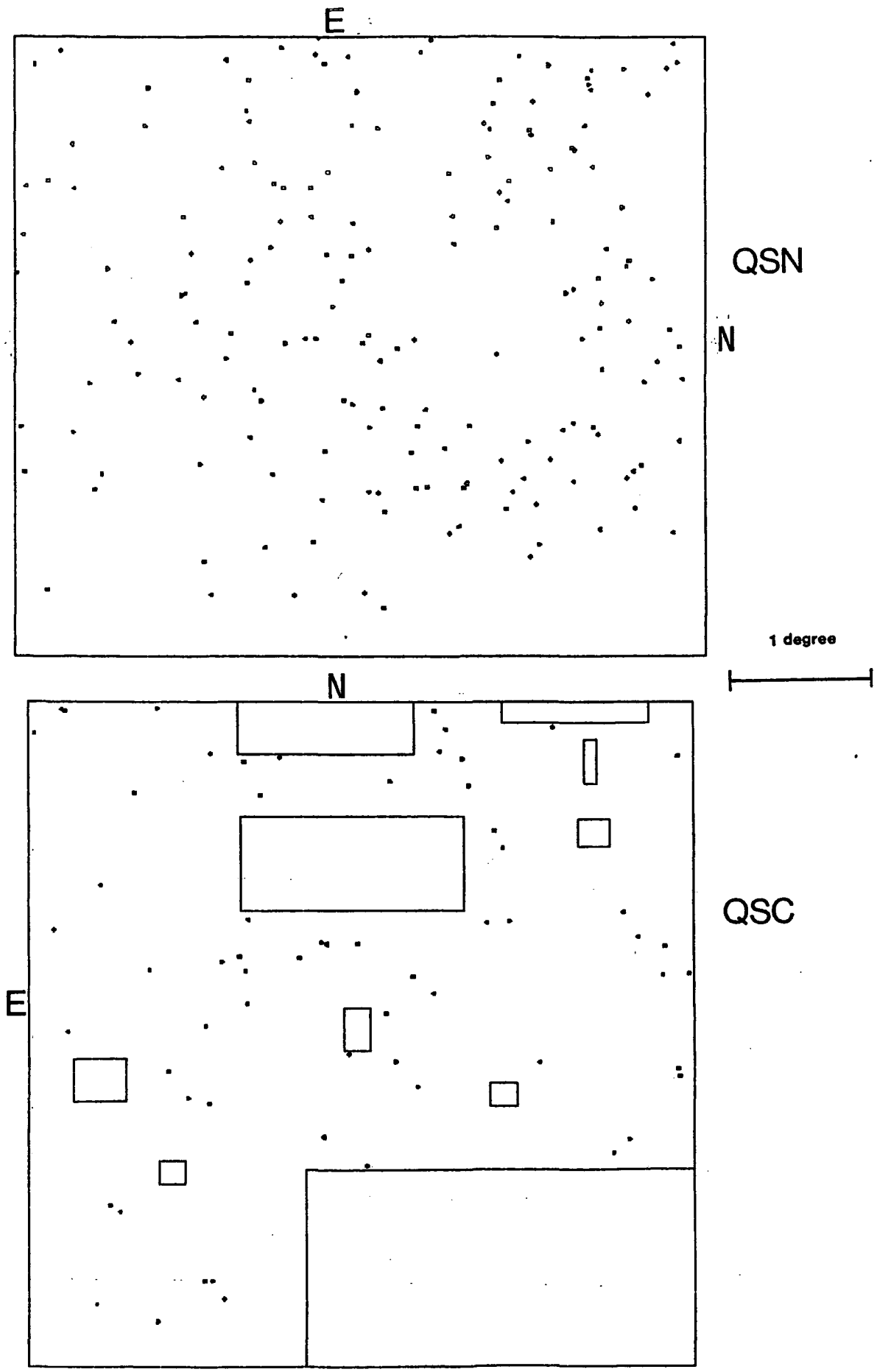

Figure 6.4 continued

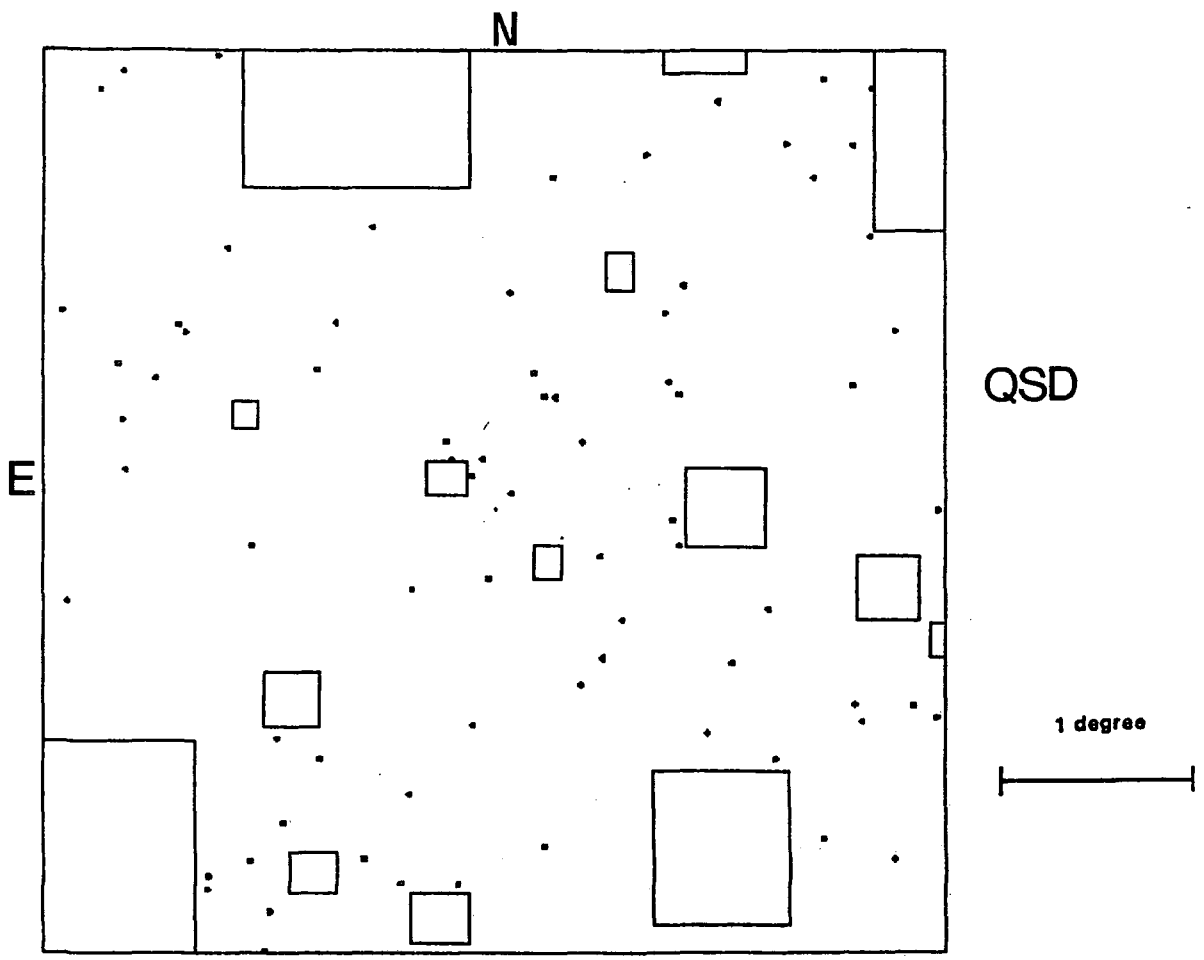

Figure 6.4 continued

6.4 RESULTS

6.4.1 The Cross-correlation Function

The cross-correlation functions for the galaxy/emission line pairs, $w_{*g}(\theta)$, is shown in figure 6.5. In this (as in all future cases) the cross-correlation functions for each individual field are displayed in the upper of the 2 diagrams in the figure, with the pair-weighted average cross-correlation function plotted below. Error bars are not displayed on the individual field cross-correlation functions, but those shown on the combined function are calculated from the rms field-to-field variation on $w_{*g}(\theta)$. These errors will be subject to errors themselves, but their true magnitude can best be estimated from the general trend of the error bars plotted on the diagrams.

We see in figure 6.5 a somewhat surprising result. Although at low signal-to-noise (1.5 σ) the correlation function is not positive (as it would be if the high redshift QSOs were truly associated with the low redshift galaxies), nor is it zero (as we would expect if QSOs were randomly distributed with respect to galaxies). In fact, it is slightly negative, although admittedly at a much lower significance level than was first reported by Shanks *et al.* (1983c) using the Clowes and Savage (1983) emission line catalogue on the SGP. While it was suspected by Shanks *et al.* (1983c) that cluster galaxies may be responsible for the observed anti-correlation, was never explicity demonstrated there. As we now have many more Schmidt fields (and therefore a much larger galaxy catalogue in total), we may test this hypothesis directly by using the large sub-sample of cluster

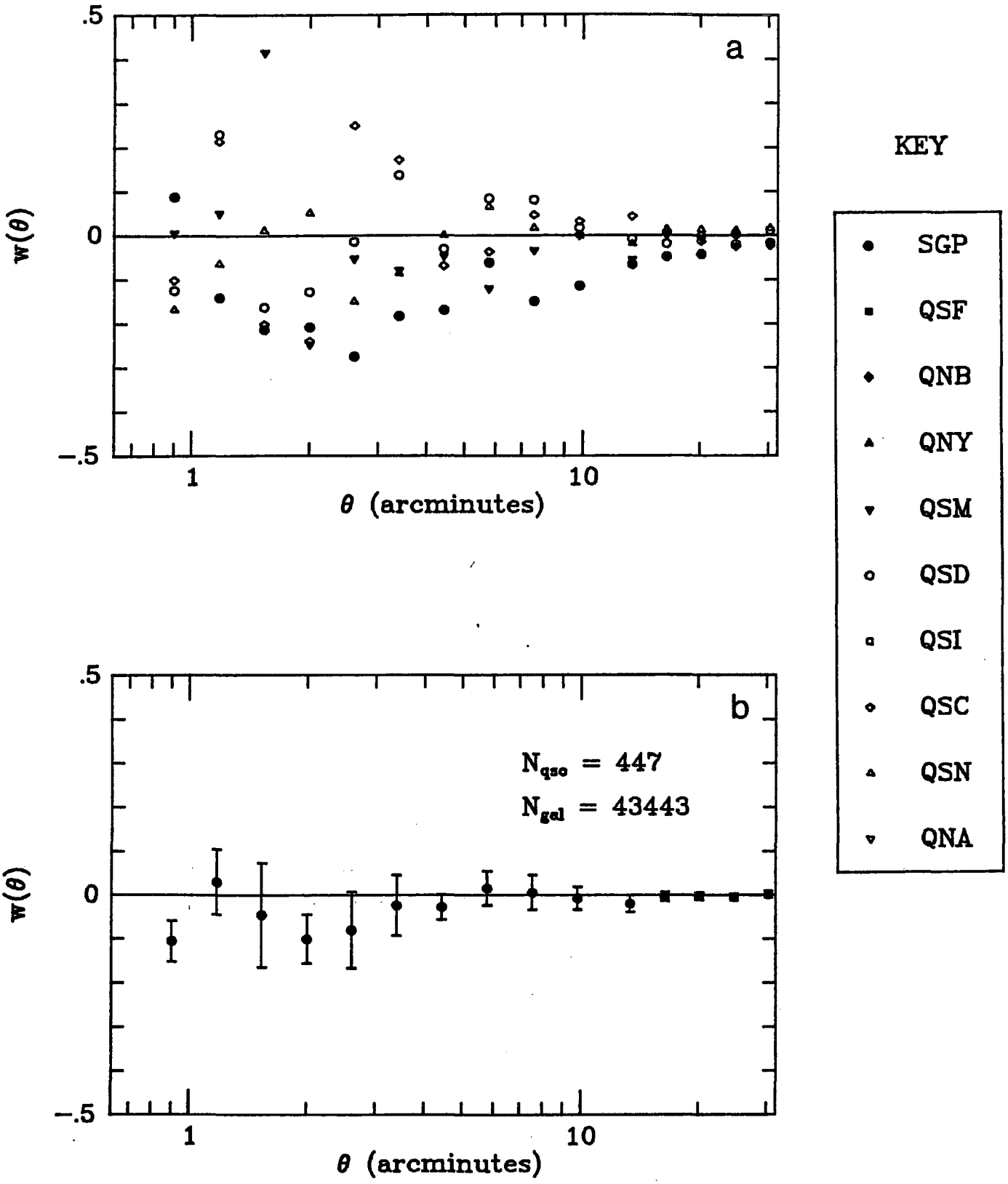

Figure 6.5 Emission line object/galaxy cross-correlation function.
a) Individual field cross-correlation function.
b) Pair-weighted average cross-correlation function.

galaxies selected from the galaxy catalogue. The cross-correlation function for the cluster galaxy/emission line pairs, $w_{c\bullet}(\theta)$, is plotted in figure 6.6 and we see a striking anti-correlation between the galaxies which are cluster members and emission line objects, the result being significant at the 2.5σ level. The level of anti-correlation is $w_{c\bullet}(\theta) = -0.3$ at scales < 4 arcmin. At the largest scales ($\theta > 20$ arcmin.) the results are consistent with a Poissonian process. Therefore, the anti-clustering that was reported for the emission line catalogues for the SGP and QSM fields in Boyle *et al.* (1983) is confirmed with the addition of a further three fields. The number of pairs at each angular separation that go to make up the estimate of $w_{c\bullet}(\theta)$ are given in table 6.4, along with the value of $w_{c\bullet}(\theta)$ itself.

The anti-clustering is not caused by the merging of images in the measurement process. Although merging of images by the COSMOS machine does occur, it only does so at angular separations of less than 30 arcseconds, see Phillipps *et al.* (1981). However, as pointed out in Shanks *et al.* (1983c), this anti-clustering result could be due to a selection effect inherent in the detection of emission line objects from visual inspection of objective prism plates. For example, QSOs may be more likely to be rejected in regions where there is a high density of galaxies, for fear that their emission line spectra might merely be the result of overlapped galaxy spectra.

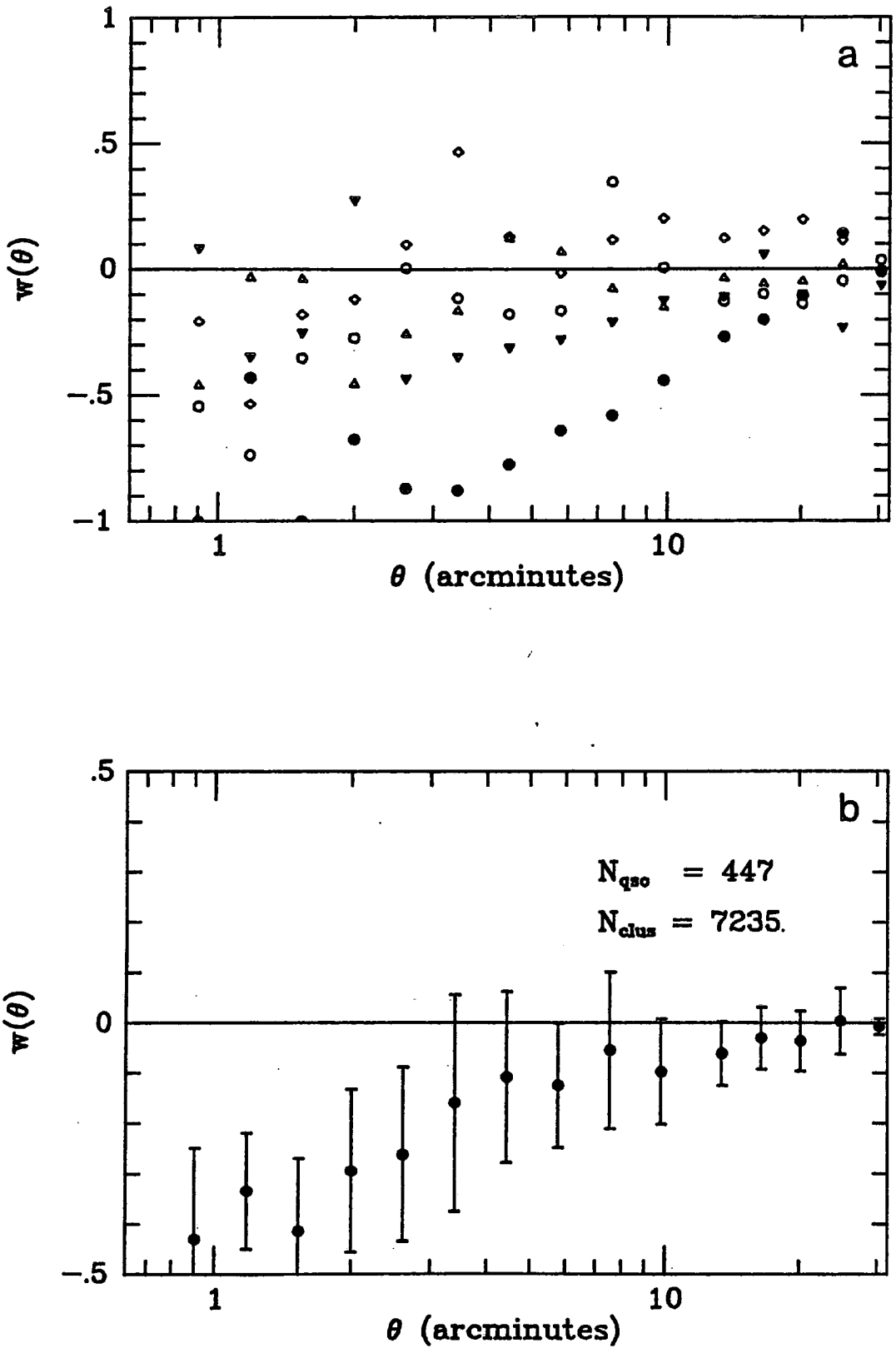

Figure 6.6 Cluster galaxy/emission line object cross-correlation function.
a) Individual field cross-correlation function.
b) Pair-weighted average cross-correlation function.
See figure 6.5 for key to symbols

θ (arcmin)	$w_{cu}(\theta)$ N_p	w	$w_{cf}(\theta)$ N_p	w	$w_{cg}(\theta)$ N_p	w
0.90	31	-0.25	79	-0.20	8	-0.43
1.18	42	-0.37	112	-0.20	16	-0.33
1.53	101	-0.11	236	-0.01	24	-0.41
2.00	155	-0.16	382	-0.03	48	-0.29
2.61	234	-0.27	583	-0.13	85	-0.26
3.40	447	-0.16	1000	-0.11	163	-0.16
4.43	913	-0.10	1760	-0.07	295	-0.11
5.77	1504	-0.01	3180	0.01	480	-0.12
7.52	2461	-0.03	5163	-0.03	867	-0.06
9.80	3864	-0.08	8491	-0.04	1396	-0.10
13.36	5242	-0.12	11205	-0.07	2028	-0.06
16.39	8265	-0.06	17539	-0.04	3060	-0.03
20.12	12471	-0.05	26249	-0.03	4465	-0.04
24.68	17767	-0.06	38429	-0.03	6841	0.00
30.29	26600	-0.03	56828	-0.01	9775	-0.01

Table 6.4 Pair count and Estimates for w_{cu}, w_{cf} and w_{cf}

However, in our UVX sample no such selection effect will operate. To test the reality of the anti-clustering result, we therefore performed the above analysis on the machine based UVX samples. We first calculated $w_{ug}(\theta)$, the galaxy/UVX cross-correlation function, over all 7 fields. The result is plotted in figure 6.7 and, although negative, is not significantly different from zero. Thus the anti-clustering result found by Shanks *et al.* (1983c) for the galaxy/UVX pairs is not reproduced at the same level on the other fields. We do note, however, that, even with a revised UVX criterion and a brighter magnitude limit for the galaxies, we still find that the SGP exhibits the largest anti-correlation of all the fields (filled circles in figure 6.7a). But, more expediently, if we once again restrict our attention to the galaxy cluster members and compute the cluster galaxy/UVX cross-correlation function, $w_{cu}(\theta)$, we find the much more significant result plotted in figure 6.8. We see a significant (2.7σ) anti-correlation with an amplitude of $w_{cu}(\theta) \simeq -0.22$ at scales < 4 arcmin, thus confirming the anti-clustering in the cluster/UVX pairs seen on the SGP,QSM and QNY fields reported by Boyle *et al.* (1984). We also compute $w_{cf}(\theta)$, the cluster galaxy/faint UVX cross-correlation function. From figure 6.9 we see that it is similar to w_{cu}, but has a reduced amplitude of $w_{cf} \simeq -0.12$. The number of pairs, together with the values of $w_{cu}(\theta)$ and $w_{cf}(\theta)$, are also given in table 6.4 for each angular separation plotted in figures 6.8 and 6.9.

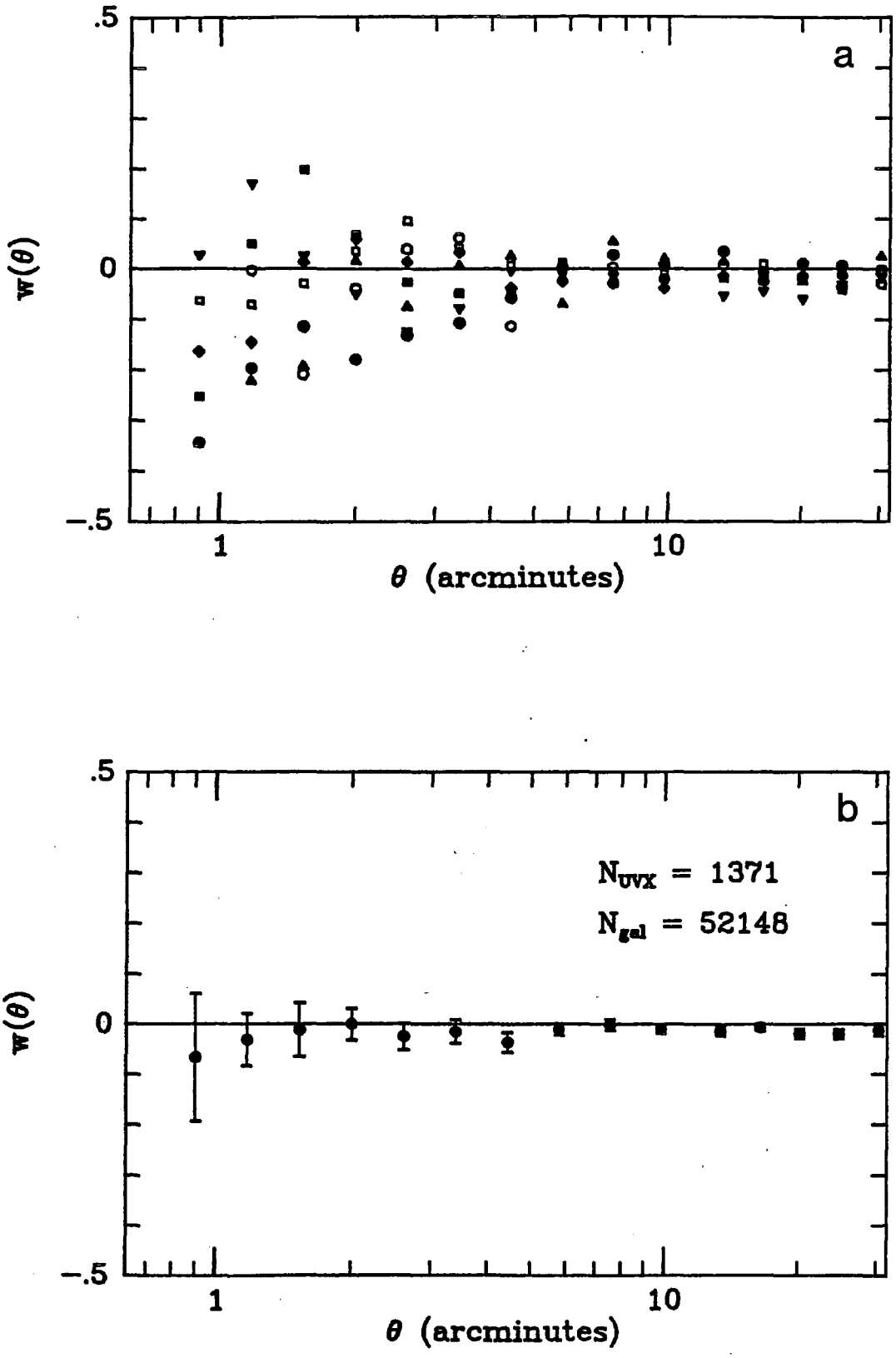

Figure 6.7 UVX/galaxy cross-correlation function.
a) Individual field cross-correlation function.
b) Pair-weighted average cross-correlation function.
See figure 6.5 for key to symbols

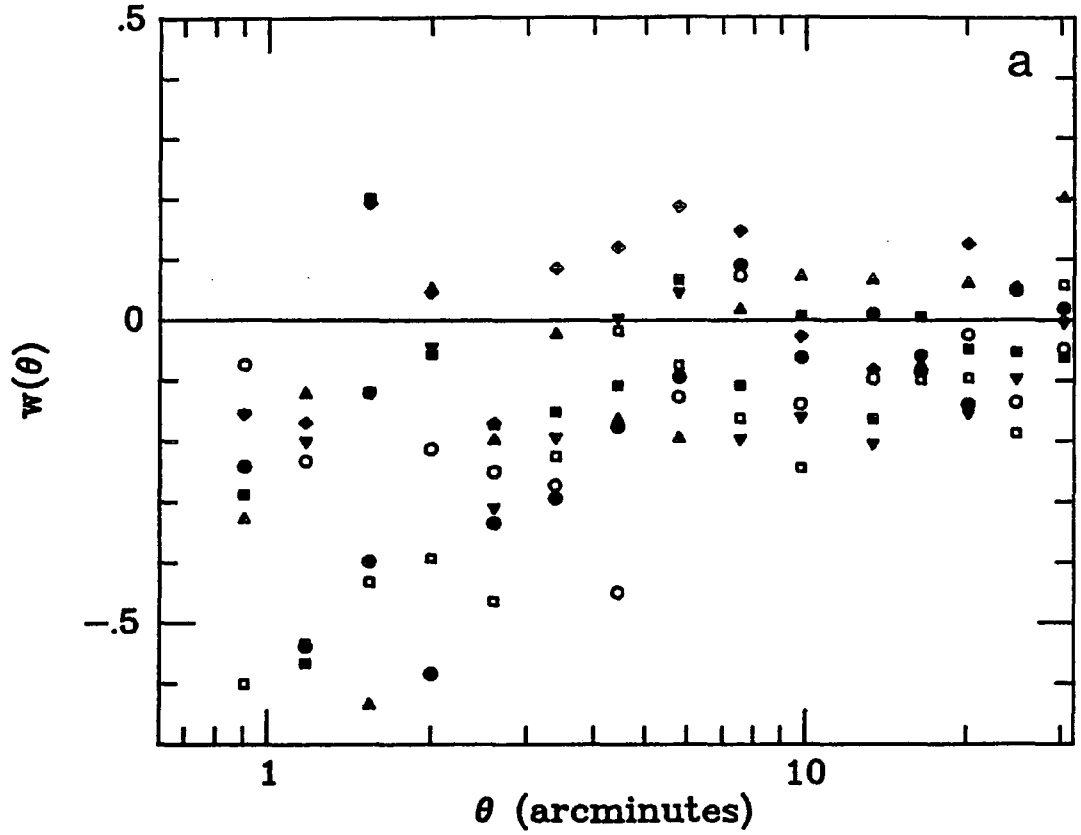

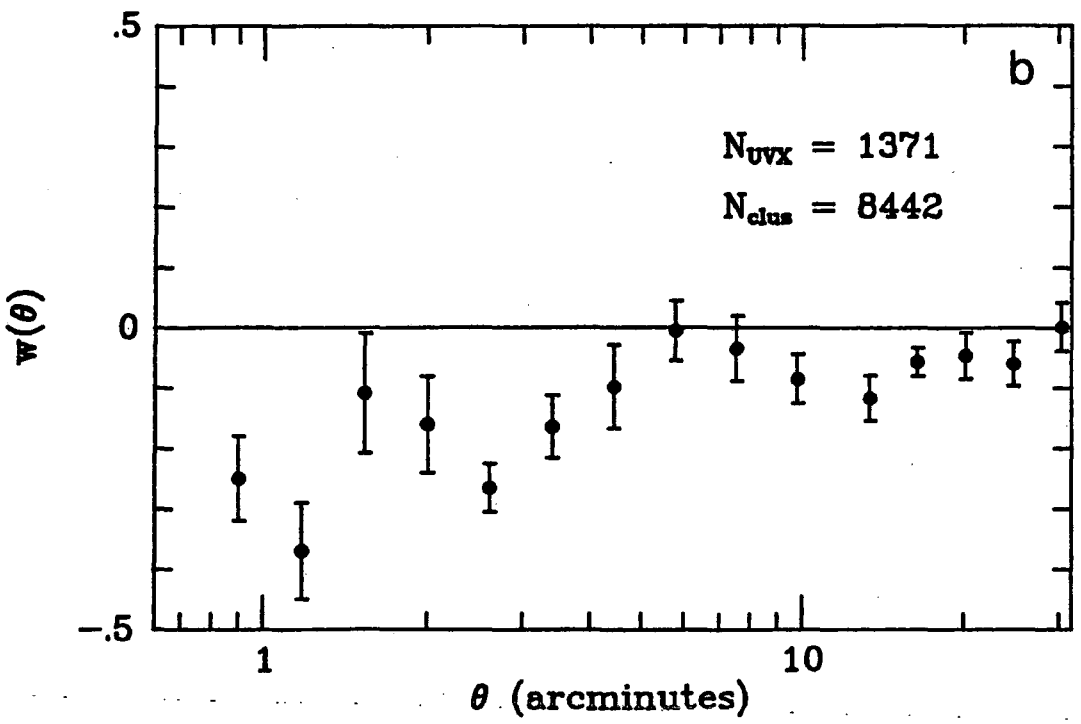

Figure 6.8 Cluster galaxy/UVX cross-correlation function.
a) Individual field cross-correlation function.
b) Pair-weighted average cross-correlation function.
See figure 6.5 for key to symbols

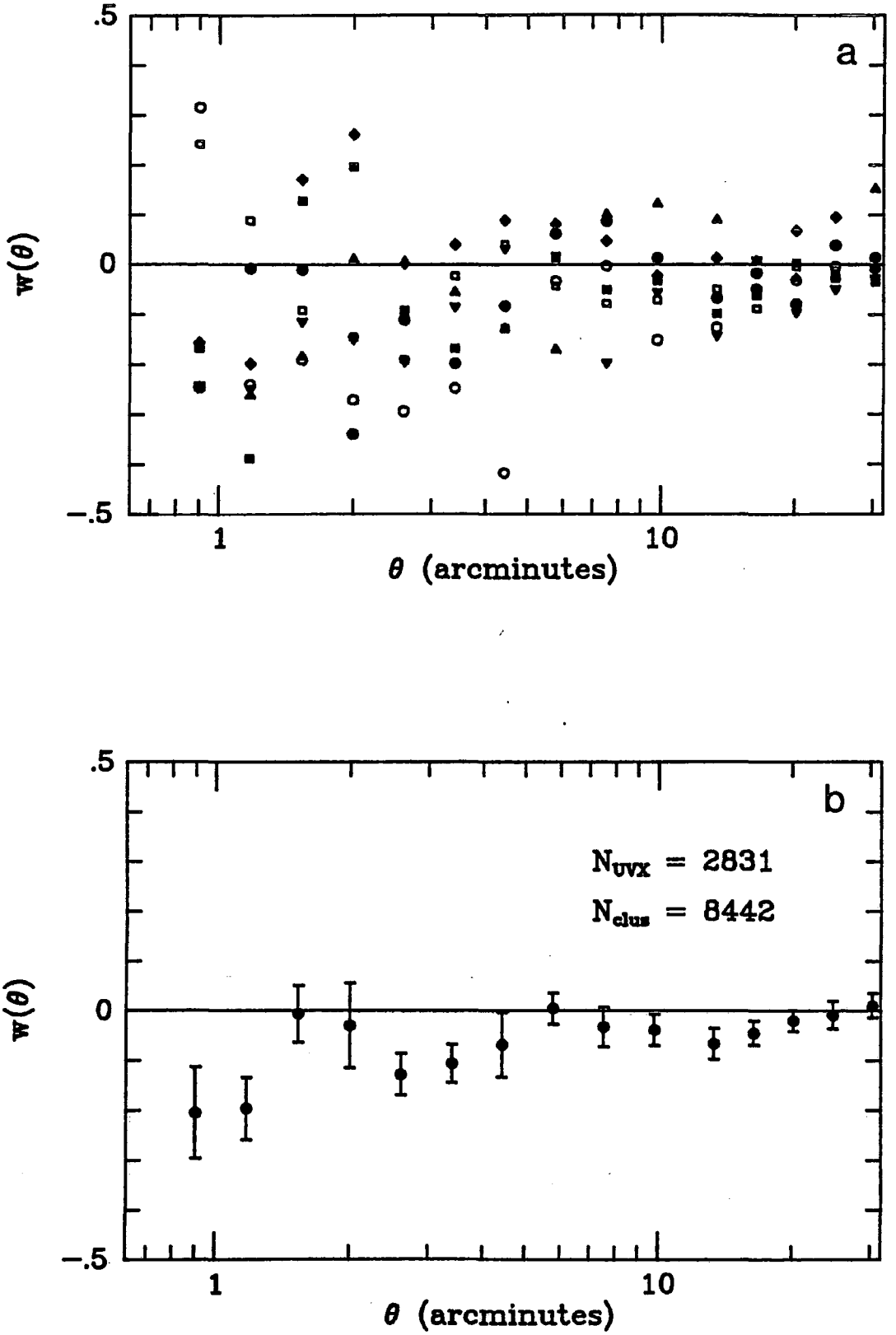

Figure 6.9 Cluster galaxy/faint UVX cross-correlation function.
a) Individual field cross-correlation function.
b) Pair-weighted average cross-correlation function.
See figure 6.5 for key to symbols

To ensure that this anti-clustering result with clusters is not merely attributable to some poorly understood bias in the selection of cluster galaxies, or, indeed, to some artefact in the COSMOS measurement process, we introduced a control sample of faint ($b < 20.25$ mag), ordinary Galactic stars (0.0 mag $< u-b <$ 0.5 mag) which could be cross-correlated with the cluster galaxy sample. The result, $w_{c*}(\theta)$, is illustrated in figure 6.10. The Poissonian result for stars at all scales indicates that the anti-clustering seen between cluster galaxies and UVX objects is likely to be real. Amongst the individual field cross-correlation functionsplotted, we also present $w_{c*}(\theta)$ for the QNA field (inverted open triangles in figure 6.10). The QNA field consistently gives the largest non-zero value for $w_{c*}(\theta)$ and thus amply demonstrates why this field was not considered for the correlation analysis.

We now compare the amplitudes of cluster/emission line and cluster/UVX cross-correlation functions. We know that the UVX sample is contaminated by stars at the 25% level. These stars are distributed randomly with respect to the cluster galaxies and serve to reduce the cluster/UVX cross-correlation function by 25% over what would have been expected had the UVX sample been entirely composed of QSOs. Thus the real level of anti-correlation between cluster galaxies and QSOs with $b < 20$ mag will be nearer $w_{cq} \simeq -0.3$. As determined from table 3.12, the average limiting magnitude for the emission line catalogues used in this analysis is $b \simeq 20$ mag. Since the contamination of the emission line catalogues by stars is $< 5\%$ (Savage *et al.*

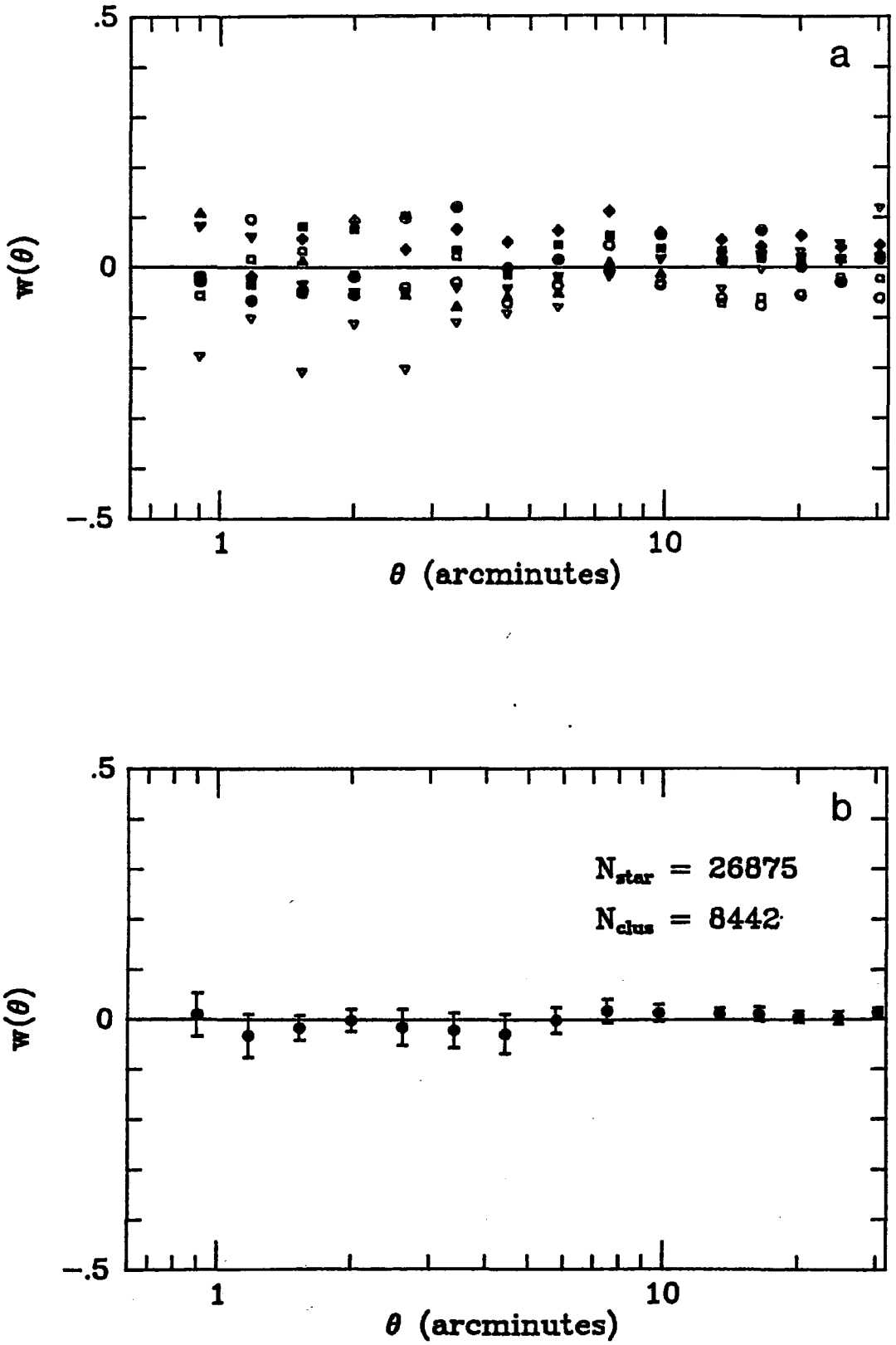

Figure 6.10 Cluster galaxy/Galactic star cross-correlation function.
a) Individual field cross-correlation function.
b) Pair-weighted average cross-correlation function.
See figure 6.5 for key to symbols

1985), it can be seen that the amplitudes of w_{cu} and w_{c*} are entirely consistent with a 30% deficiency of bright ($b < 20$ mag) QSOs within 5 arcmin of cluster galaxies. For fainter QSOs ($b < 20.75$ mag) there is only a drop of 15% in the QSO density within similar angular separations from cluster members. A possible explanation for this discrepancy is given in chapter 6.5.

6.4.2 The Auto-correlation Function

The auto-correlation functions for the emission line objects, $w_{**}(\theta)$, the UVX samples, $w_{uu}(\theta)$, and the Galctic stars, $w_{**}(\theta)$, are displayed in figures 6.11, 6.12 and 6.13. Table 6.5 lists the numbers of pairs found and the auto-correlation function estimate at each angular separation for the functions plotted in figures 6.11 and 6.12. We see that, while the emission line objects show a small positive correlation, it is at a very low level of significance. Indeed, the UVX objects show no correlation amongst themselves at all, exhibiting the same random correlation as the Galactic stars. This is in contrast to the clustering shown to exist in the UVX sample for the SGP (Shanks *et al.* 1983c) and for the combined SGP, QSM and QNY samples (Boyle *et al.* 1983). Thus the inclusion of further fields and a more accurately defined UVX sample (made possible by the spectroscopic observations) has removed any apparent clustering seen.

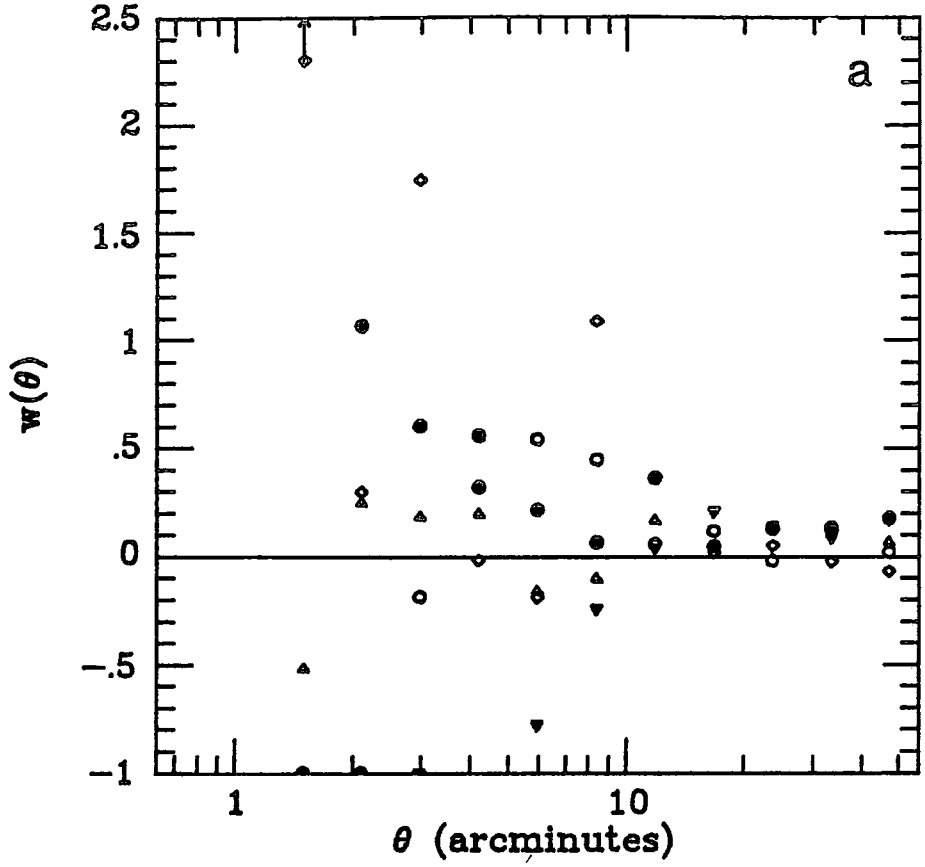

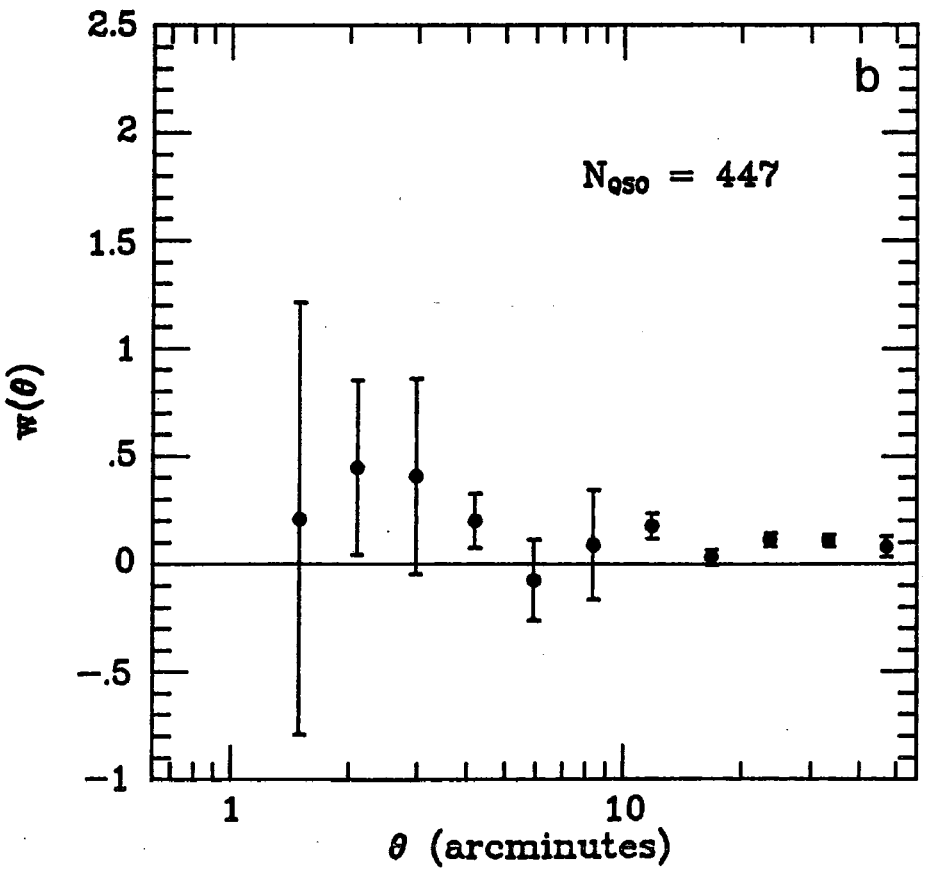

Figure 6.11 Auto-correlation function for emission line objects.
a) Individual field auto-correlation function
b) Pair-weighted average auto-correlation function
See figure 6.5 for key to symbols

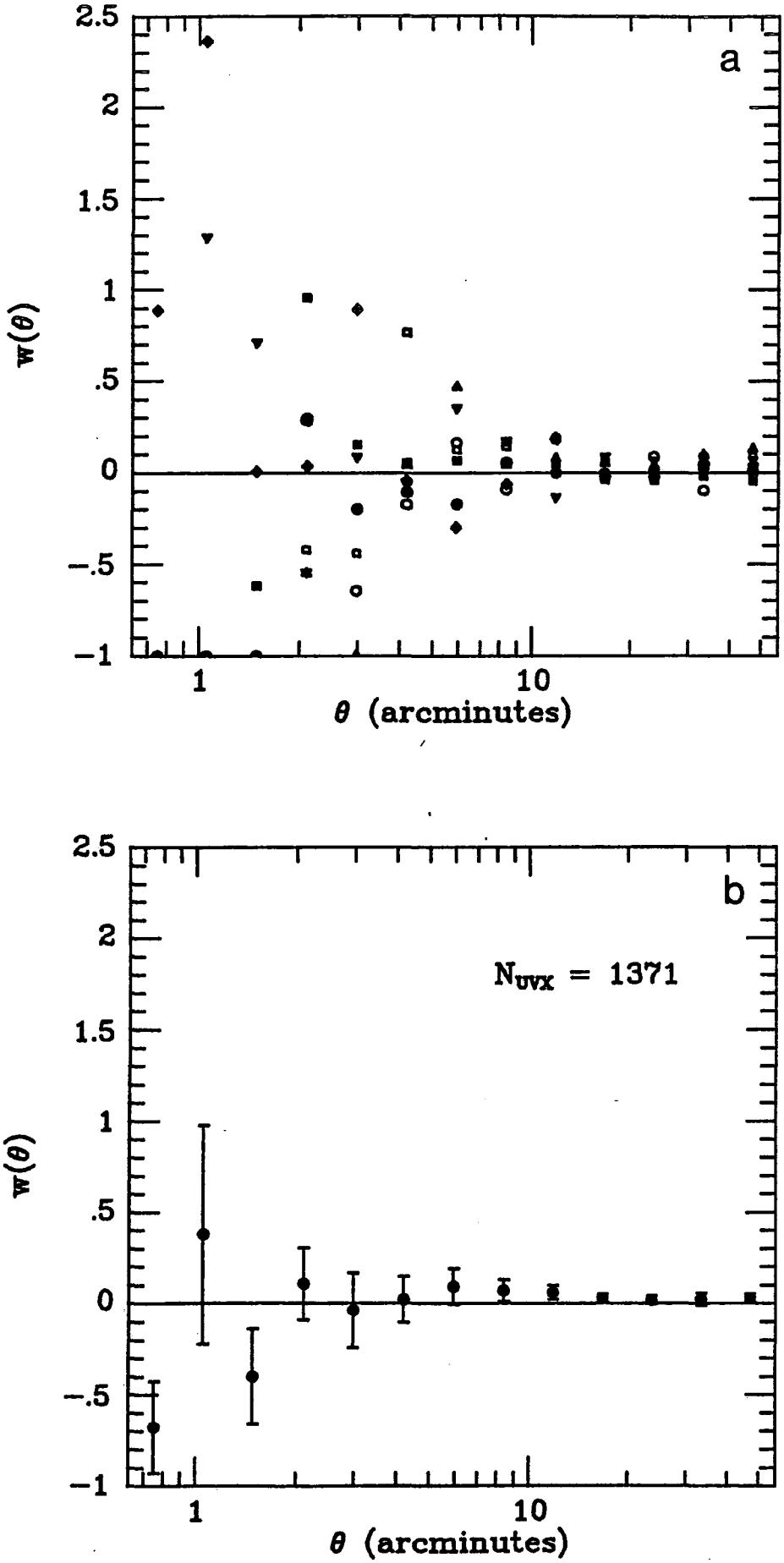

Figure 6.12 Auto-correlation function for UVX stars.
a) Individual field auto-correlation function
b) Pair-weighted average auto-correlation function
See figure 6.5 for key to symbols

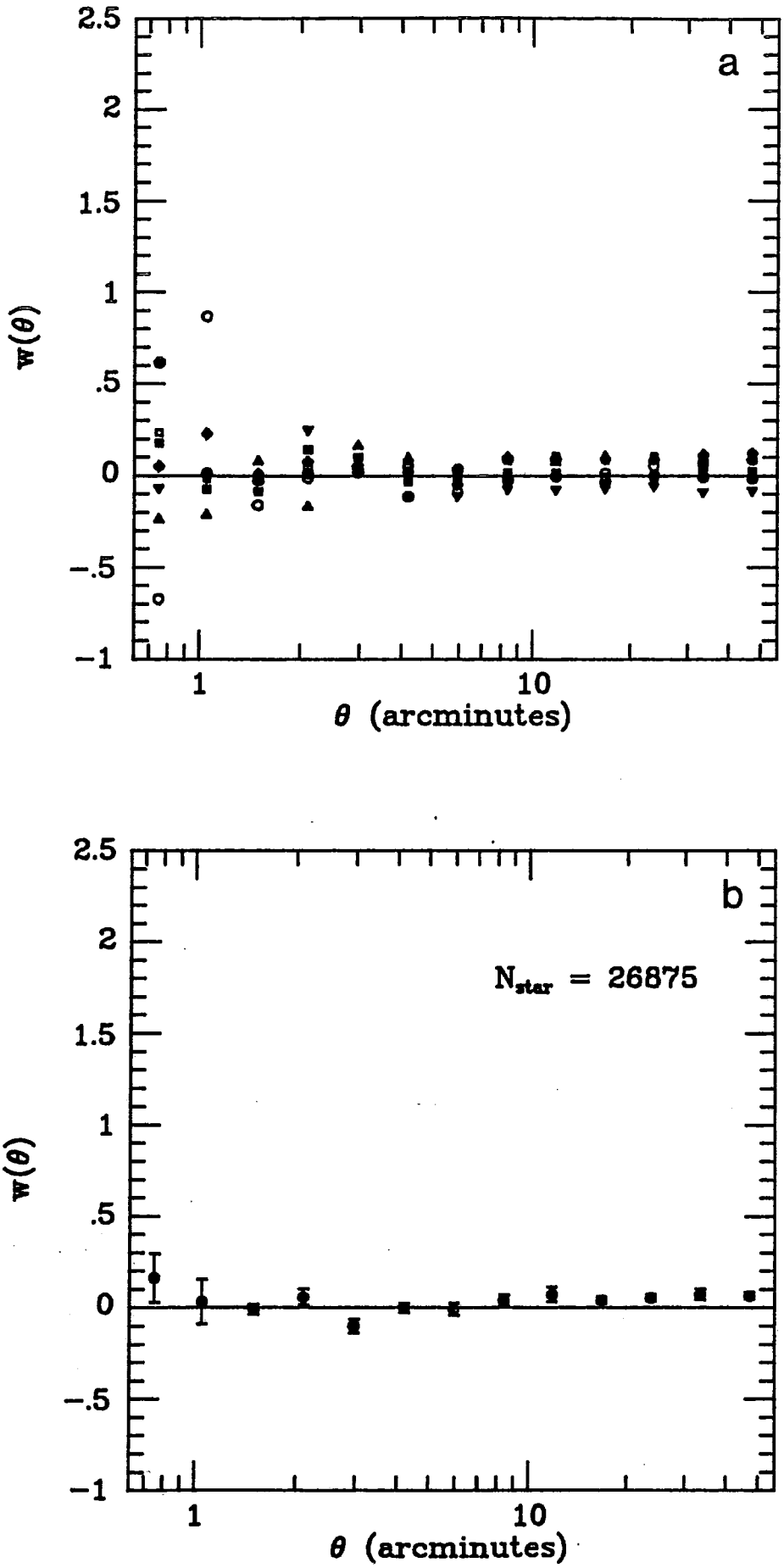

Figure 6.13 Auto-correlation function for Galactic stars.
a) Individual field auto-correlation function
b) Pair-weighted average auto-correlation function
See figure 6.5 for key to symbols

θ (arcmin)	$w_{e\,e}(\theta)$ N_p	w	$w_{u\,u}(\theta)$ N_p	w
0.75	0	-	1	-0.68
1.05	0	-	8	0.38
1.49	3	0.21	7	-0.40
2.10	9	0.45	30	0.11
2.97	18	0.41	47	0.04
4.19	36	0.20	118	0.02
5.92	55	-0.08	241	0.09
8.37	124	0.09	439	0.07
11.82	259	0.18	882	0.06
16.70	446	0.03	1610	0.03
23.59	926	0.11	3091	0.02
33.31	1758	0.11	5689	0.02
47.06	3178	0.08	10562	0.03

Table 6.5 Number of Pairs and estimates for $w_{e\,e}$ and $w_{u\,u}$

6.5 Discussion

6.5.1 The Dust Model

The simplest explanation of the observed anti-correlation between cluster galaxies and QSOs is that dust lying in line-of-sight clusters obscures the QSOs lying behind them at the distances implied by a cosmological interpretation of their redshifts. If we are to accept this explanation we must consider a number of points. Firstly, how much absorption is needed per cluster to explain the level of anti-correlation observed ?

To calculate this we assume that QSOs are cosmologically distributed with an n(m) relation of the form:

$$n(<B) \propto 10^{0.86B} \quad (B < 20 \text{ mag}) \qquad \ldots (6.3a)$$

$$n(<B) \propto 10^{0.32B} \quad (B > 20 \text{ mag}) \qquad \ldots (6.3b)$$

These relations are obtained from a smooth fit to the integral n(m) counts for UVX QSOs plotted in figure 6.14 (this is just the integral form of the differential UVX QSO n(m) counts presented in figure 4.3). If each galaxy cluster has associated with it an absorption of A_B magnitudes, then it can easily be shown that, by comparing the surface density of QSOs behind clusters (N_b) with the average surface density of QSOs over the whole measured area (N_q) the QSO/cluster cross-correlation function will be given by

$$1 + w_{cq} = N_b / N_q \qquad \ldots (6.4a)$$

where

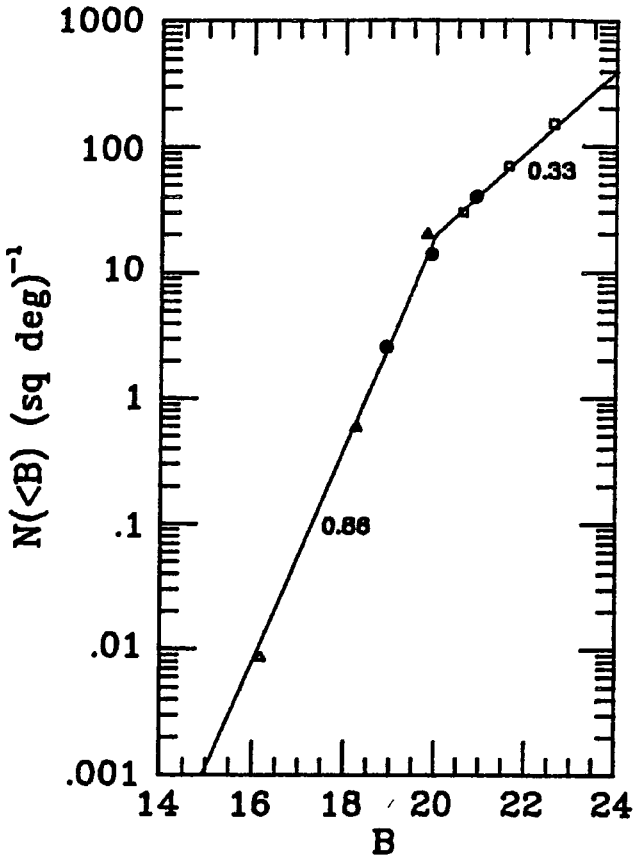

Figure 6.14 Integral n(<B) relation for spectroscopically confirmed QSOs. ▵ Schmidt and Green (1983), ▲ Marshall et al. (1984), ▫ Koo (1986), • this work.

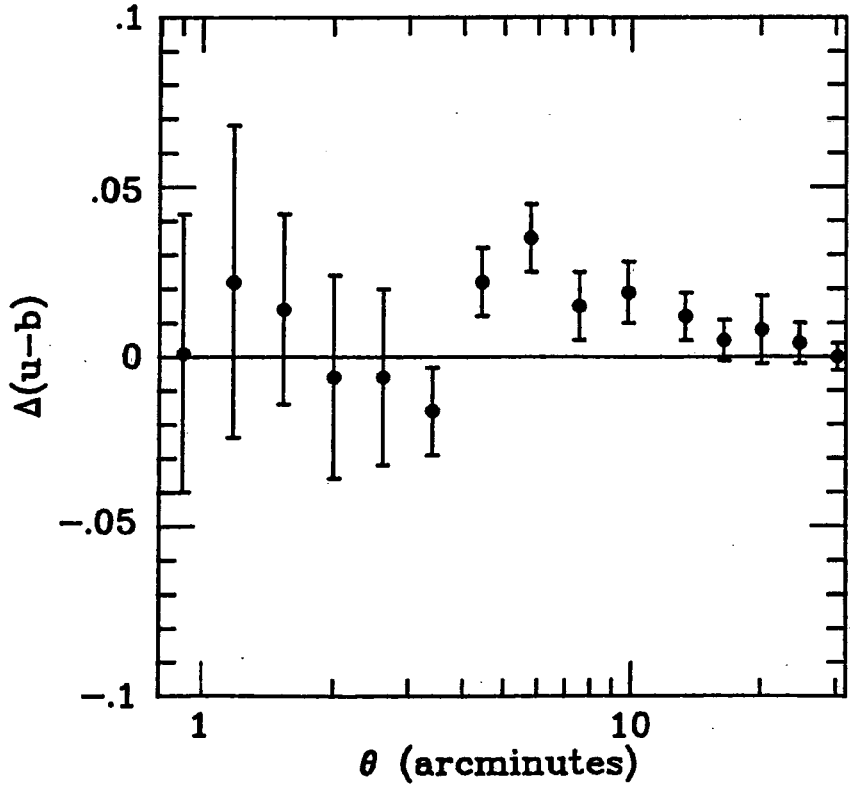

Figure 6.15 Δ(u-b) v angular separation from cluster galaxy for UVX objects used in the correlation analysis.

$$N_q = A_c N_B + (1-A_c) N_f \quad \ldots (6.4b)$$

N_f being the true density of QSOs in the absence of obscuration, and A_c the area of the plate covered by detected clusters. Typically, the clusters selected here only cover $\simeq$ 10% of the plate and so we may approximate equation (6.4a) to:

$$1 + w_{cq} = N_b / N_f \quad \ldots (6.4a')$$

Thus the cross-correlation function can be given in terms of the absorption A_B as:

$$w_{cq} = \mathrm{dex}(d\log n(<B)/dB\ A_B) - 1 \quad \ldots (6.5)$$

This represents a much simpler determination of A_B than that made by Shanks *et al.* (1983c). There, the fraction of cluster galaxies contributing to the anti-clustering result was unknown and had to be estimated by indirect means.

Thus from (6.4a') and (6.5) we have that, with $w_{cq} = -0.3$ at $b < 20$ mag for both the UVX stars and emission line objects, the extinction per cluster is $A_B \simeq 0.20$ mag. Similarly, for the faint UVX sample, the average amplitude of $w_{cf} = -0.15$ also gives an $A_B \simeq 0.20$ mag. Although both values for the amplitudes of the bright and faint UVX/cluster cross-correlation functions are subject to substantial errors the decrease in amplitude from w_{cu} to w_{cf} is consistent with the flattening of the integral UVX QSO counts beyond $B \simeq 20$ mag.

In this determination of A_B we have only considered the loss of QSOs by dimming. In the UVX samples QSOs will also be 'lost' behind clusters through reddening. However, the magnitude of this effect is so small in comparison to the dimming effect of dust that it can safely be neglected in the estimation of A_B. This can easily be seen from the following demonstration. Extinction in u-b will amount to be approximately $0.18A_B$ (Mihalas and Binney 1981) which, for the case in consideration here, will be at most 0.035 mag (the true value of A_B can only be less than 0.20 mag if reddening is included). From figure 3.8 we see that, for all the fields observed in the spectroscopic survey, the restricted u-b limits lie on average $\simeq 1\sigma$ away from the mean u-b colour for UVX QSOs (σ being the standard deviation in the u-b colours for $z < 2.2$ QSOs, which is of the order 0.30 mag). Assuming a normal distribution for the u-b colours for QSOs we see that less than 3% of the QSOs will be lost by reddening. Thus the effect of reddening is an order of magnitude less than that of dimming.

The value for A_B differs from that derived in Shanks *et al.* (1983c) and Boyle *et al.* (1983,1984). The discrepancy from Shanks *et al.* (1983c) arises because of the more direct method used to determine A_B in this analysis which does not rely on the value of w_{qq}. The high value quoted for w_{qq} of 0.25 - 1.0 in Shanks *et al.* (1983c) was responsible in part for the high value of A_B derived there. The overestimation of A_B in Shanks *et al.* (1983c) was also partly due to the low value adopted for the slope of 0.6 for the QSO number counts which, now better

information is available, has been revised to a more accurate value. The lower value assumed for the slope of the n(m) counts also led to the overestimation of A_B in Boyle *et al.* (1983,1984).

The large spread in the u-b colours for QSOs ($\simeq$ 0.3 mag) implies that a classic test to detect extinction by dust, namely the reddening of QSOs, will not be sensitive to an extinction as small as $\Delta(u-b) \simeq 0.035$. In fact, with 25% contamination of the UVX QSOs by Galactic stars, this effect will be reduced even further to $\Delta(u-b) \simeq 0.025$. Indeed, tests to look for reddening have produced no significant results. The result of one such test is plotted in figure 6.15. Here we have computed the average u-b colours for the UVX objects in the cluster/UVX pairs at each particular angular separation. This was then subtracted from the mean u-b colour for all UVX objects in the field and the result, $\Delta(u-b)$, plotted as a function of angular separation of the cluster galaxy/UVX pair. The noise on the values for $\Delta(u-b)$ is so large that no significant reddening with decreasing angular separation is observed.

The avoidance of galaxy clusters by QSOs may also be reflected in the distribution of QSOs amongst themselves, making them appear clustered. Such an effect was noted by Masson (1978) who suggested that 'regions of incompleteness' in the 4C radio catalogue were responsible for the observed clustering between catalogue members (Seldner and Peebles 1979), an effect analogous to Babinet's principle in optics. We must ascertain, therefore, whether the size of such an effect in the dust model is compatible with the zero (but noisy) amplitudes for w_{**} and w_{uu}.

In the simple 2-dimensional model of Shanks *et al.* (1983c), background QSOs are obscured by foreground clusters (whether detected or not by the multiplicity technique) distributed on the plane of the sky over a fractional area, $1-A_u$, we have

$$w_{qq} = \frac{\Delta^2 A_u (1-A_u)}{(1 + \Delta A_u)^2} \quad \ldots (6.6)$$

where $\Delta = 1/(1 + w_{cq}) - 1$. As demonstrated by Phillipps (1985) w_{qq} has a maximum value at

$$w_{qq} = \Delta^2/4(1+\Delta) \quad \ldots (6.7)$$

which, for $w_{cq} = -0.3$, is equal to 0.032. Consequently the zero amplitude observed for the correlation function is perfectly consistent, within the errors, to that expected on the basis of the dust model.

The intrinsic spatial clustering of QSOs, as inferred from the high amplitude of $\xi(r)$ found for the UVX survey QSOs in the previous chapter, will also contribute, in projection, to the amplitude of w_{qq}. Since the evolution of the QSO correlation function with redshift is unknown, the most direct way to estimate w_{qq} from $\xi(r)$ i.e. Limber's formula (see Phillipps 1978), can not be employed as it involves explicit use of the evolution of $\xi(r)$. We can, however, make an order of magnitude estimate for the contribution of $\xi(r)$ to w_{qq} by the following approach. There is a well defined scaling relation for galaxies between the amplitude of the galaxy correlation function , $w(\theta)$, and the depth of the galaxy sample for which it was calculated (see Stevenson 1985). The greater the redshifts to which the

galaxy sample extends, the more washed out in projection the intrinsic clustering amongst galaxies becomes, and the lower the amplitude of $w(\theta)$. From the relation derived in Stevenson (1985), the amplitude of $w(\theta)$ for a B = 25.0 mag limited galaxy sample will be $\simeq$ 0.004 at 5 arcminutes. From our UVX survey we know that the average absolute magnitude for QSOs selected by the UVX technique is $M_B \simeq -24.0$. This is some 4 - 5 magnitudes brighter than the absolute magnitudes for a typical (M^*) galaxy. Therefore, a QSO sample limited at b = 20-21 mag will extend to approximately the same average depths as a galaxy sample limited at b = 25.0 mag. From chapter 5 we know that the amplitude of $\xi(r)$ for QSOs is $\simeq$ 10 times that for galaxies and thus the contribution of the intrinsic clustering of QSOs to $w_{q,q}$ at 5 arcminutes will be only $w_{q,q} \simeq 0.04$. Even if QSOs clustered as strongly as rich clusters ($20\xi(r)_{gal}$), no detectable effect would be produced in the current estimate of $w_{q,q}$.

Evidence for dust in clusters has been produced by a number of other authors. First Zwicky (1957) and then Karachentzev and Lipovetskii (1969) found evidence for dust in clusters of galaxies by counting the numbers of distant and extremely distant clusters as a function of angular separation from nearby clusters in the Zwicky catalogue. From this result Karachentzev and Lipovetskii (1969) estimated an extinction of A_B = 0.20 mag per cluster. More recently Bogart and Wagoner (1973) inferred an extinction of A_B = 0.5 mag per Abell cluster when performing a similar analysis with different richness classes of clusters in the Abell catalogue.

6.5.2 The Ejection Model

Another model which could account for the deficiency of QSOs close to galaxies is one in which QSOs are ejected from galaxies in such a way as to leave them at large distances from their parent galaxy. We consider this model as unlikely for the following reasons:

a. It does not naturally explain the decrease in amplitude of the UVX/cluster cross-correlation function beyond b = 20.0 mag.

b. It does not naturally explain why the effect is seen only in clusters. Indeed it would seem more difficult to eject QSOs from the large gravitational potential well in clusters than from 'isolated' field galaxies.

c. There is now no excess seen at any scale in the cluster/UVX correlation function, which, in Shanks *et al.* (1983c), was cited as a possible characteristic distance to which the QSOs were shot out of the galaxy.

d. Finally, ejection models were originally suggested to account for the proposed excess of QSOs around galaxies. If we were now to favour the ejection hypothesis it would be on precisely the reverse observation - a somewhat unsatisfactory state of affairs.

6.5.3 Implications of the Dust Model

If we model the absorption of A_B magnitudes within each cluster as a uniform sphere, radius R, of dust grains, then its mass can be obtained from (Martin 1978):

$$M = 2\times10^{11} A_B (R/1\mathrm{Mpc.})^2 \ M_\odot \qquad \ldots (6.8)$$

where we have assumed the grain parameters of specific density (1 g cm^{-3}) and radius (0.1 μm) to be the same as for silicate grains in our own galaxy (Martin 1978).

From the results of the cross-correlation analysis we take the average angular extent of this dust absorption to be 4 arcminutes. At the average redshift, $\langle z \rangle = 0.15$, for clusters in the $b < 20.16$ mag sample, this corresponds to a characteristic linear radius of $500h^{-1}$kpc for the absorption effect due to the dust grains. With an absorption of 0.2 magnitudes associated with each cluster, we therefore estimate the mass of dust to be $10^{10}h^{-2}M_\odot$. Although this represents a small fraction of the mass contained in luminous material ($10^{11}h^{-2}M_\odot$) within each cluster, we may wonder whether this mass of dust is compatible with the conditions of high density and temperature known to exist inside rich clusters.

We can answer this question by first considering a simple order of magnitude calculation. Within the central megaparsec of the Coma cluster estimates of the mass in luminous material, $10^{12}h^{-2}M_\odot$, (Metcalfe 1983), and the mass of the hot (10^8K) gas, $4 \times 10^{13}h^{-5/2}M_\odot$ (Lea *et al.* 1973) combine to give a

luminosity-to-gas ratio of $0.025h^{5}$. Assuming the same luminosity-to-gas ratio in the clusters detected by the multiplicity algorithm, we obtain an estimate of $4 \times 10^{12} h^{-5/2} M_{\odot}$ for the amount of gaseous material in these clusters. With a gas-to-dust ratio similar to that seen in our own galaxy (100:1) we arrive at a dust mass of $4 \times 10^{10} h^{-5/2} M_{\odot}$ within the central megaparsec ($2 \times 10^{10} h^{-5/2} M_{\odot}$ within the central 0.5 Mpc if mass profile of $M(<r) \propto r$ is assumed).

While this simple estimate is certainly compatible with the dust mass derived from the absorption, we could ask how correct is the assumption that the gas-to-dust ratio in these clusters is the same as that in our own galaxy, given that the dust can readily be destroyed by sputtering in rich clusters. From X-ray observations of rich clusters such as Coma we know that the intra-cluster gas is hot (10^{8}K) and estimates of its mass (Lea *et al.* 1973) give a density (within the central 0.5 Mpc) of $10^{-3} h^{0.5}$ cm^{-3}. From Margolis and Schramm (1977, hereafter MS), the lifetime of a dust grain against sputtering (Λ_{s}) is dependent on both gas density (n) and temperature (T):

$$\Lambda_{s} = 2 \times 10^{10} (10^{-3} cm^{-3}/n)(10^{6}/T)^{0.5} \text{ yr} \quad \ldots (6.9)$$

Thus a dust grain in Coma has a lifetime only $\simeq 2 \times 10^{7} h^{0.5}$ yr. In the clusters used in this analysis, however, the densities and temperatures are much lower. From above, the density of gas within our clusters will be $n \simeq 10^{-4} h^{0.5} cm^{-3}$ and the temperatures can be estimated from their observed velocity dispersions ($\simeq$ 300 km sec^{-1} - Shanks private communication) to be

$T \simeq 10^7 K$. This will give lifetimes of $\simeq 10^9 h^{0.5}$ yr for grains in our clusters - 50 times longer than those in the Coma cluster. Following MS the equilibrium density of dust grains ρ_d can then be given by:

$$\rho_d = \tau_d r \qquad \ldots (6.10)$$

where τ_d is merely the grain lifetime in units of the Hubble time and r, the dust creation rate, is also given in units of the Hubble time. From MS typical estimates of r are $\simeq 0.03 h^{-1} \rho_{gas}$, where ρ_{gas} is the gas density within the cluster. Using equation (6.10) we therefore find that the gas to dust ratio in our clusters can be expressed as

$$\rho_{gas}/\rho_d \simeq 3 \times 10^{-3} h^{-3/2} \qquad \ldots (6.11)$$

With a suitable value for h ($\simeq 0.5$) our initial assumption of a gas to dust ratio in these clusters of 100:1 is thus vindicated. Although very much an order of magnitude calculation, we have shown that the amount of dust necessary to produce 0.2 magnitudes of absorption in B can indeed survive in these clusters.

However, the dust model could still be ruled out on the grounds that the integrated effect of dust in all clusters may produce prohibitively large cosmological effects.

As an example, the presence of dust will make galaxies appear fainter than they really are and so values of q_0 obtained from the Hubble diagram will be underestimated by an amount:

$$(\Delta q_0)_{dust} = 2.8 \times 10^3 (A/1 \text{ mag Mpc}^{-1}) h^{-1} \qquad \ldots (6.12)$$

where A is the absorption due to dust in magnitudes per Megaparsec (from MS). Equation (6.12) is only strictly valid for uniformly distributed dust, but it will provide a useful order of magnitude illustration for the limits on the amount of intergalactic dust tolerated by present observations. We therefore estimate A by simply distributing out the dust in each cluster uniformly over all space. The local space density of these clusters ($2 \times 10^{-4} h^3 Mpc^{-3}$) thus gives $A = 3 \times 10^{-5} h$ mag Mpc^{-1} and so $(\Delta q_0)_{dust} = 0.08$, a negligibly small effect. Moreover, we note that our averaged value for the extinction due to cluster dust is well below the upper limits quoted by other authors from studies of extinction, reddening and the spectra of distant galaxies and QSOs. To date, the most stringent upper limit on the amount of intercluster dust comes from Crane and Hoffman (1973). They used a λ^{-4} extinction law applied to the reddening of elliptical galaxies to estimate that the effect of dust could amount to no more than $A = 2 \times 10^{-4} h$ mag Mpc^{-1}, an order of magnitude greater than that found here.

Dust will also have an effect on the evolution of the QSO LF discussed in chapter 4. At high redshifts cosmological effects will become important and so the simple treatment followed above will no longer apply. From Ostriker and Heisler (1984), the mean absorption suffered by a QSO at a redshift z, $\Delta m(z)$, for an unevolving population of absorbers, can be expressed as follows:

$$\Delta m(z) = 0.4 n_0 \sigma (c/H_0) A_B [(1+z)^{2.5} - 1] \quad \ldots \quad (6.13)$$

where n_0 and σ are the space density and cross-section of the

absorbers (in this case clusters) involved. We find that this amount of absorption implied by equation (6.13) merely necessitates an increase in k_L from 3.7 to 4.0 in the standard q_0 = 0.5 evolution model of chapter 4. The n(m) and n(z) predictions for such a model are illustrated in figure 6.16. At low redshifts, therefore, the dust model does not require major revisions of our luminosity evolution model. However, we will see in the next chapter that this is not necessarily the case at high redshifts.

Although we fully recognise the naivety of this model, we do not feel justified in constructing a more complex one when many of the parameters of this model remain so ill-defined. In particular, the assumption that the clusters are unevolving is almost certainly unrealistic.

6.6 Conclusions

We have found that emission line objects and complete samples of UVX objects are anti-clustered with respect to galaxies in clusters at angular separations less than 4 arcmin. Results from the UVX and emission line auto-correlation studies and the reddening of UVX objects close to clusters have proven inconclusive.

We propose that the most likely explanation for the anti-correlation result is that dust associated with clusters of galaxies in the line-of-sight obscures the QSOs lying behind them at cosmological distances.

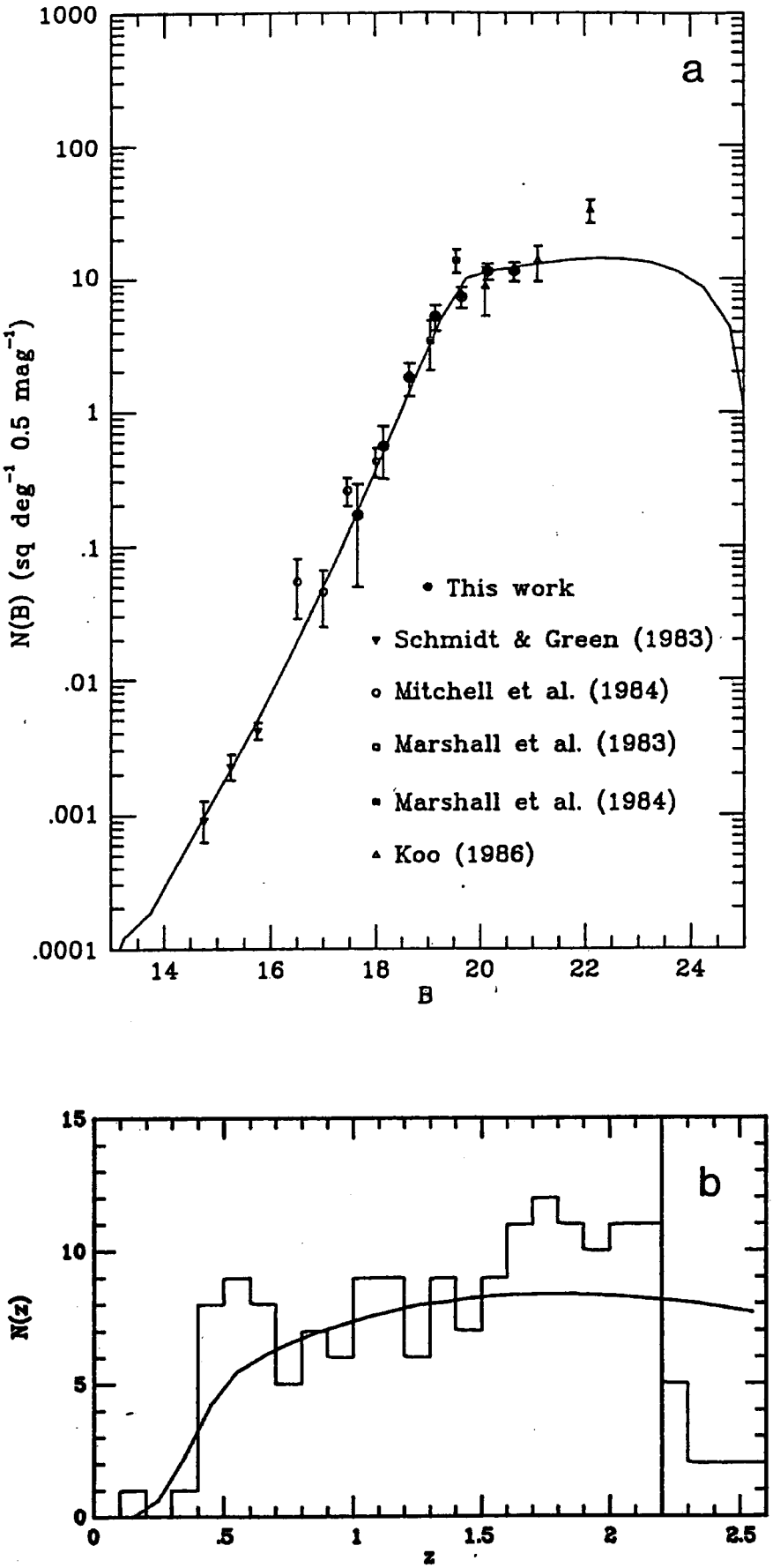

Figure 6.16 a) Differential n(m) counts for UVX QSOs. Solid line represents prediction from standard evolution model, corrected for dust obscuration.
b) Number redshift relation for QSOs discovered in faint UVX survey (all redshift classes). Solid line as for a) above.

From the amplitude of the cluster galaxy/QSO cross-correlation function, we derive a value of A_B = 0.2 mag for the amount of absorption associated with each galaxy cluster. This is in good agreement with previously determined values.

The amount of dust necessary to produce the absorption seen is quite small, 10^{10} $M_\odot$/cluster. The dust has no appreciable effect on the Hubble diagram or the evolution of low z QSOs, and is well below current observational upper limits on the amount of intergalactic dust.

CHAPTER SEVEN

THE EVOLUTION OF QSOs BEYOND z = 2.2

7.1 Introduction

As discussed in chapter 1, the form of QSO evolution at high redshifts, in particular the nature of the QSO 'cut-off', has long been the source of much intensive study. However, to establish the reality of such a 'cut-off', we require both an accurate model for the evolution of QSOs at low redshift and an unbiased method of detecting high redshift QSOs. In this chapter we therefore consider both these aspects in our discussion of the evolution of QSOs at high ($z > 2.2$) redshift.

We first describe techniques devised to select unbiased samples of QSOs with $z > 2.2$. Such techniques are based on broadband methods similar to the UVX technique used at low ($z < 2.2$) redshift, but utilise additional information either in the form of further broadband colours (obtained from the inclusion of V,R and I plates in addition to the U and J plates used previously) or from inspection of spectra on objective prism plates.

Surface densities of high redshift QSOs found from these searches can then be compared to those predicted from extrapolation of the evolutionary model proposed for low redshift ($z < 2.2$) QSOs in chapter 4. From such a comparison, constraints on the decrease in numbers of high redshift QSOs can be obtained.

7.2 The Colour of z > 2.2 QSOs

We begin our description of the broadband techniques used here to select high redshift QSOs, with a discussion of the colours of such objects. We have predicted the colours of high redshift QSOs analytically, by redshifting a composite QSO spectrum through the UK Schmidt passbands (see figure 2.1) and computing the observed colour. The composite spectrum used is plotted in figure 7.1. The long wavelength (λ > 1200 Å) part is taken from the observations of Richstone and Schmidt (1980), with the spectrum at wavelengths shorter than this value being obtained from the spectra of high redshift (z > 2.8) QSOs plotted in Osmer and Smith (1976).

As indicated in chapter 2.2 the ubvri system, in which stellar magnitudes are quoted throughout this thesis, was calibrated using standards quoted in Johnson and Kron-Cousins magnitude systems with no prior correction to the Schmidt passbands. Thus the predicted colours of high redshift QSOs based solely on the above computation, will exhibit zero-point shifts with respect to the colours obtained for stellar images in the ubvri system employed here. Zero-points for the predicted colours were therefore obtained by normalisation to the ubvri colours for the low redshift (z < 2.2) Clowes and Savage (1983) QSOs found on the measured area of the SGP UJVR and I plates. In figure 7.2 we plot the predicted u-b, b-v, v-r and r-i colours (solid line) for QSOs with z < 4. Also plotted are the Clowes and Savage (1983) QSOs (filled circles) used to zero-point these colours. The spread in colours observed for the Clowes and

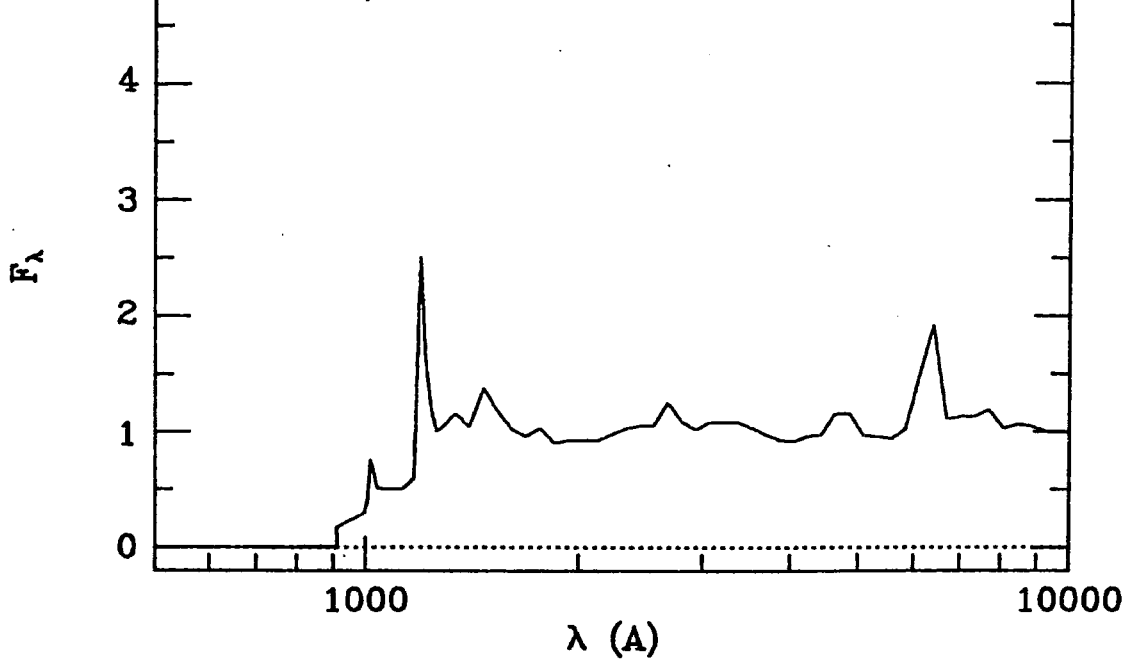

Figure 7.1 Composite QSO spectrum used to predict colours of high redshift ($z > 2.2$) QSOs.

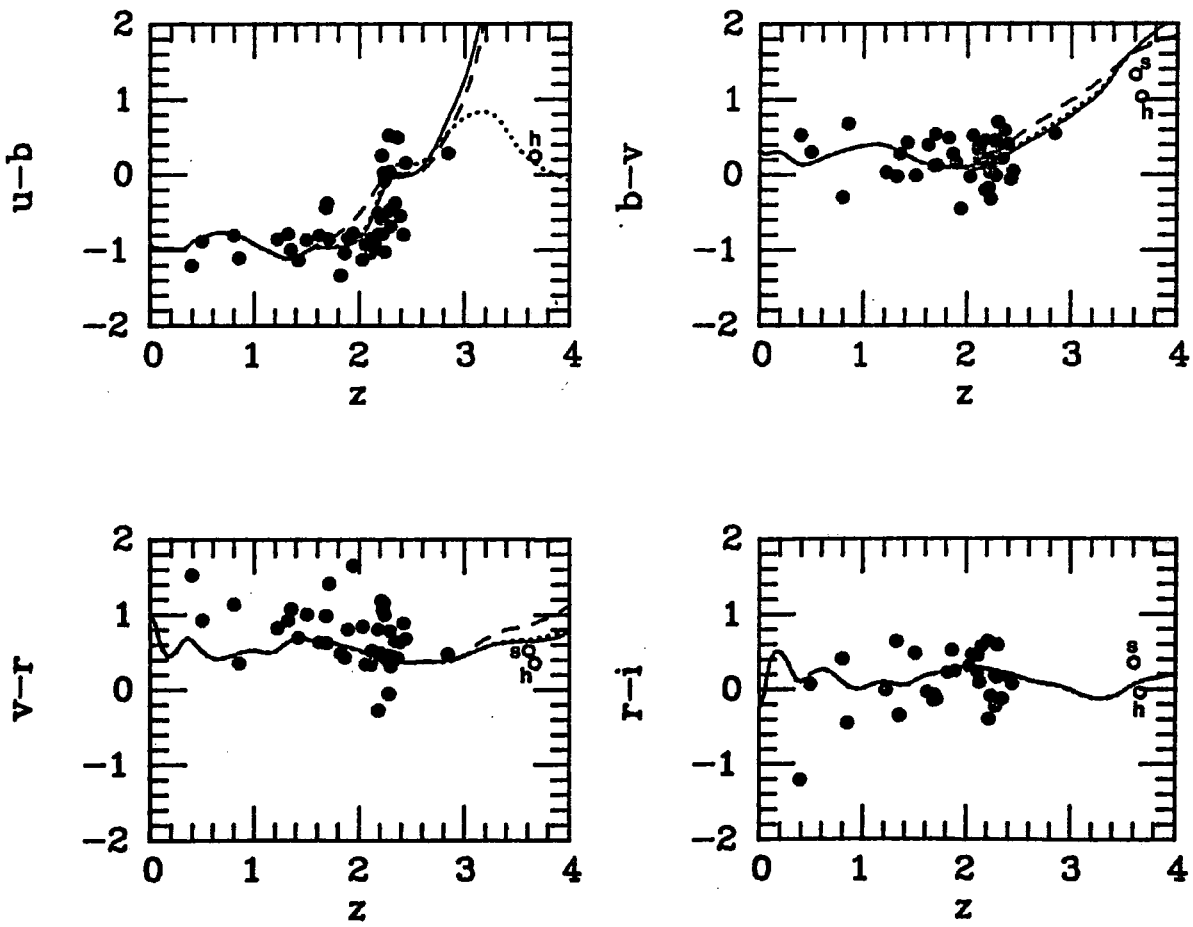

Figure 7.2 Colour-redshift diagram for QSOs. Solid lines indicate prediction for spectrum plotted in figure 7.1. Dashed lines indicate predictions for QSOs with no Lyman α emission. Dotted lines indicate colours of QSOs with a weak Lyman limit (see text). Filled circles denote QSOs from Clowes and Savage (1983) and open circles denote the high redshift QSOs of Shanks *et al.* (1983) and Hazard and McMahon (1984).

Savage (1983) QSOs ($\simeq$ 0.2 - 0.3 mag) about the predicted colour-redshift relations in figure 7.2 will represent a combination of the intrinsic spread in the QSOs' spectral properties coupled with the error in colours obtained from machine measurement (see chapter 2.6)

In figure 7.2 we note that the reddening in the u-b colour index beyond z=2.2 is due primarily to the depression in the continuum bluewards of the Lyman α line (see figure 7.1) being redshifted into the u band. This decrease in flux is caused by the large number of Lyman α absorption lines (the Lyman α forest) seen shortward of Lyman α emission at 1216A blending together and thus depressing the continuum at these wavelengths. The increase in u-b index is also due, in part, to the broad Lyman α line appearing in the J passband at $z > 2.2$. The relative contribution of each of these effects to the reddening of QSO u-b colours at $z > 2.2$ is also demonstrated in figure 7.2. The dashed line in figure 7.2 indicates the colours for QSOs with no Lyman α emission and we see that, while the u-b colour is slightly different for such QSOs, it still reddens as dramatically as for QSOs with strong Lyman α, indicating that the principle cause of the reddening is the Lyman α forest.

The reddening in the b-v index by more than 1.0 mag at $z > 2.9$ occurs for precisely the same reasons - namely, at these redshifts, the Lyman α forest now becomes redshifted into the b band, while the Lyman α emission line appears in the v band. In contrast, the v-r and r-i colours stay reasonably constant (0.3 mag $<$ v-r $<$ 1.0 mag, -0.4 mag $<$ r-i $<$ 0.4 mag) with redshift.

The implications that these changes in colour have on the detection of high redshift QSOs are illustrated in figures 7.3 and 7.4 where we plot various colour-colour diagrams for a sample of stellar images (18 mag < b < 20 mag) on the SGP and the predicted colours for QSOs respectively. We see that, in the range 2.2 < z < 3.0 the predicted colours of QSOs lie in the Galactic star locus for all colour combinations plotted. Although photometric and intrinsic variations in the spectra of QSOs will cause some QSOs to lie outside the Galactic star locus at these redshifts, we can confirm that many QSOs with 2.2 < z < 3.0 have colours indistinguishable from Galactic stars on inspection of figure 7.5. Here we have re-plotted the Clowes and Savage (1983) QSOs on the same colour-colour planes as for the Galactic stars and theoretical redshift tracks in figures 7.3 and 7.4, with the dashed lines in figure 7.5 representing the Galactic star locus in each colour-colour diagram.

Even though the best discrimination from the colours of Galactic stars is obtained for the Clowes and Savage (1983) QSOs (all have z < 3) on the u-b/b-v diagram, at least 7 out of the 16 z > 2.2 QSOs in this sample would not have been detected in a survey which selected QSOs on the basis on their anomalous broadband u-b/b-v colours. It is interesting to note that Koo and Kron (1982) select high redshift (z > 2.2) QSOs from 4m telescope plates using the U-J/J-F diagram, which is similar to the u-b/b-v diagram plotted here. Koo (1986) acknowledges that their survey may be incomplete for z > 2.2 and estimates this incompleteness at 20%.

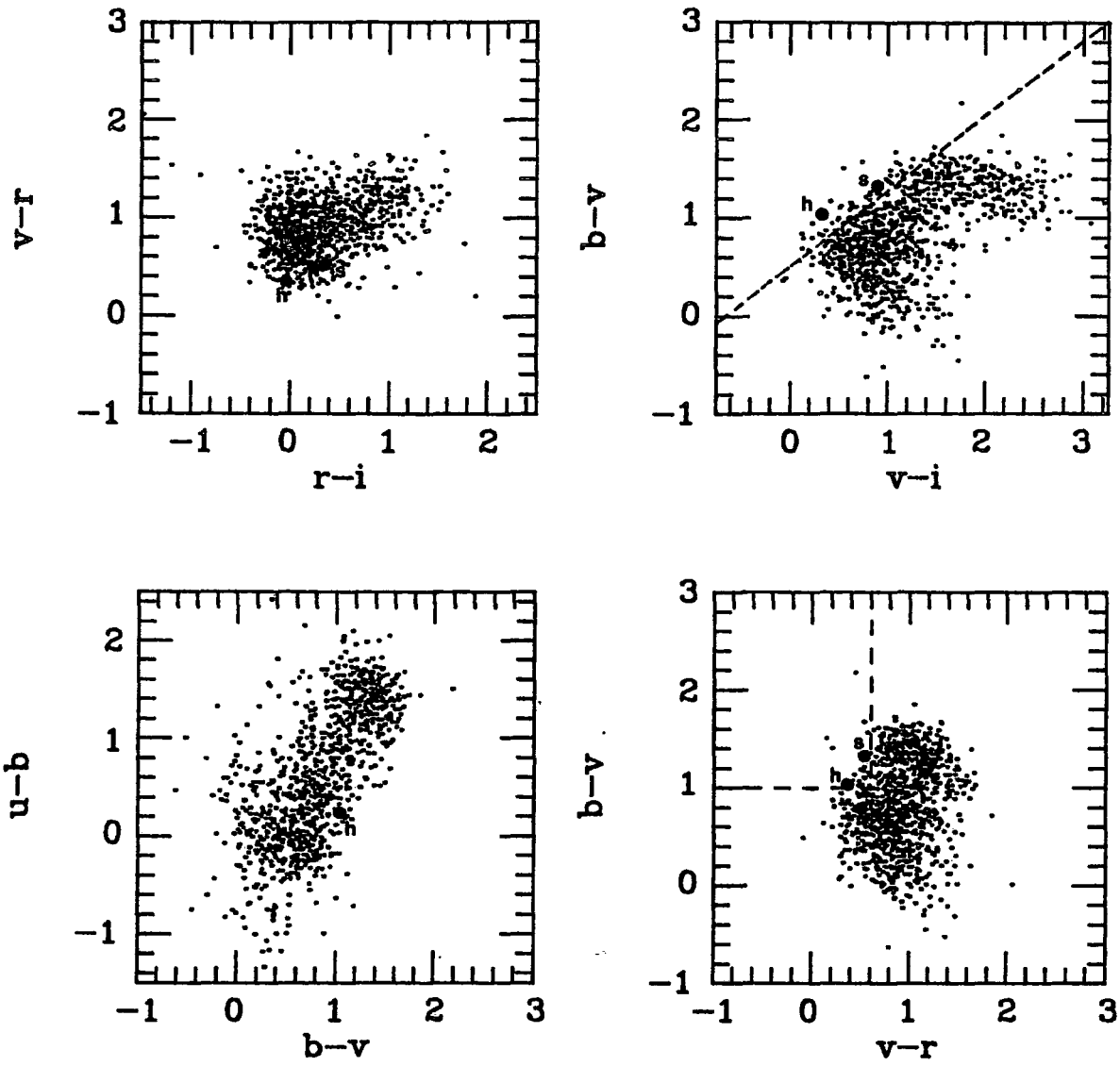

Figure 7.3 Colour-colour plots for stellar images with 18 mag < b < 20 mag in a central 4 square degree area on the SGP field. Large, filled circles denote the high redshift QSOs of Shanks *et al.* (1983) and Hazard and McMahon (1984). Dashed lines indicate selection criteria used to search for high redshift QSOs.

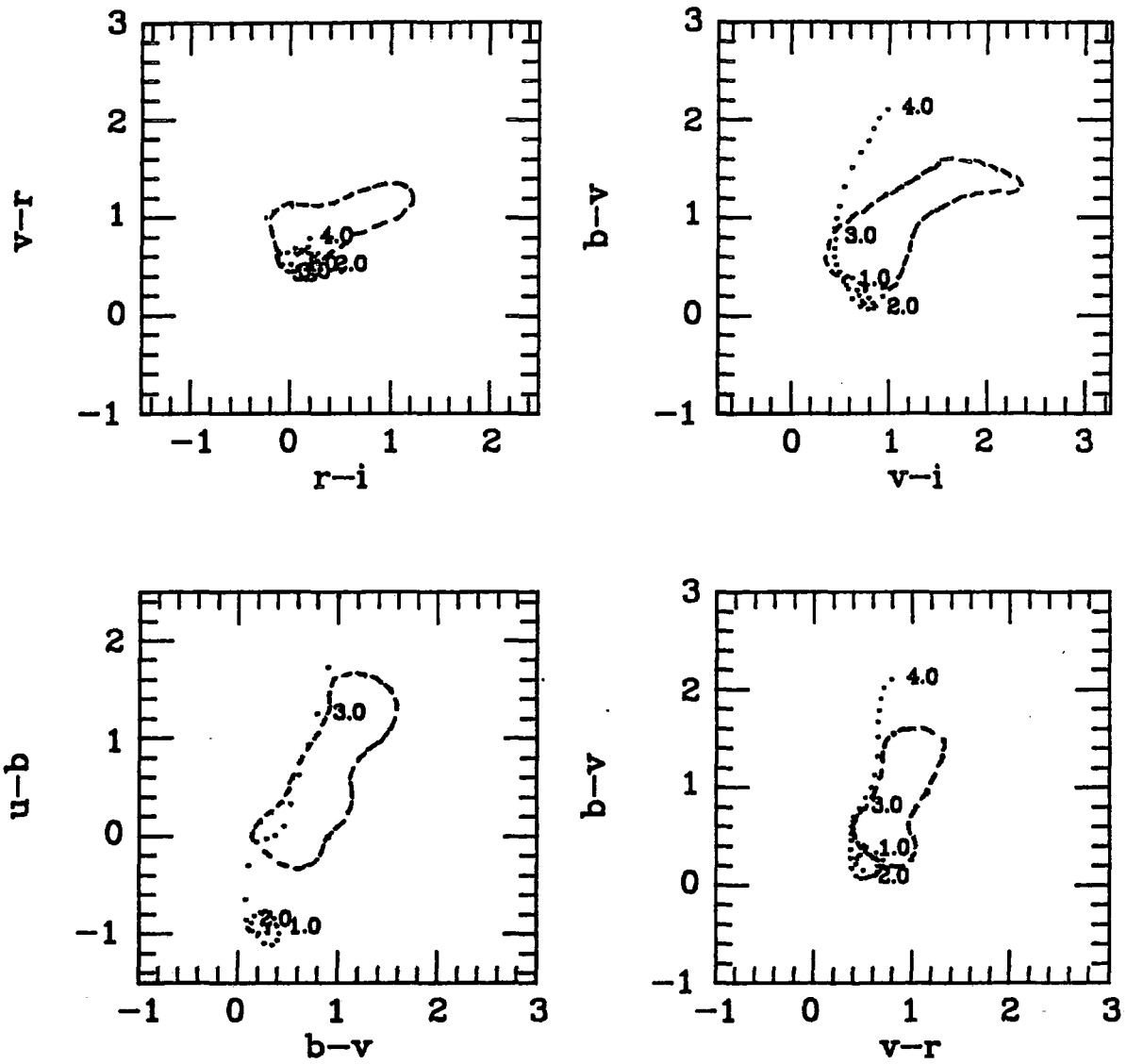

Figure 7.4 Colour-colour predictions for the composite spectrum plotted in figure 7.1. Each dot in the redshift track represents a step of 0.1 in redshift. Major redshift intervals are written alongside the track. Dashed lines represent approximate Galactic star locus (see figure 7.3) in each colour-colour plot.

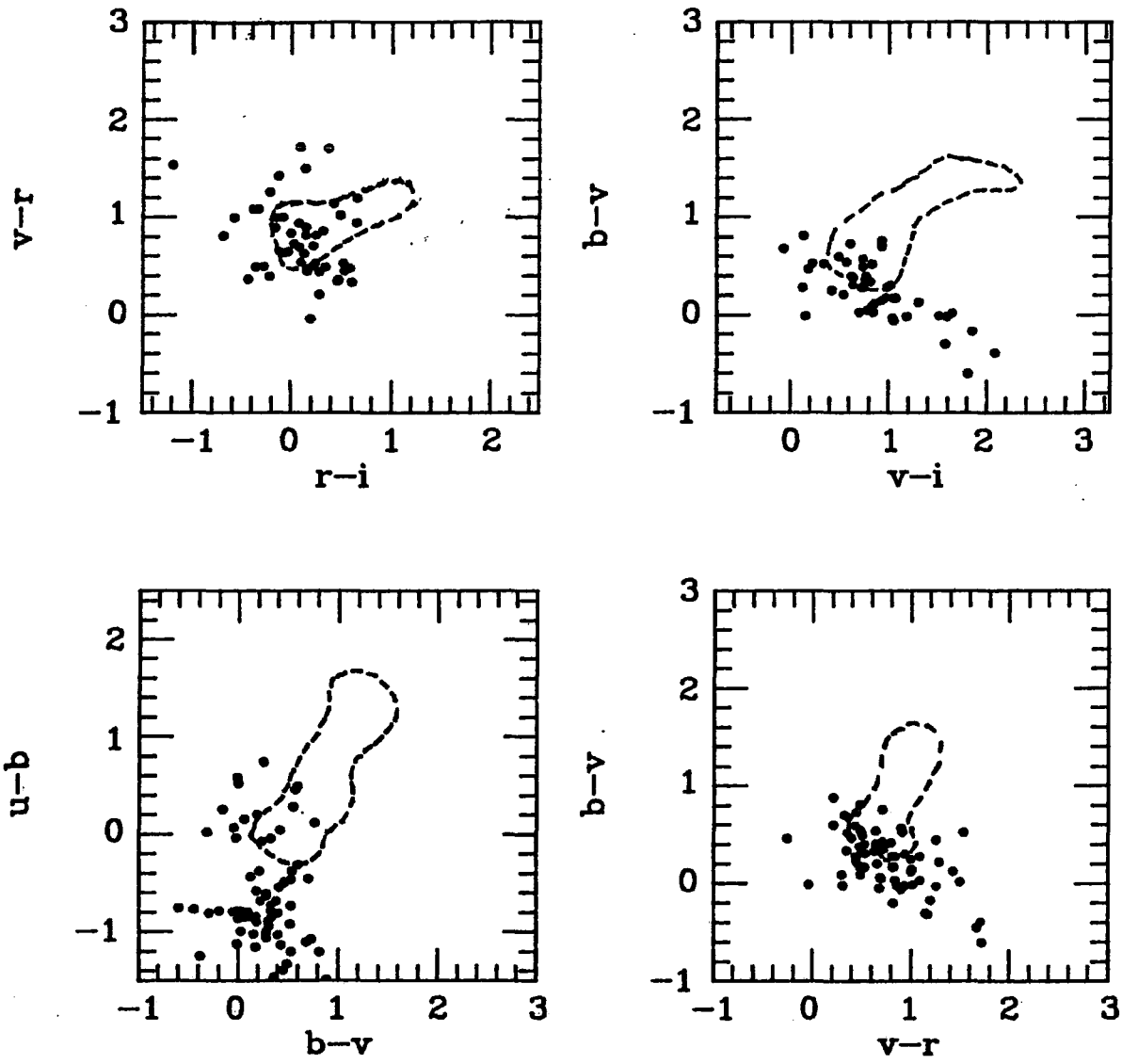

Figure 7.5 Colour-colour diagrams for Clowes and Savage (1983) QSOs. Dashed lines represent approximate Galactic star locus (see figure 7.3) in each colour-colour plot.

At $z > 3.0$ the reddening in the b-v index for QSOs once again takes the predicted colour-colour locus for such high redshift QSOs away from that of the Galactic stars. The best discrimination between the colours of Galactic stars and those predicted for QSOs can be achieved using the b-v/v-i colour-colour plot. This is because the largest contaminant in any sample of stars with red b-v colours will be the late-type K and M stars. Since these stars have redder V-R ($\simeq$ 1.0 mag) and R-I (also $\simeq$ 1.0 mag) colours (Johnson 1963) than those predicted for high redshift QSOs, by taking the largest possible baseline in these colours (v-i), we should be assured of obtaining the best separation from Galactic stars. Although we concede that the sizeable spread ($\simeq$ 0.30 mag) seen in QSO colours about the predicted colour-redshift relations in figure 7.2 could degrade the discrimination provided on the b-v/v-i diagram, we conclude that, even with such a large spread, a considerable fraction (>75%) of $z > 3.5$ QSOs will exhibit anomalous colours with respect to normal Galactic stars on this diagram.

Using the results obtained in this chapter for the colours of high redshift ($z > 2.2$) QSOs we now go on to describe two techniques designed to select QSOs in the redshift range $2.2 > z > 3.0$ and $z > 3.5$.

7.3 The Search for Intermediate Redshift (2.2 < z < 3.0) QSOs

As shown in the previous section broadband colours alone can not be used to select complete samples of QSOs in the redshift range 2.2 < z < 3.0. A method has therefore been devised by Shanks *et al.* (in preparation) which uses additional information from objective prism plates to compile unbiased QSO samples at these redshifts.

The technique is fully detailed in Shanks *et al.* (in preparation) and so only a very brief description will be given here. The method rests on the belief that, in all QSOs, the Lymanα/NV emission line is sufficiently broad to be identified on an objective prism plate when redshifted into the wavelength region over which the relevant photograhic emulsion is sensitive. At the magnitude limit of the search employed here (b = 19.5 mag), all lines with an equivalent width greater than 100Å should be easily identified on a good 'seeing' IIIaJ objective prism plate (Clowes and Savage 1983). Since the smallest measured equivalent width for a Lymanα/NV emission line in the spectroscopic surveys was ≃200Å, all QSOs which exhibit Lymanα/NV should, in principle, be detectable. The spectra for all stars with 18.5 mag < b < 19.5 mag are then visually inspected on a IIIaJ objective prism plate and those objects with strong emission are selected. Knowing that the u-b colour of QSOs reddens dramatically after z = 2.2, high redshift QSOs can be identified from their non-UVX colours and a redshift assigned from the identification of the emission line as Lymanα.

Two objective prism plates have been searched in this manner (UJ3682P (SGP) and UJ2460P (QSM)) by Dr. Shanks and Alison Broadbent, a summer student at the University of Durham. Full details of these searches appear in Shanks *et al.* (in preparation) and only the results directly relevant to the problem of the redshift cut-off will be quoted here.

Over the 11 square degree area searched on the SGP objective prism plate, Miss Broadbent identified 13 emission line objects with red colours, 7 in the redshift range $2.2 < z < 2.5$ and 6 between $2.5 < z < 3.0$. By comparing the surface densities of QSOs in the redshift region in which the UVX and objective prism techniques overlap, we conclude that the search is probably 75% complete, 6 out of the 8 $z > 1.8$ QSOs found in the UVX surveys having been re-discovered in the objective prism search. Tom Shanks found eight $2.2 < z < 2,5$ and three $2.5 < z < 3.0$ QSOs on a 5.7 square degree area searched on the QSM field. As above comparison with known UVX, $z > 1.8$ QSOs on this area revealed that the search was approximately 40% incomplete, although this estimate is based on a small number of objects (3 detections out of 5 possible).

This method will, of course, not identify high redshift QSOs that exhibit UVX. The numbers of such objects can, however, be deduced from the spectroscopic survey as follows. We found 8 UVX QSOs with $2.2 < z < 2.5$ and 2 with $2.5 < z < 3.0$ in the survey, representing approximately 5% and 1% respectively of the total UVX QSO population. Between 18.5 mag < b < 19.5 mag the UVX QSO density is $\simeq$ 8 per square degree (see chapter 4.2.2) and

therefore the corrections to be applied to the surface densities of high redshift QSOs are 0.35 per square degree for UVX QSOs with $2.2 < z < 2.5$ and 0.08 for UVX QSOs with $2.5 < z < 3.0$. Combining the results of the searches on the SGP and QSM fields, we thus arrive at surface densities of 1.7 ± 0.4 and 0.9 ± 0.3 per square degree for $2.2 < z < 2.5$ and $2.5 < z < 3.0$ QSOs respectively, when due account is taken of incompleteness and UVX high redshift QSOs. These values will be discussed further in chapter 7.5.

7.4 The Search for High Redshift ($z > 3.5$) QSOs

As demonstrated in chapter 7.2, the reddening in the b-v index predicted for high redshift ($z > 3.5$) QSOs enables such objects to be selected on the basis of their anomalous colours with respect to ordinary Galactic stars. Samples of high redshift QSO candidates have therefore been compiled on the SGP field using the colour selection criteria indicated by dashed lines in figure 7.3. Selection by colour alone, however, still leaves many Galactic stars in the sample (scattered into the sample through photometric errors, variability etc.) and the samples were reduced further by inspection of objective prism plates (both IIIaJ and IIIaF) to remove all candidates with stellar or featureless spectra.

This broadband technique has already proved successful in detecting DHM0054-284 (Shanks *et al.* 1983b), a QSO with $z = 3.61$. The colours for both this QSO and for the $z = 3.67$ QSO (Q0055-2659) found by Hazard and McMahon (1984) on the SGP are

illustrated (open circles) in figure 7.2. While DHM0054-284 was originally selected on the basis of its anomalous position in the b-v/v-r diagram (as indicated by the dashed lines on this colour-colour diagram in figure 7.3) and Q0055-2659 was found from an objective prism search, both are easily distinguishable from stars on the b-v/v-i diagram (large circles), occupying the same region of this colour-colour plot (see figure 7.3). From the colour-redshift diagram in figure 7.2, we also see that both objects exhibit colours close to those expected from the composite spectra modelling (although only when the variation in Lyman limit systems is taken into account - see below). We note that Q0055-2659 was not selected in our original survey of the SGP area as a candidate high redshift QSO since one of the criteria employed in that search was that high redshift candidates had to have u magnitudes fainter than the U plate limit (i.e. $u > 20.5$ mag $\equiv u-b > 1.5$ mag). We expected that if they existed, high redshift QSOs would exhibit a strong Lyman limit system (see e.g. Tytler 1982) and consequently very little flux would be observed in the U passband. This is certainly the case with DHM0054-284 but Q0055-2659 does not show as strong a Lyman limit. The dramatic effect of even a small variation in the Lyman limit is illustrated in figure 7.2. The solid lines represent the colour redshift relations for a QSO with a strong Lyman limit ($F(\lambda_{<912}) = 0$) whereas the dotted lines indicates those for a QSO with a weaker Lyman limit ($F(\lambda_{<912}) = 0.5F(\lambda_{>912})$). The wide range in the u-b colours for the two types of QSO at $z > 3$ therefore makes the u-b colour a poor discriminator for high redshift QSOs. Removing the u magnitude

criterion in the original survey allowed Q0056-264 to be easily selected as a high redshift candidate (although anything is easy in hindsight).

The implication is that a survey which selects off all stellar images in the region of the b-v/v-i plane indicated by the dashed line in figure 7.3 will contain a number of extremely high redshift ($z > 3.5$) QSOs, if, indeed, they exist. However, there are too few complete samples of high redshift ($z > 3.5$) QSOs with which we can assess the completeness of this technique, and until spectroscopy can be obtained of some of our candidates selected in b-v/v-i, the success rate of this technique is also unknown. Certainly the two $z > 3.5$ QSOs already known to exist on the SGP can readily be distinguished from the bulk of the Galactic stars using this method.

7.5 The Redshift Cut-off

7.5.1 Constraints from Broadband Searches

We now compare the observed surface densities of high redshift QSOs with those predicted from extrapolations of the evolutionary model obtained at low redshift. The surface densities of high redshift QSOs found using the techniques described in the previous sections are presented in table 7.1. The surface density for $3.5 < z < 4.0$ QSOs is based on the two QSOs found on the SGP at these redshifts. While not intended to represent a secure surface density it may be compared to those predicted from models for illustrative purposes. We also give in table 7.1 the surface densities predicted from 3 different

Magnitude and Redshift Ranges	Surface Densities (per square degree)			
	Observed	Predicted		
		A	B	C
18.4 < B < 19.4				
2.2 < z < 2.5	1.7±0.4	1.4(0.66)	1.1(0.54)	1.4(0.66)
2.5 < z < 3.0	0.9±0.3	2.8(0.88)	0.8(0.24)	2.0(0.60)
17.9 < B < 19.9				
3.5 < z < 4.0	0.18?	4.0(0.3)	0.2(0.01)	0.4(0.02)

Table 7.1 Surface densities for High Redshift QSOs

$\langle L_x / L_o \rangle$	α_x	Contribution to X-Ray Background (percentage)		
		A	B	C
1.6×10^{-4}	0.5	78	53	60
8.0×10^{-5}	1.2	19	14	15

Table 7.2 X-Ray Background

extrapolations of the standard luminosity evolution model for a $q_0 = \frac{1}{2}$ universe proposed in chapter 4.3.4. The extrapolations are as follows:

A. Continuous evolution model - rate of evolution at high redshifts ($z > 2.2$) same as that for low redshifts.

B. No evolution model - evolution ceases beyond $z = 2.2$ and the QSOs with $z > 2.2$ remain at same luminosity and number density as those at $z = 2.2$.

C. Composite evolution model - rate of evolution same as that at low redshifts for $z < 2.5$ (as model A), after which evolution ceases (as model B).

The numbers in parentheses are the corresponding surface densities if the evolution derived for the obscuration model proposed in chapter 6 (i.e $k_{L\ dust} = 4.0$, $A_B = 0.2$ mag) is correct.

Of course, much more sophisticated extrapolations than these (i.e. ones in which the evolution changes sign etc.) can be constructed. As we shall see below, however, the observations do not merit such accurate modelling.

On first inspection of table 7.1 it appears that we can clearly rule out model A as its predictions become more and more discrepant with increasing redshift, predicting 3 times as many QSOs as are observed in the redshift range $2.5 < z < 3.0$, giving a surface density of 4 QSOs per square degree (corresponding to

100 over a Schmidt plate) in the range $3.5 < z < 4.0$, 18.4 mag < b < 19.4 mag. Indeed, it would appear that the form of the evolution must change quite soon after redshifts of $z \simeq 2.2$-2.5, as model B is the only one which gives good agreement with the observations, particularly in the redshift range $2.5 < z < 3.0$.

When possible obscuration by dust is taken into account, however, we see a very different story. In this case model A provides a much closer fit to the data, although we note that the numbers in the lowest redshift bin are discrepant. This result is in qualitative agreement with that of Ostriker and Heisler (1984) who argued that small amounts of dust alone could be sufficient to explain the lack of high redshift QSOs, although we note that such a model predicts too few QSOs at intermediate redshifts.

Of course the obscuration model could be discounted on the grounds that it may produce too much reddening in high redshift QSOs. At $z = 3.6$, $\Delta m(z) = 1.5$ mag and objects are reddened by $E_{B-V} = 0.4$ mag. Thus the intrinsic b-v colours of the two high redshift QSOs observed on the SGP will be bluer than their observed b-v colours by this amount. As their b-v colours are already somewhat bluer than those predicted, any further de-reddening will only serve to increae this discrepancy. Thus the colours of such QSOs do place constraints on the amount of dust absorption at high redshift and further, more accurate, measurements of the colours of high redshift QSOs may help to rule out such a model.

Even ignoring the presence of dust, the inferences drawn from the comparison of the observed and predicted surface densities are dependent on the supposition that high redshift QSOs look like their low redshift counterparts, and thus would have been found with the selection techniques whose use is justified on their success at low redshifts. However, most mechanisms (see e.g. Osmer 1982) that have been invoked to account for changes in the spectra for QSOs at high redshift (e.g. disappearance of emission line region, QSOs shrouded by material) require significant changes either internally to the QSO or in the surrounding intergalactic medium. As such, both imply evolution in an even more direct manner than that derived from the study of the statistical properties of the QSO population as a whole.

7.5.2 Constraints from the X-Ray Background

The diffuse X-ray background may also be used to derive contraints on the numbers of QSOs at high redshift, since integrated X-ray luminosity of all QSOs predicted at high redshifts can not exceed the observed X-ray background. The X-ray background is particularly relevant in the light of the work above as X-rays observed at energies greater than 1 keV will have been unaffected by dust and unequivocal constraints may be obtained. From Schwartz (1979), the observed X-ray background intensity at 2 kev is 5.84 keV $cm^{-2}s^{-1}sr^{-1}keV^{-1}$. The contribution from QSOs ($I_{x,q}$) to this background can be expressed as follows (from Marshall *et al.* 1983a):

$$I_{x,q} = \frac{c}{4\pi H_o}\left\langle\frac{L_x}{L_o}\right\rangle\int_{L_{min}}^{\infty}\int_{0}^{z_{max}}\frac{L\Phi(z,L)}{(1+2q_0z)^{0.5}(1+z)^{2+\alpha_x}}\,dzdL \qquad \ldots (7.1)$$

where $\langle L_x/L_o\rangle$ is the average value for the ratio of X-ray luminosity to optical luminosity for radio-quiet QSOs and α_x is the slope of the X-ray spectrum at 2keV. Their values quoted in Zamorani *et al.* (1981) are 1.6 x 10^{-4} and 0.5 respectively. Both these values are, however, extremely uncertain. $\langle L_x/L_o\rangle$ for optically selected QSOs is based on few objects (see Zamorani 1983) and consists mainly of non-detections of these objects at X-ray wavelengths. Correspondingly, the value of $\langle L_x/L_o\rangle$ could be much lower (by as much as 50% from an inspection of figure 4 in Zamorani 1983), thereby reducing the contribution of QSOs to the X-ray background. In addition, recent values for the mean α_x for QSOs have been given as high as 1.2 (Elvis *et al.* 1985) based on a re-examination of Einstein data. This revision will again reduce the contribution from QSOs to the observed X-ray background.

With these uncertainties in mind we calculate the percentage of the X-ray background due to QSOs with z < 4 for models A, B and C of chapter 7.4.1 using two sets of parameters for $\langle L_x/L_o\rangle$ and α_x. The results are presented in table 7.2. All QSOs brighter than a present day value of M_B = -15 were assumed to contribute to the X-ray background, thus including the low luminosity active galactic nuclei and Seyfert galaxies. Because of the flatness of the QSO luminosity function fainter than M_B = -21.5, decreasing this minimum magnitude to M_B = -21 only decreased the contributions given in table 7.2 by, on average,

5%. Similarly, revising the value of $k_L = 4$, to account for obscuration by dust increased the percentage quoted in table 7.2 by $\simeq$ 5%.

We see from table 7.2 that uncertainties in the X-ray spectrum for QSOs do not permit us to put constraints on the evolution of QSOs at high redshift. Even allowing for the $\simeq$ 30% contribution from galaxy clusters and BL Lacs (Schmidt 1986) we see that only model A exceeds the X-ray background and then it is only for one particular choice of parameters. Indeed, the contribution from QSOs may be very low indeed for a different set of parameters. As such, more accurate data is needed on the X-ray spectra of QSOs before the X-ray background can be used to set limits on the evolution of QSOs at high redshift.

7.6 Conclusions

We have demonstrated that broadband techniques are successful in detecting high redshift QSOs, although estimates of their success rates and completeness at the highest redshifts will have to wait until more spectroscopic information is available. Surface densities of high redshift QSOs selected using these broadband techniques have been compared to those predicted from extrapolations of the evolutionary law derived previously for low redshift QSOs. If significant obscuration by dust could be ruled out, the low surface densities for QSOs at $z > 2.5$ indicate that the rate of evolution of the QSO population is 'slowing down' in the range $2.2 < z < 2.5$. However, small amounts of dust could wholly account for the low surface

densities observed. Unfortunately, constraints on the numbers of QSOs at high redshifts are not possible from observations of the X-ray background, as the X-ray spectra of QSOs are not yet sufficiently well defined.

CHAPTER EIGHT

DISCUSSION AND CONCLUSIONS

8.1 Introduction

In previous chapters we have presented results on the clustering and evolution of QSOs obtained from statistical analyses of QSO catalogues. In this chapter we summarise these results, interpreting them in terms of physical models for QSOs derived from theoretical considerations. We attempt to reconcile any models thus favoured with other observations of QSOs, in particular those that are non-statistical in nature. Future observations, which may contribute further to our understanding of the physical processes that govern the QSO phenomenon, are also suggested.

8.2 Theoretical Considerations

Since we will be discussing our results in the context of theoretical models for QSOs, we begin with a brief summary of the work in this field. As remarked on by Rees (1984), the basic theory for the energy production in QSOs has undergone few changes since QSOs were first discovered some twenty years ago. The high luminosities ($10^{45} < L < 10^{48}$ ergs s^{-1}) and rapid variability (over timescales less than 1 day in some cases) have led to the generally accepted conclusion that the energy source in QSOs is gravitational in origin, with material accreting onto a compact object. The best candidate for such an object is a

black hole, as it almost certainly represents the inevitable evolutionary outcome for any such compact system (Rees 1984). Many origins have been suggested for the gas supply to the central black hole, e.g. stellar debris arising from tidal disruptions or stellar collisions in a dense star cluster surrounding the black hole (McMillan *et al.* 1981, Duncan and Shapiro 1983), or from interactions with other galaxies (Stockton 1982).

The luminosities obtainable from such processes are given by (Duncan and Shapiro 1983):

$$L=\varepsilon \dot{M}_h c^2 = 7 \times 10^{45} (\varepsilon/0.1)(\dot{M}_h / M_\odot \, yr^{-1}) \text{ ergs } s^{-1} \quad \ldots (8.1)$$

where $\dot{M}_h$ is the matter accretion rate on the black hole and ε the efficiency of the conversion of gravatational energy into luminosity. Taking ε = 0.1, this being fractional gravitational binding energy for matter at the inner edge of the accretion disk (Shakura and Sunyaev 1976), we find that accretion rates of 0.1 - 10 $M_\odot \, yr^{-1}$ are required to power luminous QSOs. Both stellar collisions and galaxy mergers are probably capable of supplying these fuel input rates (see McMillan *et al.* 1981 and Stockton 1982).

Other mechanisms for the means of energy production in QSOs have also been proposed. In particular, models in which a rotating Kerr black hole taps its spin energy to produce the observed luminosity (Blandford and Znajek 1977), have received much attention. However, it appears unlikely that such mechanisms are capable of supplying the energy source for

luminous QSOs (Cavaliere *et al.* 1983), but gain increasing importance at Seyfert luminosites.

We will therefore take as our working model a scenario in which the energy production in QSOs is dominated by the release of gravitational energy in an accretion disk surrounding a black hole. Material can be supplied to the accretion disk either as the result of local effects, such as debris from stellar collisions or by external effects i.e. an interaction or merger between galaxies. While we recognise that the above picture is perhaps over-simplified, we note that Rees (1984) has stressed how little is still known about the physical processes occurring in QSOs, emphasising that the basic model adopted above still provides the 'best-bet' after some 20 years of research.

8.3 The Luminosity Evolution of QSOs

In chapter 4 we demonstrated that the statistical evolution of the QSO LF could be parameterised by a uniform shift towards higher luminosities in the past, with no corresponding increase in the density of QSOs. There are at least two possible interpretations of this parameterisation:

a. The form obtained reflects the evolution of individual, and therefore long lived, QSOs.

b. The parameterisation represents the evolution in average luminosity for successive generations of short lived QSOs.

The true interpretation may, of course, be more complex than the alternatives proposed here, but it will be of profound physical importance to establish which is closer to reality.

We first consider alternative a). The long QSO lifetimes (from $z = 2.2$ to $z = 0$ represents $4 \times 10^9 h^{-1}$ yr in a $q_0 = \frac{1}{2}$ universe) imply that interactions, with their relatively short timescales ($\simeq 10^7$ yr, see Stockton 1982), are unlikely to form the fuel supply in such QSOs. However, such long lifetimes are consistent with models in which the fuel supply to the black hole is dominated by gas from stellar collisions (Duncan and Shapiro 1983). Moreover, these models also predict a power law evolution with time in the gas supply rate to the QSO ($\dot{M}_h \propto t^n$), which, by equation (8.1), would give rise to the same power law evolution in the QSO luminosity ($L \propto t^n$) as inferred from our study of the QSO LF in chapter 4. Typical values for n are $\simeq 2$ (McMillan *et al.* 1981), close to the value of $n = 2.5$ we obtain from our standard evolution model in a $q_0 = \frac{1}{2}$ universe.

In this long lived model Seyfert galaxies could then be interpreted as the end points of QSO evolution, where the gas supply rate has dwindled almost to exhaustion. One important consequence of the assumption that QSOs are long lived (to be discussed later) is that only the fraction of galaxies that we observe today as Seyferts (0.1-1%, as determined from the Seyfert and galaxy luminosity functions, see chapter 4.3.6) have ever exhibited QSO activity in the past.

Within this basic model, the real situation is likely to be more complex. In particular, alternative energy generating mechanisms (e.g spin energy) may compete with those that are gravitational in origin at low, Seyfert-type, luminosities, slowing down the rate of luminosity evolution in such objects. The effect on the QSO LF would then be to cause the faint end of the LF to steepen at low redshifts (Cavaliere *et al.* 1985) as more and more QSOs 'pile up' at faint luminosities. Cavaliere *et al.* (1985) demonstrate that the effect is small and it will require further observations of faint, B > 20 mag, QSOs before the LF is sufficiently well defined at these luminosities for such an effect to be detectable.

Such considerations, however, do not change the basic assumption that QSOs are long lived. We now go on to discuss whether such an assumption is consistent with other observations of QSOs.

The lifetime for a QSO which radiates at its Eddington luminosity (i.e. the luminosity at which radiation pressure balances the gravitational force), L_{Edd}, is given by (Rees 1984):

$$t = 4 \times 10^7 h(\varepsilon/0.1)yr \quad \ldots (8.2)$$

For a QSO to be long lived ($\simeq 10^{10}$yr) it must therefore radiate below its Eddington luminosity, which, from Rees (1984) can be expressed as:

$$L_{Edd} = 1.3 \times 10^{46} M_8 \text{ ergs } s^{-1} \quad \ldots (8.3)$$

where M_8 is the mass of the black hole in units of $10^8 M_\odot$. A

'typical' M^* (M_B = -26) QSO at z = 2.2 has a luminosity, L, given by (Marshall *et al.* 1984)

$$L = \mathrm{dex}[0.4(89.82-M)] \quad \ldots (8.4)$$

of 2 x 10^{46} ergs s^{-1}. The QSO described above will therefore radiate at sub-Eddington luminosities for a black hole of mass greater than 2 x $10^8 M_\odot$. The mass of this black hole will, of course, be steadily increasing as it accretes gas. From equation (8.1), the gas supply necessary to attain a luminosity of 2 x 10^{46} ergs s^{-1} will be $\simeq$ 3 $M_\odot yr^{-1}$ (ε = 0.1). As more and more matter accretes onto this black hole, it will continue to increase in mass, finally ending up (assuming the model of McMillan *et al.* with $M_h \propto t^{-2}$ from z = 2.2, after initial constant phase lasting $\simeq 10^8$ year) with a mass of 0.5 - 1.0 x $10^9 M_\odot$. This is just below the upper limits of 10^9-$10^{10} M_\odot$ derived for the masses of black holes in QSOs from X-ray variability studies (Zamorani *et al.* 1984). Light travel time arguments (Rees 1984) give an upper limit to the mass of any compact object observed to vary over a time scale of t seconds as follows:

$$M_\odot = t/(500 \text{ seconds}) \quad \ldots(8.5)$$

Thus the timescales of < 10^5 secs seen by Zamorani *et al.* (1984) place tight constraints on the massive black holes required by this long lived model. The prediction of 0.5 - 1.0 x $10^9 M_\odot$ is, however, born out by the observations of Ulrich *et al.* (1984). From an analysis of the variability in the IUE spectrum of NGC 4151, they estimate the mass of the compact object at the centre of this Seyfert galaxy to be 0.5 - 1.0 x $10^9 M_\odot$.

We conclude, therefore, that alternative a) is not inconsistent with current theoretical predictions and other observations of active galactic nuclei. We note, however, that the masses of the remnant black holes in such a model are large and if variability time scales over periods of less than an hour are observed then this model will have to be re-considered.

What, then, of alternative b? At first sight, the short lifetimes ($\simeq 10^7$ yr) inferred (Longair and Riley 1979) for the radio emission in double lobed radio QSOs might imply that the optical properties are also short lived. However, such short lifetimes imply that, with $\simeq$ 1000 generations of QSOs since $z = 2.2$, every galaxy at the present day has undergone QSO activity for $\simeq 10^7 - 10^8$ yr during its life. Assuming that energy is derived gravitationally, accretion rates of 0.1 - 1 $M_\odot$ yr^{-1}, would imply that massive black holes ($10^7 - 10^8 M_\odot$)[1] will reside in all galaxies at the present epoch. In the centre of our own galaxy, at least, this appears not to be the case. While a compact object may exist here (Lo *et al.* 1985), lastest estimates of its mass are only $\simeq 100 M_\odot$ (Allen and Sanders 1985).

Conclusive evidence for massive black holes in other galaxies from studies of radial velocity measurements (Sargent *et al.* 1978) or surface brightness profiles (Young *et al.* 1978) is difficult to obtain as the resolution of such studies are

[1] We note that independent arguments by Rees (1984) and Soltan (1982) also give remnant masses of $10^9 M_\odot$ and $10^7 - 10^8 M_\odot$ for long and short lived QSOs respectively.

critically limited by 'seeing'. As demonstrated by Dressler (1980) the evidence for the massive black hole at the centre of M87 is dependent on structure within the central 20pc. Such resolution is only attainable with the Hubble Space Telscope (HST).

We conclude that the necessity to have massive black holes in the centres of most galaxies makes the short lived QSO model less consistent with the observations than the simpler, long lived interpretation for the statistical evolution of the QSO LF. However, since it is clear that estimation of the mass of compact objects at the centres of galaxies and QSOs is crucial to our understanding of how QSOs evolve, we may therefore hope that the proposed observations to determine such masses with the HST will prove invaluable in this respect.

A critical test of pure luminosity evolution that can also be carried out with the HST is to establish whether significant numbers of low redshift ($z<2.2$) QSOs exist at $B > 25$ mag. According to PLE, such objects will be the luminous, evolved counterparts of the faint ($M_B \simeq -12$), nearby ($z \simeq 0.01$) galactic nuclei observed by Filippenko and Sargent (1985) to have broad QSO-like components in their emission line spectra. Consequently, if no $z<2.2$ QSOs are found at $B = 25$ mag this will imply a cut-off in the LF at faint magnitudes in the redshift range $0.5 < z < 2.2$ that is not observed in the present day Seyfert LF (see figure 4.8), and thus that the 'conservation of number' implicit in the PLE hypothesis does not hold.

Up until now we have been concerned with interpreting the optical properties of QSOs in terms of a physical model for the QSO phenomenon. Although not explicitly dealt with in previous chapters, how then do we explain the radio properties of QSOs in terms of our long lived model for QSOs? We have already mentioned the fact that the lifetime for radio emission from QSOs is likely to be much less than that we infer from the optical properties of QSOs. Moreover, there are further problems in integrating radio QSOs into the evolutionary scenario described above, in that luminosity dependent density evolution derived for the radio QSO population from statistical studies (Peacock and Gull 1981), is at variance with the PLE model favoured here for optically selected QSOs.

To reconcile the observed properties of radio QSOs and optical QSOs we need to establish whether or not these properties in individual QSOs are correlated. However, Peacock *et al.* (1986) conclude that the data available at present is insufficient to establish any such correlation (or lack of it) and they stress the importance of obtaining complete radio coverage (down to sub-mJy flux levels) on optical surveys of QSOs limited at faint magnitudes. In this respect radio observations of the QSOs found in our faint UVX survey will be particularly useful. Indeed the areas over which we obtained spectroscopic identifications (i.e. the 40 arcmin FOCAP fields) are ideally matched to the 'field of view' of the C array on the Very Large Array (VLA). Radio observations can therefore be carried out on $\simeq$ 15 optically selected QSOs simultaneously. Thus integration

times sufficient to reach sub-mJy level can be obtained, whereas previously the low surface density of bright (B < 20 mag) QSOs permitted only brief 'snapshots' of single QSOs if one wished to obtain complete radio coverage for an optically selected sample.

8.4 QSOs at High Redshift

As discussed in chapter 7, results regarding the evolution of QSOs at high redshift have proven somewhat inconclusive. If we can discount the effect of dust at high redshift (see below), the observed surface densities of high redshift ($z > 2.2$) QSOs are consistent with the luminosities of QSOs ceasing to increase beyond a redshift of $z \simeq 2.2$-2.5 and remaining constant up to a redshift of 4, a period of $4 \times 10^8 h$ Gyr. This is in qualitative agreement with the short ($\simeq 10^8$ yr), constant luminosity phase predicted by the theoretical models in whch the black hole is fuelled by debris from stellar collisions (see e.g. McMillan *et al.* 1981), discussed in chapter 8.2. However, further spectroscopic surveys of high redshift QSOs are needed to enable explicit construction of the QSO LF at high redshifts and thus track evolution in a similar manner to the procedure followed for the UVX QSOs.

At present, probably the best way to provide such catalogues will be based on the selection procedures combining broadband colours and objective prism searches described in chapter 7. In particular, if several Schmidt plates can be obtained for every passband in a particular area, the errors associated with the Schmidt magnitudes can be driven down to a level where colour

selected samples of anomalous objects will contain minimal contamination from Galactic stars. However, no matter how accurate they may be, broadband surveys for high redshift QSOs are always open to criticism on the grounds of incompleteness. Such objections can only be removed by spectroscopically surveying all stellar images in a magnitude limited sample. Unfortunately, to obtain sufficiently large surface densities for high redshift ($z > 2.2$) QSOs (50 per square degree) to construct an accurate LF, such a survey would have to extend to $B \simeq 23$ mag, where the surface density of Galactic stars is $\simeq 1000$ per square degree. While, at present, such observations of large numbers of extremely faint objects are clearly out of the question, current advances in new multi-slit spectrographs (e.g. the Low Dispersion Slit Spectrograph), coupled with the development of new, large format CCD detectors by Tektronix, make such surveys an exciting prospect for the future.

As a tailpiece to this section we consider the problem of dust associated with galaxy clusters invoked in chapter 6 to explain the observed anti-correlation of QSOs with respect to galaxy clusters. If we ever wish to ascertain the true evolution of QSOs at high redshifts, it is vital that any significant effect due to dust be either quantified or, better still, ruled out. To do so, we require some independent method of estimating the amount of dust present in clusters. Perhaps the most encouraging prospect is to look for thermal emission from dust in clusters as observed by IRAS. While the sensitivity of IRAS is still too low to detect dust from the more distant clusters, it

may be present in nearby clusters. In addition, since the effect of dust is expected to be at its strongest for the highest redshift QSOs, further observations of their broadband BVRI colours may help to rule out significant reddening (and thus large amounts of intervening dust) at these high redshifts.

8.5 QSO Clustering

We choose to end this discussion of our results by concentrating on the property of the QSO population which perhaps holds the greatest potential for future investigation, namely the clustering of QSOs.

We have already demonstrated in chapter 5 that the QSO correlation function is a powerful diagnostic tool for ascertaining the structure of the universe at large scales. Strong constraints have been placed on the homogeneity of the universe at scales $> 100h^{-1}$ Mpc. In addition, low S/N features have been identified which, if confirmed with further observations, may not only provide evidence for a baryon dominated universe, but also afford a test for q_0.

However, it is not only in its role as a probe of the structure of the universe that the clustering of QSOs is of fundamental importance. At the smallest scales the amplitude of the QSO correlation function may reveal vital clues to their environment and consequently to the mechanisms giving rise to the QSO phenomenon.

As shown in chapter 5, QSOs do indeed exhibit strong clustering at scales $\leq 10h^{-1}$Mpc. Although further observations are required to determine accurately the amplitude of this clustering, at present it appears that QSOs cluster more strongly than galaxies but less strongly than rich clusters of galaxies. We view it as highly significant that numerous studies (e.g. Weymann *et al.* 1978, Yee and Green 1984) involving direct imaging of low redshift QSOs and their cross-correlation with galaxies find that, while QSOs do not inhabit the richest of clusters (Abell class 1 and greater), they are found in small compact clusters whose central densities are at least as high as those observed in the richest of clusters (Yee and Green 1984). As discussed before, the assumption that QSOs are long lived implies that only 0.1-1% of all galaxies have ever undergone QSO activity. We may therefore expect that the conditions which give rise to QSOs are extremely selective. As QSOs require both massive black holes and large stockpiles of energy close to this source, we may therefore expect QSOs to form only in the centres of the strongest density inhomogeneities in the early universe, which we see today as these compact clusters. However, this is far from the only implication that can be drawn from the observation that QSOs are found in small, dense clusters. Stockton (1982) cites the existence of close, and therefore possibly interacting, companions to QSOs in these tight groups as a mechanism for fuelling QSOs. While mergers are unlikely to be capable of fuelling QSOs over the timescales (10^{10}yr) required by the long lived scenario favoured above, we note that Stockton (1982) based his conclusions on observations of radio QSOs,

which, as discussed above, do exhibit differences in their evolution from their optically selected counterparts.

A scenario in which, as the result of a merger or an interaction between galaxies, radio QSOs are merely rejuvenated optical QSOs could be invoked to reconcile the observed properties of radio QSOs with those of optically selected QSOs (e.g. short/long lifetimes, elliptical/spiral morphology) but such a model will remain speculative until further observations are made.

There are two possible ways in which future work into the environment of QSOs can be directed.

1. More direct imaging of distant QSOs in the range $0.5 < z < 1.0$. Many scenarios requiring some form of density evolution in the QSO population predict (Stocke and Perronod 1981) that, at these redshifts, QSOs will be found in richer clusters than they are presently observed in at lower ($z < 0.5$) redshifts. Galaxy counts around Seyferts should also be made, since, under the PLE hypothesis, Seyferts are merely evolved QSOs. Comparison of the galaxy clustering around Seyferts may then be compared to that around QSOs at $z \simeq 0.5$ to determine any evolution in the environment of QSOs at low redshifts. Futhermore, similar studies should also be carried out around the broad line radio galaxies, since they may be interpreted as the evolutionary counterparts of the radio QSOs. Establishing the link between the environments of these two different classes of object might then, by

association, similarly establish an environmental (and perhaps evolutionary) link between radio-quiet and radio-loud QSOs

2. More spectroscopic observations of UVX catalogues using FOCAP to drive the noise down on the amplitude of the QSO correlation function at small scales.

8.6 Coda

In this chapter we have attempted to draw together all the various results presented in this thesis, interpreting them in terms of a coherent physical model for QSOs. In doing so, it is clear that, while much of the observational and theoretical work is compatible, many problems have yet to be resolved. We find that the results obtained from our statistical approach can be interpreted in terms of a model for optically selected QSOs in which they are long lived, having formed prior to redshifts of 2.2, and dim gradually in luminosity until the present epoch, possibly fuelled by mechanisms internal to the host galaxy (e.g. debris from stellar collisions).

Within this simple picture the real situation is undoubtedly more complex, in particular we still have to explain the role of radio QSOs and other subsets of the QSO phenomenon (e.g. BL Lacs, BAL QSOs) which this particular statistical approach has prevented us from investigating closely.

However, with the advance in modern astronomical instrumentation represented by the advent of multi-object spectroscopy, large CCD detectors and the imminent launch of the HST, we are surely on the verge of a new era in QSO research. Properly used this new technology can only lead us to a better understanding of the QSO phenomenon and the role it plays in the universe.

REFERENCES

The following non-standard abbreviations to journals are used:

A.J. - Astronomical Journal

Ap.J. - Astrophysical Journal

Ap.J. Suppl. - Astrophysical Journal, Supplement Series

MNRAS - Monthly Notices of the Royal Astronomical Society

PASP - Publications of the Astronomical Society of the Pacific

Abell,G.O. 1975, in *Stars and Stellar Systems Vol IX*, p601, eds A.Sandage,M.Sandage and J.Kristian, (University of Chicago Press).

Allen,D.A. and Sanders,R.H. 1985, Nature, submitted.

Allen,C.W. 1973, *Astrophysical Quantities*, 3rd. edition, (University of London).

Arp,H. 1970, A.J., **75**, 1.

Arp,H. 1981, Ap.J., **250**, 31.

Arp,H. 1984, Ap.J., **277**, L27.

Arp,H. and Hazard,C. 1980, Ap.J., **240**, 726.

Avni,Y. and Bachall,J.N. 1980, Ap.J., **235**, 694.

Bachall,N.A. and Soneira,R.M. 1983, Ap.J., **270**, 20.

Blair,M. and Gilmore,G. 1982, PASP, **94**, 742.

Blandford,R.D. and Znajek,R.L. 1977, MNRAS, **179**, 433.

Bogart,R.S. and Wagoner,R.V. 1973, Ap.J., **181**, 609.

Boyle,B.J.,Fong,R. and Shanks,T. 1983, in *Quasars and Gravitational Lenses*, 24th Liege Astrophysical Symposium, p348.

Boyle,B.J.,Fong,R. and Shanks,T. 1984, in *Astronomy with Schmidt-Type Telescopes*, p467, ed. M.Capaccioli, (D.Reidel).

Boyle,B.J.,Fong,R.,Shanks,T. and Clowes,R.G. 1985, MNRAS, **216**, 623.

Braccesi,A.,Formiggini,L. and Gandolfi,E. 1970, Astron. & Astrophys., 5, 264.

Braccesi,A.,Zitelli,V.,Bonoli,F. and Formiggini,L. 1980, Astron. & Astrophys., **85**, 80.

Burstein,D. and Heiles,C. 1982, A.J., **87**, 1165.

Campusano,L.E. and Torres,C. 1983, A.J., **88**, 1304.

Cannon,R.D. 1974, MNRAS, **167**, 551.

Carswell,R.F. and Strittmatter,P.A. 1973, Nature, **242**, 394.

Cavaliere,A.,Giallongo,E. and Vagnetti,F. 1983, Ap.J., **269**, 57.

Cavaliere,A.,Giallongo,E. and Vagnetti,F. 1985, Ap.J., **296**, 402.

Chen,J.-S. 1984, Astron. & Astrophys., **134**, 306.

Chu,Y. and Zhu,X. 1983, Ap.J., **267**, 4.

Clowes,R.G. 1981, MNRAS, **197**, 731.

Clowes,R.G.,Cooke,J.A. and Beard,S.M. 1984, MNRAS, **207**, 99.

Clowes,R.G. and Savage,A. 1983, MNRAS, **204**, 385.

Crane,P. and Hoffman,A. 1973, Ap.J., **186**, 787.

de Vaucouleurs,G. and Buta,R. 1983, A.J., **88**, 939.

Dressler,A. 1980, Ap.J., **240**, L11.

Duncan,M.J. and Shapiro,S.L. 1983, Ap.J., **268**, 565.

Ellis,R.S.,Gray,P.M.,Carter,D. and Godwin,J.G. 1984, MNRAS, **206**, 285.

Elvis,M.,Wilkes,B.J. and Tanenbaum,H. 1985, Ap.J., **292**, 357.

Fairall,A.P. 1976, Mon. Not. astr. Soc. S. Afr., **35**, 53.

Ferguson,D.H.,Green,R.F. and Liebert,J. 1985, Ap.J., **287**, 320.

Field,G.B., Arp,H. and Bachall,J.N. 1973,
The Redshift Controversy, (W.A.Benjamin Inc.).
Filippenko,A.V. and Sargent,W.L.W. 1985, Ap.J. Suppl., **57**, 503.
Fong,R.,Godwin,J.G.,Green,M.R. and Shanks,T. 1983,
Occ. Rep. R. Obs. Edin., **10**, 61.
Formiggini,L.,Zitelli,V.,Bonoli,F. and Braccesi,A. 1980,
Astron. & Astrophys. Suppl., **39**, 129.
Garstang,R.H. 1977, Rev. Mod. Phys., **40**, 105.
Gehren,T.,Fried,J.,Wehinger,P.A. and Wyckoff,S. 1984,
Ap.J., **278**, 11.
Godwin,J.G. and Peach,J.V. 1977, MNRAS, **181**, 323.
Gott,J.R. and Turner,E.L. 1977, Ap.J., **216**, 357.
Grandi,S.A. 1981, Ap.J., **251**, 451.
Grandi,S.A. 1982, Ap.J., **255**, 25.
Gray,P.M. 1984, in *Instrumentation in Astronomy*,
SPIE proc. **V445**, 57.
Green,R.F. 1980, Ap.J., **238**, 685.
Hawkins,M.R.S. 1981, MNRAS, **194**, 551.
Hawkins,M.R.S. and Stewart,N.J. 1981, Ap.J., **251**, 1.
Hazard,C. and McMahon,R. 1985, Nature, **314**, 238.
Hazard,C,Morton,D.C.,Terlevich,R. and McMahon,R. 1984,
Ap.J., **282**, 33.
Hewett,P.C.,Irwin,M.J., Bunclark,P.,Bridgeland,M.T.,
Kibblewhite,E.J.,He,X.T. and Smith,M.G. 1985, MNRAS, **213**, 971.
Hoag,A.A. and Schroeder,D.J. 1970, PASP, **82**, 1141.
Hoag,A.A. and Smith,M.G. 1977, Ap.J., **217**, 362.
Jacoby,G.H.,Hunter,D.A. and Christian,C.A. 1984,
Ap.J. Suppl., **56**, 257.

Johnson,H.L. 1963, in *Stars and Stellar Systems Vol. III*, p204, ed. K.A.Strand, (University of Chicago).

Karachentzev,I.D. and Lipovetskii,V.A. 1969, Soviet Astron. A.J., **12**, 909.

Kaiser,N. 1984, Ap.J., **284**, L9.

Koo,D.C. 1983, in *Quasars and Gravitational Lenses*, 24th Liege Astrophysical Symposium, p240.

Koo,D.C. 1986, in *The Structure and Evolution of Active Galactic Nuclei*, ed. F.Mardirossian, (D.Reidel), in the press.

Koo,D.C. and Kron,R.G. 1982, Astron. & Astrophys., **105**, 107.

Kron,R.G. 1978, Ph.D. Thesis, University of California, Berkeley.

Kron,R.G. and Chiu,L.T. 1981, PASP, **93**, 397.

Lang,K.R. 1980, *Astrophysical Formulae*, (Springer-Verlag).

Lea,S.M.,Silk,J.,Kellogg,E. and Murray,S. 1973, Ap.J., **184**, L105.

Liebert,J.,Schmidt,G.D.,Green,R.F.,Stockman,H.A. and McGraw,J.T. 1983, Ap.J., **264**, 262.

Liebert,J.,Schmidt,G.D.,Sion,E.M.,Starrfield,S.G.,Green,R.F. and Boronson,T.A. 1985, PASP, **97**, 156.

Lo,K.Y.,Backer,D.C.,Ekers,R.D.,Kellerman,K.I.,Reid,M and Moran,J.M. 1985, Nature, **315**, 124.

Longair,M.S. and Riley,J.M. 1979, MNRAS, **188**, 615.

Longair,M.S. and Scheuer,P.A.G. 1970, MNRAS, **151**, 45.

Lynden-Bell,D. 1971, MNRAS, **155**, 95.

MacAlpine,G.M.,Lewis,D.W. and Smith,S.B. 1977, Ap.J. Suppl., **35**, 203.

MacGillivray,H.T.,Martin,R.,Pratt,N.M.,Reddish,V.C.,Seddon,H., Alexander,L.W.G.,Walker,G.S. and Williams,P.R. 1976, MNRAS, **176**, 265.

MacGillivray,H.T. and Dodd,R.J. 1982, Observatory, **102**, 141.

MacGillivray,H.T. and Stobie,R.S. 1985,
Vistas in Astronomy, **27**, 433.

Malkan,M.A. 1984, Ap.J., **287**, 555.

Marano,B.,Zamorani,G. and Zitelli,V. 1986, in
The Structure and Evolution of Active Galactic Nuclei,
ed. F.Mardirossian, (D.Reidel), in the press.

Margolis,S.H. and Schramm,D.N. 1977, Ap.J., **214**, 339.

Marshall,H.L. 1985, Ap.J., in the press.

Marshall,H.L. 1986, in *The Structure and Evolution of Active Galactic Nuclei*, ed. F.Mardirossian, (D.Reidel), in the press.

Marshall,H.L.,Avni,Y.,Tananbaum,H. and Zamorani,G. 1983a,
Ap.J., **269**, 35.

Marshall,H.L.,Tananbaum,H.,Huchra,J.P.Braccesi,A.
and Zitelli,V. 1983b, Ap.J., **269**, 42.

Marshall,H.L.,Avni,Y.,Braccesi,A.,Huchra,J.P.,Tanenbaum,H.,
Zamorani,G. and Zitelli,V. 1984, Ap.J., **283**, 50.

Martin,P.G. 1978, *Cosmic Dust*, (Oxford: Clarendon Press).

Masson,C.R. 1978, MNRAS, **185**, 9P.

Mathez,G. 1976, Astron. & Astrophys., **53**, 15.

Matthews,T.A. and Sandage,A.R. 1963, A.J., **138**, 50.

McMillan,S.L.W.,Lightman,A.P. and Cohn,H. 1981,
Ap.J., **251**, 436.

Metcalfe,N. 1983, D.Phil. Thesis, Oxford University.

Mihalas,D. and Binney,J. 1981, *Galactic Astronomy*,
2nd. Edition, (Freeman).

Mitchell,K.J., Warnock,A. and Usher,P.D. 1984, Ap.J., **287**, L3.

Morton,D.C. and Tritton,K.P. 1982, MNRAS, **198**, 669.

Nieto,J.-L. and Seldner,M. 1982, Astron. & Astrophys., **112**, 321.

Oke,J.B. 1974, Ap.J. Suppl., **27**, 21.

Oort,J.H., Arp,H. and de Ruiter,H. 1981,
Astron. & Astrophys., **95**, 7.

Osmer,P.S. 1980, Ap.J. Suppl., **42**, 523.

Osmer,P.S. 1981, Ap.J., **247**, 762.

Osmer,P.S. 1982, Ap.J., **253**, 28.

Osmer,P.S. and Smith,M.G. 1976, Ap.J.,**210**, 267.

Osmer,P.S. and Smith,M.G. 1977, Ap.J., **217**, L73.

Osterbrock,D.E. 1984, Q. J. of the Roy. astr. Soc., **25**, 1.

Ostriker,J.P. and Heisler,J. 1984, Ap.J., **278**, 1.

Peacock,J.A. and Gull,S.F. 1981, MNRAS, **196**, 611.

Peacock,J.A.,Millar,L. and Longair,M.S. 1986, MNRAS, in the press.

Peebles,P.J.E. 1980, *The Large Scale Structure of the Universe*,
(Princeton University Press).

Peebles,P.J.E. 1981, Ap.J., **248**, 885.

Peebles,P.J.E. 1982, Ap.J., **258**, 415.

Peterson,B.A.,Savage,A.,Jauncey,D.L. and Wright,A.E. 1982,
Ap.J., **260**, L27.

Petrosian,V. 1973, Ap.J., **183**, 359.

Phillipps,S. 1978 Ph.D. Thesis, University of Durham.

Phillipps,S. 1985 Astrophys. Lett., in the press.

Phillipps,S.,Fong,R. and Shanks,T. 1981, MNRAS, **194**, 49.

Phillipps,S.,Fong.R.,Ellis,R.S.,Fall,S.M. and
MacGillivray,H.T. 1978, MNRAS, **182**, 673.

Rees,M. 1984, Ann. Rev. Astron. Astrophys., **22**, 471.

Reid,N. and Gilmore,G. 1984, MNRAS, **206**, 19.

Richstone,D.O. and Schmidt,M. 1980, Ap.J., **235**, 377.

Ryle,M. and Sandage,A. 1964, Ap.J., **139**, 419.

Sandage,A. 1961, Ap.J., **134**, 916.

Sandage,A. 1965, Ap.J., **141**, 1560.

Sandage,A. 1969, Ap.J., **158**, 1115.

Sandage,A. 1972, Ap.J., **178**, 25.

Sandage,A. 1973, Ap.J., **183**, 711.

Sandage,A. and Luyten,W.J. 1967, Ap.J., **148**, 767.

Sandage,A. and Luyten,W.J. 1969, Ap.J., **155**, 913

Sandage,A. and Veron,P. 1965, Ap.J., **142**, 412.

Sargent,W.L.W.,Young,P.J.,Boksenberg,A.,Shortridge,K,Lynds,C.R. and Hartwick,F.D.A. 1978, Ap.J., **221**, 731.

Savage,A.,Bolton,J.G.,Tritton,K.P. and Peterson,B.A. 1976, MNRAS, **183**, 473.

Savage,A. and Bolton,J.G. 1979, MNRAS, **188**, 599

Savage,A.,Trew,A.S.,Chen,J.-S. and Weston,T. 1984, MNRAS, **207**, 393

Savage,A.,Clowes,R.G.,Cannon,R.D.,Cheung,K.,Smith,M.G., Boksenberg,A. and Wall,J.V. 1985, MNRAS, **213**, 485.

Schechter,P. 1976, Ap.J., **203**, 297.

Schmidt,M. 1963, Nature, **197**, 1040.

Schmidt,M. 1968, Ap.J., **151**, 393.

Schmidt,M. 1970, Ap.J., **162**, 371.

Schmidt,M. 1972, Ap.J., **176**, 273.

Schmidt,M. 1978, Physica Scripta, **17**, 329.

Schmidt,M. 1986, in *The Structure and Evolution of Active Galactic Nuclei*, ed. F.Mardirossian, (D.Reidel), in the press.

Schmidt,M. and Green,R.F. 1983, Ap.J., **269**, 352.

Schwartz,D. 1979, in *X Ray Astronomy*,
eds. W.A.Baity and L.E. Peterson, (New York: Pergamon).
Seldner,M. and Peebles,P.J.E. 1979, Ap.J., **227**, 30.
Setti,G. and Woltjer,L. 1973,
Annals. N.Y. Acad. Sciences, **224**, 8.
Shakura,N.I. and Sunyaev,R.A. 1976, MNRAS, **175**, 613
Shanks,T. 1979, Ph.D. Thesis, University of Durham.
Shanks,T.,Bean,A.J.,Efstathiou,G.,Ellis,R.S.,Fong,R. and
Peterson,B.A. 1983a, Ap.J., **274**, 529.
Shanks,T.,Fong,R. and Boyle,B.J. 1983b, Nature, **303**, 156.
Shanks,T.,Fong,R.,Green,M.R.,Clowes,R.G. and Savage,A. 1983c,
MNRAS, **203**, 181.
Shanks,T.,Fong,R.,Ellis,R.S. and MacGillivray,H.T. 1980,
MNRAS, **192**, 209.
Shanks,T. 1986, Vistas in Astronomy, in the press.
Shaver,P.A. 1984, Astron. & Astrophys., **136**, L9.
Shaver,P.A. and Roberstson,J.G. 1983, Nature, **303**, 155.
Smith,M.G. 1978, Vistas in Astronomy, **22**, 321.
Smith,M.G. 1981, in *Investigating the Universe*, p151,
ed. F.D.Kahn, (D.Reidel) .
Soltan,A. 1982, MNRAS, **200**, 115.
Sramek,R.A. and Weedman,D.W. 1978, Ap.J., **221**, 468
Stevenson,P.R.F. 1985 Ph.D. Thesis, University of Durham.
Stocke,J.T. and Perrenod,S.C. 1981, Ap.J., **245**, 375.
Stockton,A. 1978, Ap.J., **223**, 747.
Stockton,A. 1982, Ap.J., **257**, 33.
Terrell,J. 1977, Am. J. Phys., **45**, 869.
Tritton,K.P. and Morton,D.C. 1984, MNRAS, **209**, 429.

Tritton,K.P.,Savage,A. and Morton,D.C. 1984, MNRAS, **206**, 843.

Turnshek,D.A.,Foltz,C.B.,Weymann,R.J.,Lupie,O.J.,McMahon,R.G. and Peterson,B.M. 1985, Ap.J., **294**, L1.

Tytler,D. 1982, Nature, **298**, 427.

Ulrich,M.H.,Boksenberg,A.,Bromage,G.E.,Clavel,J.,Elvius,A., Penston,M.V.,Perola,G.C.,Pettini,M.,Snijders,M.A.J.,Tanzi,E.G. and Tarenghi,M. 1984, MNRAS, **206**, 221; erratum **209**, 479.

Usher,P.D. 1981, Ap.J. Suppl., **46**, 117.

Usher,P.D.,Warnock,A. and Green,R.F. 1983, Ap.J., **269**, 73.

Veron,P. 1983, in *Quasars and Gravitational Lenses*, 24th Lige Astropysical Symposium, p210.

Veron,P. and Veron,M.P. 1982, Astron. & Astrophys., **105**, 405.

Veron-Cetty,M.P. and Veron,P. 1984, ESO Scientific Report No. 1.

Walker,A.R. 1984, MNRAS, **209**, 83.

Wampler,E.J. 1985, Ap.J., **296**, 416.

Wampler,E.J.,Robinson,L.B.,Baldwin,J.A. and Burbidge,E.M. 1973, Nature, **243**, 336.

Wampler,E.J. and Ponz,D. 1985, Ap.J., **298**, 448.

Webster,A. 1982a, MNRAS, **199**, 683.

Webster,A. 1982b, MNRAS, **200**, 47P.

Weedman,D.W. 1976, Ap.J., **208**, 30.

Weedman,D.W. 1986, in *The Structure and Evolution of Active Galactic Nuclei*, ed. F.Mardirossian, (D.Reidel), in the press.

Weinberg,S. 1973, *Gravitation and Cosmology*, (New York: Wiley).

Weymann,R.J.,Boronson,T.A.,Peterson,B.M. and Bucher,H.R. 1978, Ap.J., **226**, 603.

Weymann,R.J.,Carswell,R.F. and Smith,M.G. 1981, Ann. Rev. Astron. Astrophys., **19**, 41.

Weymann,R.J. and Foltz,C. 1983, in *Quasars and Gravitational Lenses,* 24th Liege Astrophysical Symposium, p538.

Wilkes,B.J. 1985, Ap.J., **288**, L1.

Wills,D. 1983, Ap.J., **270**, 48.

Woltjer,L. and Setti,G. 1982 in *Astrophysical Cosmology,* eds G.V.Coyne,H.A. Bruck and M.S.Longair, (Pontifica Academia Scientiarum).

Yee,H.K.C. and Green,R.F. 1984, Ap.J., **280**, 79.

Young,P.J.,Westphal,J.A.,Kristian,J.,Wilson,C.P. and Landauer,F.P. 1978, Ap.J., **221**, 721.

Zamorani,G. 1983, in *Progress in Cosmology,* p203 ed. A.W.Wolfendale, (D.Reidel).

Zamorani,G.,Henry,J.P.,Maccacaro,T.,Soltan,A.,Avni,Y.,Liebert,J., Stocke,J.,Strittmatter,P.A.,Weymann,R.J.,Smith,M.G. and Condon,J.J. 1981, Ap.J., **245**, 357.

Zamorani,G.,Giommi,P.,Maccacaro,T. and Tananbaum,H. 1984, Ap.J., **278**, 28.

Zwicky,F. 1957, *Morphological Astronomy,* (Springer Verlag).

APPENDIX A

FAINT UVX SURVEY: SPECTRA

SGP1

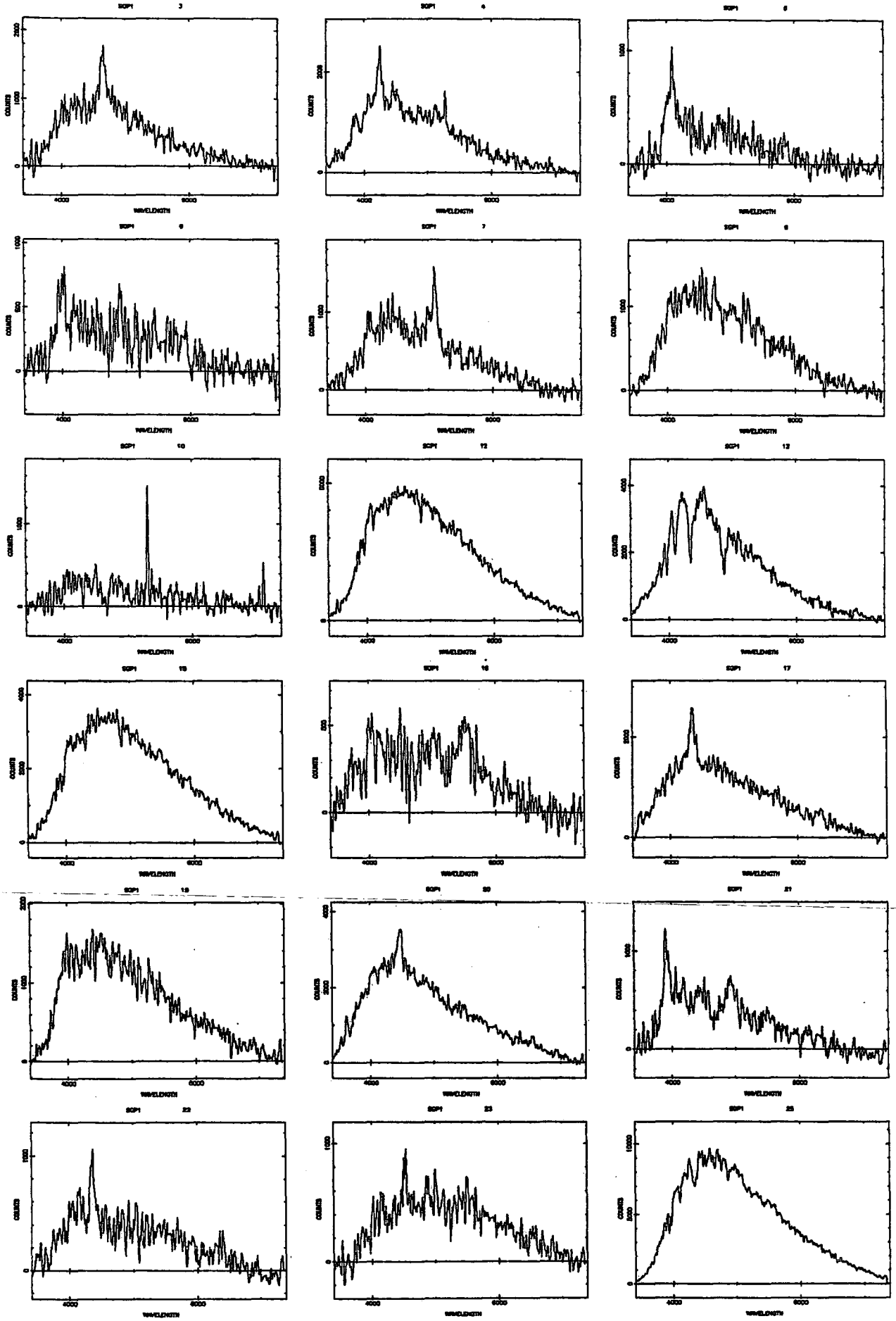

A1

SGP 1

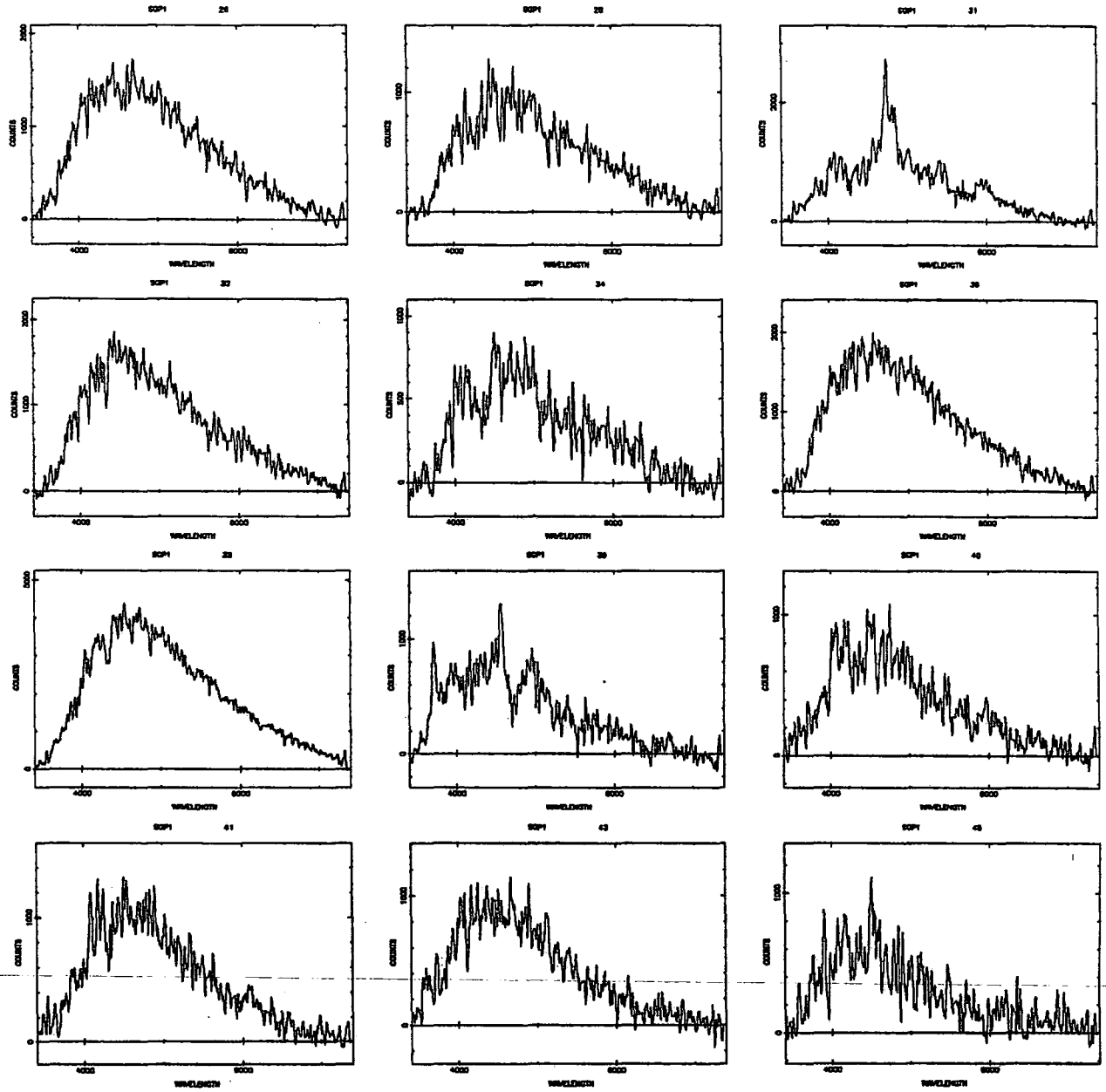

SGP2

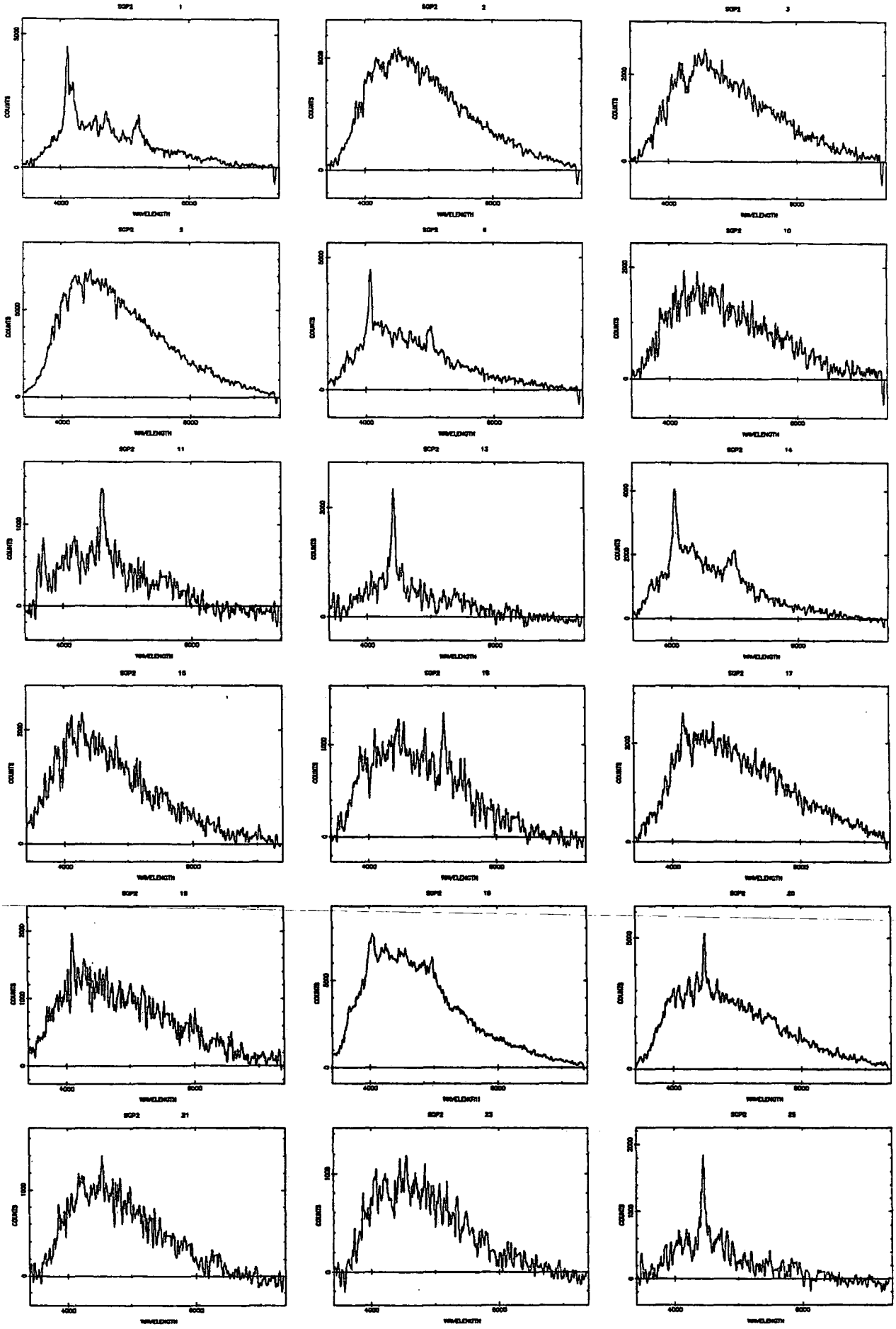
SGP2 1
SGP2 2
SGP2 3
SGP2 9
SGP2 10
SGP2 11
SGP2 13
SGP2 14
SGP2 15
SGP2 16
SGP2 17
SGP2 19
SGP2 20
SGP2 21
SGP2 23
SGP2 25
COUNTS
WAVELENGTH

SGP 2

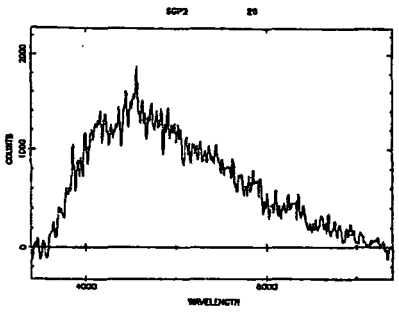
SGP2 26
COUNTS
WAVELENGTH

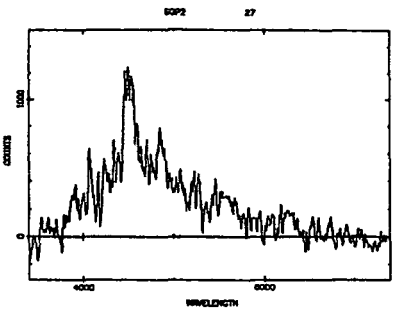
SGP2 27
COUNTS
WAVELENGTH

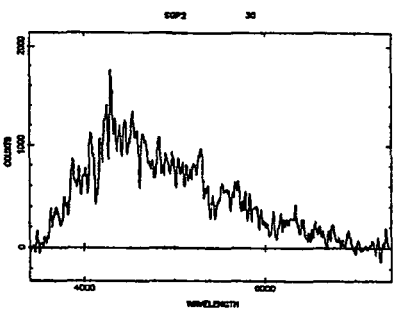
SGP2 30
COUNTS
WAVELENGTH

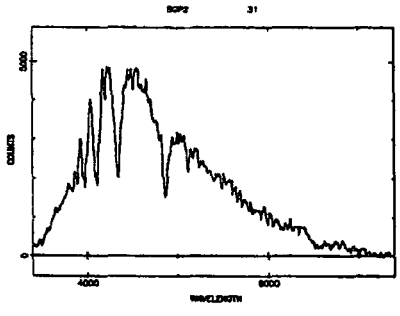
SGP2 31
COUNTS
WAVELENGTH

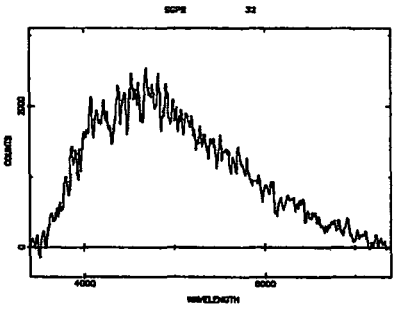
SGP2 32
COUNTS
WAVELENGTH

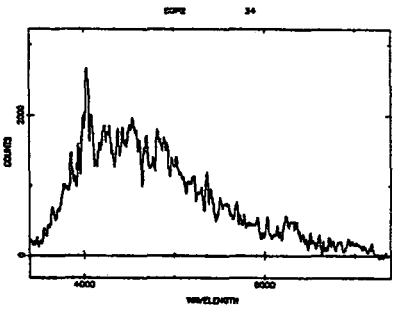
SGP2 34
COUNTS
WAVELENGTH

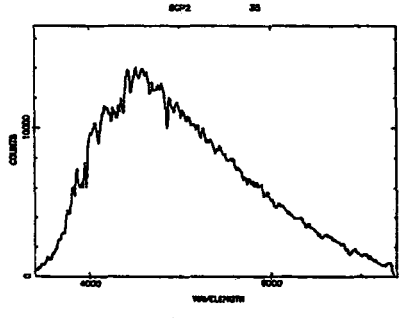
SGP2 35
COUNTS
WAVELENGTH

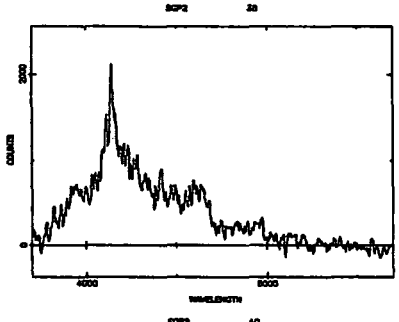
SGP2 36
COUNTS
WAVELENGTH

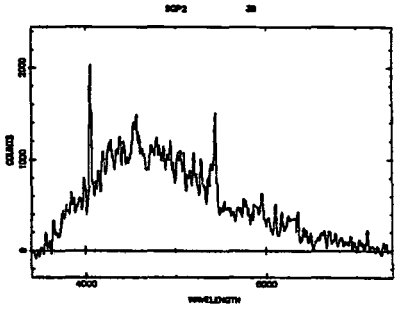
SGP2 38
COUNTS
WAVELENGTH

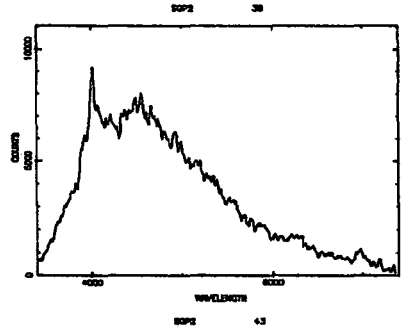
SGP2 39
COUNTS
WAVELENGTH

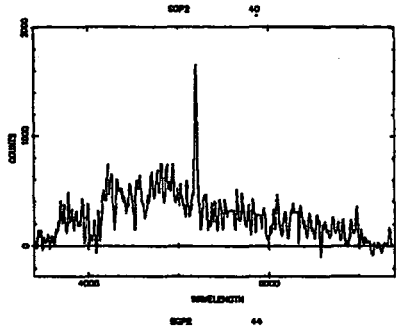
SGP2 40
COUNTS
WAVELENGTH

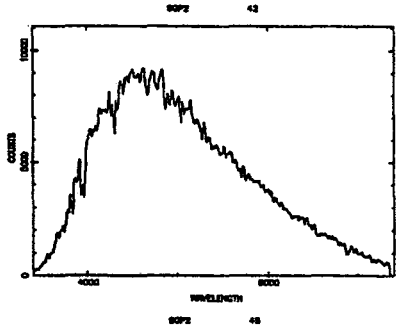
SGP2 42
COUNTS
WAVELENGTH

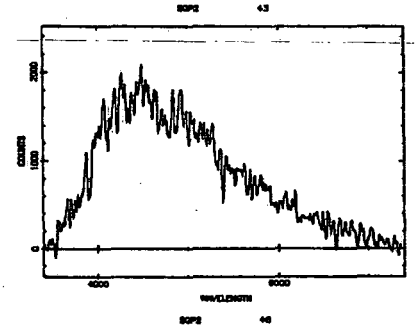
SGP2 43
COUNTS
WAVELENGTH

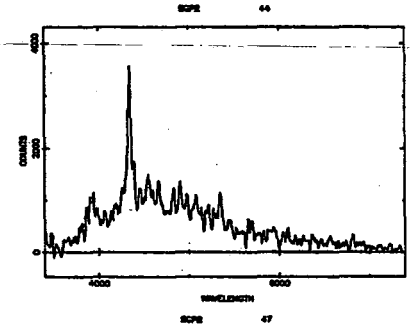
SGP2 44
COUNTS
WAVELENGTH

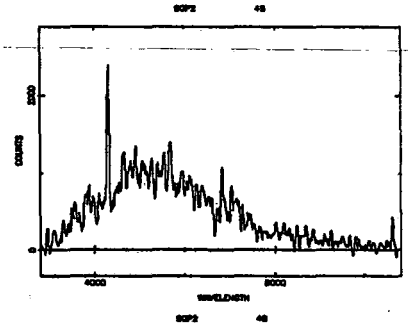
SGP2 45
COUNTS
WAVELENGTH

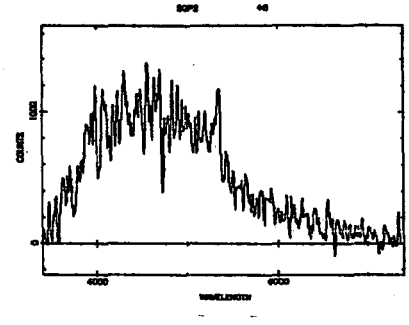
SGP2 46
COUNTS
WAVELENGTH

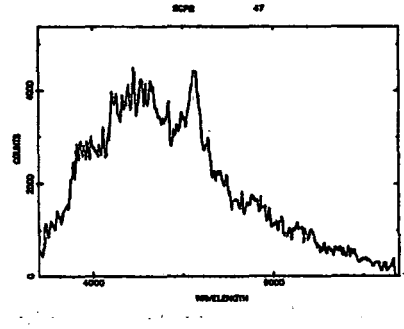
SGP2 47
COUNTS
WAVELENGTH

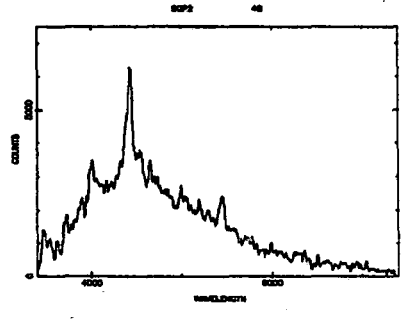
SGP2 48
COUNTS
WAVELENGTH

SGP3

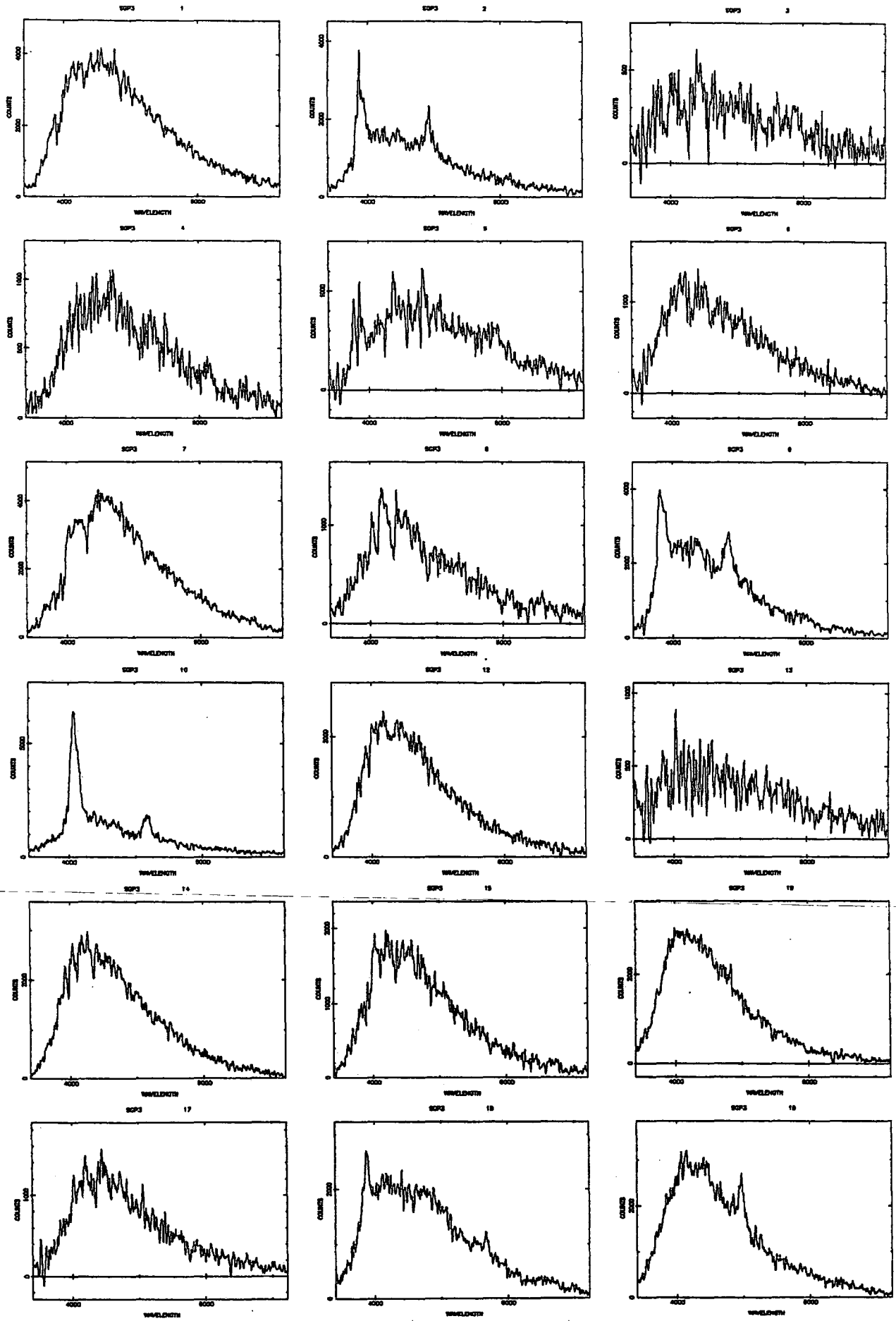

SGP3

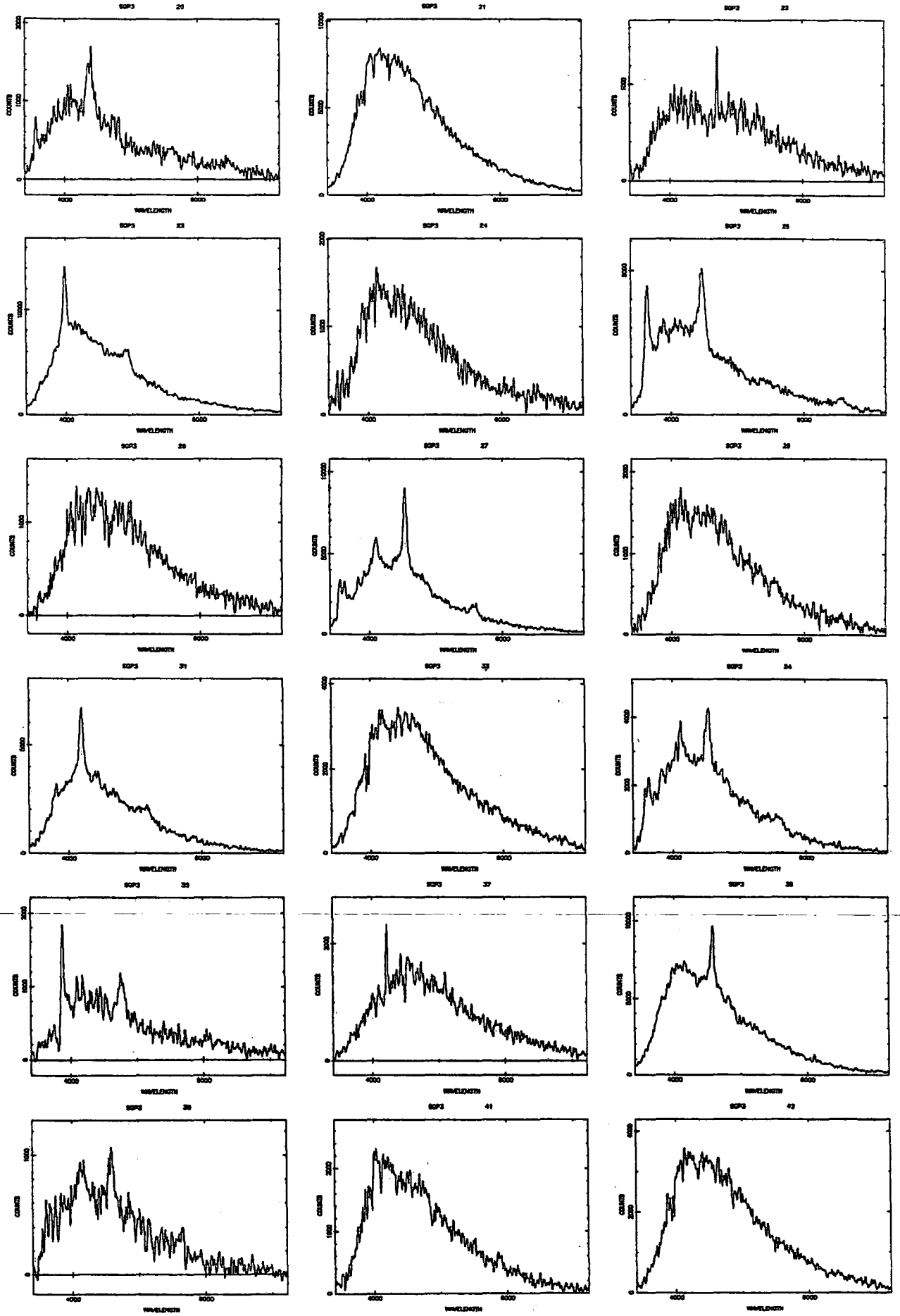

SGP3

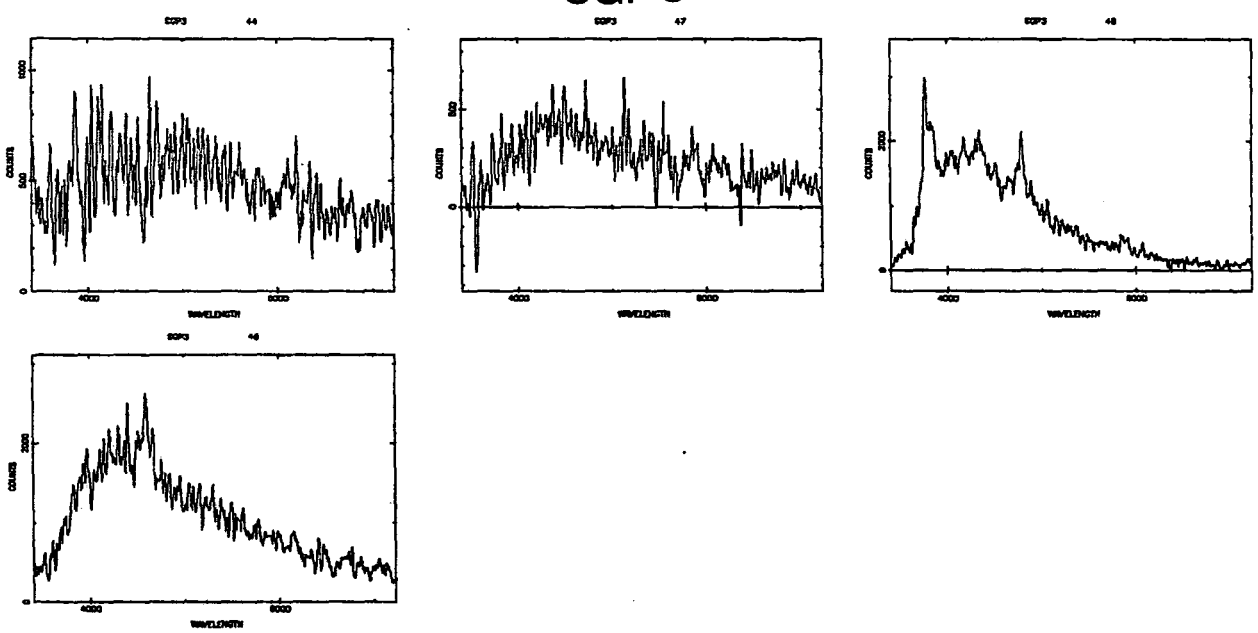

QSF1

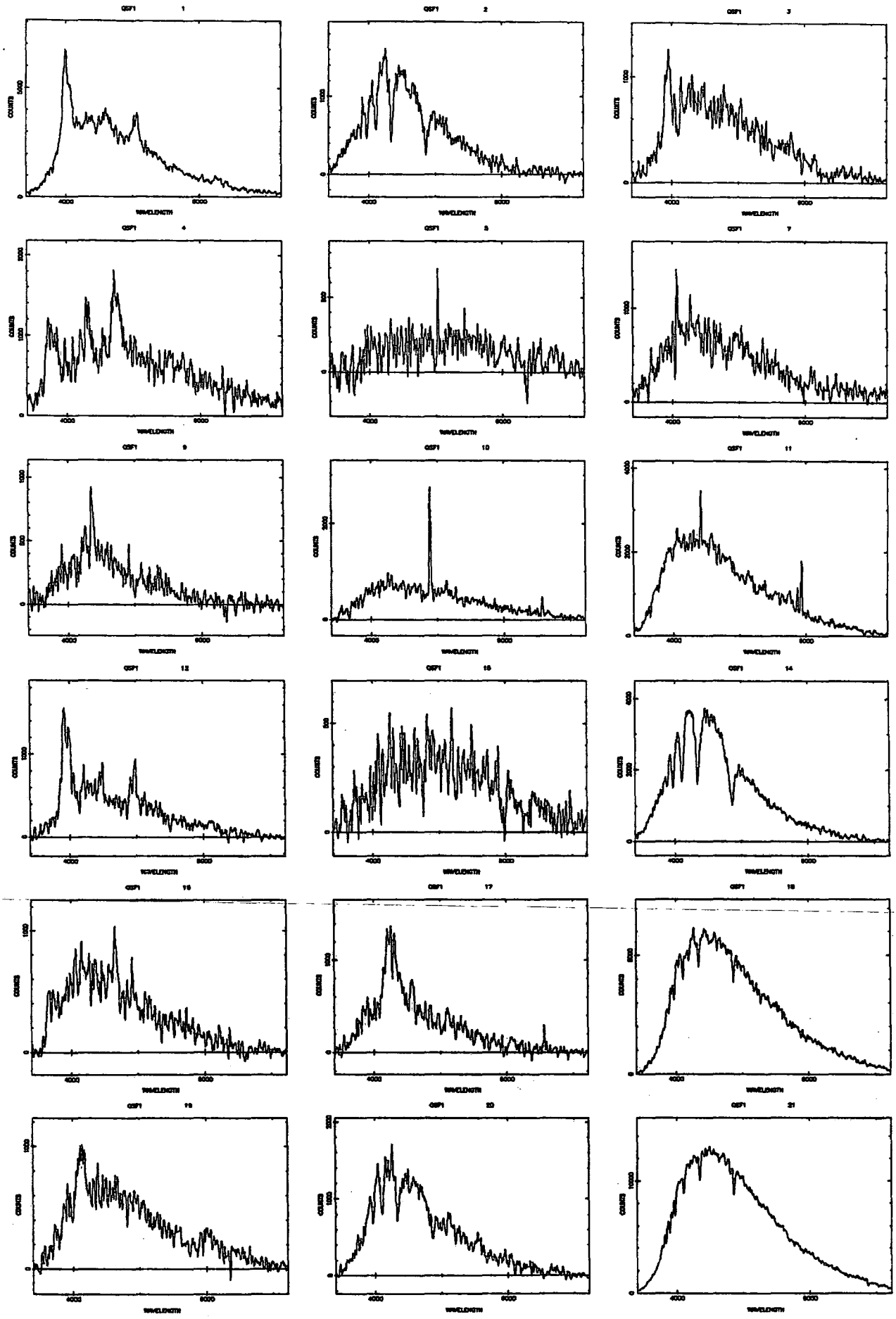

QSF 1

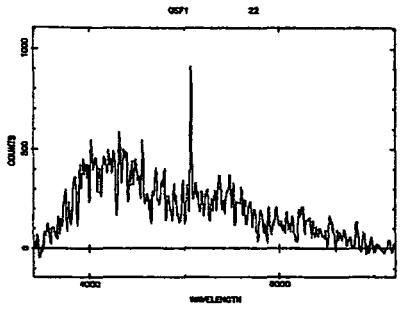
QSF1 22
COUNTS
WAVELENGTH

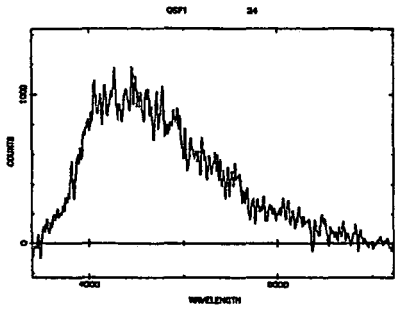
QSF1 24
COUNTS
WAVELENGTH

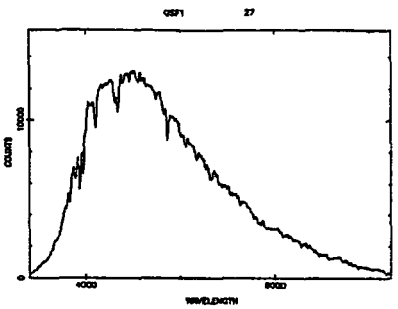
QSF1 27
COUNTS
WAVELENGTH

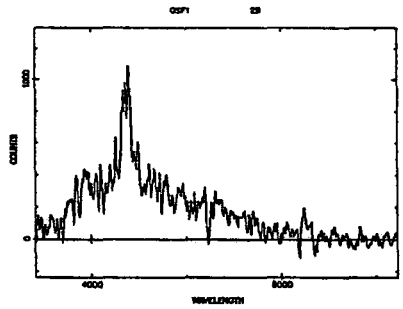
QSF1 29
COUNTS
WAVELENGTH

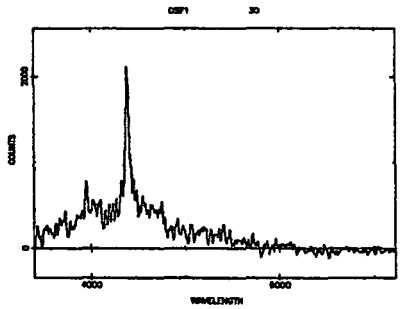
QSF1 30
COUNTS
WAVELENGTH

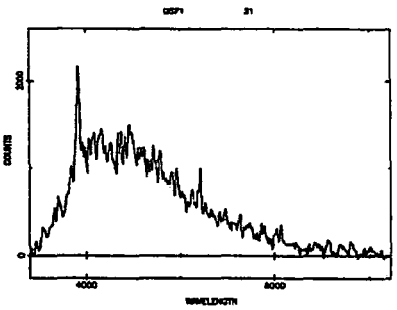
QSF1 31
COUNTS
WAVELENGTH

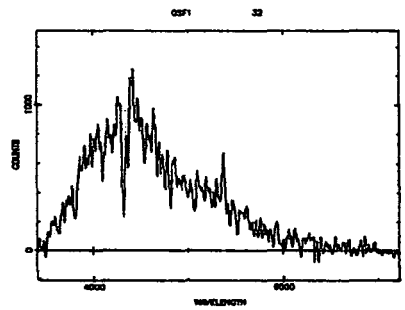
QSF1 32
COUNTS
WAVELENGTH

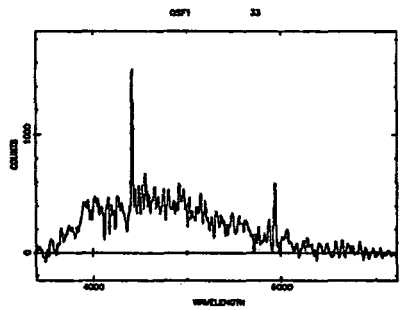
QSF1 33
COUNTS
WAVELENGTH

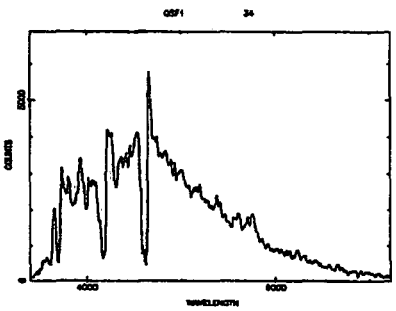
QSF1 34
COUNTS
WAVELENGTH

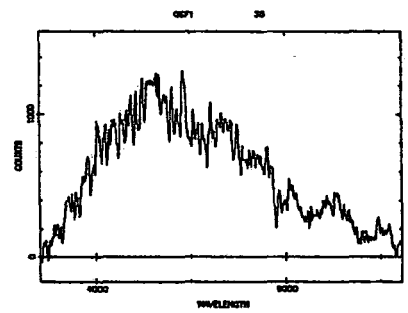
QSF1 36
COUNTS
WAVELENGTH

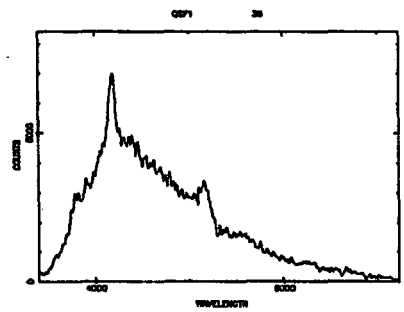
QSF1 38
COUNTS
WAVELENGTH

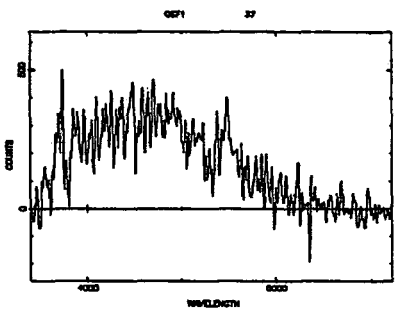
QSF1 37
COUNTS
WAVELENGTH

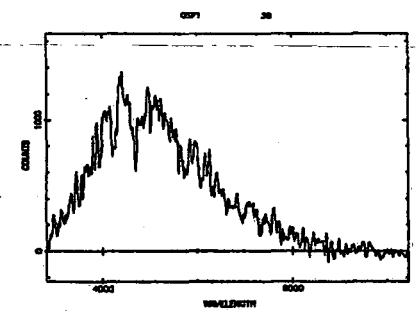
QSF1 39
COUNTS
WAVELENGTH

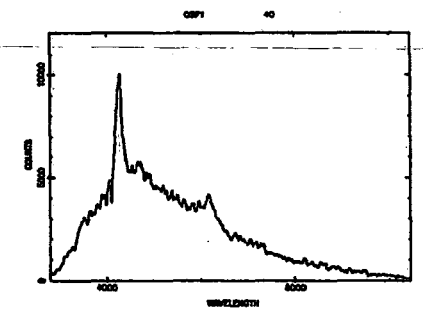
QSF1 40
COUNTS
WAVELENGTH

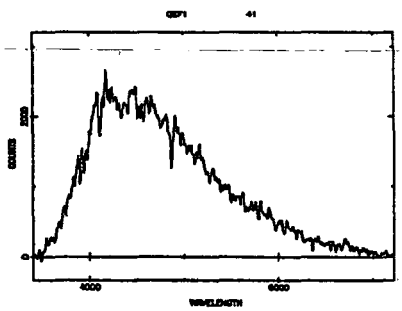
QSF1 41
COUNTS
WAVELENGTH

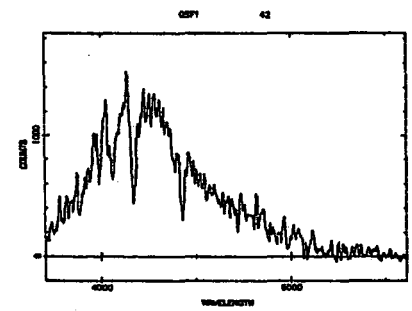
QSF1 42
COUNTS
WAVELENGTH

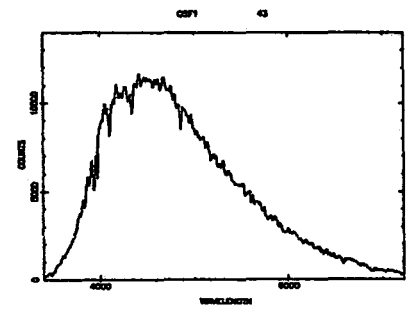
QSF1 43
COUNTS
WAVELENGTH

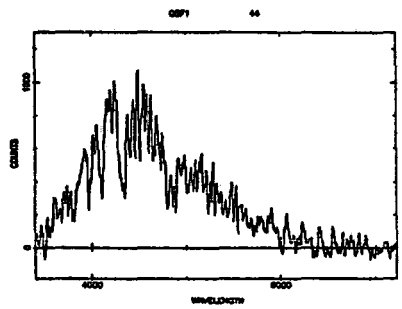
QSF1 44
COUNTS
WAVELENGTH

QSF2

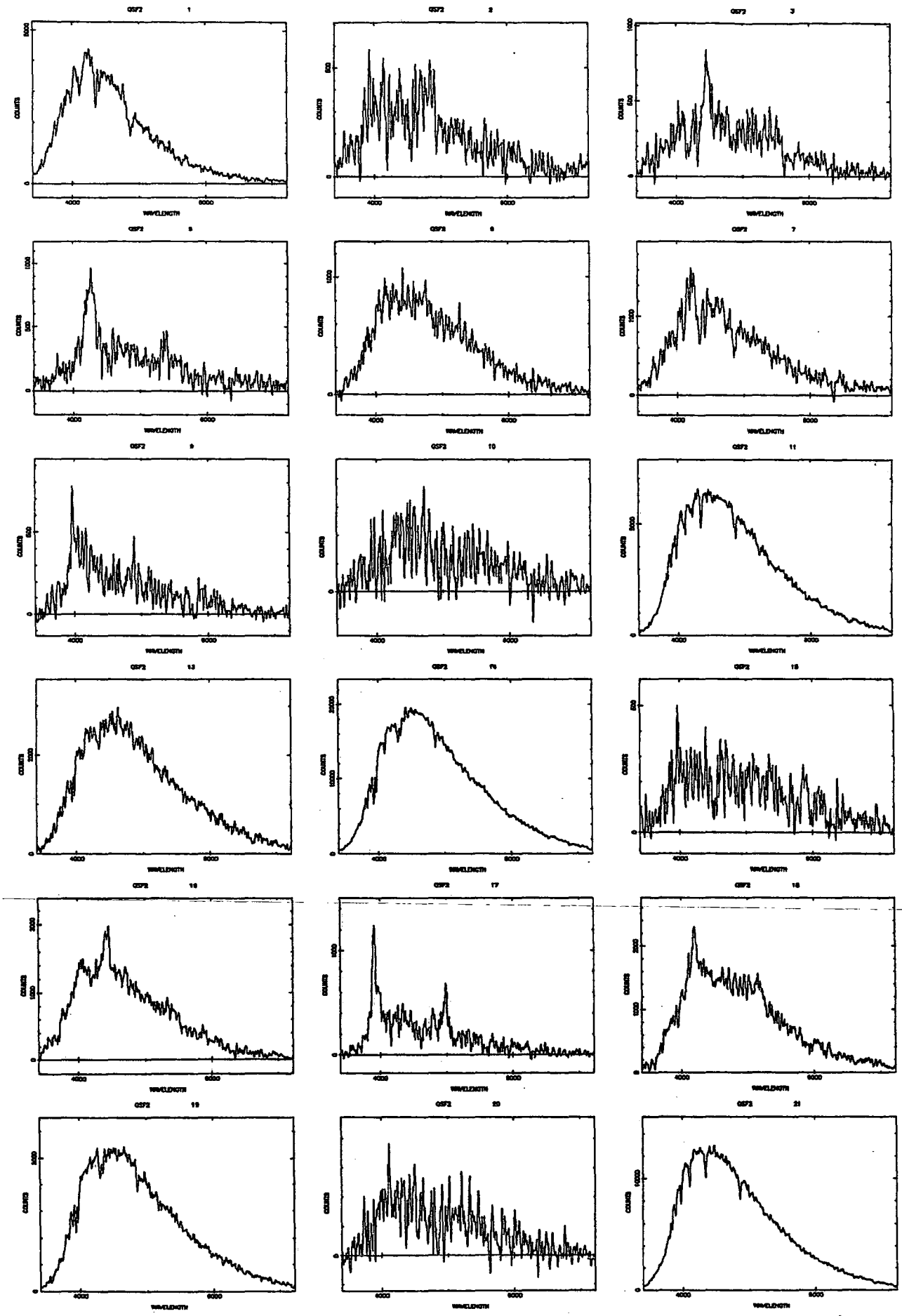
QSF2 1
QSF2 2
QSF2 3
QSF2 5
QSF2 6
QSF2 7
QSF2 9
QSF2 10
QSF2 11
QSF2 13
QSF2 14
QSF2 15
QSF2 18
QSF2 17
QSF2 18
QSF2 19
QSF2 20
QSF2 21
COUNTS
WAVELENGTH

QSF2

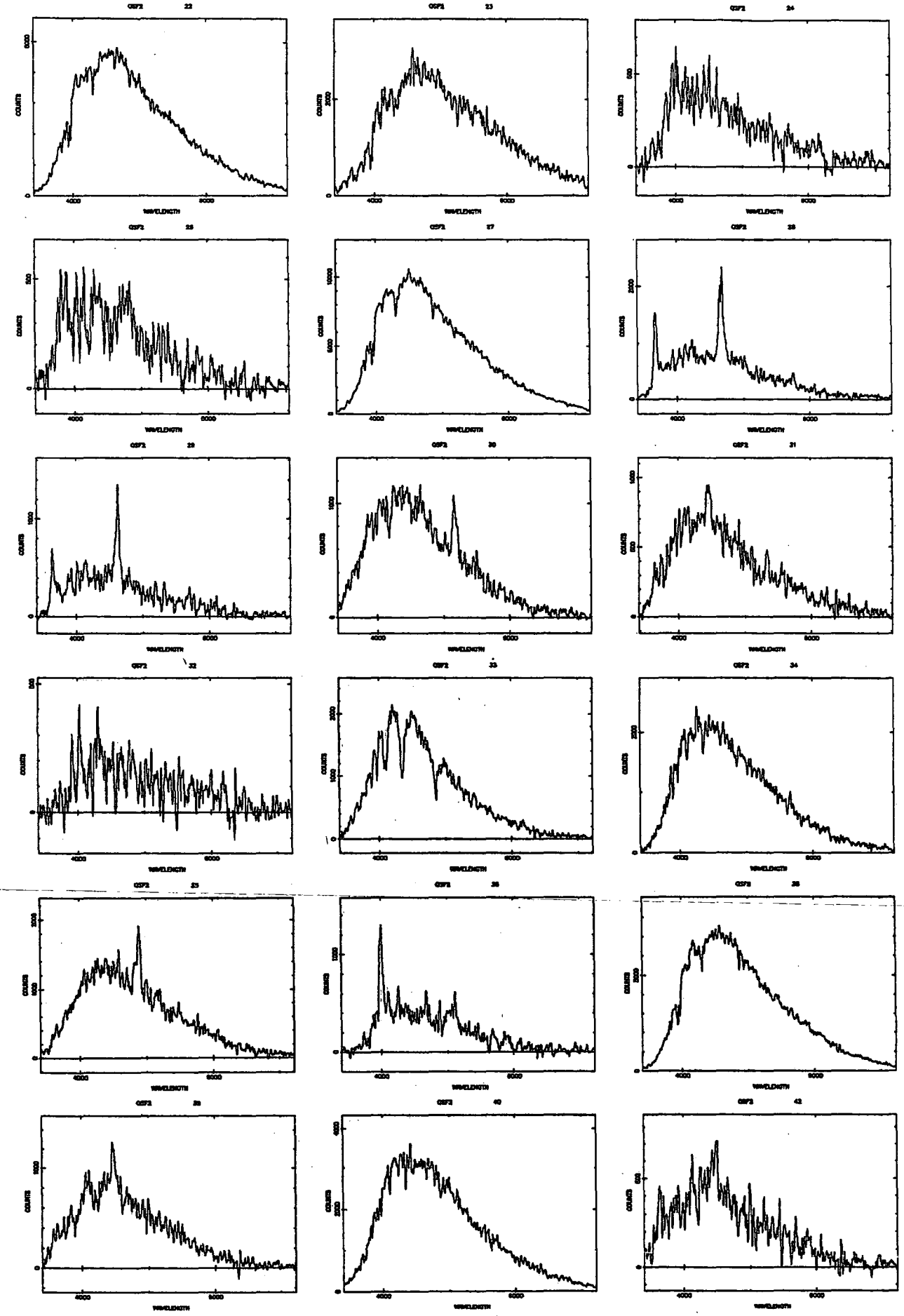

QSF 2

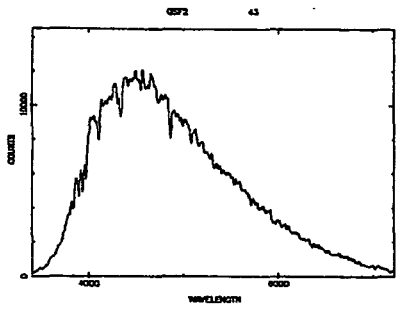

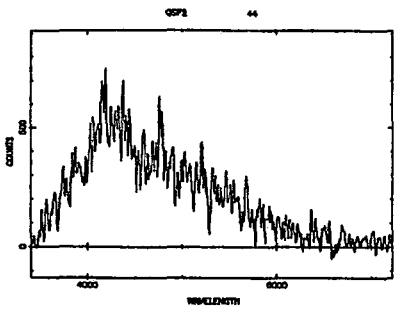

QNB 1

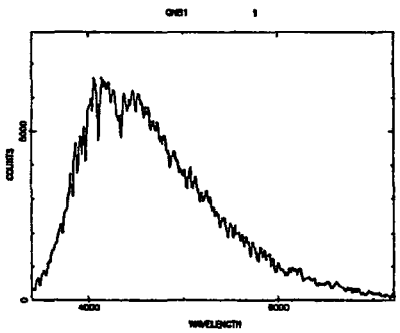

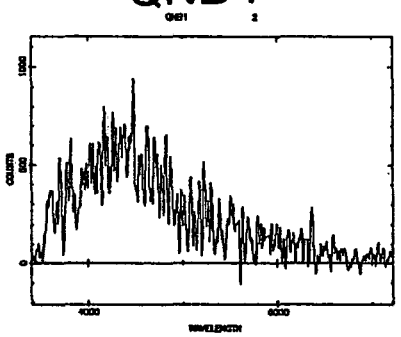

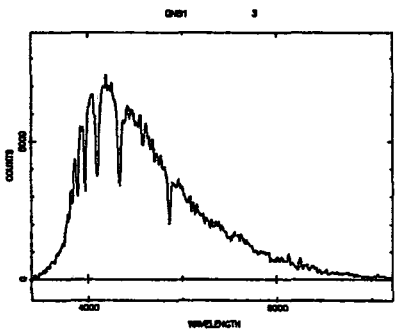

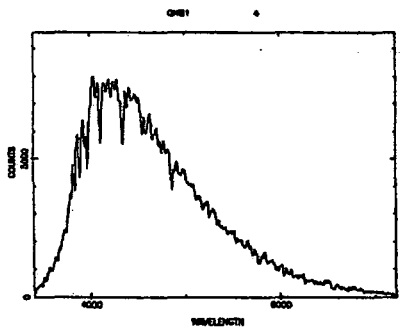

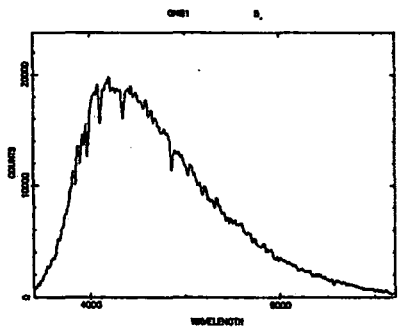

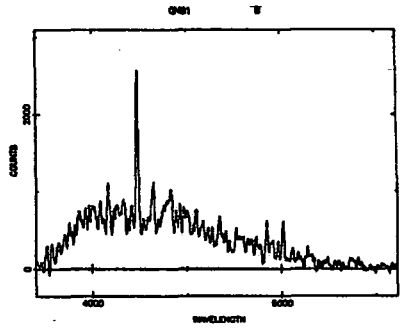

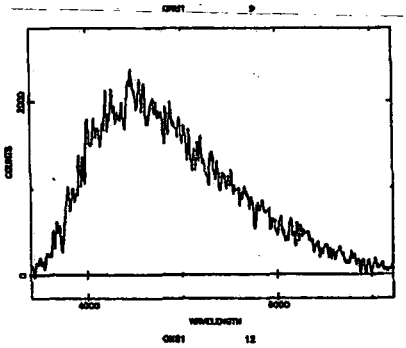

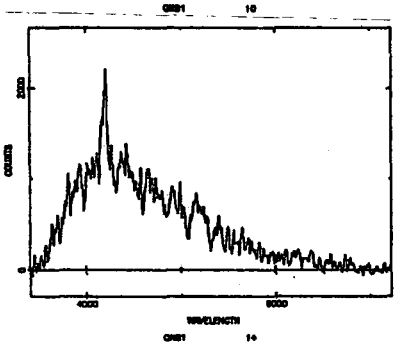

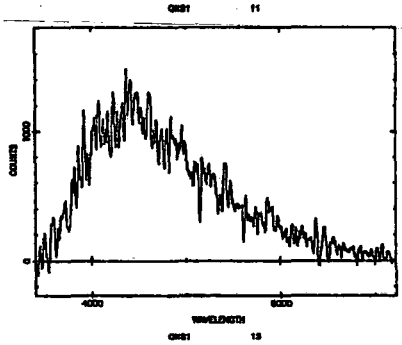

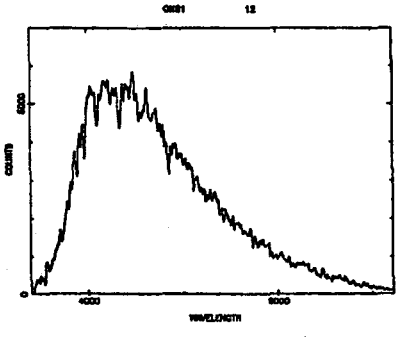

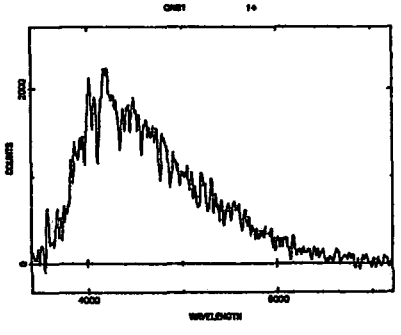

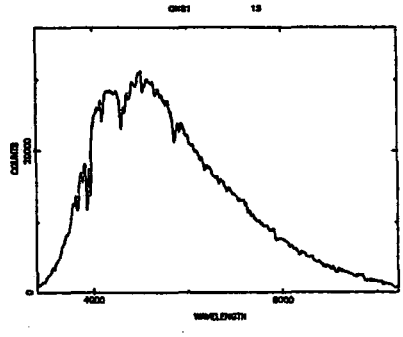

QNB1

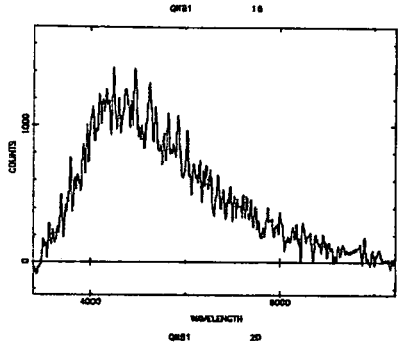
QNB1 16
COUNTS
WAVELENGTH

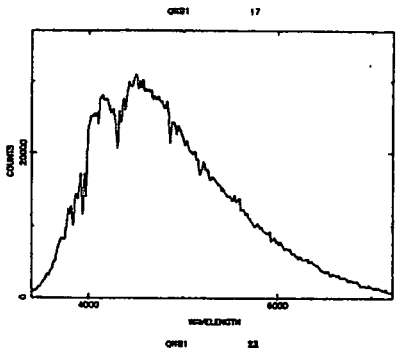
QNB1 17
COUNTS
WAVELENGTH

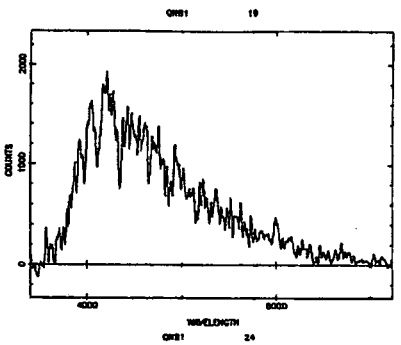
QNB1 19
COUNTS
WAVELENGTH

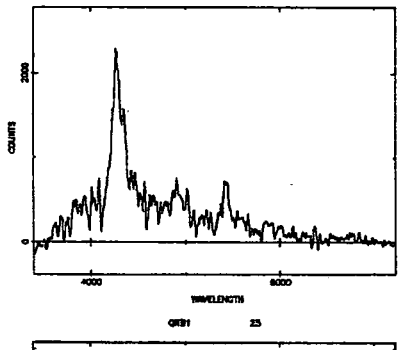
QNB1 20
COUNTS
WAVELENGTH

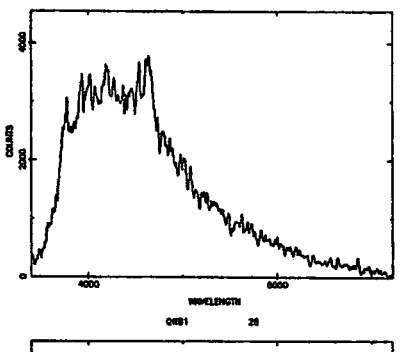
QNB1 22
COUNTS
WAVELENGTH

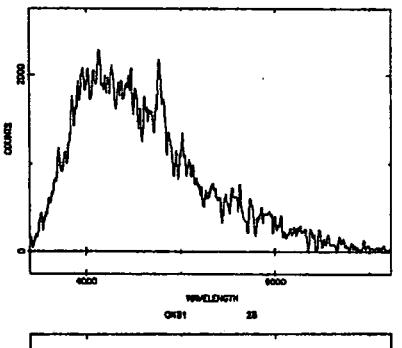
QNB1 24
COUNTS
WAVELENGTH

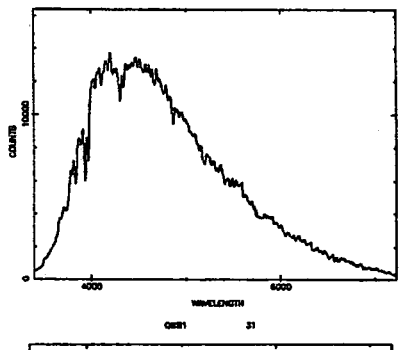
QNB1 25
COUNTS
WAVELENGTH

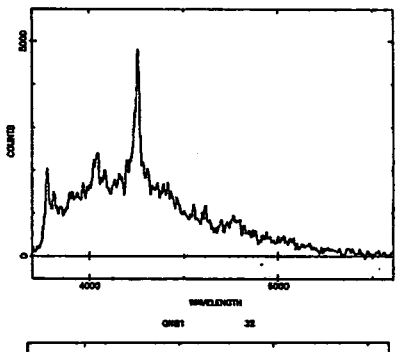
QNB1 26
COUNTS
WAVELENGTH

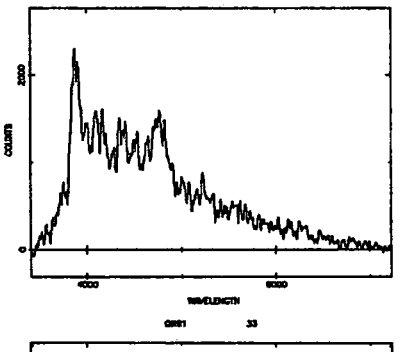
QNB1 28
COUNTS
WAVELENGTH

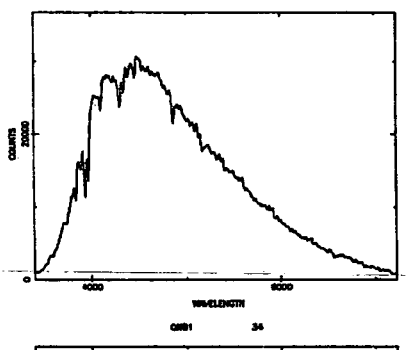
QNB1 31
COUNTS
WAVELENGTH

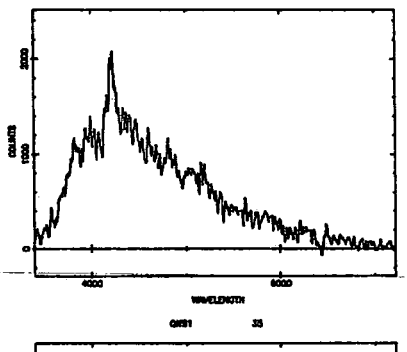
QNB1 32
COUNTS
WAVELENGTH

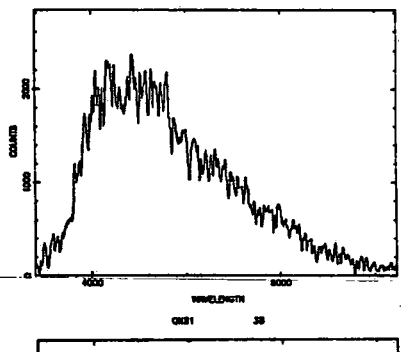
QNB1 33
COUNTS
WAVELENGTH

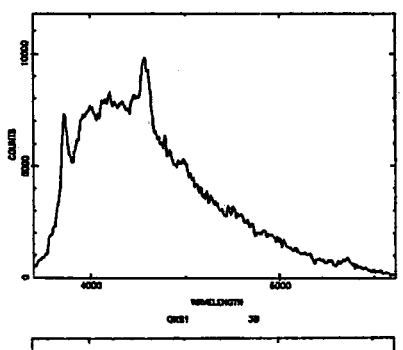
QNB1 34
COUNTS
WAVELENGTH

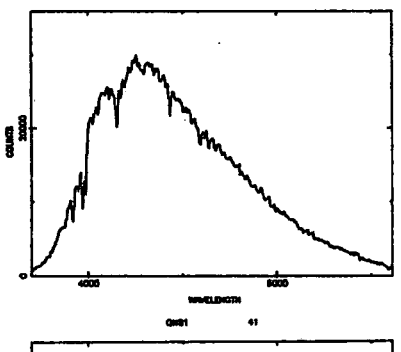
QNB1 35
COUNTS
WAVELENGTH

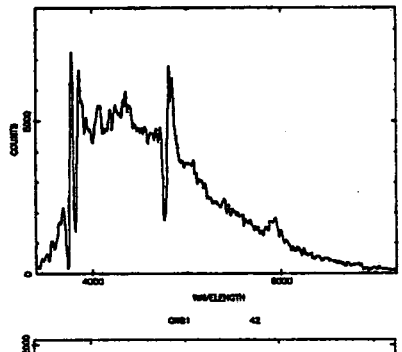
QNB1 38
COUNTS
WAVELENGTH

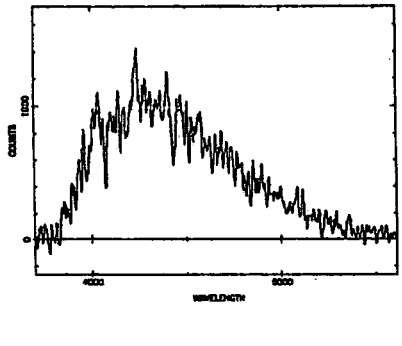
QNB1 39
COUNTS
WAVELENGTH

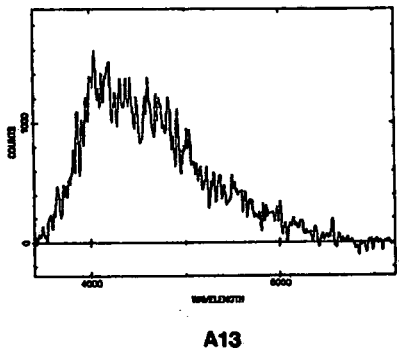
QNB1 41
COUNTS
WAVELENGTH

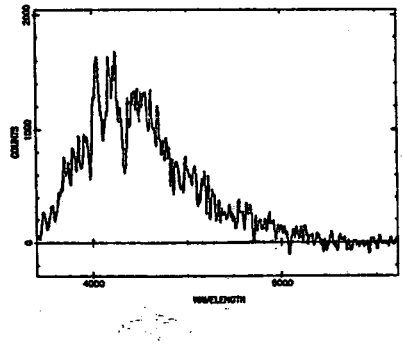
QNB1 42
COUNTS
WAVELENGTH

QNB1

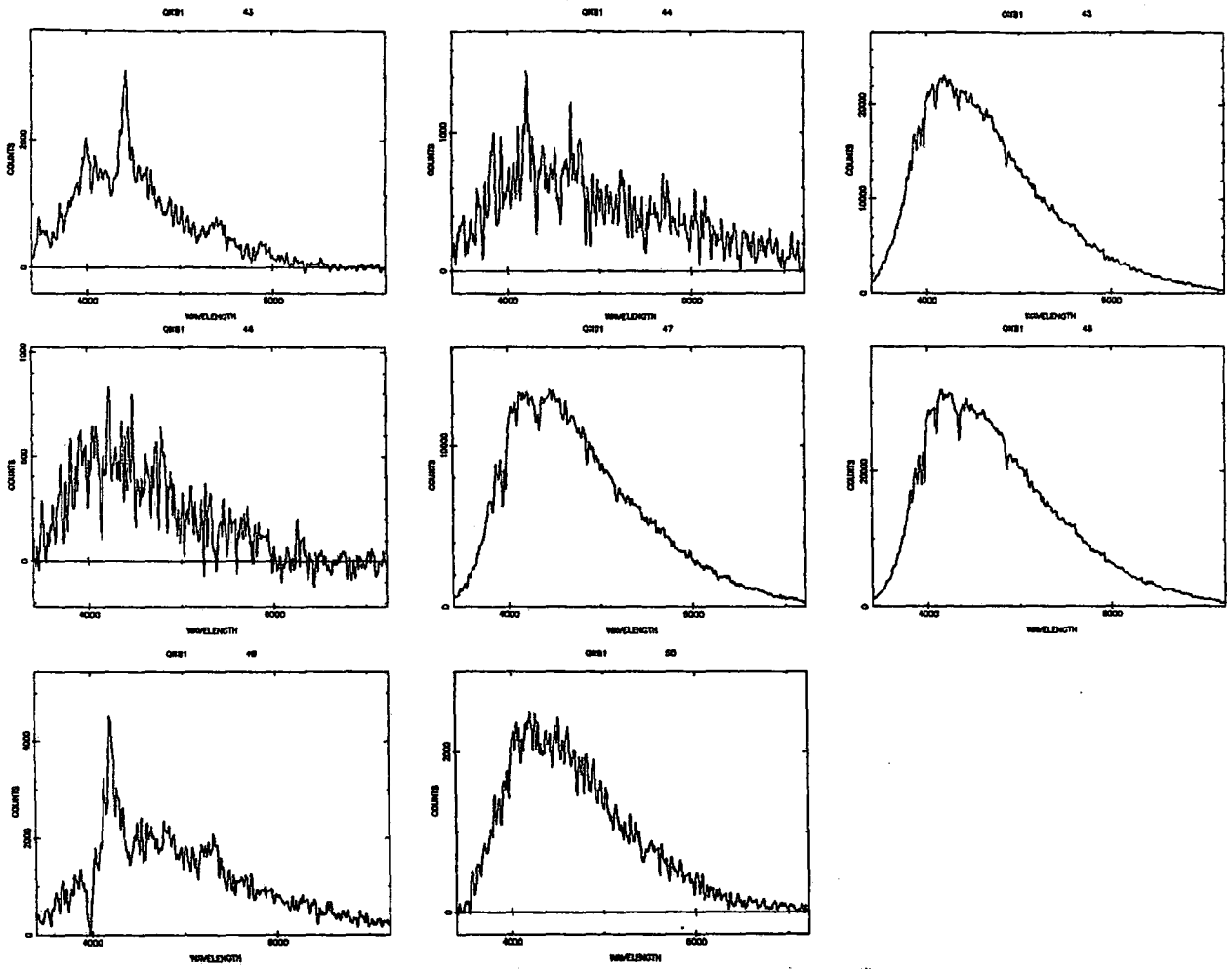

QNB2

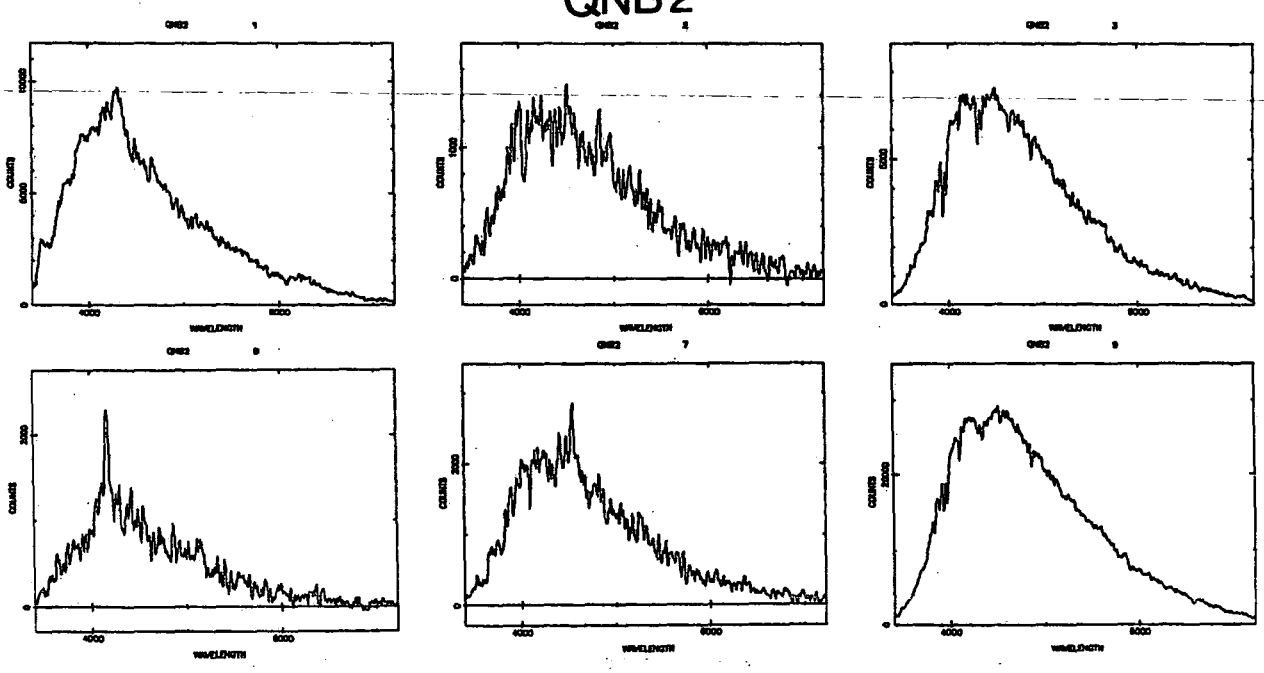

QNB 2

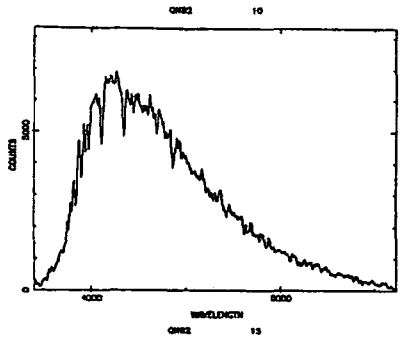
COUNTS
WAVELENGTH

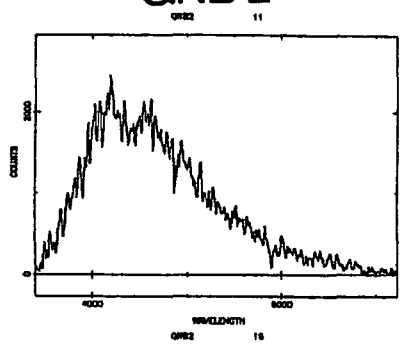
COUNTS
WAVELENGTH

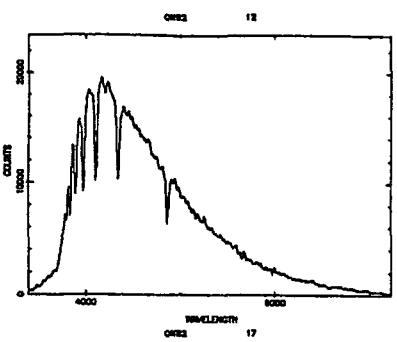
COUNTS
WAVELENGTH

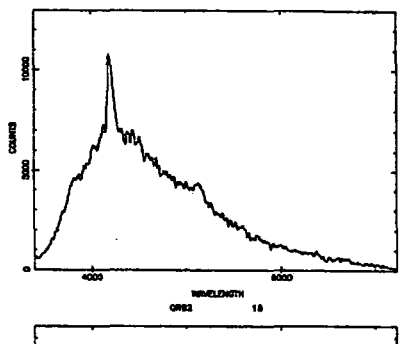
COUNTS
WAVELENGTH

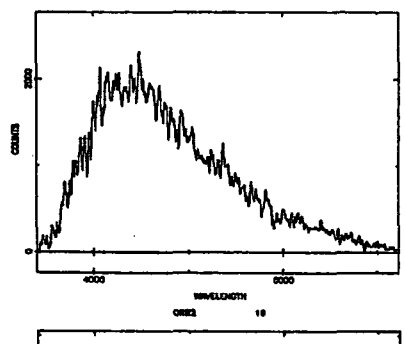
COUNTS
WAVELENGTH

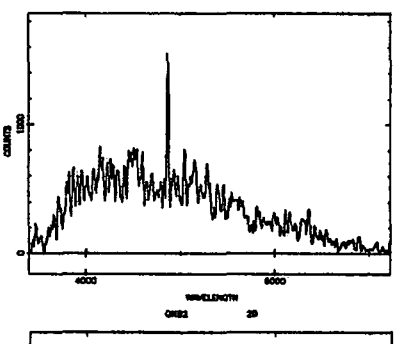
COUNTS
WAVELENGTH

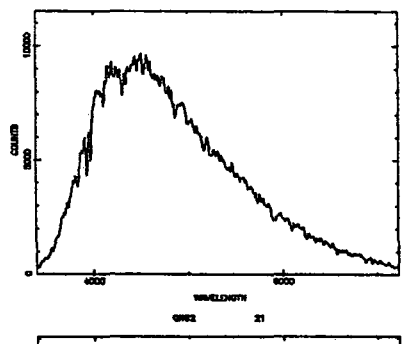
COUNTS
WAVELENGTH

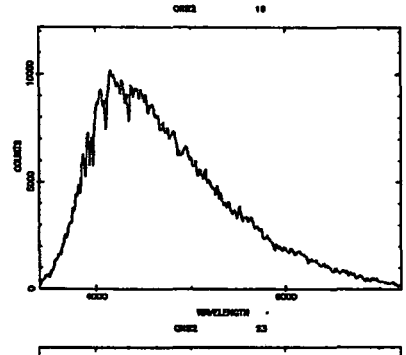
COUNTS
WAVELENGTH

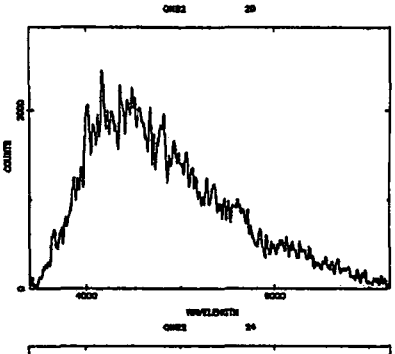
COUNTS
WAVELENGTH

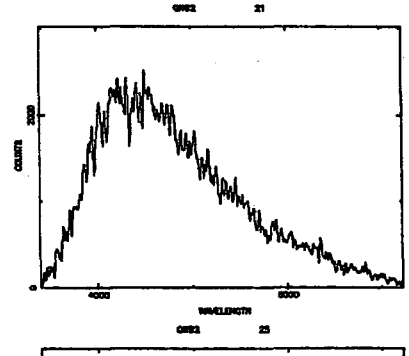
COUNTS
WAVELENGTH

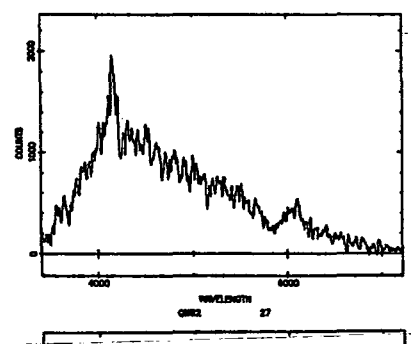
COUNTS
WAVELENGTH

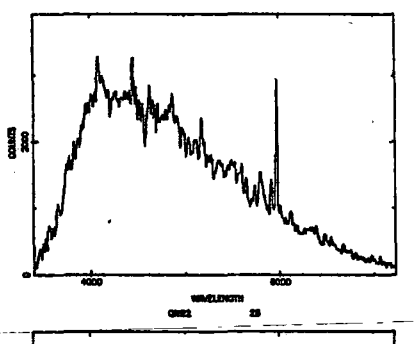
COUNTS
WAVELENGTH

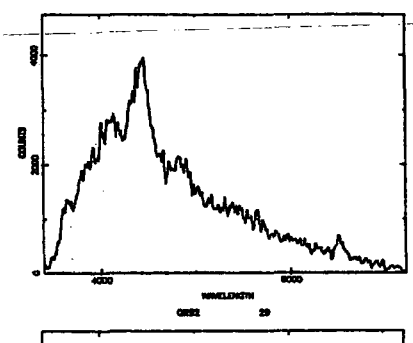
COUNTS
WAVELENGTH

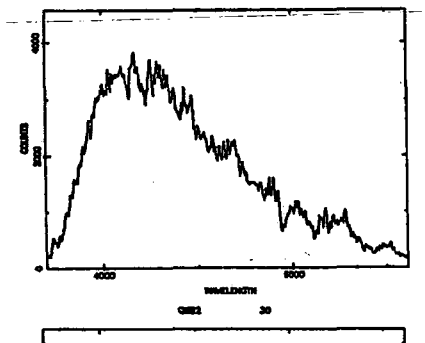
COUNTS
WAVELENGTH

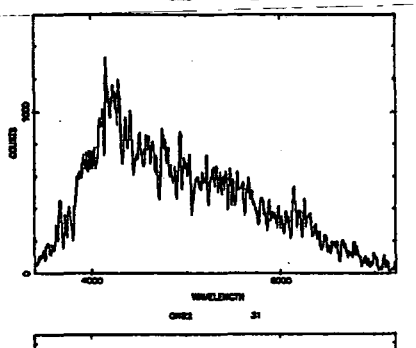
COUNTS
WAVELENGTH

QNB 2

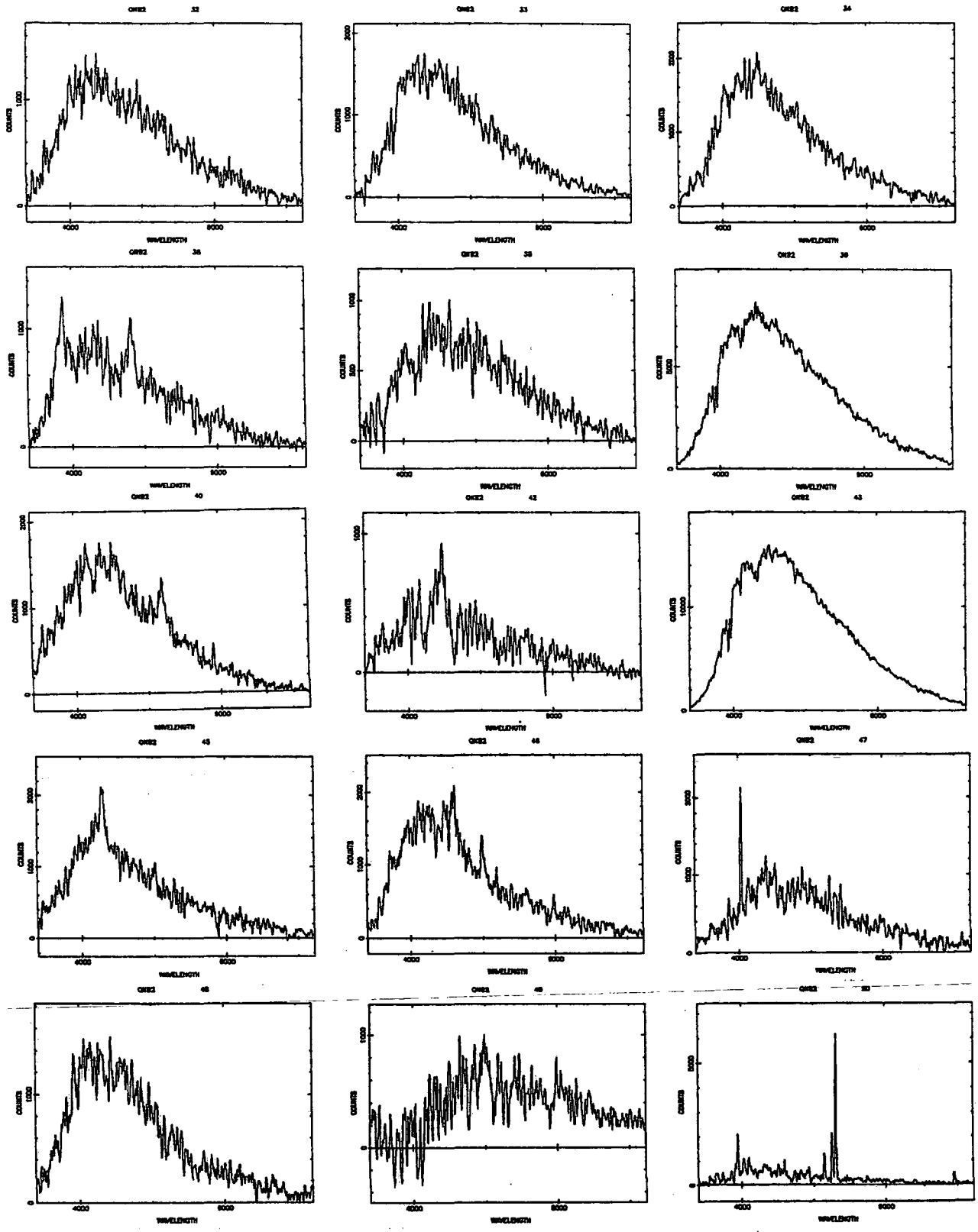

QNY 1

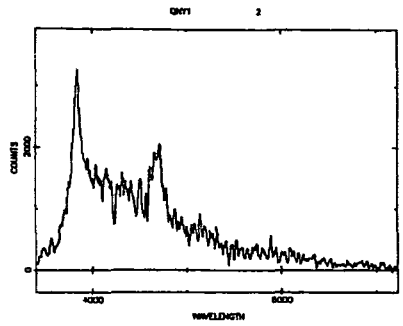
QNY1 2
COUNTS
WAVELENGTH

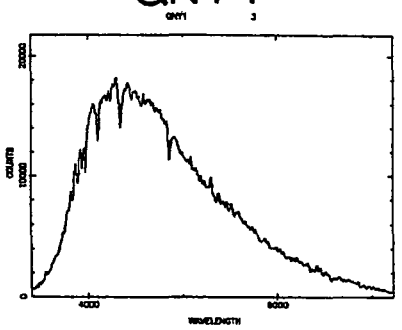
QNY1 3
COUNTS
WAVELENGTH

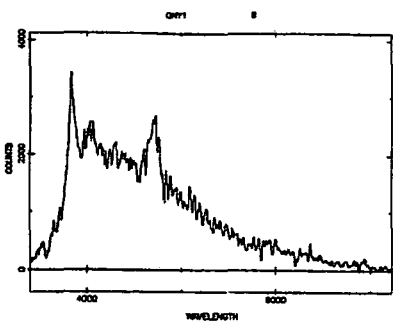
QNY1 6
COUNTS
WAVELENGTH

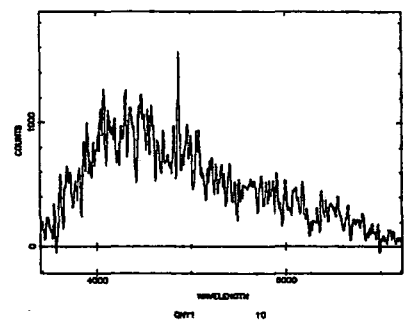
QNY1 7
COUNTS
WAVELENGTH

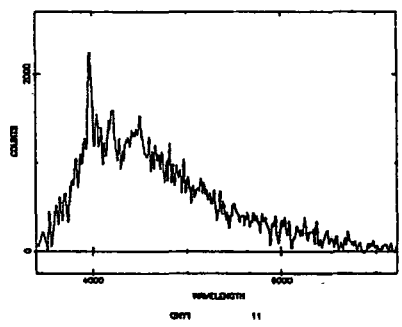
QNY1 8
COUNTS
WAVELENGTH

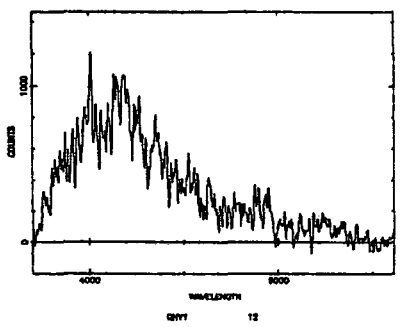
QNY1 9
COUNTS
WAVELENGTH

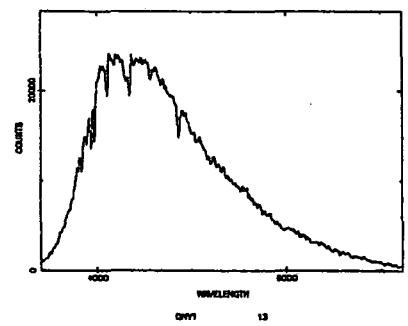
QNY1 10
COUNTS
WAVELENGTH

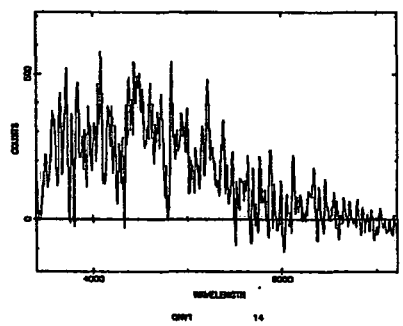
QNY1 11
COUNTS
WAVELENGTH

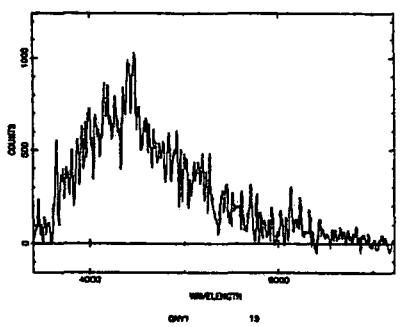
QNY1 12
COUNTS
WAVELENGTH

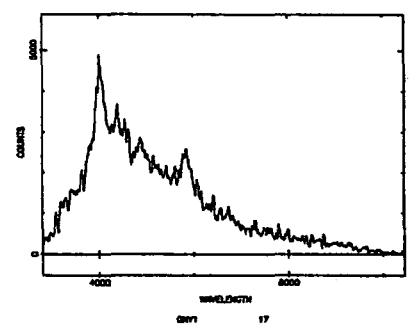
QNY1 13
COUNTS
WAVELENGTH

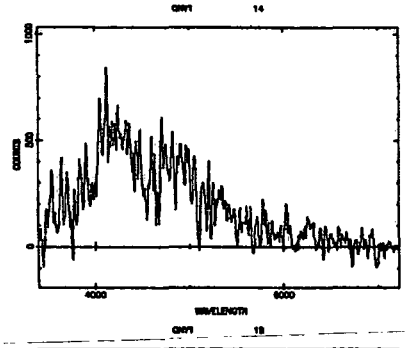
QNY1 14
COUNTS
WAVELENGTH

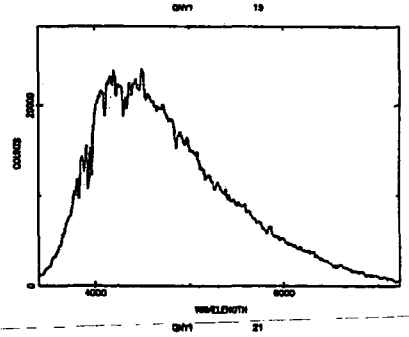
QNY1 15
COUNTS
WAVELENGTH

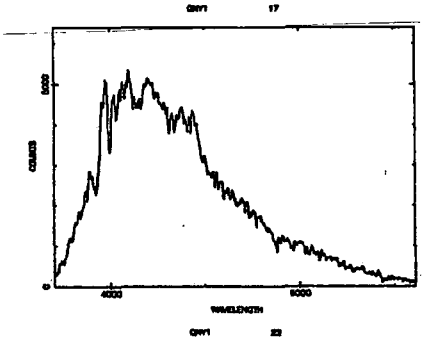
QNY1 17
COUNTS
WAVELENGTH

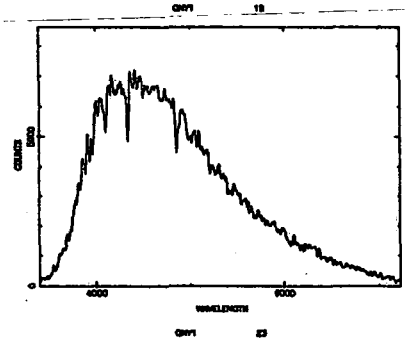
QNY1 19
COUNTS
WAVELENGTH

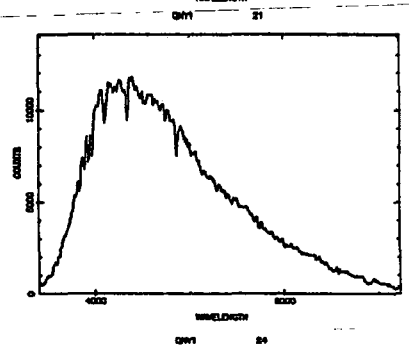
QNY1 21
COUNTS
WAVELENGTH

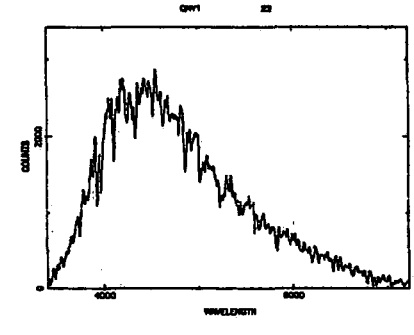
QNY1 22
COUNTS
WAVELENGTH

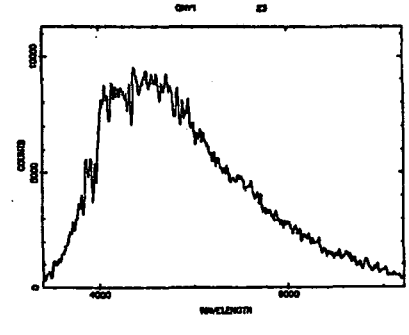
QNY1 23
COUNTS
WAVELENGTH

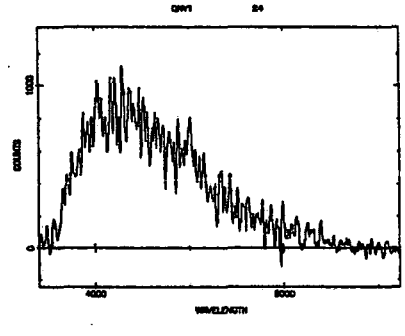
QNY1 24
COUNTS
WAVELENGTH

COUNTS
WAVELENGTH

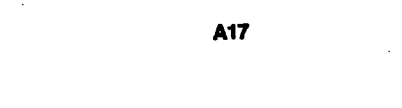
COUNTS
WAVELENGTH

COUNTS
WAVELENGTH

QNY1

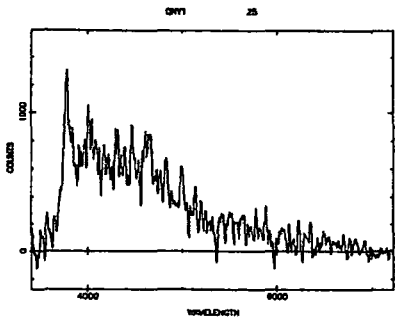
QNY1 25
COUNTS
WAVELENGTH

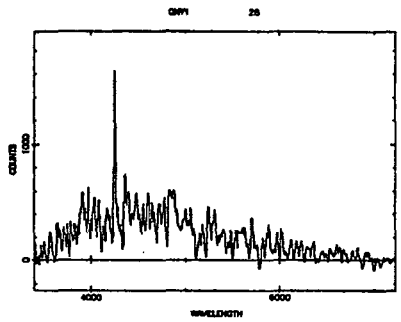
QNY1 26
COUNTS
WAVELENGTH

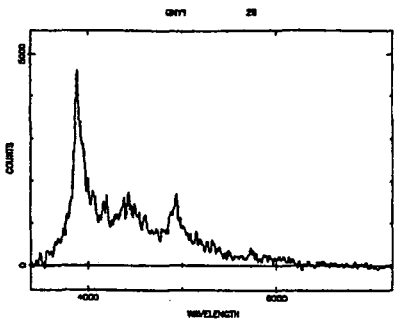
QNY1 28
COUNTS
WAVELENGTH

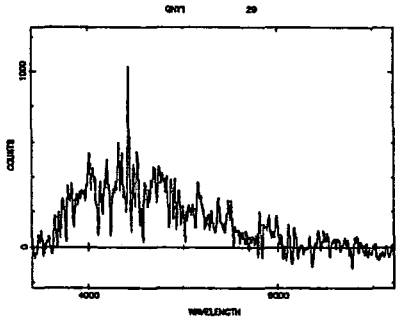
QNY1 29
COUNTS
WAVELENGTH

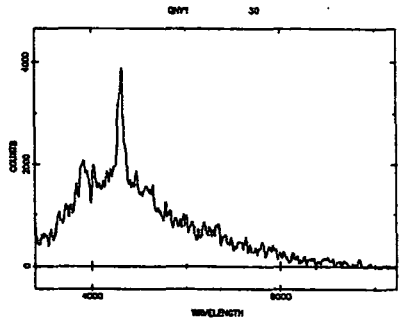
QNY1 30
COUNTS
WAVELENGTH

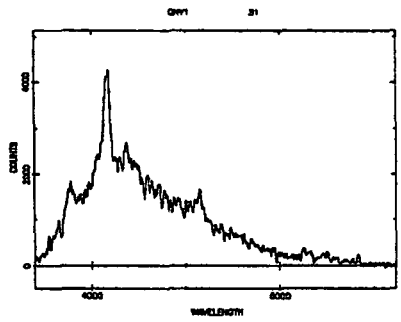
QNY1 31
COUNTS
WAVELENGTH

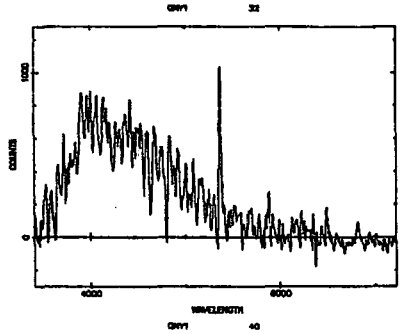
QNY1 32
COUNTS
WAVELENGTH

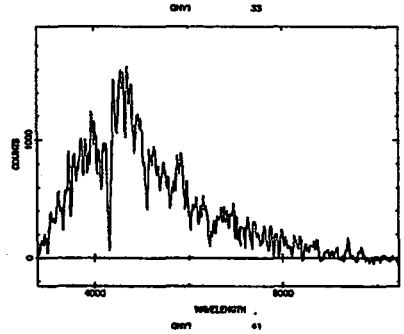
QNY1 33
COUNTS
WAVELENGTH

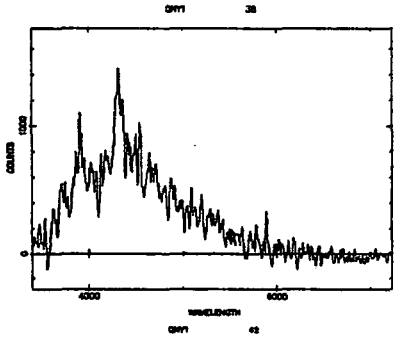
QNY1 38
COUNTS
WAVELENGTH

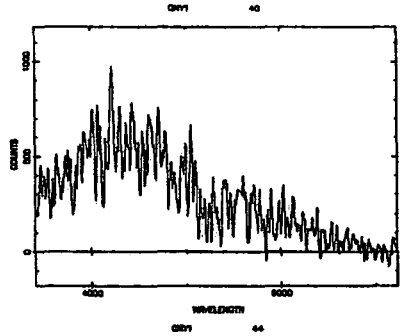
QNY1 40
COUNTS
WAVELENGTH

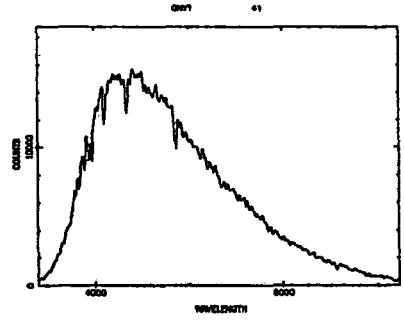
QNY1 41
COUNTS
WAVELENGTH

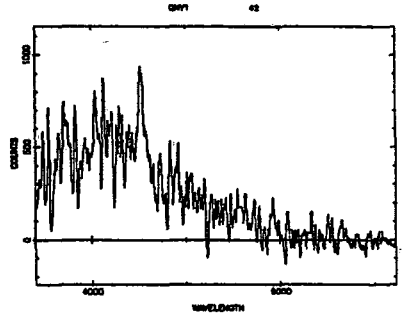
QNY1 42
COUNTS
WAVELENGTH

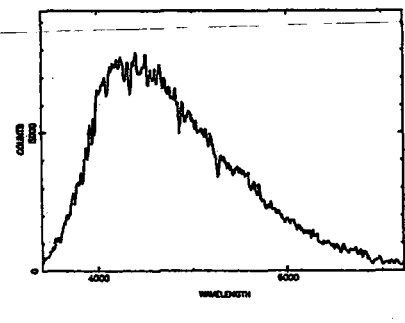
QNY1 44
COUNTS
WAVELENGTH

QNY 2

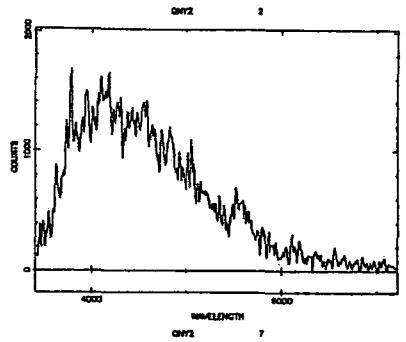
QNY2 3
COUNTS
WAVELENGTH

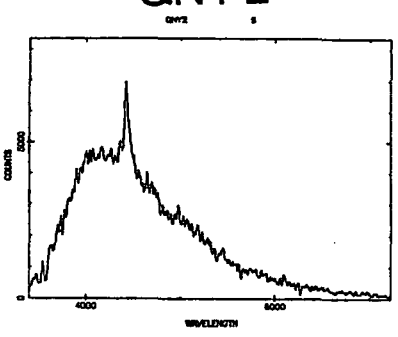
QNY2 5
COUNTS
WAVELENGTH

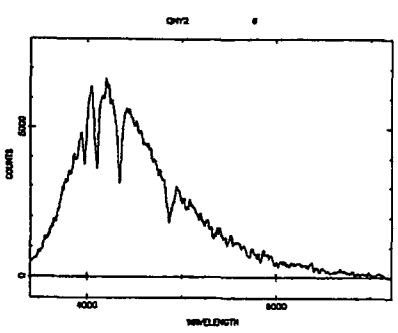
QNY2 6
COUNTS
WAVELENGTH

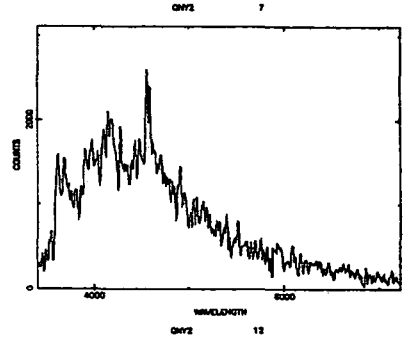
QNY2 7
COUNTS
WAVELENGTH

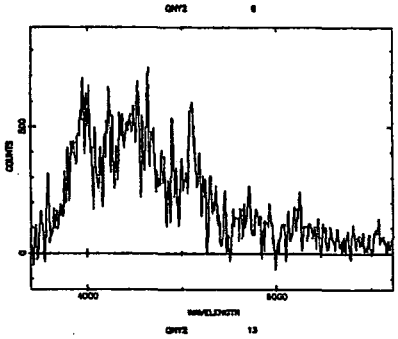
QNY2 8
COUNTS
WAVELENGTH

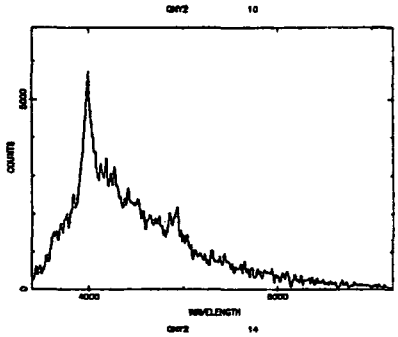
QNY2 10
COUNTS
WAVELENGTH

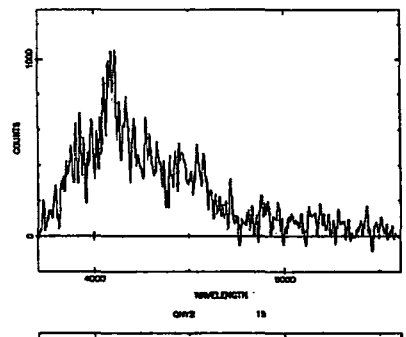
QNY2 12
COUNTS
WAVELENGTH

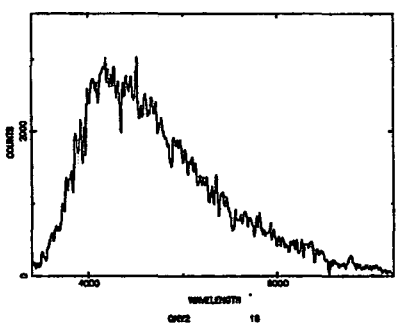
QNY2 13
COUNTS
WAVELENGTH

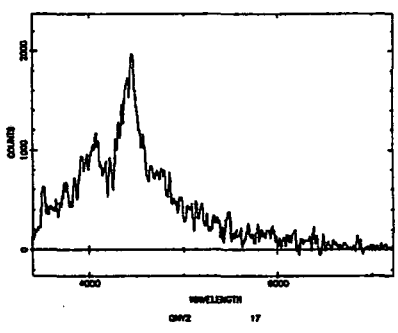
QNY2 14
COUNTS
WAVELENGTH

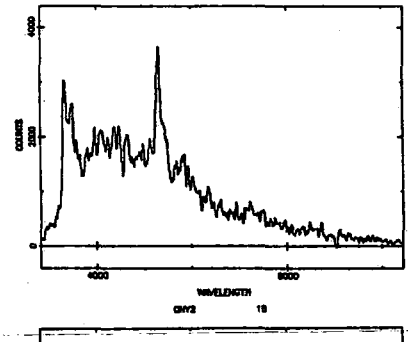
QNY2 15
COUNTS
WAVELENGTH

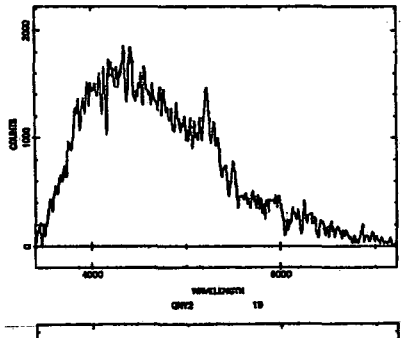
QNY2 16
COUNTS
WAVELENGTH

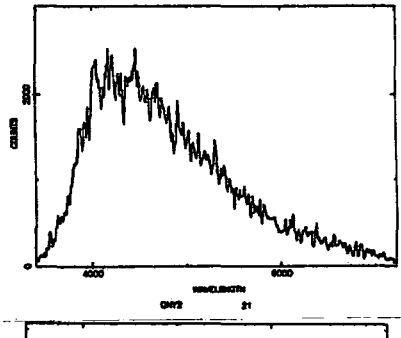
QNY2 17
COUNTS
WAVELENGTH

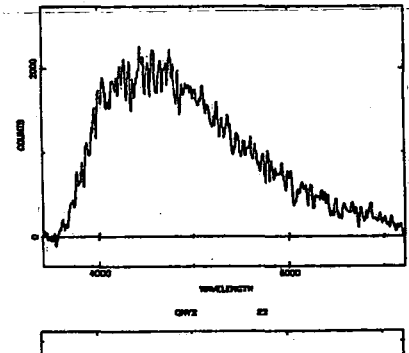
QNY2 18
COUNTS
WAVELENGTH

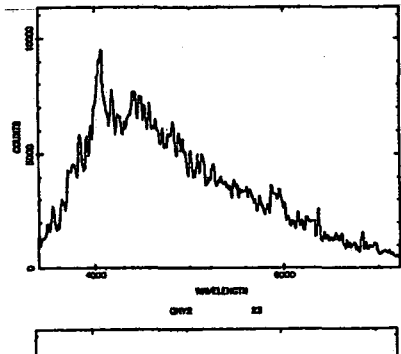
QNY2 19
COUNTS
WAVELENGTH

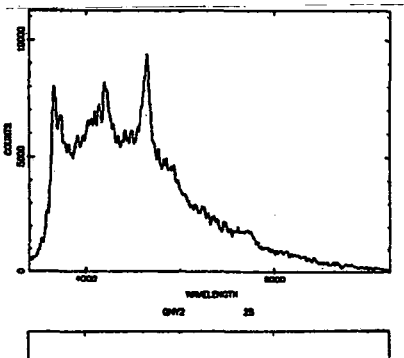
QNY2 21
COUNTS
WAVELENGTH

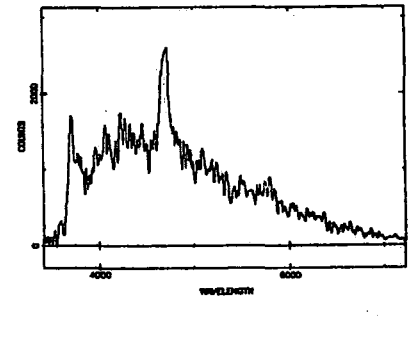
QNY2 22
COUNTS
WAVELENGTH

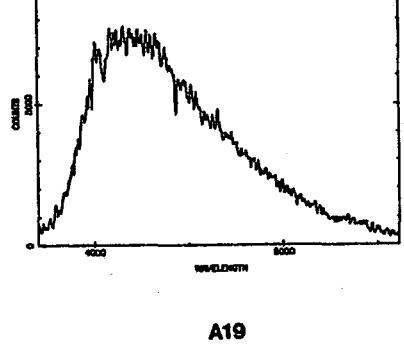
QNY2 23
COUNTS
WAVELENGTH

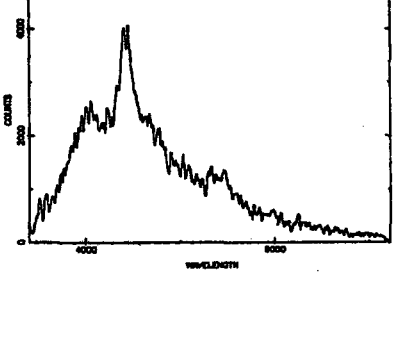
QNY2 25
COUNTS
WAVELENGTH

COUNTS
WAVELENGTH

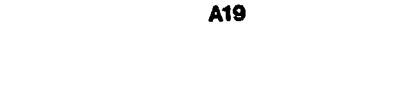
COUNTS
WAVELENGTH

COUNTS
WAVELENGTH

QNY2

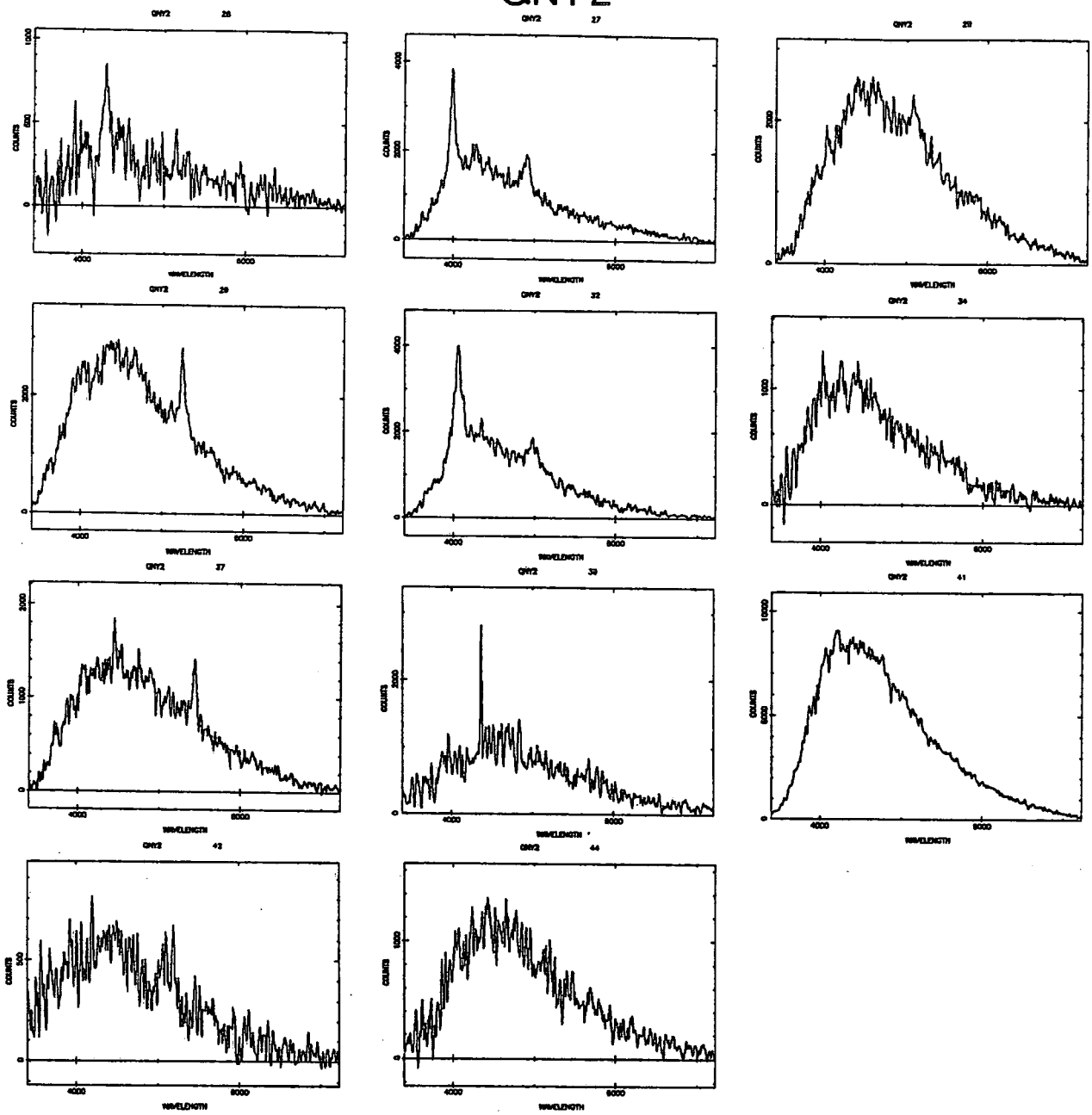
QNY2 26
QNY2 27
QNY2 28
QNY2 29
QNY2 32
QNY2 34
QNY2 37
QNY2 39
QNY2 41
QNY2 42
QNY2 44
COUNTS
WAVELENGTH

QNA1

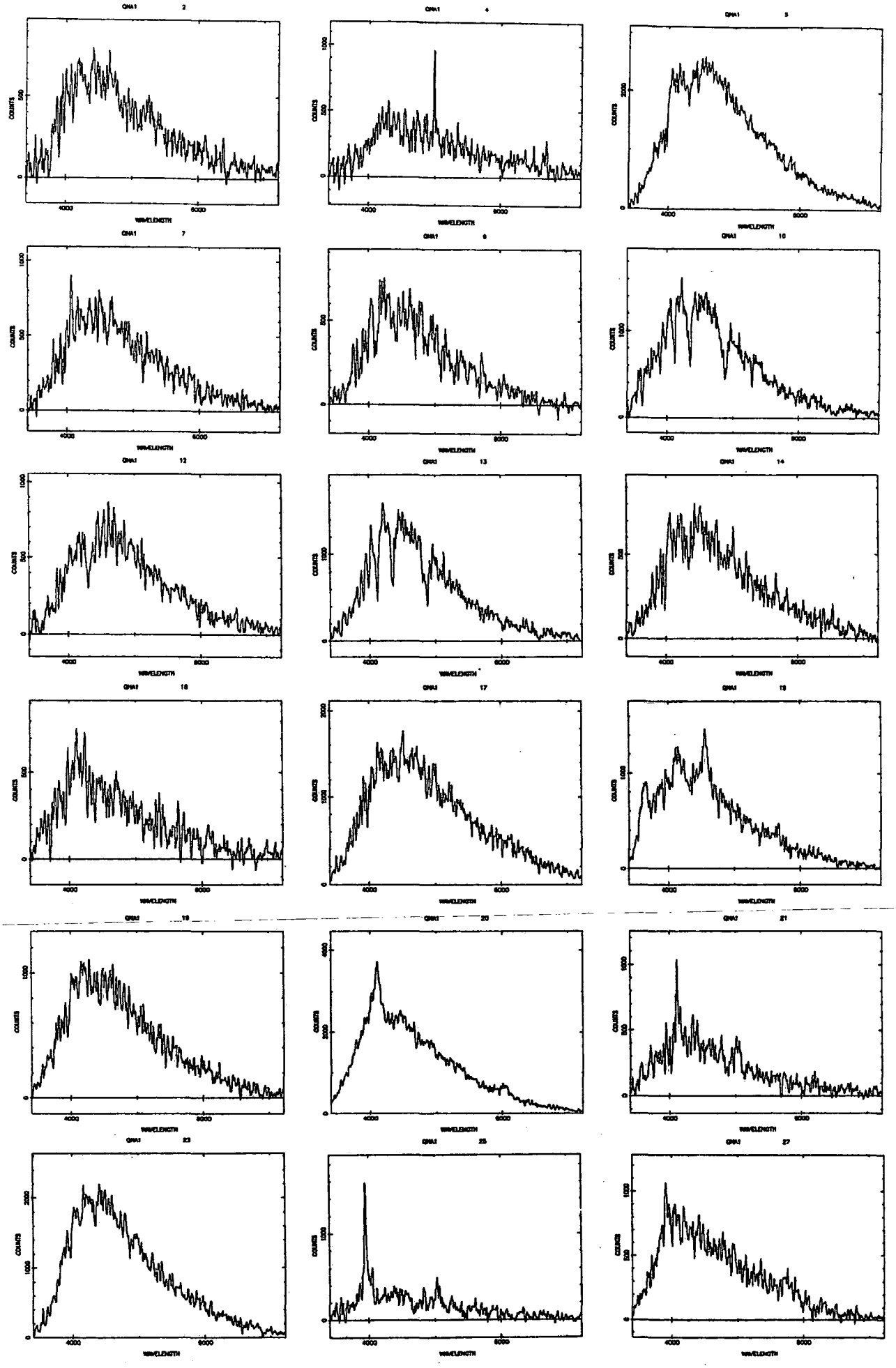
QNA1 2
QNA1 4
QNA1 5
QNA1 7
QNA1 9
QNA1 10
QNA1 12
QNA1 13
QNA1 14
QNA1 16
QNA1 17
QNA1 18
QNA1 19
QNA1 20
QNA1 21
QNA1 23
QNA1 25
QNA1 27
COUNTS
WAVELENGTH

QNA1

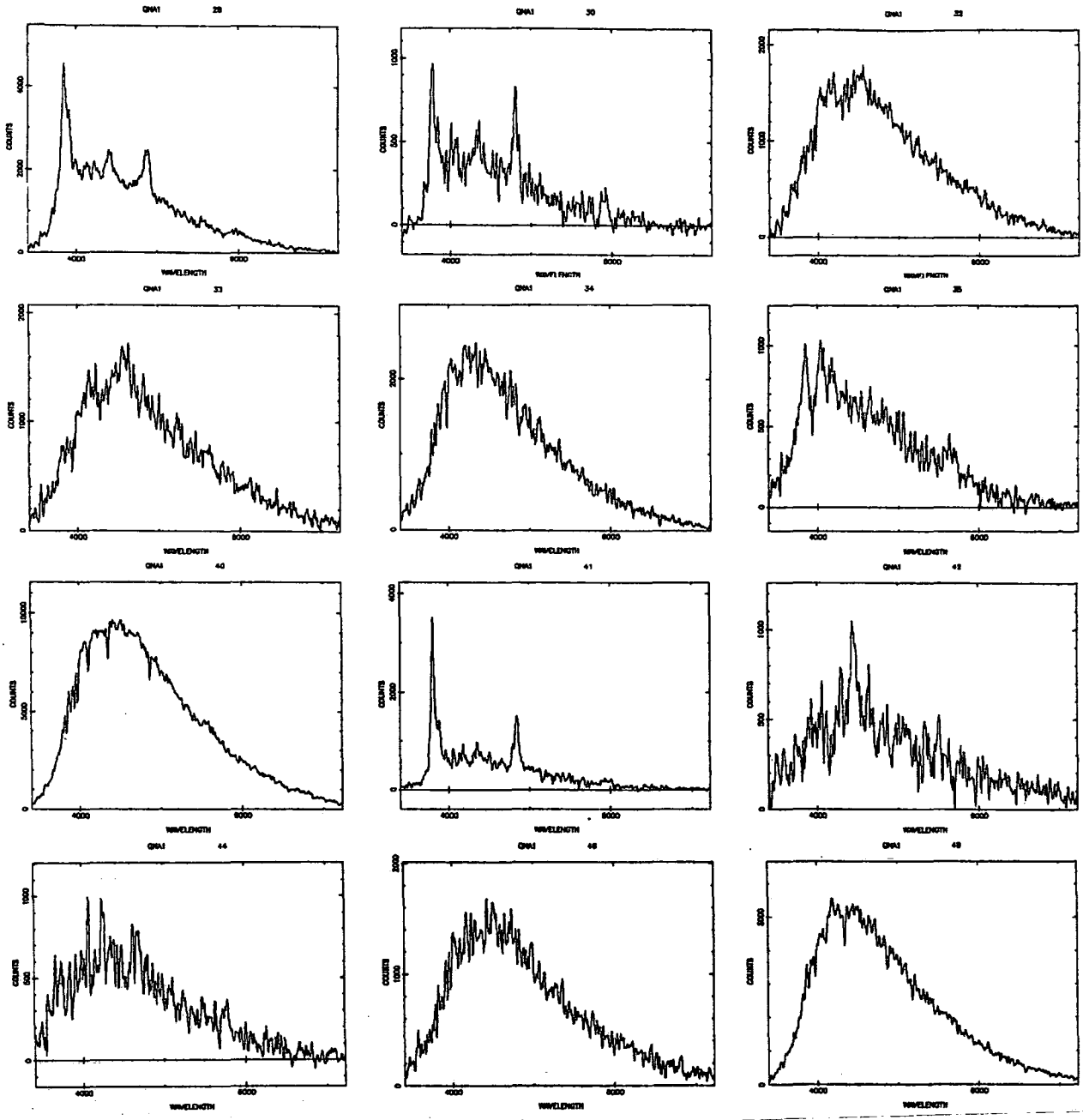
QNA1 29
QNA1 30
QNA1 33
QNA1 34
QNA1 40
QNA1 41
QNA1 44
QNA1 46
COUNTS
WAVELENGTH

QSM1

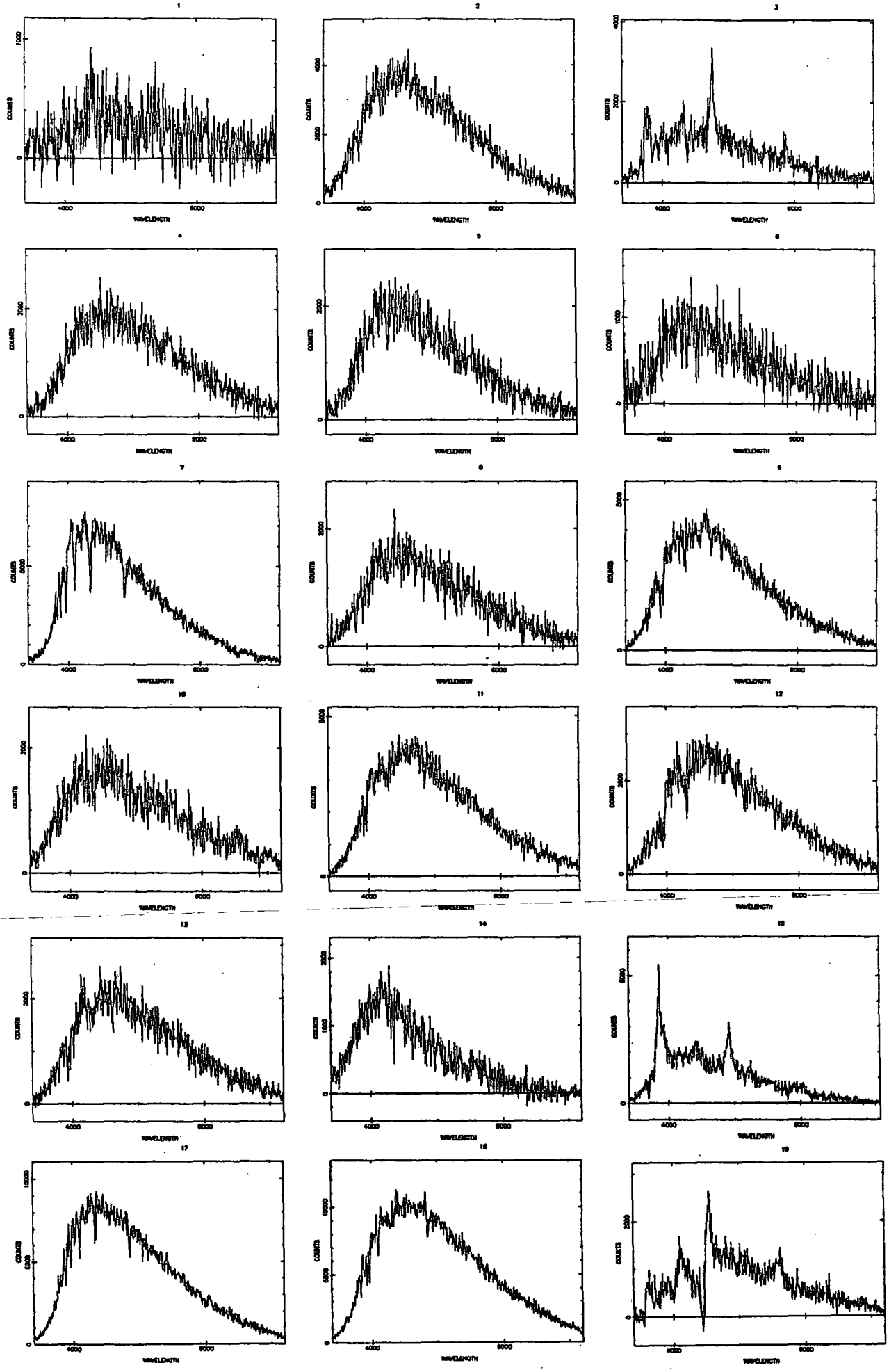
1
2
3
4
5
6
7
8
9
10
11
12
13
14
15
16
17
18
19
20
21
22
COUNTS
WAVELENGTH
4000
6000

QSM1

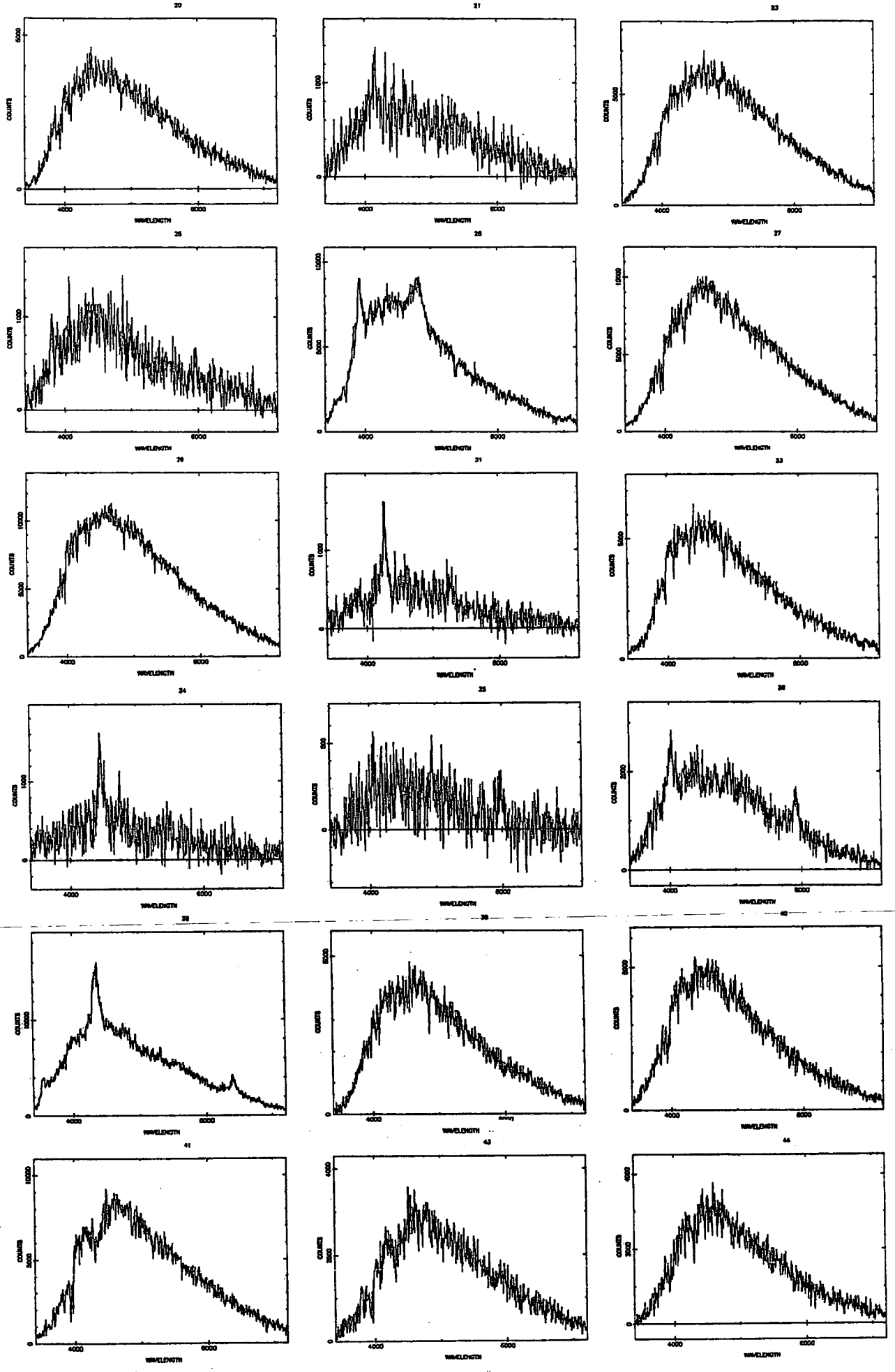
20
21
23
25
26
27
29
31
33
34
35
36
38
40
41
43
44
COUNTS
WAVELENGTH
4000
6000

QSM 2

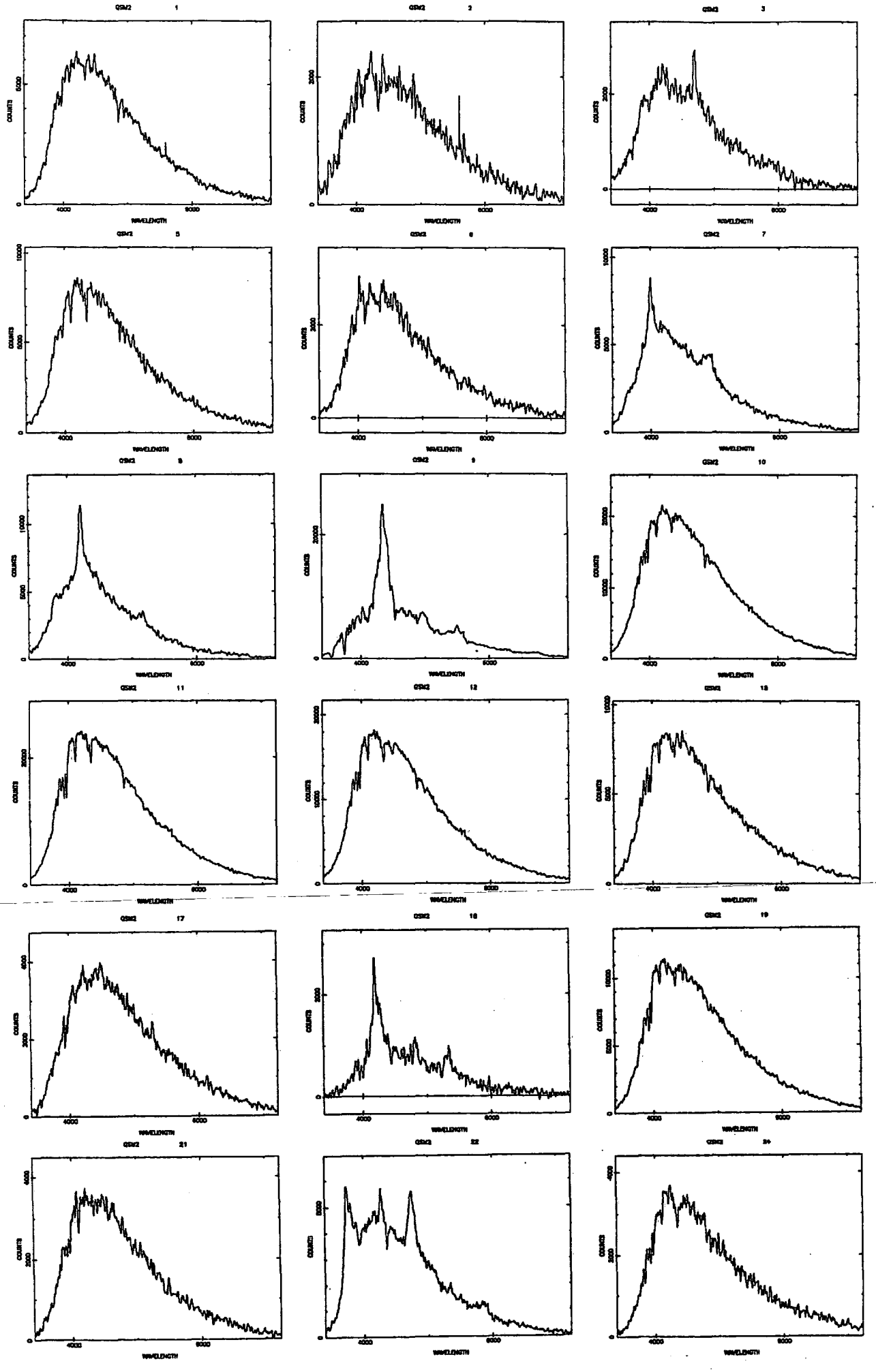
QSM2 1
QSM2 2
QSM2 3
QSM2 5
QSM2 6
QSM2 7
QSM2 9
QSM2 10
QSM2 11
QSM2 12
QSM2 17
QSM2 18
QSM2 19
QSM2 21
QSM2 22
COUNTS
WAVELENGTH

QSM 2

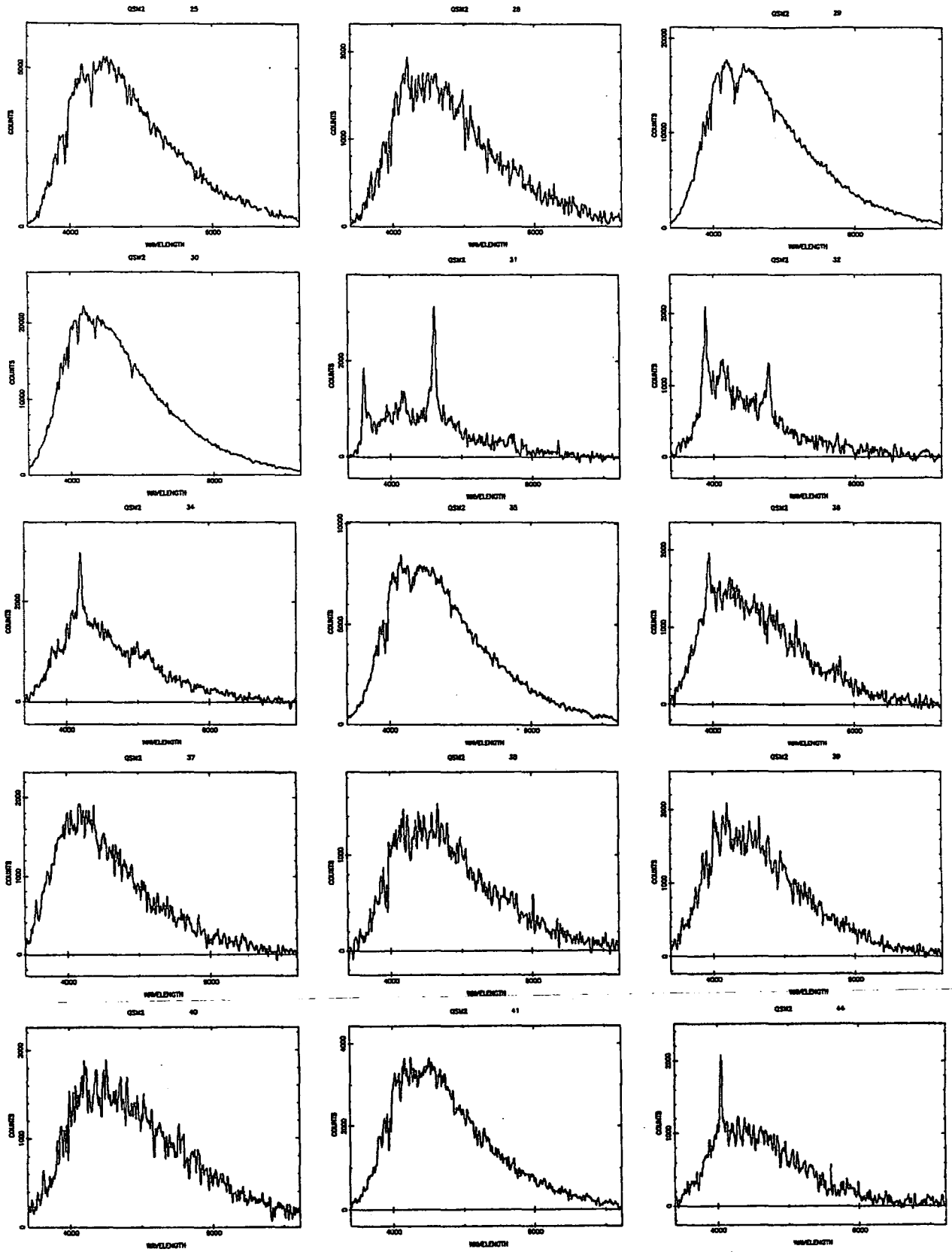

SKY

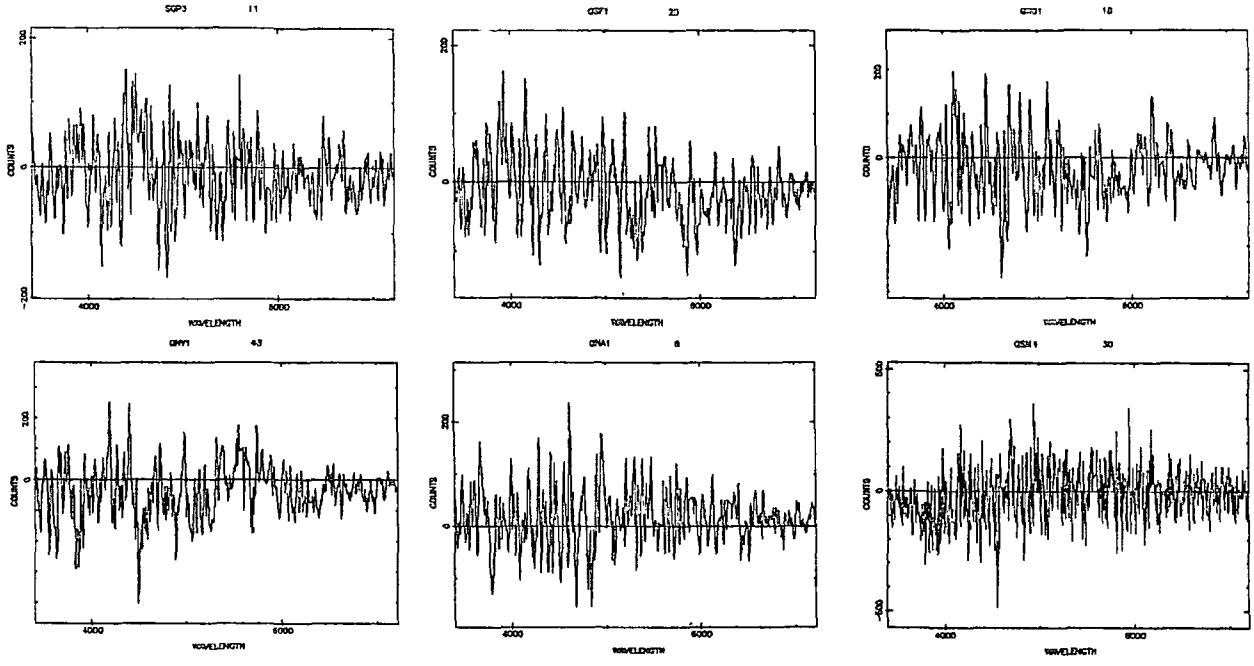

APPENDIX B

FAINT UVX SURVEY: CATALOGUE OF EMISSION LINE OBJECTS

Name	R.A. (1950)	Dec.	b	u-b	ID	z	Class	Lines
SGP1:03	00h 57m 01s.9	-28° 35′ 42″	19.45	-0.53	Q	0.662	2	MgII 4650
SGP1:04	00 56 18.1	-28 45 53	19.91	-0.91	Q	1.740	2	SiIV 3850
								CIV 4240
								CIII? 5200
SGP1:05	00 57 07.2	-28 38 11	20.63	-0.60	Q	0.454	3	MgII 4073
								[NeV](3426) 4971
SGP1:06	00 57 20.3	-28 37 40	20.90	-0.88	Q	1.564	2	CIV 3971
								CIII] 4900
SGP1:07	00 56 12.5	-28 43 26	20.11	-0.65	Q	0.818	1	MgII 5088
SGP1:10	00 55 49.0	-28 32 08	20.86	-0.72	NL	0.426	1	[OII] 5303
								Hβ 6912
								[OIII](4959) 7062
								[OIII](5007) 7135
SGP1:16	00 56 18.0	-28 41 44	20.48	-0.58	Q	0.965	3	MgII 5500 (Q?)
SGP1:17	00 55 42.9	-28 41 20	20.09	-1.31	Q	1.278	1	CIV 3531
								CIII] 4354
								MgII 6363
SGP1:20	00 56 34.5	-29 05 30	19.87	-1.54	Q	1.334	1	CIV 3611
								CIII] 4461
								MgII 6533
SGP1:21	00 56 51.9	-29 04 10	20.47	-0.54	Q	2.170	2	NV* 3900
								CIV 4910
SGP1:22	00 56 51.8	-29 01 46	20.79	-0.81	Q	1.281	3	CIV? 3531
								CIII] 4350
								MgII? 6380
SGP1:31	00 57 30.5	-28 48 50	20.28	-0.49	Q	0.692	1	MgII 4719
								[ArIV](2855) 4825
								FeII(2950)* 5000
								HeII(3203) 5411
SGP1:39	00 55 19.1	-28 52 38	20.70	-1.27	Q	1.388	1	CIV 3700
								CIII] 4558

Name	R.A. (1950)	Dec.	b	u-b	ID	z	Class	Lines
SGP2:01	00h 48m 52s.1	-29° 07'20"	19.93	-0.68	Q	2.375	1	Lyα 4106 NV 4187 SiIV 4694 CIV 5227
SGP2:06	00 49 31.4	-29 18 50	20.18	-1.39	Q	1.631	1	CIV 4075 CIII] 5020
SGP2:11	00 50 12.9	-29 07 30	20.98	-0.93	Q	1.976	1	Lyα 3616 NV* 3700 CIV 4612
SGP2:13	00 49 37.9	-29 08 38	20.31	-1.01	Q	0.578	2	MgII 4415 [ArIV](2855) 4520 [ArIV](2869) 4550
SGP2:14	00 50 11.8	-29 03 56	20.46	-1.08	Q	1.619	1	CIV 4061 CIII] 4993
SGP2:16	00 50 28.2	-29 07 42	20.22	-0.51	Q	0.852	2	CIII]? 3520 MgII 5182 FeII(2950)* 5450
SGP2:18	00 49 41.5	-29 06 34	20.41	-1.02	Q	0.466	3	MgII 4085 Hδ 6002 (z=1.140? CIII]/MgII)
SGP2:19	00 50 05.8	-29 05 36	18.97	-0.73	Q	1.605	1	CIV 4037 CIII] 4971
SGP2:20	00 49 27.5	-29 31 18	19.45	-0.58	Q	0.601	2	MgII 4482 FeII(2950)* 4680 [NeV](3426) 5471 [OII] 5970 Hδ 6563
SGP2:25	00 49 42.1	-29 34 08	20.76	-0.63	Q	1.868	2	Lyα* 3487 CIV 4442
SGP2:27	00 49 47.8	-29 35 26	20.86	-0.48	Q	1.920	3	SiIV 4061 CIV 4500 CIII] on sky?
SGP2:34	00 48 28.2	-29 21 15	19.83	-0.64	Q	1.602	3	CIV 4030
SGP2:36	00 48 48.6	-29 21 38	20.83	-1.16	Q	1.756	2	CIV 4275 CIII] 5250
SGP2:38	00 48 16.3	-29 15 29	20.36	-0.31	NL	0.086	1	[OII] 4054 [OIII](3727) 5438 Hα 7125
SGP2:39	00 48 26.4	-29 18 15	19.13	-1.01	Q	0.428	1	MgII 4010 Hβ 6950
SGP2:40	00 50 27.5	-29 32 34	20.91	-0.37	NL	0.396	1	[OII] 5195 [OIII] 6975
SGP2:44	00 50 38.3	-29 22 35	20.37	-1.09	Q	1.800	1	SiIV* 3920 CIV 4620 OIII(1665) 4665 NIII(1750) 4896 CIII] 5340
SGP2:45	00 49 51.1	-29 20 34	20.64	-0.34	NL	0.111	1	[OII] 4136 Hβ 5145
SGP2:46	00 50 35.8	-29 37 02	20.37	-0.97	Q	0.917	3	MgII 5364
SGP2:47	00 50 36.9	-29 29 13	18.92	-0.51	Q	0.830	1	MgII 5120
SGP2:48	00 49 46.2	-29 21 40	19.77	-1.34	Q	1.852	1	Lyα 3475 SiIV 3987 CIV 4425

Name	R.A. (1950)	Dec.	b	u-b	ID	z	Class	Lines
SGP3:02	00h 52m 16s.1	-28° 32′ 31″	20.46	-0.58	Q	2.181	1	Lyα 3869 SiIV 4462 CIV 4926
SGP3:05	00 51 23.0	-28 26 23	20.56	-0.60	Q	2.110	1	Lyα 3780 NV 3861 SiIV 4367 CIV 4840
SGP3:09	00 51 52.4	-28 22 28	19.57	-0.51	Q	2.133	2	Lyα 3815 CIV 4847
SGP3:10	00 52 38.9	-28 23 46	19.34	-0.33	Q	2.350	1	Lyα 4076 CIV 5169
SGP3:18	00 53 37.1	-28 30 12	19.97	-0.79	Q	1.029	1	CIII] 3875 MgII 5674
SGP3:19	00 52 33.8	-28 30 45	20.37	-1.47	Q	0.779	1	CII 4143 MgII 4973
SGP3:20	00 53 33.8	-28 36 49	20.76	-1.48	Q	1.306	1	CIV 3573 CIII] 4400 MgII 6445
SGP3:22	00 52 51.8	-28 37 02	20.60	-0.17	NL	0.130	3	[OII] 4720
SGP3:23	00 51 21.7	-28 39 57	18.65	-1.16	Q	1.574	1	CIV 3990 CIII] 4909
SGP3:25	00 51 39.5	-28 46 47	19.40	-1.33	Q	1.338	1	CIV 3651 CIII] 4462 MgII 6543
SGP3:27	00 53 30.9	-28 36 26	19.05	-0.84	Q	1.920	1	Lyα 3554 NV 3623 SiIV 4100 CIV 4523 CIII] 5570
SGP3:31	00 53 18.3	-28 51 19	19.59	-0.75	Q	1.706	1	OIV(1406) 3801 CIV 4191 HeII(1640) 4425 CIII] 5166
SGP3:34	00 53 37.0	-28 43 11	19.27	-1.00	Q	1.933	1	Lyα 3590 NV 3637 SiIV 4109 CIV 4537
SGP3:35	00 53 17.1	-28 38 36	20.31	-0.30	BQ	1.498	1	CIV* 3878 CIII] 4758
SGP3:37	00 53 18.3	-28 51 19	19.32	0.80	NL	0.130	3	[OII] 4210
SGP3:38	00 52 51.4	-28 53 34	19.14	-0.82	Q	0.636	1	MgII 4576 FeII(2950)* 4819 [OII] 6105
SGP3:39	00 53 18.2	-28 40 23	20.86	-0.67	Q	0.639	1	MgII 4587 FeII(2500)* 4120
SGP3:48	00 52 22.0	-28 48 10	20.47	-0.90	Q	2.097	1	Lyα 3772 NV 3836 SiIV 4344 CIV 4797
SGP3:49	00 52 18.0	-28 47 34	19.49	-0.99	Q	1.402	3	CIII] 4586

Name	R.A. (1950)	Dec.	b	u-b	ID	z	Class	Lines
QSF1:01	03h 39m 26s.2	-45° 05'53"	19.09	-0.80	Q	2.268	1	Lyα 3975 SiIV 4575 CIV 5062
QSF1:03	03 39 18.1	-45 02 07	20.86	-0.95	Q	1.072	2	CIII] 3955 MgII 5798
QSF1:04	03 39 47.4	-45 08 15	19.92	-0.72	Q	2.049	1	Lyα 3707 SiIV 4269 CIV 4723
QSF1:05	03 39 03.8	-45 02 51	20.98	-0.55	NL	0.346	3	[OII] 5016
QSF1:07	03 41 50.7	-45 17 41	20.16	-0.62	Q	1.615	1	SiIV 3661 CIV 4051 CIII]? 4992
QSF1:09	03 41 06.4	-45 20 50	20.56	-0.43	Q	0.550	1	MgII 4362 HeII(3203) 4950
QSF1:10	03 40 10.3	-45 10 20	19.78	-0.43	NL	0.312	1	[OII] 4890 [OIII](5007) 6569
QSF1:11	03 40 57.8	-45 12 06	19.37	-0.43	NL	0.182	1	[OII] 4405 Hβ 5746 [OIII](4959) 5862 [OIII](5007) 5918
QSF1:12	03 40 33.9	-45 21 29	20.12	-0.49	Q	2.212	1	Lyα 3905 NV 3982 CIV 4975 CIII] 6131
QSF1:16	03 40 45.8	-45 13 03	20.99	-0.64	Q	2.000	1	Lyα 3648 CIV 4640 HeII(1640) 4920
QSF1:17	03 39 48.1	-44 52 00	20.57	-0.74	Q	1.745	2	CIV 4250 CIII]? 5146 CII]? 6520
QSF1:19	03 39 42.4	-44 58 51	20.48	-0.78	Q	1.146	1	CIII] 4097 MgII 6010
QSF1:22	03 39 49.4	-44 52 27	20.65	-0.48	NL	0.360	1	[OII] 5068 [OIII](5007) 6809
QSF1:29	03 41 43.9	-45 04 26	20.97	-1.12	Q	0.566	2	FeII(2500)* 3950 MgII 4382
QSF1:30	03 42 07.2	-44 56 18	20.47	-0.55	Q	0.569	2	HeII(2512) 3953 MgII 4390
QSF1:31	03 42 00.9	-45 10 55	19.95	-0.95	Q	0.397	2	MgII 3910
QSF1:32	03 41 41.0	-45 10 41	20.33	-0.71	Q	1.311	3	CIII] 4416 CII 5371
QSF1:33	03 42 11.5	-44 56 38	20.66	-0.59	NL	0.182	1	[OII] 4405 [OIII](4959) 5866 [OIII](5007) 5913
QSF1:34	03 40 50.1	-45 05 27	19.26	-0.67	BQ	2.004	1	Lyα 3649 NV 3732 SiIV 4204 CIV 4660
QSF1:36	03 42 13.5	-45 03 04	18.87	-0.75	Q	1.700	1	CIV 4185 CIII] 5152
QSF1:37	03 41 11.9	-44 46 19	20.37	-0.62	Q	0.957	1	CIII] 3732 MgII 5480
QSF1:40	03 41 32.7	-44 58 14	18.92	-0.97	Q	1.662	1	CIV 4122 CIII] 5084

Name	R.A. (1950)	Dec.	b	u-b	ID	z	Class	Lines
QSF2:03	03h 44m 29s.7	-45° 52' 47"	20.03	-0.82	Q	1.871	3	NV 3567
								SiIV 4024
								CIV 4447
QSF2:05	03 45 34.2	-45 47 51	20.31	-0.57	Q	2.494	1	Lyα 4246
								CIV 5400
QSF2:09	03 43 33.2	-46 03 45	20.58	-0.81	Q	1.589	1	CIV 3949
								CIII] 4895
QSF2:15	03 44 32.2	-46 10 21	20.46	-0.66	Q	1.082	2	CIII] 3959
								MgII 5846
QSF2:16	03 44 01.2	-46 01 03	19.52	-0.66	Q	0.592	3	MgII 4453
								Hδ? 6506
QSF2:17	03 46 23.0	-46 12 01	20.51	-0.64	Q	2.213	1	Lyα 3904
								CIV 4982
QSF2:18	03 45 12.1	-46 13 51	19.75	-1.54	Q	1.699	1	CIV 4183
								CIII] 5151
QSF2:20	03 46 05.6	-46 19 14	20.95	-0.66	NL	0.103	3	[OII] 4110
QSF2:26	03 46 20.2	-46 15 25	20.72	-0.58	Q	2.118	1	Lyα 3790
								NV? 3868
								CIV 4831
QSF2:28	03 44 20.7	-46 21 03	19.78	-1.02	Q	2.015	1	Lyα 3660
								CIV 4678
								CIII] 5755
QSF2:29	03 45 13.8	-46 19 54	20.07	-0.83	Q	1.984	1	Lyα 3629
								CIV 4622
QSF2:30	03 44 00.0	-46 13 52	19.62	-0.59	Q	0.844	1	MgII 5159
								FeII(2950)* 5450
QSF2:31	03 44 53.9	-46 17 04	20.06	-0.70	Q	0.906	1	CIII] 3634
								CII 4441
								MgII 5325
QSF2:35	03 45 19.3	-46 23 44	19.34	-0.54	Q	0.743	2	[MgVII](2632) 4581
								MgII 4886
QSF2:36	03 44 36.1	-46 17 26	20.52	-0.68	Q	2.293	1	Lyα 3996
								CIV 5117
QSF2:39	03 45 55.7	-46 04 37	20.07	-0.56	Q	1.329	3	CIII] 4454
QSF2:42	03 46 26.2	-46 11 21	20.07	-0.41	Q	1.351	3	CIV 3629
								CIII] 4495
QSF2:44	03 45 45.5	-46 04 22	20.47	-1.03	Q	0.490	2	MgII 4181
								HeII(3203) 4760

Name	R.A. (1950)	Dec.	b	u-b	ID	z	Class	Lines
QNB1:08	$10^h 39^m 21^s.4$	+01° 47′ 22″	20.16	-0.64	NL	0.202	1	[OII] 4475 Hβ 5845 [OIII](4959) 5970 [OIII](5007) 6019
QNB1:10	10 39 03.2	+01 31 56	20.90	-1.19	Q	1.704	2	CIV 4189 CIII]? 5162
QNB1:16	10 38 56.6	+01 36 13	20.31	-0.28	NL	0.236	1	[NeV](2973) 3672 [NeII](3063)? 3777 [NeV](3426) 4232 [OII] 4611
QNB1:20	10 40 32.3	+01 24 33	20.86	-0.55	Q	2.503	1	Lyα 4258 NV 4340 SiIV 4907 CIV 5432
QNB1:22	10 40 17.4	+01 28 46	19.91	-1.11	Q	1.426	3	CIV 3763 CIII] 4621
QNB1:24	10 40 14.5	+01 23 06	20.66	-1.13	Q	0.700	2	MgII 4727 FeII(2950)° 5011
QNB1:26	10 40 40.0	+01 17 54	19.82	-1.55	Q	1.917	1	Lyα 3548 NV 3615 SiIV 4048 CIV 4519
QNB1:28	10 40 40.5	+01 21 25	20.53	-0.81	Q	1.494	1	CIV 3860 CIII] 4766
QNB1:32	10 39 21.8	+01 21 50	20.56	-0.70	Q	0.505	3	MgII 4211 HeII(3203) 4810
QNB1:34	10 39 56.5	+01 15 45	18.45	-1.45	Q	1.398	1	CIV 3717 NIII](1750) 4196 CIII] 4564 MgII 6725
QNB1:38	10 39 59.7	+01 17 50	18.90	-0.76	BQ	2.109	1	Lyα 3772 NV 3852 SiIV 4355 CIV 4818 CIII] 5950
QNB1:43	10 40 10.2	+01 33 33	20.25	-1.59	Q	1.845	1	SiIV 3978 CIV 4407 CIII] 5388
QNB1:44	10 40 21.9	+01 47 25	20.26	-0.78	Q	0.500	3	MgII 4197
QNB1:49	10 40 18.0	+01 33 21	19.53	-0.94	BQ	0.493	2	MgII 4191 HeII(3203) 4779

Name	R.A. (1950)	Dec.	b	u-b	ID	z	Class	Lines
QNB2:01	$10^h\ 41^o\ 13^s.1$	+01° 05' 48"	19.07	-1.63	Q	1.253	2	CIV 3493
								CIII] 4296
QNB2:02	10 40 29.7	+01 10 04	19.18	-0.95	Q	0.730	3	MgII 4841
QNB2:06	10 40 35.6	+01 06 41	20.68	-1.01	Q	0.493	2	MgII 4177
QNB2:07	10 40 47.5	+00 59 06	19.61	-0.42	Q	0.627	2	MgII 4552
QNB2:15	10 41 26.6	+01 06 40	18.88	-0.79	Q	1.697	1	CIV 4180
								CIII] 5154
QNB2:17	10 41 16.7	+01 11 08	20.94	-0.69	NL	0.305	3	[OII] 4864
QNB2:23	10 42 21.6	+00 53 10	20.00	-0.92	Q	1.166	1	CIII] 4138
								MgII 6055
QNB2:24	10 41 43.2	+00 53 10	19.25	-0.61	Q	0.192	1	Hδ 4876
								Hβ 5799
								[OIII](4959) 5911
								[OIII](5007) 5973
QNB2:25	10 41 49.1	+00 56 42	19.36	-1.16	Q	1.324	1	CIII] 4424
								MgII 6520
QNB2:28	10 41 28.4	+00 56 46	20.91	-0.98	Q	1.194	1	CIII] 4188
								MgII* 6175
QNB2:36	10 40 19.5	+00 48 50	20.53	-1.05	Q	2.116	1	Lyα 3882
								CIV 4834
QNB2:40	10 42 19.1	+00 44 01	20.39	-1.00	Q	0.857	2	CIII] 3543
								MgII 5200
QNB2:42	10 41 49.7	+00 43 28	20.84	-1.20	Q	0.600	3	MgII 4477
QNB2:45	10 42 00.0	+00 47 47	20.74	-1.37	Q	1.253	2	CIII] 4301
QNB2:46	10 41 07.0	+00 45 52	20.19	-1.08	Q	1.145	2	CII 4990
								MgII 6000
QNB2:47	10 41 06.0	+00 43 23	20.66	-0.54	NL	0.080	3	[OII] 4025
QNB2:50	10 41 47.7	+00 51 44	20.45	0.07	NL	0.060	1	[OII] 3961
								Hβ 5153
								[OIII](4959) 5261
								[OIII](5007) 5307
								Hα 6957

Name	R.A. (1950)	Dec.	b	u-b	ID	z	Class	Lines
QNY1:02	12h 33m 13s.7	-00° 52' 35"	20.07	-1.42	Q	1.471	1	CIV 3830
								CIII] 4713
QNY1:06	12 33 19.7	-00 55 18	19.44	-1.19	Q	1.470	1	CIV 3828
								CIII] 4713
QNY1:07	12 33 35.1	-00 34 44	20.40	-0.55	NL	0.308	3	[OII] 4875
QNY1:08	12 33 34.9	-00 42 56	19.86	-0.60	Q	1.874	3	CIV 4451
QNY1:09	12 33 28.6	-00 36 04	20.87	-1.26	Q	1.097	3	CIII] 4003
								MgII° 5850
QNY1:13	12 32 56.1	-00 25 10	19.03	-0.73	Q	1.579	1	CIV 4000
								CIII] 4918
QNY1:17	12 34 16.0	-00 42 55	19.00	-1.11	Q	1.545	2	CIV 3943
								NIII(1750) 4450
								CIII]° 4860
QNY1:24	12 34 59.5	-00 36 19	20.66	-1.05	Q	0.788	2	MgII 5002
QNY1:25	12 34 16.0	-00 40 39	20.88	-1.24	Q	1.437	1	CIV 3776
								CIII] 4650
QNY1:26	12 34 12.1	-00 36 40	20.50	-0.50	NL	0.135	3	[OII] 4230
QNY1:28	12 34 54.1	-00 27 44	20.78	-1.46	Q	2.193	1	Lyα 3882
								SiIV 4473
								CIV 4943
QNY1:29	12 33 54.1	-00 37 27	21.32	-0.88	NL	0.179	3	[OII] 4394)
QNY1:30	12 34 07.6	-00 33 24	19.55	-1.17	Q	1.792	1	SiIV° 3910
								CIV 4324
QNY1:31	12 34 23.1	-00 24 37	20.00	-1.46	Q	1.686	1	SiIV 3759
								CIV 4161
								CIII] 5125
QNY1:32	12 34 02.8	-00 20 53	20.82	-0.67	NL	0.445	3	[OII] 5385
QNY1:36	12 33 57.9	-00 36 30	20.91	-0.85	Q	1.784	2	CIV 4309
								SiIV 3900

Name	R.A. (1950)	Dec.	b	u-b	ID	z	Class	Lines
QNY2:02	12h 35m 54s.5	+00° 35′35″	20.14	-0.86	Q	0.976	1	CIII] 3767 MgII 5534
QNY2:05	12 35 39.1	+00 31 45	19.33	-0.51	Q	1.847	2	NV 3530 CIV 4415 CIII] 5430
QNY2:07	12 35 24.5	+00 36 14	20.01	-1.05	Q	1.948	1	Lyα 3600 NV 3681 SiIV* 4140
QNY2:09	12 35 04.5	+00 31 57	20.98	-0.96	Q	0.822	3	MgII 5097
QNY2:10	12 34 28.9	+00 31 07	20.13	-0.94	Q	1.581	1	CIV 3996 CIII] 4930
QNY2:12	12 35 22.6	+00 25 45	21.33	-1.03	Q	1.188	3	CIII] 4176)
QNY2:14	12 35 07.7	+00 33 57	20.00	-1.03	Q	1.873	1	SiIV* 4050 CIV 4456 CIII] 5479
QNY2:15	12 34 39.2	+00 28 29	20.44	-1.05	Q	2.003	1	Lyα 3650 NV 3730 CIV 4649
QNY2:16	12 35 20.2	+00 33 07	20.97	-1.58	Q	0.866	2	MgII 5221 FeII(2950)* 5500
QNY2:19	12 35 22.8	+00 17 28	20.92	-0.79	Q	1.122	1	CIII] 4050 MgII 5937
QNY2:21	12 34 34.9	+00 19 59	19.20	-1.13	Q	2.003	1	Lyα 3650 NV 3730 SiIV 4185 CIV 4644
QNY2:22	12 34 30.6	+00 13 09	20.09	-0.61	Q	2.038	1	Lyα 3701 CIV 4701 CIII] 5794
QNY2:25	12 34 23.3	+00 10 12	20.62	-1.51	Q	1.854	1	CIV 4415 CIII] 5456
QNY2:26	12 35 33.6	+00 14 14	21.19	-1.09	Q	0.526	3	MgII 4269)
QNY2:27	12 35 55.0	+00 05 52	20.13	-0.79	Q	1.568	1	CIV 3972 CIII] 4909
QNY2:29	12 36 10.7	+00 04 48	19.28	-0.82	Q	0.870	2	MgII 5232
QNY2:32	12 36 06.8	+00 10 33	19.95	-0.50	Q	1.610	1	CIV 4050 CIII] 4974
QNY2:37	12 34 39.4	+00 06 51	20.11	-0.45	Q	0.943	1	CIII] 3712 MgII 5430
QNY2:39	12 35 09.9	+00 01 17	20.29	-2.01	NL	0.169	1	[OII] 4345 Hβ 5702

Name	R.A. (1950)	Dec.	b	u-b	ID	z	Class	Lines
QNA1:04	$13^h\,35^o\,16^s.3$	+00° 32'07"	20.77	-0.70	NL	0.336	3	[OII] 4985) Hβ 6496 [OIII](5007) 6092
QNA1:18	13 36 23.4	+00 42 31	19.76	-0.88	Q	1.940	1	NV 3640 SiIV 4129 CIV 4553
QNA1:20	13 36 30.8	+00 37 34	19.11	-0.73	Q	1.152	1	CIII] 4103 MgII 6028
QNA1:21	13 36 25.5	+00 26 42	20.27	-0.61	Q	1.648	1	CIV 4102 CIII] 5050
QNA1:25	13 36 30.4	+00 24 57	21.20	-0.37	Q	2.242	1	Lyα 3946) CIV 5018
QNA1:27	13 36 31.2	+00 25 23	20.08	-1.27	Q	1.050	1	CIII] 4102 MgII 5747
QNA1:28	13 35 49.5	+00 31 25	19.24	-0.86	Q	2.153	1	Lyα 3842 NV 3910 SiIV 4414 CIV 4883
QNA1:30	13 36 06.3	+00 38 45	21.28	-1.48	Q	2.103	1	Lyα 3777) NV 3848 SiIV 4358 CIV 4805
QNA1:35	13 35 54.8	+00 32 45	20.18	-1.08	Q	1.014	1	CIII] 3845 MgII 5635
QNA1:41	13 37 05.4	+00 25 33	19.83	-0.80	Q	2.122	1	Lyα 3796 NV 3876 CIV 4883
QNA1:42	13 37 11.8	+00 24 57	19.94	-0.77	Q	1.859	3	CIV? 3587 CIII] 4430
QNA1:44	13 36 33.0	+00 10 48	19.85	-0.63	Q	2.023	2	Lyα 3662 CIV 4675 CIII] 5773

Name	R.A. (1950)	Dec.	b	u-b	ID	z	Class	Lines
QSM1:01	22^h 06^m 51^s.5	-19° 09' 27"	20.59	-0.77	Q	1.829	3	CIV 4382 CIII]° 5383
QSM1:03	22 06 30.4	-19 27 16	19.79	-0.78	Q	2.076	1	Lyα 3737 CIV 4769 CIII] 5872
QSM1:15	22 07 06.6	-19 10 59	19.64	-0.87	Q	2.171	1	Lyα 3858 SiIV 4420 CIV 4908
QSM1:19	22 08 14.0	-19 26 46	19.83	-0.81	BQ	1.930	1	NV 3628 SiIV 4102 CIV 4542 CIII]° 5590
QSM1:21	22 08 08.2	-19 35 08	20.62	-0.87	Q	0.488	3	MgII 4150
QSM1:25	22 07 40.9	-19 38 51	20.13	-0.63	Q	1.128	3	CIII] 4073 MgII 5956
QSM1:26	22 08 03.6	-19 27 37	18.51	-0.63	Q	1.520	1	CIV 3906 CIII] 4806
QSM1:31	22 07 15.0	-19 38 32	20.51	-1.06	Q	1.748	1	CIV 4253 CIII] 5250
QSM1:34	22 06 31.1	-19 44 21	19.95	-0.52	Q	0.591	1	MgII 4441 [NeV](2972) 4737
QSM1:35	22 07 40.6	-19 40 01	20.73	-0.79	Q	1.123	1	CIII] 4043 CII 4940 MgII 5949
QSM1:36	22 07 11.4	-19 30 44	19.36	-0.99	Q	1.119	1	CIII] 4041 MgII 5934
QSM1:38	22 05 59.3	-19 40 14	18.15	-1.07	Q	1.285	1	CIV 3535 CIII] 4632 CII 5308 MgII 6400

Name	R.A. (1950)	Dec.	b	u-b	ID	z	Class	Lines
QSM2:03	22^h 06^m 14^s.8	-20° 19'03"	19.85	-0.84	Q	0.682	2	MgII 4706
QSM2:07	22 06 15.6	-19 59 04	18.86	-0.79	Q	1.578	1	CIV 4000 CIII] 4914
QSM2:08	22 05 51.7	-20 01 30	18.04	-1.24	Q	1.711	1	CIV 4198 CIII] 5168
QSM2:09	22 06 07.0	-19 58 44	17.93	-0.52	Q	2.577	1	Lyα 4350 CIV 5536
QSM2:18	22 07 29.0	-20 05 17	20.27	-0.89	Q	2.454	1	Lyα 4200 SiIV 4835 CIV 5353
QSM2:22	22 07 58.3	-20 08 37	19.13	-1.50	Q	2.062	1	Lyα 3720 NV 3801 SiIV 4296 CIV 4733
QSM2:31	22 07 36.2	-19 56 37	20.11	-1.20	Q	1.978	1	Lyα 3630 SiIV 4160 CIV 4612
QSM2:32	22 07 09.7	-20 06 14	20.44	-0.95	Q	1.515	1	CIV 3895 CIII] 4801
QSM2:34	22 08 04.8	-19 52 36	20.03	-0.62	Q	1.708	1	CIV 4194 CIII]* 5160
QSM2:36	22 07 11.0	-20 04 09	20.20	-1.10	Q	1.070	1	CIII] 3951 MgII* 5795
QSM2:44	22 07 40.4	-19 49 05	20.23	-1.57	Q	0.452	2	MgII 4062

Wavelengths adopted for standard lines are as follows (taken from Lang 1980):

Lyα 1216Å, NV 1240Å, SiIV 1400Å, CIV 1549Å, CIII] 1909Å, CII 2326Å, and [OII] 3727Å.

FeII lines from Grandi (1981)

* Redshift not determined using this line
? Possible Emission Feature

APPENDIX C

FAINT UVX SURVEY: CATALOGUE OF GALACTIC STARS

Name	R.A. (1950)	Dec.	b	u-b	ID
SGP1:02	00h 57m 24s.0	-28° 41′16″	20.87	-0.48	-
SGP1:09	00 55 45.5	-28 43 49	19.94	-0.42	F
SGP1:11	00 58 48.1	-28 39 29	20.74	-0.45	-
SGP1:12	00 55 52.6	-28 48 04	18.83	-0.32	F
SGP1:13	00 56 14.1	-28 40 36	18.75	-0.65	WD
SGP1:14	00 56 14.4	-28 40 03	20.60	-0.39	-
SGP1:15	00 55 39.8	-28 41 20	18.70	-0.30	F
SGP1:18	00 55 33.0	-29 03 44	20.65	-0.30	-
SGP1:19	00 55 47.5	-29 04 37	19.56	-0.93	A
SGP1:25	00 55 37.1	-28 56 17	18.40	-0.41	F
SGP1:26	00 55 17.7	-28 57 51	19.97	-0.52	F
SGP1:27	00 56 56.5	-28 59 23	20.99	-0.39	-
SGP1:28	00 57 21.4	-28 57 28	20.33	-0.42	G
SGP1:29	00 56 51.2	-28 57 53	20.78	-0.39	-
SGP1:32	00 56 39.6	-28 51 53	20.21	-0.46	F
SGP1:33	00 57 55.6	-28 43 31	20.60	-0.41	-
SGP1:35	00 57 31.6	-28 55 52	20.86	-0.46	-
SGP1:36	00 56 22.4	-28 58 08	19.91	-0.35	F
SGP1:37	00 57 40.3	-28 46 42	20.71	-0.38	-
SGP1:38	00 56 27.4	-28 56 36	19.08	-0.33	F
SGP1:40	00 55 24.4	-28 35 16	19.94	-0.37	G
SGP1:41	00 55 35.0	-28 33 19	19.87	-0.35	F
SGP1:42	00 55 34.8	-28 37 37	20.57	-0.40	-
SGP1:43	00 55 06.6	-28 53 13	20.50	-0.39	F
SGP2:02	00 48 59.0	-29 06 30	19.40	-0.43	F
SGP2:03	00 48 47.6	-29 06 06	20.08	-0.33	G
SGP2:04	00 48 45.2	-29 11 28	20.94	-0.45	-
SGP2:05	00 49 22.7	-29 17 18	19.18	-0.45	A
SGP2:07	00 49 29.0	-29 20 10	20.72	-0.57	-
SGP2:08	00 49 05.5	-29 15 09	20.97	-0.70	-
SGP2:09	00 48 52.6	-29 17 27	20.74	-0.36	-
SGP2:10	00 50 00.4	-29 10 16	20.31	-0.45	F
SGP2:15	00 49 31.8	-29 11 59	19.97	-0.65	F
SGP2:17	00 49 38.3	-29 20 30	20.41	-0.80	F
SGP2:24	00 50 00.4	-29 31 32	20.71	-0.57	-
SGP2:28	00 49 59.1	-29 33 40	20.78	-0.37	-
SGP2:29	00 49 47.0	-29 40 04	20.51	-0.31	-
SGP2:31	00 48 45.6	-29 25 59	19.14	-0.47	WD
SGP2:32	00 48 11.7	-29 23 36	19.94	-0.34	F
SGP2:35	00 48 11.8	-29 20 08	18.06	-0.36	F
SGP2:37	00 48 44.5	-29 25 39	18.60	-0.44	F
SGP2:41	00 50 27.7	-29 16 31	20.91	-0.31	-
SGP2:42	00 50 04.6	-29 17 53	18.79	-0.30	G
SGP2:43	00 50 15.4	-29 35 34	19.90	-0.47	G
SGP2:50	00 50 36.1	-29 14 49	20.14	-0.38	F

Name	R.A. (1950)	Dec.	b	u-b	
SGP3:01	00h 51m 57s.0	-28° 36′18″	19.42	-0.31	F
SGP3:07	00 52 15.6	-28 21 41	18.52	-0.51	F
SGP3:08	00 51 41.5	-28 20 04	20.17	-0.36	WD
SGP3:12	00 52 48.9	-28 33 39	20.44	-0.31	F
SGP3:14	00 53 05.7	-28 21 14	19.51	-0.14	A
SGP3:15	00 52 33.6	-28 16 17	20.21	-0.38	F
SGP3:17	00 53 20.6	-28 31 27	20.47	-0.21	F
SGP3:21	00 51 22.2	-28 44 44	18.54	0.07	F
SGP3:24	00 51 15.2	-28 39 46	20.31	-0.14	F
SGP3:26	00 51 41.8	-28 37 50	19.71	0.60	F
SGP3:28	00 53 54.8	-28 38 43	20.89	-0.37	-
SGP3:29	00 51 21.4	-28 34 58	20.48	-0.31	F
SGP3:32	00 53 15.6	-28 52 58	20.98	-0.41	-
SGP3:33	00 53 04.7	-28 44 46	19.76	-0.33	F
SGP3:36	00 53 31.4	-28 39 38	20.58	-0.43	-
SGP3:41	00 51 42.5	-28 49 25	20.18	-0.37	F
SGP3:42	00 53 58.3	-28 33 48	19.68	-0.32	F
SGP3:45	00 52 35.7	-28 19 49	20.87	-0.65	-
SGP3:46	00 52 10.1	-28 48 23	20.41	-0.51	-
SGP3:50	00 52 22.1	-28 45 28	20.54	-0.41	-

Name	R.A. (1950)	Dec.	b	u-b	ID
QSF1:02	03h 39m 47s.9	-45° 10′22″	20.26	-0.56	WD
QSF1:08	03 41 29.1	-46 16 11	20.96	-0.41	-
QSF1:14	03 40 06.0	-45 23 06	19.29	-0.61	WD
QSF1:18	03 40 58.3	-44 51 18	18.55	-0.41	F
QSF1:20	03 40 15.4	-44 59 49	20.17	-0.64	WD
QSF1:21	03 39 33.0	-45 00 24	17.94	-0.64	A
QSF1:24	03 40 13.4	-45 01 38	20.42	-0.40	G
QSF1:25	03 40 12.7	-45 02 40	20.66	-0.45	-
QSF1:26	03 40 35.0	-44 44 39	20.79	-0.53	-
QSF1:27	03 41 16.1	-45 10 19	18.12	-0.48	F
QSF1:35	03 41 56.7	-45 00 49	20.16	-0.52	BIN
QSF1:39	03 41 38.8	-44 52 52	20.10	-0.45	F
QSF1:41	03 41 09.0	-44 49 15	19.63	-0.43	F
QSF1:42	03 40 26.9	-44 59 00	20.28	-0.56	WD
QSF1:43	03 41 09.7	-44 59 30	18.25	-0.50	F
QSF1:44	03 41 26.2	-44 57 11	20.43	-0.65	WD
QSF2:01	03 45 10.6	-45 48 51	18.55	-1.34	WD(DAB)
QSF2:06	03 45 56.1	-45 55 48	19.92	-0.40	F
QSF2:07	03 44 00.7	-45 58 41	19.21	-0.97	WD(DAB)
QSF2:08	03 44 05.8	-46 06 31	20.91	-0.66	-
QSF2:11	03 44 26.8	-46 04 31	18.02	-0.43	B
QSF2:13	03 44 32.3	-46 07 22	18.96	-0.49	F
QSF2:14	03 43 30.4	-46 10 30	17.02	-0.56	F
QSF2:19	03 45 17.8	-46 09 37	18.27	-0.45	F
QSF2:21	03 45 08.9	-46 10 29	17.51	-0.65	A
QSF2:22	03 45 11.7	-46 11 52	18.35	-1.20	F
QSF2:23	03 45 48.8	-46 14 11	17.92	-0.42	G
QSF2:27	03 43 57.1	-46 17 38	17.60	-0.41	F
QSF2:33	03 44 23.1	-45 54 40	19.19	-0.93	WD
QSF2:34	03 45 57.9	-46 18 32	19.06	-0.46	F
QSF2:37	03 45 33.0	-46 04 49	20.54	-0.44	-
QSF2:38	03 46 11.8	-45 57 25	20.47	-1.03	F
QSF2:40	03 46 01.3	-46 05 39	18.85	-0.46	F
QSF2:43	03 45 45.5	-46 04 22	17.53	-0.40	F

Name	R.A. (1950)	Dec.	b	u-b	ID
QNB1:01	10h 39m 17s.8	01° 33' 07"	18.70	-0.51	F
QNB1:03	10 39 39.2	01 32 30	18.88	-0.15	A
QNB1:04	10 39 28.6	01 46 15	18.30	-0.33	A
QNB1:05	10 39 11.8	01 37 16	17.54	-0.69	F
QNB1:06	10 39 25.3	01 35 21	20.77	-0.58	-
QNB1:07	10 39 44.3	01 30 02	20.65	-0.63	-
QNB1:09	10 39 52.7	01 29 45	20.21	-0.83	G
QNB1:12	10 39 12.0	01 23 06	18.81	-0.46	F
QNB1:14	10 39 10.1	01 42 48	19.22	-0.21	A
QNB1:15	10 39 02.6	01 25 16	17.23	-0.56	F
QNB1:17	10 38 59.4	01 27 51	17.04	-0.53	F
QNB1:19	10 39 10.8	01 23 26	20.36	-0.25	A
QNB1:21	10 40 42.9	01 28 38	20.83	-0.57	-
QNB1:25	10 40 48.8	01 28 32	18.07	-0.51	F
QNB1:27	10 40 20.0	01 29 12	20.88	-0.81	-
QNB1:29	10 40 20.8	01 27 29	20.92	-0.67	-
QNB1:30	10 40 54.9	01 18 49	20.86	-0.64	-
QNB1:31	10 40 16.4	01 18 42	17.15	-0.54	F
QNB1:33	10 39 07.3	01 18 07	20.15	-0.52	F
QNB1:35	10 40 24.9	01 13 36	17.02	-0.53	F
QNB1:36	10 40 19.6	01 12 51	20.26	-0.30	-
QNB1:42	10 40 15.3	01 43 00	20.80	-0.69	-
QNB1:45	10 40 14.5	01 41 55	17.29	-0.59	F
QNB1:47	10 40 10.3	01 32 18	17.96	-0.60	F
QNB1:48	10 40 23.1	01 35 54	17.37	-0.74	F
QNB1:50	10 40 12.3	01 43 40	19.77	0.07	F
QNB2:03	10 40 24.1	01 09 10	18.45	-0.51	F
QNB2:04	10 40 28.7	00 58 30	20.77	-0.70	-
QNB2:08	10 40 27.8	01 00 39	20.62	-0.54	-
QNB2:09	10 40 45.8	01 01 51	17.04	-0.62	F
QNB2:10	10 41 36.8	01 08 22	18.54	-1.07	A
QNB2:11	10 41 51.8	01 15 06	19.99	-0.53	F
QNB2:12	10 41 46.6	01 15 54	18.88	0.01	B
QNB2:14	10 42 19.3	01 08 15	20.82	-0.66	-
QNB2:16	10 42 32.2	01 06 44	20.16	-0.66	F
QNB2:18	10 42 06.4	01 04 55	18.28	-0.51	F
QNB2:19	10 41 33.1	01 03 26	18.30	-0.56	F
QNB2:20	10 42 06.9	01 00 30	20.12	-0.67	F
QNB2:21	10 41 40.0	00 56 02	19.83	-0.47	F
QNB2:22	10 42 23.1	00 56 11	20.51	-0.54	-
QNB2:27	10 42 22.3	00 55 45	20.91	-0.98	BIN
QNB2:29	10 41 52.4	00 59 38	19.94	-0.52	F
QNB2:30	10 41 03.3	00 52 46	18.68	-0.59	F
QNB2:31	10 40 24.3	00 54 54	18.77	-0.42	A
QNB2:32	10 40 44.8	00 54 16	20.28	-0.16	F
QNB2:33	10 40 24.7	00 45 14	20.37	-0.38	F
QNB2:34	10 41 10.9	00 55 33	20.08	-0.58	G
QNB2:35	10 40 42.4	00 53 41	20.94	-0.52	-
QNB2:39	10 40 54.0	00 50 15	18.77	-0.81	F
QNB2:43	10 41 19.9	00 42 16	17.43	-0.51	F
QNB2:44	10 42 15.6	00 52 01	20.82	-0.55	-

Name	R.A. (1950)	Dec.	b	u-b	ID
QNY1:03	12h 33m 10s.0	-00° 53′ 32″	17.13	-0.55	B
QNY1:10	12 33 27.6	-00 34 40	17.03	-0.53	F
QNY1:15	12 33 19.0	-00 24 09	17.14	-0.47	F
QNY1:18	12 34 55.8	-00 38 17	18.27	-0.49	A
QNY1:20	12 34 36.5	-00 36 47	20.94	-0.46	-
QNY1:21	12 34 17.3	-00 44 48	17.70	-0.50	F
QNY1:22	12 34 49.7	-00 39 53	19.39	-0.45	F
QNY1:23	12 34 30.4	-00 43 57	17.93	-0.54	F
QNY1:34	12 34 08.2	-00 27 18	21.00	-0.58	-
QNY1:35	12 34 08.1	-00 27 43	20.67	-0.45	-
(QNY1:37	12 34 04.6	-00 49 38	21.23	-0.79	-)
QNY1:38	12 33 45.6	-00 55 50	20.98	-0.56	-
QNY1:41	12 34 23.0	-00 46 04	17.41	-0.52	F
QNY1:44	12 33 51.1	-00 45 25	18.18	-0.64	F
(QNY2:01	12 35 27.7	00 19 53	21.26	-0.78	-)
QNY2:06	12 36 03.5	00 35 12	19.20	-1.11	WD
(QNY2:08	12 35 13.2	00 31 01	21.02	-0.52	-)
QNY2:13	12 34 36.2	00 33 37	19.69	-0.47	F
QNY2:17	12 34 13.8	00 14 19	19.95	-0.45	F
QNY2:18	12 35 44.7	00 15 46	20.13	-0.48	F
(QNY2:20	12 34 07.3	00 17 56	21.18	-0.74	-)
QNY2:23	12 35 33.6	00 14 14	18.49	-0.46	F
QNY2:31	12 36 01.2	00 04 22	20.70	-0.54	-
QNY2:33	12 35 59.7	00 07 32	20.19	-0.51	F
QNY2:34	12 35 56.6	00 12 02	20.91	-0.88	-
(QNY2:35	12 36 17.9	00 08 35	21.31	-1.21	-)
QNY2:36	12 36 08.0	00 10 53	20.94	-0.71	-
QNY2:40	12 35 09.9	00 01 17	21.00	-0.54	-
QNY2:41	12 35 41.6	00 02 33	18.54	-0.47	F

Name	R.A. (1950)	Dec.	b	u-b	ID
QNA1:02	13h 35m 48s.6	00° 21′ 39″	20.33	-0.31	F
QNA1:05	13 36 01.5	00 21 21	19.07	-0.53	F
QNA1:06	13 35 10.5	00 14 34	20.34	-0.33	-
QNA1:09	13 35 22.4	00 19 32	19.96	-0.39	A
QNA1:10	13 36 04.8	00 08 00	19.48	-0.65	WD
(QNA1:11	13 35 53.5	00 08 32	21.34	-0.44	-)
QNA1:12	13 35 55.7	00 09 18	20.01	-0.39	F
QNA1:13	13 35 12.8	00 08 37	19.47	-0.30	WD
QNA1:14	13 35 42.9	00 16 30	20.31	-0.35	-
QNA1:17	13 36 11.6	00 04 53	19.13	-0.33	F
QNA1:19	13 36 39.6	00 31 27	19.75	-0.30	F
QNA1:23	13 37 01.2	00 34 51	19.27	-0.34	F
(QNA1:26	13 36 29.2	00 33 25	20.60	-0.35	-)
QNA1:29	13 35 54.7	00 26 00	20.50	-0.51	-
QNA1:32	13 35 40.8	00 30 31	19.44	-0.32	F
QNA1:33	13 35 38.0	00 36 38	19.35	-0.33	G
QNA1:34	13 35 31.8	00 29 31	19.11	-0.35	F
(QNA1:37	13 36 00.6	00 32 54	21.28	-1.48	-)
QNA1:40	13 36 34.6	00 16 13	18.05	-0.38	F
(QNA1:43	13 36 08.1	00 11 39	20.68	-0.40	-)
QNA1:46	13 37 16.8	00 20 30	19.47	-0.37	F
QNA1:48	13 36 08.1	00 20 30	18.41	-0.31	F

Name	R.A. (1950)	Dec.	b	u-b	ID
QSM1:02	22h 06m 01s.6	-19° 20′55″	19.06	-0.59	F
QSM1:04	22 05 36.3	-19 31 30	19.64	-0.52	F
QSM1:05	22 06 44.9	-19 19 49	19.46	-0.63	F
QSM1:06	22 07 36.4	-19 14 05	20.52	-0.57	-
QSM1:07	22 06 23.8	-19 18 46	18.88	-0.54	A
QSM1:08	22 07 19.1	-19 16 47	19.96	-1.11	F
QSM1:09	22 06 15.6	-19 09 56	18.88	-0.81	F
QSM1:10	22 07 18.3	-19 10 56	19.90	-0.66	BIN
QSM1:11	22 07 30.4	-19 15 01	19.16	-0.60	F
QSM1:12	22 06 43.5	-19 13 09	19.43	-0.69	F
QSM1:13	22 06 21.2	-19 24 28	19.66	-0.61	F
QSM1:17	22 06 35.2	-19 09 28	18.06	-0.58	A
QSM1:18	22 07 50.8	-19 26 05	18.39	-0.61	F
QSM1:20	22 08 12.2	-19 22 07	18.99	-0.61	F
QSM1:23	22 07 04.4	-19 40 43	18.52	-0.62	F
QSM1:27	22 08 07.3	-19 28 25	18.26	-0.53	F
QSM1:28	22 07 32.4	-19 53 59	20.74	-0.86	-
QSM1:29	22 07 27.9	-19 26 18	18.35	-0.69	F
QSM1:33	22 07 51.8	-19 24 38	18.80	-0.64	F
QSM1:39	22 07 11.5	-19 44 50	19.07	-0.55	F
QSM1:40	22 07 45.4	-19 10 13	19.04	-0.67	F
QSM1:41	22 06 20.0	-19 39 17	18.49	-0.51	F
QSM1:43	22 05 47.0	-19 36 43	19.24	-0.70	F
QSM1:44	22 06 44.4	-19 44 33	19.46	-0.58	F
QSM2:01	22 05 50.5	-20 12 50	18.49	-0.57	F
QSM2:02	22 07 02.1	-20 22 15	18.89	-0.72	F
QSM2:04	22 07 22.4	-20 20 15	20.50	-0.69	-
QSM2:05	22 06 14.8	-20 19 03	18.42	-0.74	A
QSM2:06	22 06 06.6	-20 20 27	19.67	-0.59	F
QSM2:10	22 05 58.1	-20 00 46	17.23	-0.75	F
QSM2:11	22 05 53.9	-19 55 23	17.26	-0.68	F
QSM2:12	22 06 10.9	-19 58 53	17.42	-0.57	F
QSM2:15	22 06 46.3	-20 09 13	18.35	-0.65	F
QSM2:17	22 08 22.0	-20 10 00	19.23	-0.54	F
QSM2:19	22 07 07.8	-20 06 44	18.21	-0.54	F
QSM2:21	22 07 46.3	-20 06 35	19.33	-0.80	F
QSM2:24	22 07 51.9	-20 03 08	18.96	-0.51	F
QSM2:25	22 07 13.3	-20 10 34	18.94	-0.59	F
QSM2:26	22 07 35.2	-20 09 15	19.94	-0.52	F
QSM2:29	22 07 32.4	-20 02 19	17.65	-0.61	F
QSM2:30	22 07 24.8	-20 01 07	17.50	-0.65	F
QSM2:35	22 07 21.4	-20 00 19	18.31	-0.53	F
QSM2:38	22 06 35.8	-19 50 16	19.93	-1.03	F
QSM2:39	22 06 28.7	-19 53 00	20.13	-0.68	F
QSM2:40	22 06 43.9	-20 00 53	19.75	-0.75	F
QSM2:41	22 06 56.5	-19 58 44	19.33	-0.56	F

APPENDIX D

FAINT UVX SURVEY: CATALOGUE OF UNIDENTIFIED OBJECTS

Name	R.A. (1950)	Dec.	b	u-b	ID
SGP1:23	00h 56m 41s.1	-29° 07' 36"	20.79	-0.35	Q?
SGP1:34	00 57 27.0	-28 48 51	20.76	-0.32	?
SGP1:45	00 55 15.2	-28 39 22	20.34	-1.29	Q?
SGP2:21	00 49 10.2	-29 31 31	20.79	-0.40	?
SGP2:23	00 49 01.4	-29 38 55	20.72	-0.48	?
SGP2:26	00 48 55.7	-29 37 51	20.27	-0.35	CONT
SGP2:30	00 48 30.5	-29 22 34	20.27	-0.41	Q?
SGP3:03	00 52 24.2	-28 27 39	20.94	-0.68	Q?
SGP3:04	00 51 58.2	-28 38 45	20.97	-0.54	?
SGP3:06	00 52 16.5	-28 36 08	20.90	-0.60	?
SGP3:13	00 52 43.0	-28 33 40	20.99	-0.46	NL?
SGP3:16	00 53 37.9	-28 26 54	20.09	-1.19	CONT
SGP3:44	00 52 26.9	-28 47 11	20.41	-0.52	?
SGP3:47	00 52 02.8	-28 50 08	20.90	-0.55	?
QSF1:13	03 40 05.0	-45 12 03	20.89	-0.50	?
QSF2:02	03 45 14.5	-45 47 47	20.30	-0.49	Q
QSF2:10	03 43 14.4	-46 00 47	20.69	-0.42	?
QSF2:24	03 45 41.7	-46 16 02	20.48	-0.44	Q?
QSF2:32	03 44 45.7	-46 14 43	20.85	-0.53	Q?
QNB1:02	10 39 46.2	+01 37 43	20.92	-0.73	Q?
QNB1:11	10 39 09.6	01 26 34	20.73	-0.53	?
QNB1:39	10 39 18.2	01 13 19	20.79	-0.59	?
QNB1:41	10 39 56.5	01 34 15	20.79	-0.56	?
QNB1:46	10 39 55.1	+01 48 05	20.98	-1.01	Q?
QNB2:38	10 40 42.1	00 54 42	20.81	-0.81	?
QNB2:48	10 41 03.5	00 42 11	19.94	-0.80	?
QNB2:49	10 41 13.3	00 42 00	20.11	-0.16	?
QNY1:11	12 33 36.0	-00 31 33	20.98	-0.90	Q?
QNY1:12	12 33 57.2	-00 33 03	20.89	-0.53	Q?
QNY1:14	12 33 50.8	-00 42 52	20.98	-0.90	Q?
QNY1:33	12 34 28.2	-00 21 27	19.98	-0.46	Q?
QNY1:39	12 34 16.7	-00 46 56	20.23	-0.50	?
QNY1:40	12 33 52.4	-00 54 18	20.70	-0.91	?
(QNY1:42	12 34 06.3	-00 48 39	21.07	-0.76	Q?)
QNY2:28	12 35 56.2	00 03 01	19.51	-0.52	?
QNY2:42	12 35 43.5	+00 00 21	20.82	-0.60	Q?
QNY2:44	12 34 43.6	00 02 23	20.66	-0.51	?
QNA1:07	13 35 43.5	00 19 52	20.49	-0.55	?
QNA1:16	13 35 38.3	00 05 36	20.18	-0.57	?
QNA1:38	13 36 02.4	00 20 48	20.09	-0.41	?
QSM1:14	22 07 00.9	-19 07 42	19.97	-1.47	CONT
QSM2:28	22 07 32.4	-19 53 59	20.74	-0.86	?
QSM2:37	22 06 38.5	-19 47 20	20.00	-1.23	CONT